

RADIONUCLIDE MIGRATION
PROCESSES IN A
CRYSTALLINE ROCK
ENVIRONMENT AND THE
MIGRATION PARAMETERS
OF BOHEMIAN MASSIF
ROCKS

Authors: Václava Havlová et al.

Praha, 2020

PROJECT NAME: Research support for the safety assessment of the deep geological repository

REPORT: Radionuclide migration processes in a crystalline rock environment and the migration parameters of rocks of the Bohemian Massif

Final report. Revision 1

Internal SURAO number: SURAO-2019-3620

Internal contractor number: PB-2019-ZL-S300-Transport1

Bibliography: Havlová V., Zuna M., Brázda L., Kolomá K., Galeková E., Rosendorf T., Jankovský F. (2020): Radionuclide migration processes in a crystalline rock environment and the migration parameters of rocks of the Bohemian Massif. – MS SURAO, Final report 333/2018/EN.

Institutions:

ÚJV Řež, a. s.

AUTHORS: Václava Havlová, Milan Zuna, Lukáš Brázda, Kateřina Kolomá, Eva Galeková, Tomáš Rosendorf, Filip Jankovský

Lukáš Vondrovic

Project manager (SÚRAO)

15.5.2020

Václava Havlová

Project manager (ÚJV Řež, a.s.)

15.5.2020

Content

1	Introduction	18
2	Basic set of relevant radionuclides	20
3	The transport parameters considered	21
4	Properties of the rock that affect radionuclide transport	23
4.1	Selection and preparation of the samples	23
4.1.1	Sites	23
4.1.2	Sample preparation	28
4.2	Mineralogical composition of the rocks	29
4.2.1	Methodology	29
4.2.2	Results and evaluation	30
4.3	Petrology of the fracture fillings and alterations	32
4.4	Porosity ε and density ρ of the rocks	34
4.4.1	Measurement of porosity via the water saturation method	34
4.4.1.1	Results and evaluation	36
4.4.2	Mercury porosimetry	38
4.4.3	Description of the pore space employing the micro DFN model approach	41
4.4.3.1	Samples	42
4.4.3.2	C-14 PMMA method (University of Helsinki)	47
4.4.3.3	μ DFN simulation methodology	50
	Model solution	52
	2D simulation	52
	3D simulation	56
4.4.3.4	Summary	63
4.5	Determination of the cation exchange capacity of the rock	64
4.5.1	The rock samples and their treatment	64
4.5.2	Determination of the CEC	65
4.5.3	CEC verification using sorption isotherms	67
4.5.4	Determination of the specific surface area and mercury porosity	69
5	Sorption of radionuclides on granitic rocks	73
5.1	Methodology	73
5.1.1	Description of the solid and liquid phases	75
5.1.1.1	Description of the solid phase (characterisation of the rock fractions used)	75
5.1.1.2	Properties of the solutions used	75

5.2	Results and evaluation	75
5.2.1	Caesium.....	75
5.2.2	Strontium.....	80
5.2.3	Selenium	82
5.2.4	Uranium	85
5.2.5	Chlorine.....	89
5.2.6	Iodine	90
5.2.7	Europium.....	91
5.2.8	Summary of the results	97
6	Diffusion of radionuclides in granite rock environments.....	104
6.1	Methodology	104
6.2	Arrangement of the Experimental Apparatus at ÚJV Řež	104
6.2.1	Evaluation of the results of the penetration diffusion experiments	105
6.3	Properties of the rock samples	107
6.4	Properties of the solutions	108
6.5	Results and evaluation	108
6.6	Discussion.....	117
7	Hydrochemistry of the groundwater at the Bukov URF.....	119
7.1	Composition of the water in granitic rock massifs	119
7.2	Measurement of the hydrochemical parameters in borehole S-18	122
7.2.1	Instrumentation	122
7.2.2	Measurement procedure	123
7.2.3	Results of the hydrochemical measurement of borehole S-18 (vertical profiling) 124	
7.2.4	Groundwater sampling	126
7.2.5	Long-term measurement of the electrochemical quantities in borehole S18 (ZK- 3S) 129	
7.2.6	Inflows to borehole S18 - recharge tests	133
7.2.7	Evaluation	134
8	Conclusion	136
9	Literature	138
10	Appendices.....	144
	Appendix 1 Overview of the results of the determination of porosity and density via the water saturation method for samples from the sites.....	144
	Appendix 2 Petrographic description of the fracture and altered rock samples	149

Appendix 3 Recommended procedure for determining the Hg porosimetry of rock samples	158
Appendix 4 Helsinki University "Report on the Determination of the Porosity of Samples via the C14.PMMA Method"	160

List of Figures:

Fig. 1 Images of extracted fracture fillings and altered core sections (Bukov), a) S1_40.3 m b) ZK2-13 m c) S1_87.8 m d) S8_47.8 m e) BZ_317 m f) S1_80 m.....	27
Fig. 2 a) Example of the drill-cutting of GRB (granulite) samples from a rock block, b) drill core samples following formatting for the laboratory analysis	28
Fig. 3 left: BB 200 jaw crusher (Retsch), right: crushed rock sample	29
Fig. 4 PM 200 planetary ball mill (Retsch), AS 300 sieve shaker (Retsch) and a UV bath for sieve cleaning (description from right to left).....	29
Fig. 5 Example of the assessment of the drying curve of a rock sample.....	35
Fig. 6 Density of the samples (kg m^{-3}) from the sites	36
Fig. 7 Porosity of the samples (%) from the sites.....	36
Fig. 8 Density of the samples (kg m^{-3}) from the sites	37
Fig. 9 Porosity of the samples (%) from the sites.....	37
Fig. 10 Density (kg m^{-3}) of the S-3 a S-4 core.....	38
Fig. 11 Porosity (%) of the S-3 and S-4 core samples	38
Fig. 12 Density (kg m^{-3}) of the S-3 and S-4 core samples depending on the rock type	38
Fig. 13 Porosity (%) of the S-3 and S-4 samples versus rock type	38
Fig. 14 Preparation of $7 \times 7 \times 20$ mm samples for the study of the effective and Hg porosity of the D2 sample (Deštná) (50 mm)	39
Fig. 15 Prepared $7 \times 7 \times 20$ mm samples for the study of Hg porosity.....	39
Fig. 16 Images of a sample from the Deštná site; middle, an optical microscope image (crossed nickels - E. Sasao, JAEA); bottom, the resulting porosity distribution following impregnation with C-14 PMMA	44
Fig. 17 Images of a sample from the Horka site; middle, an optical microscope image (crossed nickels - E. Sasao, JAEA); bottom, the resulting porosity distribution following impregnation with C-14 PMMA	44
Fig. 18 Images of a sample from the Čertovka site; middle, an optical microscope image (crossed nickels - E. Sasao, JAEA); bottom, the resulting porosity distribution following impregnation with C-14 PMMA.....	45
Fig. 19 Images of a sample from the Bukov URF site, amphibolite B2-1; middle, an optical microscope image (crossed nickels - E. Sasao, JAEA); bottom, the resulting porosity distribution following impregnation with C-14 PMMA	45

Fig. 20 Images of a sample from the Bukov URF site, migmatite B3-3; middle, an optical microscope image (crossed nickels - E. Sasao, JAEA); bottom, the resulting porosity distribution following impregnation with C-14 PMMA	46
Fig. 21 Porosity values as measured via the two methods (C-14 PMMA and gravimetrically at UniHelsinki and at ÚJV Řež, a. s.).....	49
Fig. 22 D_e values ($m^2 s^{-1}$) for HTO, ^{36}Cl and ^{125}I , measured for the rock samples via the penetration diffusion method	49
Fig. 23 Cumulative pixel porosity for the various samples (B2_1B orange, B3_3A purple; D2 yellow, pZV1 blue and TIV1 green)	50
Fig. 24 Schematic representation of the 2D (left) and 3D (right) microCPM models	51
Fig. 25 Locations of selected elements that represent the characteristic areas of the samples	53
Fig. 26 Effective 3H diffusion values depending on the minimum porosity involved in the transport.....	54
Fig. 27 Analytical particle trajectories suggesting the character of the fracture interconnections in the 2D simulations	55
Fig. 28 Standardised variograms of the simulated samples	57
Fig. 29 3D model of sample D2	58
Fig. 30 Selection of the elements and their order in the 3D model layers in various versions	58
Fig. 31 Porosity distribution of the calibrated models for the various samples and tracers....	62
Fig. 32 Left: PZV1 – microfracture from a C14-PMMA image - selection 1×1 mm (47×47 pixels), 1 pixel = 21 μm . (47×47 pixels), 1 pixel = 21 μm . Right: PZV1_57_11 - scanning electron microscopy	64
Fig. 33 CEC values of the rock and fracture filling samples determined via the Cu(II)-trien method	67
Fig. 34 Sorption of the caesium isotherm on sample PZV1, $c(Cs) = 1 \cdot 10^{-5} - 9 \cdot 10^{-3} mol l^{-1}$, fraction B: 0.125–0.063 mm	68
Fig. 35 Cation exchange capacity values of the rocks as calculated from the Langmuir isotherm (Q_{max}) and the Cu(II)-trien method (CEC)	69
Fig. 36 Pore size distribution in the studied fracture filling samples	71
Fig. 37 Cumulative pore distribution curves of the studied fracture filling samples.....	72
Fig. 38 Caesium R_d values, including their expanded standard uncertainties of rock samples from the candidate sites, left: fraction C (0.63–0.125 mm), right: fraction D (0.8–0.63 mm), $c(Cs) = 2 \cdot 10^{-5} mol l^{-1}$	79
Fig. 39 Strontium R_d values, including their expanded standard uncertainties, of rock samples from the candidate sites, left: fraction C (0.63–0.125 mm), right: fraction D (0.8–0.63 mm), $c(Sr) = 2 \cdot 10^{-5} mol l^{-1}$	82
Fig. 40 Selenite R_d values of rock samples from the candidate sites, left: fraction C (0.63–0.125 mm), right: fraction D (0.8–0.63 mm), $c(Se) = 2 \cdot 10^{-5} mol l^{-1}$	85

Fig. 41 Uranium R_d values of rock samples from the candidate sites, left: fraction C (0.63–0.125 mm), right: fraction D (0.8–0.63 mm), $c(U) = 2.6 \cdot 10^{-4} \text{ mol l}^{-1}$	89
Fig. 42 Chlorine R_d values of the fracture filling rock samples from the candidate sites, fraction C (0.63–0.125 mm), $c(Cl) = 2.1 \cdot 10^{-4} \text{ mol l}^{-1}$	90
Fig. 43 Iodine R_d values of the fracture filling rock samples from the candidate sites, fraction C (0.63–0.125 mm), $c(I) = 2 \cdot 10^{-5} \text{ mol l}^{-1}$	91
Fig. 44 Sorption of Eu on selected rocks (the formation of Fe-hydroxide rust layers).....	92
Fig. 45 E_h -pH diagrams of Eu in the SGW2 a) with solid phases, b) without solid phases ...	95
Fig. 46 E_h -pH diagrams of Eu in the DW a) with solid phases, b) without solid phases	96
Fig. 47 Sorption of selected radionuclides on the rock samples (Cs, Sr, Se, U) and fracture filling samples (Cs, Sr, Se, U, Cl, I) ■ fraction C: 0.63–0.125 mm, ■ fraction D: 0.8–0.63 mm	99
Fig. 48 Dependence of the R_d values of the radionuclides on the plagioclase content of the rock samples for the studied radionuclides: Cs graph - fractions C and D; Sr graph - fraction C; Se graph - fraction C; U graph - fraction C. Fraction C: 0.63–0.125 mm, fraction D: 0.8–0.63 mm (note: the Cs graph does not show the R_d value of the PZV1 durbachite, the high sorption of which on PZV1 was due to the higher biotite content in the sample)	101
Fig. 49 Dependence of the R_d values of the radionuclides on the biotite content of the rock samples for the studied radionuclides: Cs graph - fractions C and D; Sr graph - fraction C; Se graph - fraction C; U graph - fraction C. Fraction C: 0.63–0.125 mm, fraction D: 0.8–0.63 mm (note: the Cs graph does not show the R_d value of the PZV1 durbachite, the high sorption of which on PZV1 was due to the higher biotite content in the sample)	103
Fig. 50 Basic arrangement of the cells for the laboratory diffusion experiments (from left): inlet tank - sample - outlet tank	104
Fig. 51 Diffusion cell for the penetration diffusion experiments: ÚJV Řež design with various reservoir sizes	105
Fig. 52 Penetration curves (the development of relative volumetric activity in the outlet reservoirs) for the diffusion experiments with tritium (^3H), iodide (^{125}I) and chloride (^{36}Cl) ...	109
Fig. 53 Effective diffusion coefficient values (analytical solution) of tritium (^3H) versus anions (chloride ^{36}Cl , iodide ^{125}I)	110
Fig. 54 Effective diffusion coefficient values (analytical solution) of tritium (^3H) depending on the porosity of the sample (determined by the drying method).....	111
Fig. 55 Average D_e values for ^3H , ^{36}Cl and ^{125}I for igneous and metamorphic rocks.....	118
Fig. 56 Piper diagram of the groundwater composition according to Tab. 45.....	120
Fig. 57 Minisonde 5 - MS5 fy OTT multiparametric probe, packer with cable bushing	123
Fig. 58 Parameter development (ORP/Eh, LDO, EC, pH, T) in the S18 borehole (0–48 m).....	125
Fig. 59 Concentrations of Na, K, Mg, Ca in samples from depths of 3.5 and 10 m in borehole S18 (ZK3-S, Bukov URF)	128
Fig. 60 Concentrations of Cl^- , SO_4^{2-} , NO_3^- , F^- in the S18 borehole at depths of 3, 5 and 10 m	128

Fig. 61 Results of the chemical analysis of the groundwater from borehole S18 (samples from depths of 3, 5 and 10 m) plotted in the form of Durov and Piper diagrams - red points, grey points - comparative analysis of water from the Bukov URF (Bukovská et al. 2017).....	129
Fig. 62 Mechanical packer for a) borehole sealing b) sealing of the packer cable.....	130
Fig. 63 Measurement of the electrochemical quantities (ORP / E _h , O ₂ , pH, temperature, EC) in borehole S18 (ZK3-S) at a depth of 5 m (8. 8.–12. 9. 2018)	131
Fig. 64 Measurement of the electrochemical quantities (ORP / E _h , O ₂ , pH, temperature, EC) in borehole S18 (ZK3-S) at a depth of 10 m (17. 10.–15. 11. 2018)	132
Fig. 65 Measurement of the electrochemical quantities (ORP / E _h , O ₂ , pH, temperature, EC) in borehole S18 (ZK3-S) at a depth of 3 m (15. 11.–13. 12. 2018)	133
Fig. 66 Development of the recharge test on 8. 8. 2018 at a depth of 5 m	134
Fig. 67 Development of the recharge test on 17. 10. 2018 at a depth of 10 m	134
Fig. 68 pH condition and redox potential areas in the natural rock environment, the red values relate to the S-18 borehole	135

List of Tables:

Tab. 1 The set of relevant radionuclides for the assessment of DGR safety (SÚRAO).....	20
Tab. 2 Overview of the rock samples taken from potential DGR sites that were used for the sorption experiments	25
Tab. 3 List of the fracture filling and altered core section (Bukov) samples.....	26
Tab. 4 Sizes of the rock fractions used for the mineralogical analysis and sorption experiments	28
Tab. 5 Mineralogical composition of the rock samples taken from potential sites (wt%); fraction C: 0.63–0.125 mm, fraction D: 0.8–0.63 mm and wr (whole rock).....	30
Tab. 6 Results of the porosity testing of samples from Deštná dependent on the sample size	39
Tab. 7 Comparison of the Hg porosity results for the D2 samples determined at 6 scientific institutions	40
Tab. 8 Overview of the samples used for the measurement of porosity via the C-14 PMMA method (sent to HYRL).....	42
Tab. 9 Measurement of porosity (%) by means of two methods (C-14 PMMA, gravimetric method at Helsinki University and ÚJV).....	48
Tab. 10 Diffusion coefficient values used in the modelled assessment (Hofmanová 2018)...	52
Tab. 11 Results of the 2D simulation of elements selected from individual samples for ³ H testing	55
Tab. 12 Results of the calibrated 3D models for the various samples.....	59
Tab. 13 Relative porosity of the calibrated 3D models relative to the initial porosity determined via the ¹⁴ C-PMMA method	60

Tab. 14	Results of the leaching of the rock samples prior to the determination of the CEC	65
Tab. 15	CEC values of the rock samples determined via the Cu (II)-trien method	66
Tab. 16	Cation exchange capacity values of the rocks as calculated from the Langmuir isotherm (Q_{max}) and the Cu(II)-trien method (CEC)	68
Tab. 17	– Specific surface area values ($m^2 g^{-1}$) measured via (N_2 , Kr), porosity values determined by Hg porosimetry and cation exchange capacity (CEC_{Cu}) for the fracture filling and rock matrix materials (in grey)	70
Tab. 18	Chemical composition and pH of the SGW2 synthetic granitic water (Červinka and Gondolli 2016)	75
Tab. 19	Caesium R_d values, including their expanded standard uncertainties, of the C fractions of rock samples from candidate DGR sites, $c(Cs) = 2 \cdot 10^{-5} mol l^{-1}$, fraction C: 0.63–0.125 mm	78
Tab. 20	Caesium R_d values, including their expanded standard uncertainties, of the D fractions of rock samples from candidate DGR sites, $c(Cs) = 2 \cdot 10^{-5} mol l^{-1}$, fraction D: 0.8–0.63 mm	78
Tab. 21	Strontium R_d values, including their expanded standard uncertainties, of the C fractions of rock samples from candidate DGR sites, $c(Sr) = 2 \cdot 10^{-5} mol l^{-1}$, fraction C: 0.63–0.125 mm	80
Tab. 22	<i>Strontium R_d values, including their expanded standard uncertainties, of the D fractions of rock samples from candidate DGR sites, $c(Sr) = 2 \cdot 10^{-5} mol l^{-1}$, fraction D: 0.8–0.63 mm</i>	81
Tab. 23	Selenite R_d values, including their expanded standard uncertainties, of the C fractions of rock samples from candidate DGR sites, $c(Se) = 2 \cdot 10^{-5} mol l^{-1}$, fraction C: 0.63–0.125 mm	83
Tab. 24	Selenite R_d values ($ml g^{-1}$), including their expanded standard uncertainties, of the D fractions of rock samples from candidate DGR sites, $c(Se) = 2 \cdot 10^{-5} mol l^{-1}$, fraction D: 0.8–0.63 mm	84
Tab. 25	Uranium R_d values ($ml g^{-1}$), including their expanded standard uncertainties, of the C fractions of rock samples from candidate DGR sites, $c(U) = 2.6 \cdot 10^{-4} mol l^{-1}$, fraction C: 0.63–0.125 mm	87
Tab. 26	Uranium R_d values ($ml g^{-1}$), including their expanded standard uncertainties, of the D fractions of rock samples from candidate DGR sites, $c(U) = 2.6 \cdot 10^{-4} mol l^{-1}$, fraction D: 0.8–0.63 mm	88
Tab. 27	Chlorine R_d values, including their expanded standard uncertainties, of the C fractions of rock samples from candidate DGR sites, $c(Cl) = 2 \cdot 10^{-4} mol l^{-1}$, fraction C: 0.63–0.125 mm; for the fracture filling samples	89
Tab. 28	Iodine R_d values ($ml g^{-1}$), including their expanded standard uncertainties, of the C fractions of rock samples from candidate DGR sites, $c(I) = 2 \cdot 10^{-5} mol l^{-1}$, fraction C: 0.63–0.125 mm; for the fracture filling samples	90
Tab. 29	Overview of the designated reaction devices for the sorption and desorption of Eu	92
Tab. 30	Sorption and desorption of Eu on the fractured rock samples	92
Tab. 31	Sorption of europium on the device materials ($2 \cdot 10^{-5} mol l^{-1} Eu(NO_3)_3$)	93
Tab. 32	Results of the modelling of Eu speciation in SGW2 and demineralised water	94

Tab. 33 Results of the modelling of Eu speciation in SGW2	94
Tab. 34 Results of the modelling of Eu speciation in distilled water	95
Tab. 35 R_d results for selected radionuclides in the form of the C and D fractions of rock samples from the candidate sites, phase ratio 1 : 10, 7 days, fraction C: 0.63–0.125 mm, fraction D: 0.8–0.63 mm	97
Tab. 36 Comparison of the relative sorption capacities of minerals contained in granitic rocks (Ticknor et al. 1989)	100
Tab. 37 List of the diffusion experiment samples with their dimensions	107
Tab. 38 Evaluation of the effective diffusion coefficients for the D2 core samples	111
Tab. 39 Evaluation of the effective diffusion coefficients for the TIV1 core samples	112
Tab. 40 Evaluation of the effective diffusion coefficients for the PZV1 core samples	112
Tab. 41 Evaluation of the effective diffusion coefficients for the PDV1 core samples.....	113
Tab. 42 Evaluation of the effective diffusion coefficients for the GRB core samples	114
Tab. 43 Evaluation of the effective diffusion coefficients for the 2S3 core samples.....	115
Tab. 44 Evaluation of the effective diffusion coefficients for the BT core samples	115
Tab. 45 Evaluation of the effective diffusion coefficients for the GB and GC core samples.....	116
Tab. 46 Basic chemical composition of the groundwater 1) Melechov massif - average, SGW preparation (Buňatová et al. 1995), 2) Háje u Příbrami site, underground gas reservoir, seepage P-6, years 1990–1996 - average, 3) Bohemian Massif - median (Rukavičková et al. 2009), 4) Bohemian Massif, mineral waters - median (Rukavičková et al. 2009), 5) Bohemian Massif, fossil water - median (Rukavičková et al. 2009), 6) Jáchymov, source Běhounek, borehole HG-1, 7) Čertovka site, borehole TIV-1 (Havlová et al. 2015a), 8) Magdaléna site, borehole N-2 (Havlová et al. 2015), 9) Horka site, borehole NT-2 (Havlová et al. 2015), 10) Čihadlo site, borehole DE-2 (Havlová et al. 2015a), 11) Březový potok site, borehole HV-5 (Havlová et al. 2015a), 12) Hrádek site, borehole DC-1 (Havlová et al. 2015), 13) Kraví Hora site, borehole S-1, Bukov URF (Havlová et al. 2015a), 14) Bukov URF (600 m) - average, SGW2 preparation, 15) Rožná Mine (1000 m)) - average, SGW3 preparation	119
Tab. 47 Suggested chemical composition of the SGW2 and SGW3 groundwaters based on the real analysis of groundwater from the Bukov URF and Rožná mine	121
Tab. 48 Overview of the measurements in borehole S18 (ZK3-S).....	124
Tab. 49 Contents of the main cations in samples taken from borehole S-18 (from depths of 3, 5 and 10 m).....	127
Tab. 50 Content of anions in the samples taken from borehole S-18 (from depths of 3, 5 and 10 m).....	128
Tab. 51 Results of the determination of the porosity (%) and density of the samples from the candidate sites	144
Tab. 52 Results of the determination of the porosity (%) and density of samples from the Bukov URF - 170 Kraví Hora site	147

List of text appendices:

Appendix 1 Overview of the results of the determination of porosity and density via the water saturation method for samples from the sites

Appendix 2 Petrographic description of the fracture and altered rock samples

Appendix 3 Recommended procedure for determining the Hg porosimetry of rock samples

Appendix 4 Helsinki University "Report on the Determination of the Porosity of Samples via the C14.PMMA Method"

List of electronic appendices:

Appendix 1 Export of database-T1_30112018.xls, xlm

 SÚRAO	Radionuclide migration processes in a crystalline rock environment. Final report.	Evidenční označení:
		SÚRAO TZ 333/2018

List of abbreviations:

2D	two-dimensional
3D	three-dimensional
AAS	atomic absorption spectrometry
AIBN	azobisisobutyronitrile
AMS	anisotropy of magnetic susceptibility
BET	Brunauer-Emmett-Teller surface area analysis
BUT	Brno University of Technology
CAS	Czech Academy of Science
CEC	cation exchange capacity
CGS	Czech Geological Survey
CPM	counts per minutes
ČR	Czech Republic
Cu(II)-trien	Cu(II)triethylenetetramine complex
DFN	discreet fracture network
DGR	deep geological repository
DW	distilled water
EC	electrical conductivity
GWB	The Geochemists Workbench
HDPE	high density polyethylene
HTO	tritiated water
HYRL	University of Helsinki, Department of Chemistry
ICPF	Institute of Chemical Process Fundamentals
IAEA	Japan Atomic Energy Agency
LDO	dissolved oxygen content
LOD	limit of detection
MMA	methyl methacrylate
n.a.	not applicable / was not determined
ORP	redox potential
PE	polyethylene
PMMA	polymethyl methacrylate
PP	polypropylene
PVP	underground research facility

 SÚRAO	Radionuclide migration processes in a crystalline rock environment. Final report.	Evidenční označení:
		SÚRAO TZ 333/2018

RAW	radioactive waste
SEM	scanning electron microscope
SGW	synthetic granitic water
SHE	standard hydrogen electrode
SKB	Swedish Nuclear Fuel and Waste Management Company
SNF	spent nuclear fuel
SÚRAO	Radioactive Waste Repository Authority
TD	through-diffusion experiment
TDS	total dissolved solids (total salinity)
TUO	Technical University of Ostrava
UCT	University of Chemistry and Technology
URF	underground research facility
UV	ultraviolet
WDP	waste disposal package
XPL	crossed nicols (mikroskopie ve zkřížených nikolech)
wr	whole rock
ZL	subproject

 SÚRAO	Radionuclide migration processes in a crystalline rock environment. Final report.	Evidenční označení:
		SÚRAO TZ 333/2018

Abstract

This report summarises the results of the determination of the transport parameters of granite and metamorphic rocks from the Bohemian Massif as part of the Transport 1 subproject and the Characterisation of the Bukov URF. It focuses principally on the determination of those sorption and diffusion parameters that are important in terms of the migration of radionuclides. The assessment of other related properties (such as mineral composition, porosity, density, cation exchange capacity) which are essential for the accurate interpretation of the data form a further integral part of this report.

The measurement of porosity is particularly problematic with respect to rocks with a porosity of below 1%. None of the methods used (gravimetry, mercury porosimetry, C-14 PMMA impregnation) is 100% accurate and all of them have their advantages and disadvantages. In such cases, it is always advisable to supplement the measurement of porosity with the study of the size and interconnection of the pores via a visualisation method (e.g. SEM).

With respect to the diffusion characteristics (the effective diffusion coefficient – D_e), it can be stated that although the examined samples originated from different areas of the Czech Republic and consisted of differing rock types, the diffusion efficiency coefficients obtained lay within a relatively narrow range: for ^3H $(4-10) \cdot 10^{-13} \text{ m}^2 \text{ s}^{-1}$, for ^{36}Cl $(1-10) \cdot 10^{-13} \text{ m}^2 \text{ s}^{-1}$ and for ^{125}I $(1-4) \cdot 10^{-13} \text{ m}^2 \text{ s}^{-1}$. Anion exclusion was detected in the metamorphic rock samples, thus resulting in lower D_e values for ^{36}Cl and ^{125}I than for ^3H .

From the point of view of the sorption behaviour of the radionuclides, it is possible to conclude that caesium radionuclides are strongly sorbed on rock materials, strontium radionuclides exhibit a slightly lower sorption tendency, and selenite and uranium U(VI) radionuclides can be classified as non-sorbing radionuclides.

Moreover, in addition to the study of rock matrix materials, the sorption experiments also focused on the study of the sorption of the afore-mentioned radionuclides on selected fracture fillings (with contents of chlorite carbonate, kaolinite), supplemented with ^{125}I , ^{36}Cl , Eu nuclides. Here also, it was observed that Cs radionuclides sorb most intensively and that Se, I, Cl and U radionuclides behave in a non-sorbing way under the given conditions due to the occurrence of their anion forms in solution.

The geochemical conditions at the site, especially the pH and E_h and the O_2 and CO_2 contents of the water, and the presence of complexing agents, etc. constitute the most important conditions for the migration of radionuclides in the rock environment. The measured redox potential values, calculated relative to the standard hydrogen electrode $E_h(\text{SHE})$, measured in-situ, ranged from -200 to -250 mV at a pH of around 8 and a temperature of 15.2 to 15.4 °C. The Fe^{2+} contents were determined in two samples at 0.013 and 0.017 mmol l⁻¹ and the Fe^{3+} content was calculated at around $1 \cdot 10^{-8} \text{ mmol l}^{-1}$. The measured values corresponded to groundwater from the deep rock environment.

Keywords

repository, radioactive waste, migration, sorption, diffusion, porosity, groundwater, safety assessment

 SÚRAO	Radionuclide migration processes in a crystalline rock environment. Final report.	Evidenční označení:
		SÚRAO TZ 333/2018

Abstrakt

Tato zpráva shrnuje výsledky stanovení transportních parametrů granitických a metamorfovaných hornin z Českého masivu v rámci ZL Transport 1 a Charakterizace PVP Bukov. Zaměřila se především na stanovení sorpčních a difúzních parametrů, významných pro migraci radionuklidů. Nedílnou součástí jsou však i stanovení souvisejících vlastností, jako je mineralogické složení, porozita, hustota, kationtová výměnná kapacita, bez nichž tato stanovení nemají odpovídající výpovědní hodnotu.

Měření porozity je u hornin, kde se porozita pohybuje pod 1 %, velmi problematické. Žádná z metod není 100%, má své výhody a nevýhody a hodnoty se liší v závislosti na instituci, instrumentaci a personálním obsazení. V tomto případě je vždy vhodné doplnit měření porozity i o studium velikosti a propojení pórů vizualizačními metodami (např. SEM), které by pórovou sítí dostatečně kvantifikoval a měření specifického povrchu, který může i výrazně přispět k posouzení konzervativnosti stanovení sorpčních parametrů na mletých vzorcích.

Pro difúzní charakteristiky (efektivní difúzní koeficient D_e) lze říci, že, přestože zkoumané vzorky pochází z různých lokalit napříč ČR a jedná se o různé horninové typy, získané difúzní efektivní koeficienty se pohybují v poměrně úzkém rozmezí: pro ^3H ($4\text{--}10$) $\cdot 10^{-13} \text{ m}^2 \text{ s}^{-1}$, pro ^{36}Cl ($1\text{--}10$) $\cdot 10^{-13} \text{ m}^2 \text{ s}^{-1}$ a pro ^{125}I ($1\text{--}4$) $\cdot 10^{-13} \text{ m}^2 \text{ s}^{-1}$. U vzorků metamorfovaných hornin se podařilo prokázat aniontovou exkluzi, která vede k nižším hodnotám D_e pro ^{36}Cl a ^{125}I v porovnání s ^3H .

Z hlediska sorpčního chování radionuklidů lze konstatovat, že na materiály krystalických hornin Českého masivu se silně sorbuje cesium, stroncium vykazuje mírný sorpční charakter, seleničitan a uran U(VI) lze zařadit mezi nesorbující se radionuklidy.

Kromě prací s materiálem horninové matrice se sorpční experimenty zaměřily i na studium sorpce výše zmíněných radionuklidů na vybrané puklinové výplně (s obsahem karbonátů chloritu, kaolinitu), které bylo doplněno o nuklidy ^{125}I , ^{36}Cl , Eu. I zde se potvrdilo, že se Cs sorbuje nejintenzivněji a že Se, I, Cl a U se za daných podmínek chovají jako nesorbující se radionuklidy, a to z důvodu výskytu v aniontové formě.

Pro migraci radionuklidů v horninovém prostředí jsou velmi významné i geochemické podmínky na lokalitě, a to především pH, E_h , obsah O_2 a CO_2 ve vodě, přítomnost komplexotvorných látek atd. Změřené hodnoty oxidačně redukčního potenciálu, přepočtené vůči standardní vodíkové elektrodě $E_h(\text{SHE})$, změřené in-situ, se pohybovaly v rozmezí -200 až -250 mV při pH okolo 8 a teplotě 15,2 až 15,4 °C. Obsahy Fe^{2+} byly stanoveny ve dvou vzorcích a to 0,013 a 0,017 mmol l^{-1} a Fe^{3+} byl doložen kolem $1 \cdot 10^{-8}$ mmol l^{-1} . Změřené hodnoty odpovídají podzemním vodám z hlubokého horninového prostředí.

Klíčová slova

úložiště, radioaktivní odpady, migrace, sorpce, difúze, porozita, podzemní voda, hodnocení bezpečnosti, mikro DFN, modelování

 SÚRAO	Radionuclide migration processes in a crystalline rock environment. Final report.	Evidenční označení:
		SÚRAO TZ 333/2018

1 Introduction

This report was compiled as part of the SÚRAO-commissioned “Research Support for the Safety Assessment of a Deep Geological Repository” project which forms part of the development programme for the construction of the future Czech deep geological repository for radioactive waste (hereinafter referred to as DGR). The objective of the project is to collect the data, models, arguments and other information required so as to be able to construct the models necessary for the evaluation of potential sites for the construction of the DGR from the point of view of long-term safety. Following the conclusion of a public procurement procedure, a four-year contract was signed in July 2014 with ÚJV Řež, a. s. and its various subcontractors: the Czech Geological Survey; the Czech Technical University in Prague; the Technical University of Liberec; the Institute of Geonics of the Czech Academy of Sciences; and the Arcadis CZ a.s., PROGEO s.r.o.; Chemcomex Praha, a.s. and Research Centre Řež s.r.o. corporations on the provision of research support for the assessment of long-term safety in the following areas:

- (i) The behaviour of spent nuclear fuel (SNF) and those forms of radioactive waste (RAW) that are not suitable for disposal in surface repositories in a deep geological repository environment;
- (ii) The behaviour of SNF and RAW waste disposal packages (WDP) in a deep geological repository environment;
- (iii) The behaviour of buffer, backfill and other construction materials in a deep geological repository environment;
- (iv) Disposal chamber boring techniques and their influence on the properties of the surrounding rock environment;
- (v) The behaviour of the rock environment;
- (vi) The transport of radionuclides from the DGR;
- (vii) Other characteristics of the candidate sites which may potentially affect overall DGR safety.

The aim of this subproject entitled “Input parameters and process models for the assessment of radionuclide transport through the rock environment” (research field: “The transport of radionuclides from the DGR”) is to obtain the input parameters and process models necessary to form an assessment of radionuclide transport through the rock environment, which will serve as support information for the contracting authority in accordance with the above-mentioned “the transport of radionuclides from the DGR” research field (vi).

This subproject addresses the following:

- The summarisation and analysis of the transport processes, models and computational codes utilised for the determination of transport pathways and the assessment of radionuclide transport through the rock environment.
- The selection of suitable process models that allow both for the description of radionuclide transport in crystalline rock and the determination of the transport pathways of candidate sites based on input from 3D structural-geological and

 SÚRAO	Radionuclide migration processes in a crystalline rock environment. Final report.	Evidenční označení:
		SÚRAO TZ 333/2018

hydrogeological models that have been compiled in the context of previous respective subprojects, the updated analysis of research findings from abroad and the determination of transport pathways at selected sites according to requirements set by SÚRAO.

- The summarisation and updating of rock environment transport parameter estimates for the candidate sites based on the requirements of the contracting authority in the form of a parameter database that includes an estimate of the various uncertainties based on the analysis both of current knowledge obtained from the Czech DGR development programme and the analysis of foreign research findings.
- The verification of the models selected and the application of computational codes for the determination of transport pathways at the candidate sites.
- The verification and comparison of the transport characteristics of samples extracted from the various rock environments considered for the siting of the Czech DGR.

This report provides a summary of the results of the determination of transport parameters (porosity, sorption coefficients and diffusion coefficients for selected radionuclides) obtained via the experimental research of samples extracted from potential DGR sites.

 SÚRAO	Radionuclide migration processes in a crystalline rock environment. Final report.	Evidenční označení:
		SÚRAO TZ 333/2018

2 Basic set of relevant radionuclides

The basic set of relevant radionuclides was based on the Client's instructions and previous research such as the Update of the Reference Project 2011. The relevant radionuclides are listed in Tab. 1.

Tab. 1 The set of relevant radionuclides for the assessment of DGR safety (SÚRAO)

Activation products	Actinides					Fission products
Be-10	Th-229	Th-230	Th-232			Se-79
C-14	Pa-231					Sr-90
Cl-36	U-233	U-234	U-235	U-236	U-238	Zr-93
Ca-41	Np-237					Tc-99
Ni-59	Pu-238	Pu-239	Pu-240	Pu-242		Pd-107
Ni-63	Am-241	Am-242m	Am-243			Sn-126
Zr-93	Cm-244	Cm-245	Cm-246			I-129
Mo-93						Cs-135
Nb-94						Cs-137
Ag-108m						Sm-151
Ho-166m						

 SÚRAO	Radionuclide migration processes in a crystalline rock environment. Final report.	Evidenční označení:
		SÚRAO TZ 333/2018

3 The transport parameters considered

The selection of the transport parameter values is based on a report by Havlová et al. (2015a), which provided a summary of the general assumptions for the assessment of transport parameters as input data for safety assessment purposes.

The identification of the most important parameters in this report was based on the following simplification of the description of the migration of radionuclides from the repository to the biosphere. Clearly, each of the parameters listed below can be further subdivided into the additional parameters that are required for the assessment thereof.

The concentration of radionuclide j from a disposal unit i which migrates to the biosphere can be expressed by the following equation which considers only 5 processes:

- decrease in the activity of radionuclides during their transport to the biosphere due to radioactive conversion,
- precipitation of radionuclides due to the exceeding of the solubility limit,
- retardation in the geosphere,
- dilution; and
- dispersion of the radionuclides in the geosphere (Vokál et al. 2009) – see eq. (3-1)

$$C_{jibio}(t) = \frac{C_{jigeo}(t) \cdot e^{-\lambda T_i R_i}}{G_i}, \quad (3-1)$$

where C_{jibio} is the concentration of radionuclide j in the biosphere, C_{jigeo} is the concentration of radionuclide j that enters the geosphere, λ is the conversion constant, T_i is the migration time of non-sorbing radionuclides into the biosphere, R_i is the retardation coefficient of the sorbing of radionuclides in the geosphere and G_i expresses the dilution and dispersion factor of the radionuclide in the rock environment.

The migration time of non-sorbing radionuclides into the biosphere is composed of the migration time of the radionuclides in the interconnected fracture system and corresponds to the time of water flow in the fractures. The interconnection of fractures constitutes one of the most important factors that influence the migration of radionuclides in the fracture environment. The total time of radionuclide flow (T_i) from one fracture is composed of the flow time through many fractures (T_k). This time corresponds to the ratio of the length of the fracture to the rate of flow of radionuclides in the fracture. Thus, in the case of the rock surrounding the waste disposal packages (WDP), it is possible to simply consider the distance between the WDPs and the hydraulically-active fault or fracture zones and the rate of water flow in the fractures corresponding to the ratio of the Darcy velocity to the transport porosity as one of the most important parameters. The geosphere dilution factor G can then be simply defined as:

$$G = \frac{Q_{G/B}}{Q_{U/G}}, \quad (3-2)$$

where $Q_{G/B}$ is the groundwater flow at the geosphere-biosphere interface and $Q_{U/G}$ is the groundwater flow at the disposal system-geosphere interface.

 SÚRAO	Radionuclide migration processes in a crystalline rock environment. Final report.	Evidenční označení:
		SÚRAO TZ 333/2018

Macrodispersion in the fracture environment exerts the same effect as dilution and is not specifically addressed mainly since it is very difficult to determine the dispersion coefficient in the fracture environment. “Microdispersion”, represented by dilution, is included in the retardation coefficient.

In the case of radionuclide sorption, one of the most important parameters consists of the retardation coefficient R_f , which is dependent on a wide range of factors that will be discussed in more detail below. The concentration of radionuclides in the geosphere is further influenced by the maximum concentration of radionuclides in the pore water of the rock.

However, it is necessary to pose the question ‘how is it possible to guarantee that the dispersion and dilution values will remain the same over thousands of years?’ Hence, it is not appropriate to base the selection of a suitable disposal environment for a deep geological repository on favourable initial dispersion and dilution values. This factor should, however, always be taken into account in the safety analysis and a certain conservative value should be determined that reflects the potential minimum dispersion and dilution value at the respective site.

The decisive parameters in terms of the decrease in the radionuclide concentration in the rock environment in the direction from the DGR for RAW to the biosphere consist of the following processes:

- **radionuclide solubility** (see the Klajmon et al. 2017 report)
- **diffusion into the rock matrix**
- **sorption on the rock matrix**

In order to describe these processes, it is necessary to be aware of other secondary parameters that characterise the rock environment, including the groundwater, i.e.:

- the porosity of the rock matrix ε ,
- the density of the rock ρ ,
- the distance to which the rock is in equilibrium with the groundwater in the fracture δ ,
- the aperture of the fracture a ,
- the groundwater composition,
- the mineralogical composition of the rock.

 SÚRAO	Radionuclide migration processes in a crystalline rock environment. Final report.	Evidenční označení:
		SÚRAO TZ 333/2018

4 Properties of the rock that affect radionuclide transport

4.1 Selection and preparation of the samples

With respect to the study of the transport parameters, the most appropriate approach was considered to be the study of samples taken from archived drill cores extracted from deep boreholes, that closely reflect the behaviour of the rock in the planned repository and which have not been significantly influenced by weathering processes.

Drill core samples were taken from the following borehole cores: PZV-1 (Pozďátky u Třebíče - Horka), TIV-1 (Tis u Blatna - Čertovka) and PDV-1 (Panské Dubenky) that was drilled as part of the FR-TI1/367 project in 2010–2011. Selected samples of metamorphic rocks from the Kraví hora site were taken from the archived S3 and S4 borehole cores extracted at the Bukov URF (Bukovská et al. 2017).

Since no rock cores were available from the other sites, samples were taken from the surface. The samples from the Březový Potok and Hrádek sites were provided by SÚRAO and consisted of samples that had already been subjected to the determination of AMS (Hanák et al. 2017). The samples from the Čihadlo (granite) and Kraví hora (granulite) sites were collected from operational quarries from freshly broken rock blocks in cooperation with the CGS. Core samples were prepared via the drilling of the samples taken at the sites followed by formatting to the required dimensions.

Safety assessment calculations to date have assumed that fractures are not covered by mineral fillings. This approach, however, is too conservative and in order to reduce the number of uncertainties in the safety calculations it is necessary that the sorption properties of the fracture fillings be determined. Since altered minerals, newly-formed secondary minerals and fracture fillings are capable of significantly influencing the sorption and transport properties, particular attention was devoted to this area in 2019.

4.1.1 Sites

110 Březový potok (BT - Defurovy Lažany, N49°24'25.6", E13°39'57.9")

Amphibolite-biotitic granodiorite (BT – Blatná type) from Defurové Lažany was assessed as the basic rock for the Březový potok site. A further type found at the site consists of amphibolite-biotitic granodiorite (CT – Červená type) from the Barák site. Both types belong to the Blatno suite of the Central Bohemian plutonic complex (Hanák et al. 2017).

Samples of amphibolite-biotitic granodiorite from the Defurovy Lažany location (samples BT8 and BT3) were used in the diffusion experiments.

120 Čertovka (TIV-1 - Tis u Blatna, N50°04'54.4", E13°20'53.6")

The granitoids of this area belong to the Čistá-Jesenice massif (Bohemian Massif). This rock body is a particularly complicated structure in which the Čistá granodiorite takes the form of an oval bole in Tis granite. The Čistá-Jesenice massif is a whole forms part of the Louny pluton.

 SÚRAO	Radionuclide migration processes in a crystalline rock environment. Final report.	Evidenční označení:
		SÚRAO TZ 333/2018

The basic rock assessed consisted of a medium-grained biotitic granite of the Tis pluton from the Tis u Blatna location.

The rock from the TIV-1 borehole consists of coarse-grained non-porphyric biotitic Tis granite that is homogeneous over long distances (Rukavičková et al. 2011).

130 Čihadlo (D2 - Deštná quarry, N49°15'9.688", E14°55'20.150")

The designated area is located in the Moldanubian pluton, so-called Číměř granite including the surrounding rocks. The basic rock type found at this site consists of medium-grained muscovite-biotitic granite of the Eisgarn type, Klenov subtype (Hanák et al. 2017). The rock block samples were taken from freshly broken rock at the Deštná quarry consisting of medium- to coarse-grained muscovite-biotitic granite, porphyric in places.

140 Horka (PZV-1 - Pozdátky u Třebíče, N49°11'38.049", E015°56'47.274")

The Horka site is located in the Třebíč massif. The basic rock consists of porphyric amphibolite-biotitic melanocratic granite to quartz syenite (melasyenite) (Hanák et al. 2017); for the purposes of this report, the rock type is referred to hereinafter simply as syenite.

The Pozdátky location lies in the Třebíč massif of the Moldanubian pluton, which constitutes the most extensive Hercynian complex of igneous rocks in the Czech Republic (Mísař 1983).

The drill core sample was taken from the archived PZV-1 borehole core, which was extracted near to a landfill site for hazardous waste around 250 metres south of the VP-5 borehole which is located around 600 m south of the village Pozdátky u Třebíče.

150 Hrádek (GB - Boršov quarry, N49°23'46.710", E15°25'49.789)

The Hrádek site is located near the village of Horní Cerekev and is characterised principally by granites of the central Moldanubian pluton, eisgarnian granite and gneiss and migmatite enclaves. The site also includes the Čeřínek granite bole. The basic rock consists of granite of the Čeřínek (GC) type from the Bromberg location. Fine-grained muscovite-biotitic granite of the Boršov (GB) type from the Boršov quarry (Hanák et al. 2017) is considered to be very similar.

Samples GB2 and GB4 from the Boršov quarry and GC3 from the Bromberg location were used for the diffusion experiments.

160 Magdaléna

No suitable samples were found to be available at the Magdalena (160) site. The outcrops at the site are characterised by weathered rock whose transport parameters do not reflect those of deeper unweathered rock. Thus, in agreement with the client, no samples were analysed from this site.

170 Kraví hora (Dolní Bory site – quarry, 49.4250744N, 16.0401256E)

This site forms part of the Strážec Moldanubicum, i.e. the eastern part of the Moldanubicum between the Svatka crystalline complex and the Třebíč Pluton. The basic rock type is biotitic granulite to granulite gneiss of the Moldanubian. The granulite body, which is located in the centre of the region, exhibits an elongated shape (Hanák et al. 2017) and is made up of light

 SÚRAO	Radionuclide migration processes in a crystalline rock environment. Final report.	Evidenční označení:
		SÚRAO TZ 333/2018

felsic granulite (grt + ky) which is banded in places. The samples to be used in the experiments were taken from the Dolní Bory quarry.

At the same time, rock core samples from a depth of 550 m at the Bukov URF were subjected to study. The Bukov URF is situated in the Rožná-Olší ore field where deep uranium mining was conducted between 1957 and 2017. From the point of view of the regional-geological division of the Bohemian Massif (Mísař 1983), the site of interest lies in a complex of highly metamorphic rocks of the northeastern edge of units of the Strážec Moldanubian, in contact with the Svratka crystalline complex.

Samples were selected of the basic rock types of the metamorphic rock in the area (migmatite S4-2, amphibolite S4-4, migmatized amphibolite S3-3, biotitic-amphibolic paragneiss S4-3, amphibolic migmatite with biotite and garnet S3-4). Further information on these samples can be found in a report by Bukovská et al. (2017).

Panské Dubenky (PDV1 borehole, N49°12'41.103", E015°16'34.787")

The Panské Dubenky site is located in an area dominated by a massive granitoid body - the central Moldanubian massif. It consists of a late orogenic massif of deep igneous rocks which penetrated into a complex of gneisses and other metamorphic rocks of predominantly sedimentary origin at the end of the Variscan orogenic process (Černý et al. 1998). From the petrographic point of view, the deposit consists of two-mica, muscovite-biotitic granite, which is medium-grained and porphyritic; the phenocrysts consist of (especially potassium) feldspars (Černý et al. 1998).

The PDV-1 borehole is located around 100 m east of the upper quarry deposit area in Panské Dubenky.

Tab. 2 Overview of the rock samples taken from potential DGR sites that were used for the sorption experiments

Rock sample	Sampling depth (m) / metreage	Rock (simplified designation)	Origin	DGR site	Site code
BT	Surface sampling	Granodiorite	Defurovy Lažany	Březový potok	110
TIV1	89.40–89.20	Granite	Tis u Blatna	Čertovka	120
D2	Surface sampling	Granite	Deštná	Čihadlo	130
PZV1	92.80–93.00	Syenite	Pozďátky u Třebíče	Horka	140
GB	Surface sampling	Granite	Boršov	Hrádek	150

 SÚRAO	Radionuclide migration processes in a crystalline rock environment. Final report.	Evidenční označení:
		SÚRAO TZ 333/2018

GRB	Surface sampling	Granulite	Dolní Bory	Kraví hora	170
S3-3	550 m 81.63–81.98	Migmatized garnet-biotitic amphibolite	Bukov URF	Kraví hora	170
S3-4	550 m 86.70–87.00	Amphibolic migmatite with biotite and garnet	Bukov URF	Kraví hora	170
S4-3	550 m 25.00–25.28	Migmatized biotite-amphibolic paragneiss	Bukov URF	Kraví hora	170
2S4-2	550 m 10.50–10.67	Biotitic migmatite with leukosome predominance	Bukov URF	Kraví hora	170
2S4-4	550 m 36.16–36.39	Fine-grained amphibolite with biotite	Bukov URF	Kraví hora	170
PDV1	Drill core - mixed sample	Granite	Panské Dubenky	--	--

In 2019, the samples from the potential DGR sites were supplemented with selected samples of altered rocks and samples with fractures. The samples were selected in cooperation with the Client (Dr. Lukáš Vondrovic, SÚRAO) from archived borehole cores extracted at the Bukov URF site (samples S1_40.3 m, S1_87.8 m, S8_47.8 m, S1_80.6 m). A further sample was taken in-situ at the Bukov URF (ZK_13 m). In connection with the study of sorption parameters, the samples were supplemented at the request of the Client with a sample taken from a fault zone/rock fall in the BZ-XIIJ main gallery (BZ-317 m) (Tab. 3 and Fig. 1).

Tab. 3 List of the fracture filling and altered core section (Bukov) samples

Sample	Metreage (m)	Rock	Description
ZK2_13m	13	Carbonate-quartz hydrothermal vein	Chlorite, clay minerals
S1_40.3m_	40.3	Muscovite-biotitic leucogranite	Significantly affected by seritisation, kaolinisation, baueritisation; abundant clay minerals
S1_87.8m	87.8	Migmatized biotitic gneiss	Affected by shear zones with chlorite, weak seritisation
S8_47.8 m	47.8	Biotitic amphibolite	Strongly affected by alteration, seritisation, amphibolite often replaced by chlorite

 SÚRAO	Radionuclide migration processes in a crystalline rock environment. Final report.	Evidenční označení:
		SÚRAO TZ 333/2018

BZ_317 m	317	Biotitic gneiss	Hydrothermal alteration, intensive seritisation, chloritisation and baueritisation, clay minerals
S1_80.6 m	80.6 m	Biotitic migmatite	Basic rock with no alteration, migmatite with lenses of leukosome, bands of melanosome



a



b



c



d



e



f

Fig. 1 Images of extracted fracture fillings and altered core sections (Bukov), a) S1_40.3 m b) ZK2-13 m c) S1_87.8 m d) S8_47.8 m e) BZ_317 m f) S1_80 m

 SÚRAO	Radionuclide migration processes in a crystalline rock environment. Final report.	Evidenční označení:
		SÚRAO TZ 333/2018

4.1.2 Sample preparation

Due to the technical requirements of the experiments it was necessary to drill-cut the cores (archived material) to a diameter of 50 mm. Rock cores with a diameter of 48–50 mm were also drill-cut from the surface samples. The rock cores were subsequently cut into smaller samples using a diamond saw for individual analysis purposes (Fig. 2). The samples taken from the sites (BT, GB, GC) were cut into 10 mm slices for the diffusion experiments.



Fig. 2 a) Example of the drill-cutting of GRB (granulite) samples from a rock block, b) drill core samples following formatting for the laboratory analysis

The samples were subsequently registered in the sample database, documented and submitted for analysis according to the experimental plan and requirements.

Parts of the samples were crushed using a BB 200 jaw crusher (Retsch) (Fig. 3). Sieving was then performed using an AS 300 analytical sieve shaking machine (Retsch); with respect to some of the fractions it was necessary to grind the samples to the required amount of a given fraction. The grinding of the samples was performed on a PM 200 planetary ball mill (Retsch) (see Fig. 4). The C and D grain fractions listed in Tab. 4 were used in the sorption experiments.

Tab. 4 Sizes of the rock fractions used for the mineralogical analysis and sorption experiments

Fraction designation	Fraction size (mm)
A	< 0.063
B	0.125–0.063
C	0.63–0.125
D	0.8–0.63

 SÚRAO	Radionuclide migration processes in a crystalline rock environment. Final report.	Evidenční označení:
		SÚRAO TZ 333/2018

E	> 0.8
---	-------



Fig. 3 left: BB 200 jaw crusher (Retsch), right: crushed rock sample



Fig. 4 PM 200 planetary ball mill (Retsch), AS 300 sieve shaker (Retsch) and a UV bath for sieve cleaning (description from right to left)

4.2 Mineralogical composition of the rocks

4.2.1 Methodology

Samples of the various fractions were ground to analytical fineness and subsequently analysed by means of X-ray diffraction on a Bruker D8 Advance X-ray powder diffractometer in the Bragg-Brentan arrangement in the CGS laboratory (Dr. František Laufek).

	Radionuclide migration processes in a crystalline rock environment. Final report.	Evidenční označení:
		SÚRAO TZ 333/2018

Powdered samples were placed on a flat substrate (diffraction-free silicon) using Lynx Eye XE detector (CuK α radiation). The diffraction pattern was recorded in an angular range of 4–80° 2 θ in 0.015° increments and a readout time of 0.8 seconds per increment.

The X-ray diffraction patterns obtained were qualitatively assessed using the Diffrac.Eva program (Bruker AXS 2015) and the PDF 2 database. The subsequent phase analysis was performed using the Rietveld method (Post and Bish 1989) in the Topas 5 program (Bruker AXS 2014). Models of the crystal structures of individual phases were obtained from the ICSD database (FIZ 2015). The scale factors of the individual phases, their lattice parameters and the size of the coherently diffracting domains were refined during the Rietveld analysis. Correction to the preferred orientation was applied.

The limit of detection of the method lies in the range of around 0.2–0.5 wt% depending on the character of the phase and its crystallinity,

4.2.2 Results and evaluation

The results of the semiquantitative analysis of the selected C fraction (0.63–0.125 mm), D fraction (0.8–0.63 mm) and wr (whole rock) rocks are shown in Tab. 5.

Tab. 5 Mineralogical composition of the rock samples taken from potential sites (wt%); fraction C: 0.63–0.125 mm, fraction D: 0.8–0.63 mm and wr (whole rock)

Rock sample	Fraction	Quartz	Plagioclase	K-feldspar	Chlorite	Mica	Amphibolite		Biotite, annite	Kaolinite	Muscovite	Pyroxene	Calcite	Titanite	Sillimanite	Haematite	Minerals probably present
							Hornblende	Cummingtonite									
PZV1	C	24.5	21.0	20.0			15.0		19.5								
	D	25.0	24.5	26.0			14.5		10.0								a
	wr	18	21.5	27.5			18.5		14.5								
TIV1	C	46.5	29.0	18.0	0.5				1.5	0.5	4.0						
	D	44.0	30.5	19.0	0.5				5.8	0.2							
	wr	44	31.5	20.5					3		1						
PDV1	C	52.0	24.5	15.0	0.5						7.0	1.0					
	D	46.0	27.0	18.0	0.5						7.0	1.5					
D2	C	43.0	30.0	20.5					2.0	1	3.5						b
	D	37.0	32.5	24.5					1.5	1	3.5						b
	wr	38	29.5	24.5					2	1	5						d
S3-3	C	8.0	59.5		0.5		26.0	2	4.0								
	D	8.5	60.0		0.5		25.0	3	3.0								c

Rock sample	Fraction	Quartz	Plagioclase	K-feldspar	Chlorite	Mica	Amphibolite	Biotite, annite	Kaolinite	Muscovite	Pyroxene	Calcite	Titanite	Sillimanite	Dolomite	Minerals probably present
S3-4	C	29.0	49.0	0.5	0.5		17.0	4.0								
	D	29.0	52.0	1.0	0.5		15.0	2.5								
	wr	25	49.5	0.5	0.5		23	2								
S4-3	C	26.5	46.0	0.5			22.5	4.5								
	D	29.0	52.0	0.5			16.0	3.0								d
2S4-2	C	41.0	46.5		1			11				0.5				e
	D	42.0	48.5		1			8.0				0.5				e
	wr	41.5	46.5		0.5			10				1.5				
2S4-4	C	11.0	35.5		1		50.0					0.5	2.0			f
	D	9.0	39.5		0.5		49.0					0.5	1.5			
	wr	11	41		0.5		47					0.5				h,f
GRB	C	47.5	28.0	23.0				0.5						1		
	D	43.0	30.5	24.5				0.5						1		
	wr	44.5	29	24				0.5						2		
BT	C	33.0	37.0	21.5				8.5								d, g
	D	32.0	42.0	19.0				7.0								d, g
	wr	33	39	20				8								d, g
GB	C	42.0	31.0	22.0				3.5	1.5							
	D	42.0	30.0	23.0				3.5	1.5							
	wr	40.5	31.5	23				3.5	1.5							
ZK2 13m	C	39	2.5	2.5	13.5					8.5		34				
	D	38.5	3	2.5	12					9.5		34.5				
	wr	36.5	2.5	2	16					10.5		32.5				
S1 40.3 m	C	43.5	23.5	22.7	1	1.5			2.5			2			2.5	0.3d
	D	44.5	22.5	24	1	1.5			3			1.5			2.5	
	wr	43	23	22.2	1.5	2			3.5			2			2.5	0.3d

Rock sample	Fraction	Quartz	Plagioclase	K-feldspar	Chlorite	Mica	Amph.		Biotite, annite	Kaolinite	Muscovite	Pyroxene	Calcite	Titanite	Sillimanite	Haematite	Minerals probably present
							Hornblende	Dolomite									
S1 80.6m	C	30.5	30	2		0.5			35		0.5		1.5				
	wr	34	34	2		0.5			28		0.5		1				
S1 87.8m	C	34.5	26	2					19	4	9		5.5				
	D	40.5	29.5	2					13	3	7		5				
	wr	34.5	27	2					15.5	4	10		7				
S8_47.8 m	C	29.5	44.5	4.5	12		3.5		0.5				5.5				
	D	29.5	48	5	9.5		3		0.5				4.5				
	wr	29.5	45.5	5	10		4		0.5				5.5				
BZ_317 m_P	C	45			5			30		6.5	10.5		3				
	D	46			4.5			31		6.5	10		2				
	wr	46			4.5			30.5		6.5	10.5		2				

wr – whole rock

a) apatite; b) pyroxene; c) dolomite; d) chlorite, haematite; e) pyrite; f) mica, K-feldspar; g) kaolinite; h) titanite; i) anatase

4.3 Petrology of the fracture fillings and alterations

Concerning the detailed characterisation of selected altered rock samples and fracture fillings, microscopic sections of the rocks were cut and subsequently analysed with respect to their petrology (CGS, Dr. David Buriánek). A detailed description of the petrological sections is provided in Appendix 1.

The description of the rocks concentrated particularly on the homogeneity of the rock and secondary transformations. Based on the study of 6 samples (S1_80.6 m, S1_87.8 m, ZK_2_13 m, S1_40.3 m, BZ_317 m, S8_47.3 m), it was determined that:

1) Although the hydrothermal vein (ZK_2_13 m) exhibits a relatively simple mineral association, polyphase development is evident. There is a 1 mm thick zone at the edges made up of fine-grained calcite, quartz and chlorite, to which medium to coarse-grained quartz crystals surrounded by carbonate are attached; chlorite is frequently present at the contact of the two zones. This mineral association is thus affected by brittle deformation and the formation of cracks filled with younger carbonate veins.

 SÚRAO	Radionuclide migration processes in a crystalline rock environment. Final report.	Evidenční označení:
		SÚRAO TZ 333/2018

2) The biotitic migmatites to migmatised gneisses (samples S1_80.6 m, S1_87.8 m) exhibit well-developed foliation, which is defined by the orientation of the biotite flakes. The hydrothermal alteration is very weak and occurs frequently only in certain parts of feldspar grains. Carbonate is present locally on cleaved feldspar fissures or small fractures in the rock. The biotite is mostly free of significant transformations and evinces pleochroic halos around the radioactive minerals.

3) The biotitic leucogranite (S1_40,3 m) is significantly affected by secondary transformations (sericitisation, kaolinisation, carbonatisation, chloritisation).

4) The biotitic amphibolite (S8_47.3 m) and biotitic gneiss (BZ_317_P) samples are intensely hydrothermally altered compared to the other samples of metamorphic rocks studied. A number of transformations occurred during hydrothermal alteration: (a) the biotites and amphiboles were pressed by chlorite, (b) the biotite was affected by baueritisation, (c) the feldspars were affected by sericitisation, and the intensity of transformation sometimes varied within individual samples, (d) in some cases the feldspars were also affected by kaolinisation, (e) the plagioclase and biotites were often carbonatised.

5) The sericitisation and chloritisation are often intense in the vicinity of small cracks filled with carbonate. These fillings are secondary and were formed via crystallisation from hydrothermal solutions.

 SÚRAO	Radionuclide migration processes in a crystalline rock environment. Final report.	Evidenční označení:
		SÚRAO TZ 333/2018

4.4 Porosity ε and density ρ of the rocks

4.4.1 Measurement of porosity via the water saturation method

Porosity (in %) is expressed by the ratio of the pore volume which, of the total volume of the matter (V_S), accounts for the pore volume (V_P), see the equation:

$$\varepsilon = \frac{V_P}{V_S} \cdot 100 \quad (4-1)$$

The determination of the total porosity of the samples was necessary in order to allow for the assessment of the effective diffusion coefficients. The porosity of rocks can be studied employing a number of methods, one of which consists of water saturation and drying. This method, which was described in the 2402.03 subproject and is based on a method proposed by Melnyk and Skeet (1986), is a relatively simple approach that can be easily applied in laboratories equipped with standard equipment. This methodology can be used as a comparative procedure to the classical mercury porosimetry measurement approach. The determination procedure can be divided into four stages:

1. The determination of the dry weight W_D of the sample via repeated drying in an oven at 105°C to a constant weight. This ensures that all the water contained in the pores of the sample is removed.
2. The saturation of the sample under vacuum conditions in a desiccator with synthetic granitic water (possibly deionised water). Firstly, the sample is thoroughly evacuated in the desiccator. The degassed liquid (granitic water / deionised water) is then infused slowly (to avoid damaging the sample) into the evacuated desiccator until the sample is completely submerged. The sample is then left for a certain time to saturate below the surface of the water and under vacuum conditions. Air is then slowly released into the desiccator so as to equalise the vacuum with the ambient atmospheric pressure.
3. The determination of the weight of the saturated sample submerged under the liquid W_A . The sample is suspended on a suspension device under a set of scales and is then immersed in a vessel containing the degassed liquid. Care should be taken to ensure that no air bubbles adhere to the suspension device or the sample and that the sample on the suspension device and the suspension device itself is always immersed in the water at the same level (marking of the immersion level).
4. The determination of the weight of the saturated (on the surface dry) sample W_S by means of the sample drying curve. The surface of the saturated sample is wiped after being removed from the liquid. The sample is then continuously weighed and the weight on the surface of the drying sample is recorded over time. Based on the data provided, the sample drying curve is plotted until the sample is visually dry and the weight loss rate is slow and steady. The required weight W_S is calculated from the intersection of the linear extrapolations of the initial and final parts of the drying curve; an example is shown in Fig. 5.

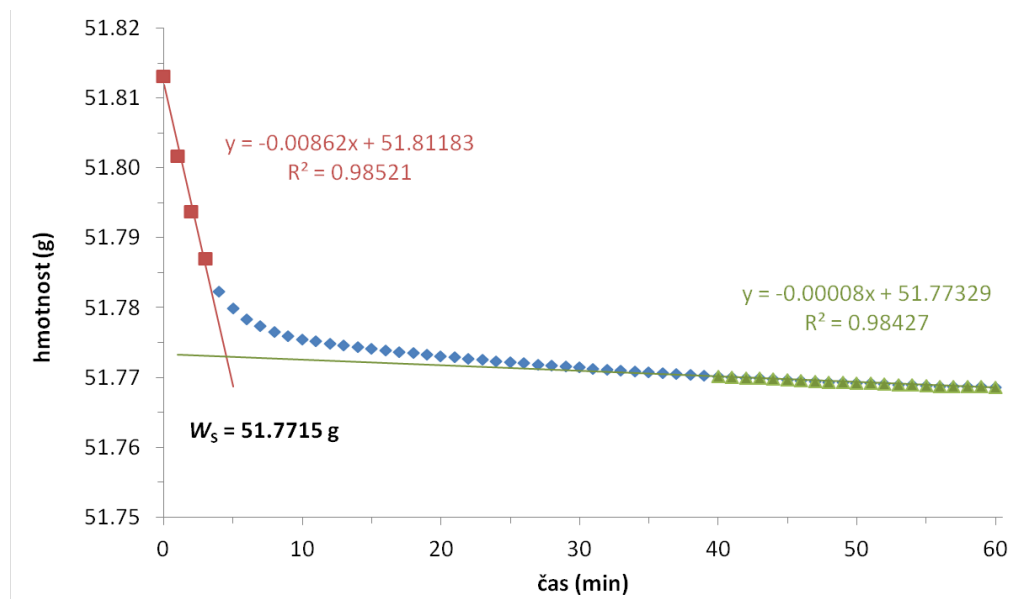


Fig. 5 Example of the assessment of the drying curve of a rock sample (according to Melnyk and Skeet, 1986)

The volume of the sample V_S and the pore volume V_P are then calculated from the weights obtained according to the following equations:

$$V_S = (W_S - W_A) / \rho \quad (4-2)$$

$$V_P = (W_S - W_D) / \rho \quad (4-3)$$

where ρ is the density of the liquid with which the sample was saturated.

The resulting porosity of the sample ε is then calculated according to the equation

$$\varepsilon = \frac{V_P}{V_S} = \frac{(W_S - W_D)}{(W_S - W_A)} \quad (4-4)$$

where V_P is the pore volume and V_S is the sample volume. Using this final equation, it is not necessary to know the density of the liquid.

This method can be used for samples that are destined for use in the penetration diffusion experiments. The sample is saturated with water primarily for the measurement of porosity, which forms the basic prerequisite for the conducting of the diffusion experiments.

4.4.1.2 Results and evaluation

Porosity

The methodology for the determination of water saturation porosity is described in Section 4.3.1. The values were determined on specially-prepared samples consisting of discs with a diameter of 48–50 mm and a height of 10 mm. Selected samples were subsequently submitted for the diffusion experiments.

Since none of the processed samples evinced high porosity levels (above 3%), it was concluded that the Melnyk and Skeet (1986) methodology would be suitable for all the various types of samples - according to experience, this method is suitable for samples with porosity of up to around 3%. The samples were saturated with synthetic granitic water (SGW2).

The porosity values of the samples from the various candidate sites ranged from 0.24% to 0.91%. The highest porosity level was recorded for the granite samples (GC and GB) from the Hrádek locality (0.91%). Conversely, the lowest values (around 0.26%) were recorded for samples from the Čertovka site (the samples extracted from the TIV1 borehole at depths of 68 m and 90 m). The surface samples evinced slightly higher values of around 0.44%. Values of around 0.35% were recorded for the granulite samples from the Kraví hora site. The granodiorites from the Březový potok site evinced porosity values of around 0.6%. The results of the measurement of porosity are shown in Tab. 51.

The porosity level thus reflects the origin of the rock: weathered samples exhibit higher porosity values. The porosity of the granitoids, originating at deeper horizons, was determined at around 0.5% and below. The higher porosity values recorded for the samples from the Hrádek (GC) and Magdalena (TT) sites most probably reflect the weathering of the samples taken from the surface.

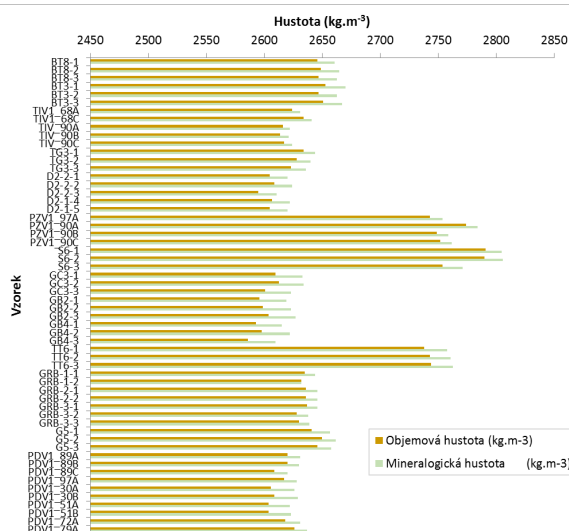


Fig. 6 Density of the samples (kg m^{-3}) from the sites

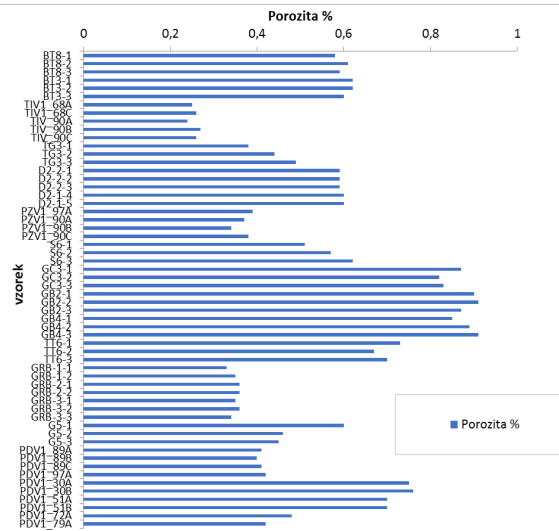


Fig. 7 Porosity of the samples (%) from the sites

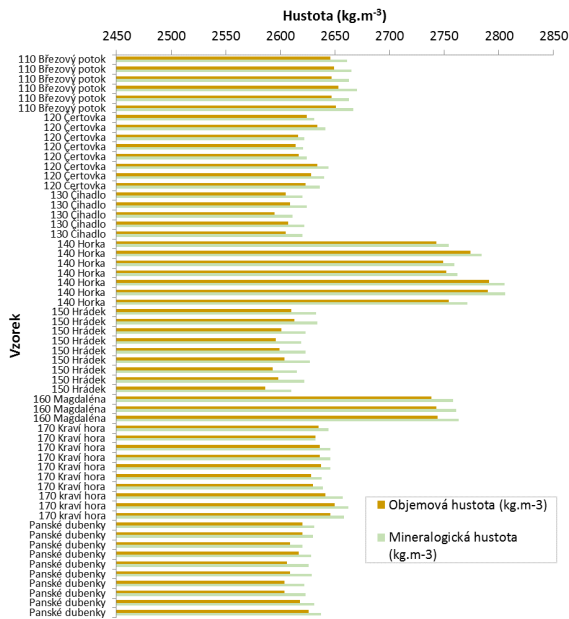


Fig. 8 Density of the samples (kg m⁻³) from the potential sites

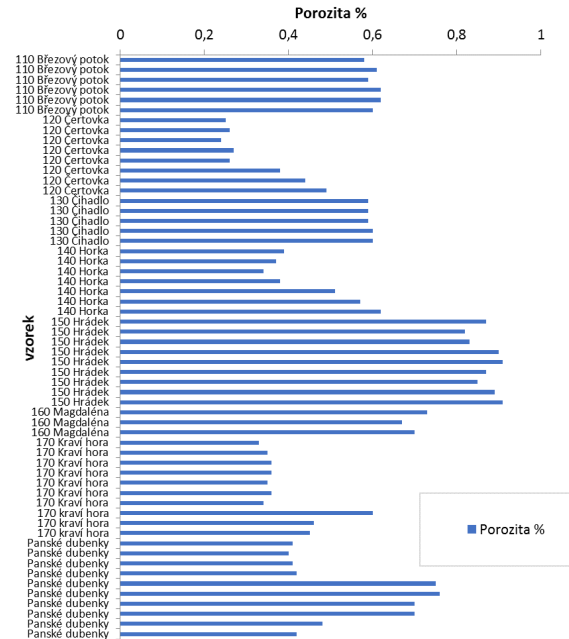


Fig. 9 Porosity of the samples (%) from the potential sites

The mineralogical densities of the monitored rocks provide an objective indicator of their substance composition. The highest densities were recorded for the syenite samples from the Horka (2777 kg m⁻³) and Magdaléna (2761 kg m⁻³) sites depending on the content of the mafic component. Conversely, the lowest mineralogical density values were recorded for the samples from the Hrádek site. The granites from the Hrádek site (GC – Čeřínek type and GB - Boršov type) evinced very similar mineralogical density values of around 2623 kg m⁻³; the values thus correspond to leukocratic granites and indicate the substance stability of both sites. Detailed results are provided in Fig. 6 and Fig. 8 and listed in Tab. 51.

The porosity of the S-3 and S-4 borehole cores at the Bukov URF location varied at between 0.14% and 0.58%. The values indicate the low disturbance of these rocks. The porosity results for the individual samples and rock types are shown in Fig. 11 and Fig. 13.

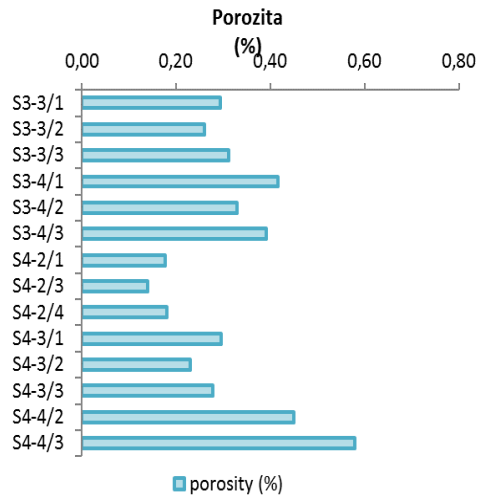
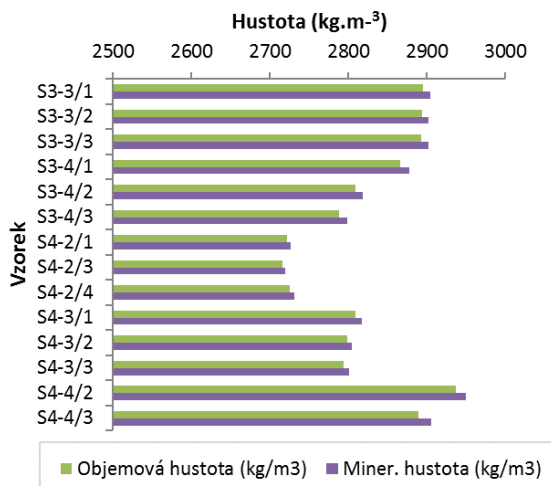


Fig. 10 Density (kg m^{-3}) of the S-3 a S-4 core samples

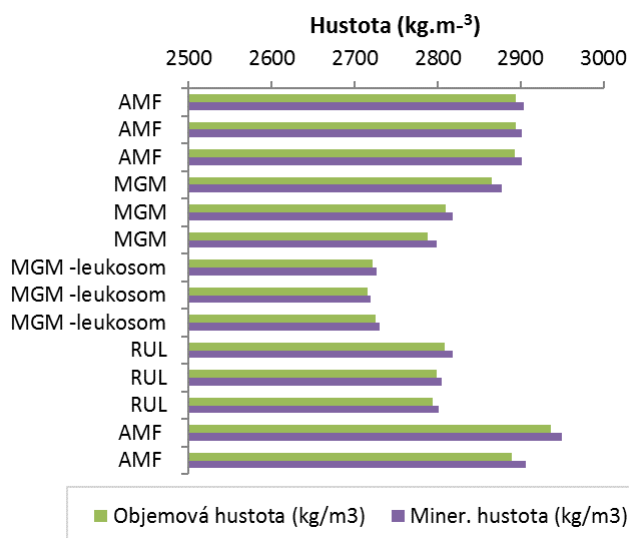


Fig. 12 Density (kg m^{-3}) of the S-3 and S-4 core samples depending on the rock type

Fig. 11 Porosity (%) of the S-3 and S-4 core samples

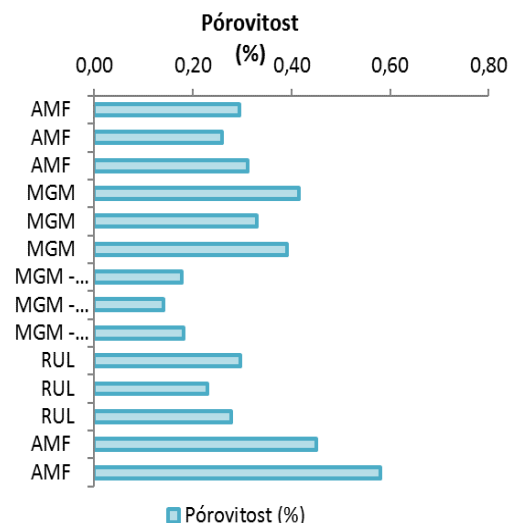


Fig. 13 Porosity (%) of the S-3 and S-4 samples versus rock type

The highest densities were recorded for the S3-3 and S4-4 amphibolite samples (in the range 2901–2950 kg m^{-3}). In contrast, the lowest mineralogical densities were observed with respect to the S4-2, 2S3-2 and S3-4 migmatite samples (2720–2799 kg m^{-3}) (Fig. 12). More detailed results can be found in the Bukovská et al. 2017 report.

The mineralogical density of the intrusive depends principally on their colour index, which leads to the highest differences in values; lower mineralogical density is influenced by the quartz-feldspar ratio in the modal composition (the tabular density of quartz is 2650 kg m^{-3} , of plagioclases - according to basicity (albite-oligoclase) around 2620–2640 kg m^{-3} and of orthoclase 2560 kg m^{-3}). The density of the dark components (biotite, amphibolites, pyroxenes) varies in the range of approximately 2700–3200 kg m^{-3} . The bulk density is given by the relationship between the porosity and the mineralogical density (Hanák et al. 2017).

The porosity values available for the rocks of the Bohemian Massif were assessed in Havlová et al. (2015a). The assessment covered a set of 71 samples of granite rocks from boreholes without the consideration of extreme samples (e.g. cassiterite with a porosity of 1.5–4.9%). The porosity values of the set of rock samples ranged from 0.23% to 2.70% with a mean value of 0.63%. The values determined in this report had a mean value of 0.55% \pm 0.20%.

4.4.2 Mercury porosimetry

The study of pore spaces and porosity focused in the first phase on the measurement of the porosity of selected samples employing established mercury porosimetry methodology, the measurement of the specific surface and, subsequently, the study of microDFN models of selected rock samples from the candidate sites. With respect to the study of Hg porosity, 20

 SÚRAO	Radionuclide migration processes in a crystalline rock environment. Final report.	Evidenční označení:
		SÚRAO TZ 333/2018

samples with dimensions of $7 \times 7 \times 20$ mm were created from a homogeneous part of a borehole core from the Deštná location (sample D2, 50 mm) (Fig. 14 and Fig. 15).



Fig. 14 Preparation of $7 \times 7 \times 20$ mm samples for the study of the effective and Hg porosity of the D2 sample (Deštná) (50 mm)

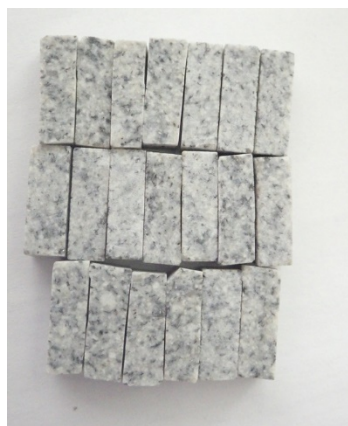


Fig. 15 Prepared $7 \times 7 \times 20$ mm samples for the study of Hg porosity

The first phase consisted of the testing of the porosity of selected samples according to the procedure outlined in Section **Chyba! Nenalezen zdroj odkazů.**; depending on the size of the samples and saturation time. Samples of dimensions $7 \times 7 \times 20$ mm (4) and 7×50 mm (2) were subjected to measurement. The samples were repeatedly dried and saturated (6 and 12 days). A summary provided in Tab. 6 suggests that the results are generally consistent for both large and small samples and that the porosity values of the samples hovered at around 0.67%.

Tab. 6 Results of the porosity testing of samples from Deštná dependent on the sample size

Sample designation	Porosity (%)	Bulk density (kg m^{-3})	Saturation time (h)	Dimensions
D2-3-1	0.60	2606	264	disc 10 mm
D2-3-2	0.59	2607	264	disc 10 mm
D2-3-A1	0.71	2732	264	$7 \times 7 \times 20$ mm
D2-3-A2	0.72	2602	264	$7 \times 7 \times 20$ mm
D2-3-A3	0.72	2668	264	$7 \times 7 \times 20$ mm
D2-3-A4	0.66	2624	264	$7 \times 7 \times 20$ mm
D2-3-1	0.68	2609	144	disc 10 mm
D2-3-2	0.66	2610	144	disc 10 mm

 SÚRAO	Radionuclide migration processes in a crystalline rock environment. Final report.	Evidenční označení:
		SÚRAO TZ 333/2018

Sample designation	Porosity (%)	Bulk density (kg m ⁻³)	Saturation time (h)	Dimensions
D2-3-A1	0.67	2704	144	7 × 7 × 20 mm
D2-3-A2	0.65	2637	144	7 × 7 × 20 mm
D2-3-A3	0.70	2698	144	7 × 7 × 20 mm
D2-3-A4	0.65	2690	144	7 × 7 × 20 mm
D2-3-1	0.67	2614	288	disc 10 mm
D2-3-2	0.64	2605	288	disc 10 mm
average	0.67	2643		
standard deviation	0.04	45		

A further part of the study focused on a comparison of the mercury porosimetry values determined by various institutions in the Czech Republic that have been engaged in this research field over the long term. Two samples were submitted for analysis and the samples were tested in the laboratories of 6 different institutions. A summary of the results is provided in Tab. 7.

Tab. 7 Comparison of the Hg porosity results for the D2 samples determined at 6 scientific institutions

Institution	Sample number	Porosity (%)	Bulk density (g ml ⁻¹)		Method
UJV	1–4	0.67		2.643 ± 45	gravimetric
CAS, ICPF	5.6	0.79	2.605		Hg por.
BUT	7	2.35	2.578	2.609	Hg por., gravimetric
BUT	8	1.80	2.574	2.609	Hg por., gravimetric
UCT Prague	9.10	0.38	2.620		Hg por.
TUO	11	0.42	2.542		Hg por.
TUO	12	0.50	2.487		Hg por.
BUT, Institute of technology of building materials and components	13.14	0.41	2.715		Hg por.

The results demonstrate that although the laboratories analysed the “same” samples, the results from the various institutions differed, i.e. the porosity values ranged from 0.38% to 2.35%. The bulk density values were determined at between 2.487 and 2.715 g cm⁻³. This

 SÚRAO	Radionuclide migration processes in a crystalline rock environment. Final report.	Evidenční označení:
		SÚRAO TZ 333/2018

dispersion was the result of the measurement methodologies applied, including the settings of the experimental measurement conditions that significantly affected the measured parameters. The test results were assessed in detail and, subsequently, an optimised procedure covering both the preparation and experimental settings was recommended (see Appendix 3 for the suggested procedure).

Specific surface measurements employing Kr and N₂ were also performed on the same samples, see chapter 4.2. The porosity of the unaffected granite from the Čihadlo site (D2) was determined at 0.19%, which increased to 1.93% following the grinding of the sample. The specific surface area of the intact granite sample (D2) via Kr (BET) was determined at around 0.871 m² g⁻¹. Similar values were recorded via the assessment of the Hg porosimetry, i.e. 0.043, 0.069 m² g⁻¹ for samples 11 and 12 respectively, and 0.075 m² g⁻¹ (samples D2_13 and 14). The average pore aperture ranged between 0.04 and 0.07 µm.

It is clear that the grinding of the samples significantly influenced the transport properties of the granitic samples (porosity, specific surface and the resulting sorption of radionuclides and, possibly, diffusivity). Hence, in this respect, a combination of methods (e.g. the gravimetric determination of porosity according to Melnyk and Skeet (1986) in combination with the determination of the specific surface, etc.) appears to provide the most suitable approach.

The measurement of the Hg porosimetry of low-porosity rocks constitutes a specific porosity measurement field and, to date, no clear methodology has been determined concerning the preparation and testing of rocks with particularly low porosities (around 0.5%). The results show that the porosity values determined at the various scientific institutions reflect the differing methodologies applied by, and the experience of, individual operators. This field requires further detailed study, which cannot be conducted without the modification of standard porosimeters and supplementary materials (e.g. the customised production of a penetrometer with a probe with an abnormally low volume for increasing the accuracy of the determination of low porosities). However, this procedure would have to be available to laboratories that already employ mercury porosimeters and, in general; they are not particularly inclined to change their standard procedures. Therefore, due to the limited options concerning the study of porous spaces employing the mercury porosity procedure, attention was subsequently devoted to the study of porous spaces via the C-14 PMMA method (autoradiography), based on the results of which, micro DFN models of the porous network were constructed.

4.4.3 Description of the pore space employing the micro DFN model approach

The aim of this part of the project was to study the porosity of the rocks via sophisticated experimental and modelling methods that are not currently applied in the Czech Republic and which enable the description of diffusion as a process underway in the pore spaces of crystalline rocks.

A method for the study of pore spaces involving the impregnation of samples with polymethylmethacrylate resin enjoys a long tradition at the University of Helsinki (Hellmuth et al. 1993; Siitari-Kauppi 2002; Siitari-Kauppi et al. 2003) and continues to be applied today

 SÚRAO	Radionuclide migration processes in a crystalline rock environment. Final report.	Evidenční označení:
		SÚRAO TZ 333/2018

supplemented by a number of other sophisticated methods (Aromaa et al. 2019; Iraola et al. 2017; Kuva et al. 2015a,b; Nenonen et al. 2018, Sammaljärvi et al., 2017, 2019; Voutilainen et al. 2009, 2017, 2012, 2018, 2019a, b).

One of the aims of this study was to study the pore spaces of igneous and metamorphic rocks employing this method so as to allow for both a comparison of the porosity values obtained via conventional methods (see 4.4) and the use of the visualised results so as to describe the interconnected microfracture networks employing μ DFN models (see 4.4.3.3).

The C-14 PMMA method consists of saturating rock samples with a polymethylmethacrylate resin, designated C-144, with the provision that the viscous liquid penetrates all the pores. The resin is then irradiated (or heated) and an autoradiogram is taken of the sample which reflects, on a grey scale, the level of radioactivity directly proportional to the amount of C-14 in the rock matrix. The porosity of the sample can then be calculated based on recalculations and assessment (Hellmuth et al. 1993).

4.4.3.1 Samples

Five samples were selected for the application of the C-14 PMMA impregnation method, i.e. 3 representative igneous rocks (syenite - Pozdátky PZV, Tis TIV1 and Deštná D2 granites) and 2 representative metamorphic rocks from the Bukov URF (amphibolite and migmatite) - see Tab. 8.

Tab. 8 Overview of the samples used for the measurement of porosity via the C-14 PMMA method (sent to HYRL)

Sample code / designation	Site	Location (borehole)	Depth of sampling (m)	Diameter (cm) and height (cm) of the sample	Type of sample
2016_1 PZV1_97A	Pozdátky (140 Horka)	PZV1	97–98	47 5	Durbachite, amphibolite biotitic syenite
1216_1 B3_3_A	Rožná-Bukov URF (171 Kravi Hora)	ZK1	550	47 5	Migmatite
816_2 B2_1_B	Rožná-Bukov URF (171 Kravi Hora)	ZK1	550	47 5	Amphibolite
1916_2 TIV1_90B	Tis u Blatna (120 Čertovka)	TIV1	90.17–91.0	47 5	Biotitic granite,

 SÚRAO	Radionuclide migration processes in a crystalline rock environment. Final report.	Evidenční označení:
		SÚRAO TZ 333/2018

Sample code / designation	Site	Location (borehole)	Depth of sampling (m)	Diameter (cm) and height (cm) of the sample	Type of sample
					weakly altered
3517_2_3 D2_2/3	Deštná (130 Čihadlo)	Deštná quarry	30	47 5	Granite

Photographs of the samples with optical microscope images (E. Sasao, JAEA), which highlight the different structures and textures of the igneous and metamorphic samples, are provided in Fig. 16–

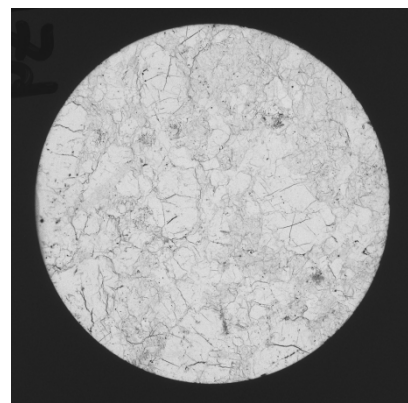
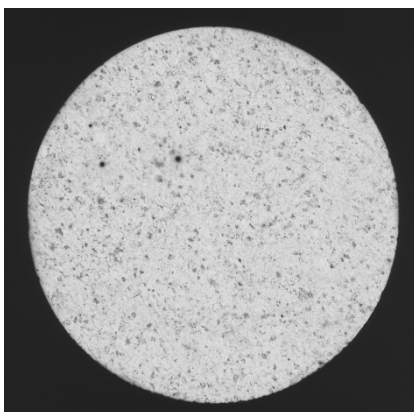
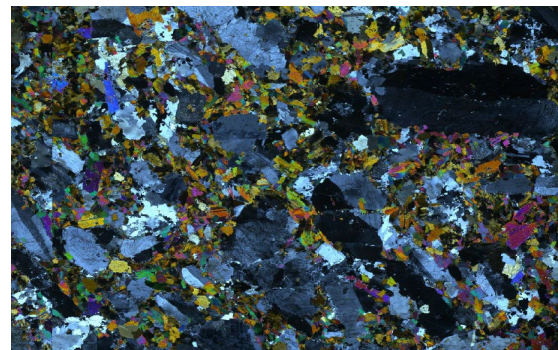
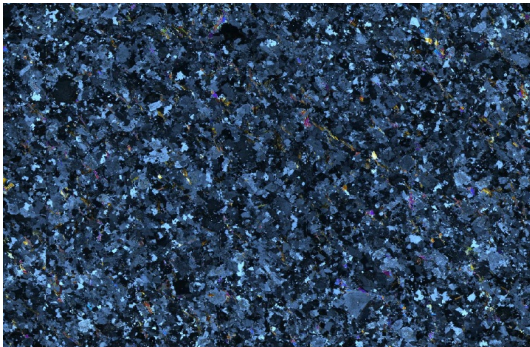
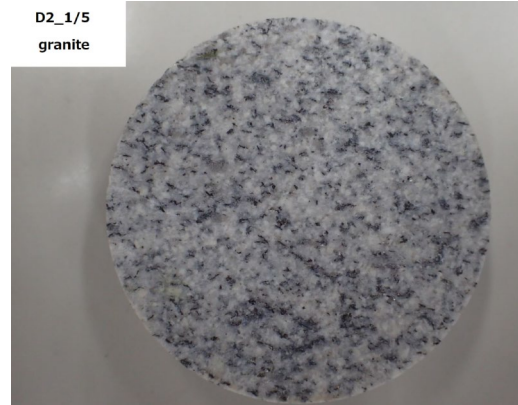


Fig. 16 Images of a sample from the Deštná site; middle, an optical microscope image (crossed nickels - E. Sasao, JAEA); bottom, the resulting porosity distribution following impregnation with C-14 PMMA

Fig. 17 Images of a sample from the Horka site; middle, an optical microscope image (crossed nickels - E. Sasao, JAEA); bottom, the resulting porosity distribution following impregnation with C-14 PMMA

TIV1_90A
biotite granite/
slight alteration



5 cm

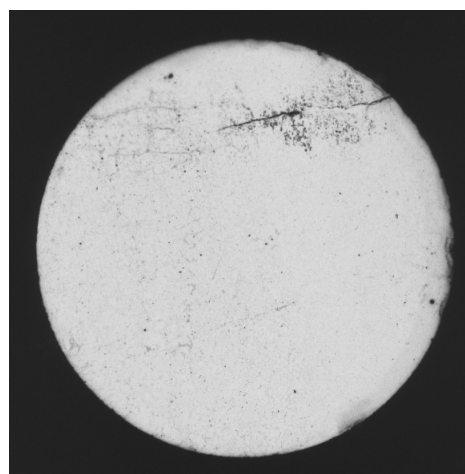
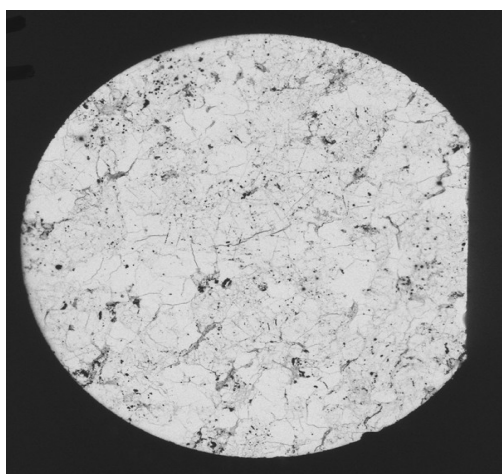
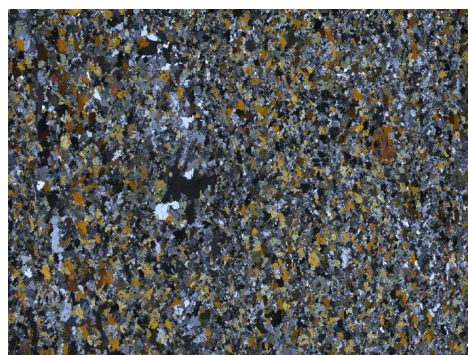
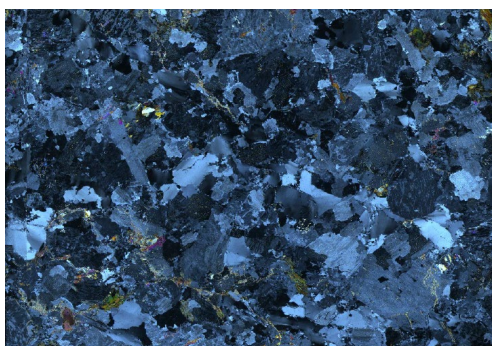


Fig. 18 Images of a sample from the Čertovka site; middle, an optical microscope image (crossed nickels - E. Sasao, JAEA); bottom, the resulting porosity distribution following impregnation with C-14 PMMA

Fig. 19 Images of a sample from the Bukov URF site, amphibolite B2-1; middle, an optical microscope image (crossed nickels - E. Sasao, JAEA); bottom, the resulting porosity distribution following impregnation with C-14 PMMA

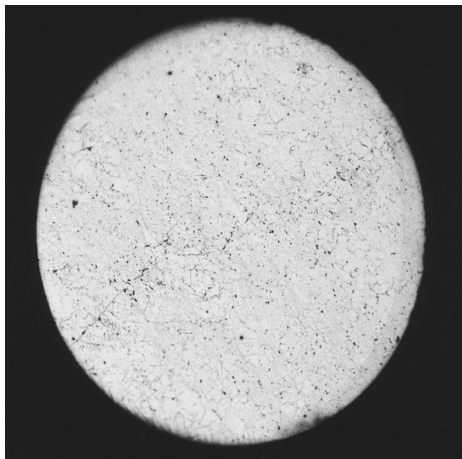
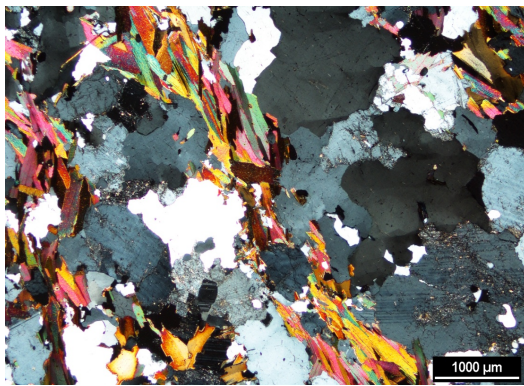


Fig. 20 Images of a sample from the Bukov URF site, migmatite B3-3; middle, an optical microscope image (crossed nickels - E. Sasao, JAEA); bottom, the resulting porosity distribution following impregnation with C-14 PMMA

 SÚRAO	Radionuclide migration processes in a crystalline rock environment. Final report.	Evidenční označení:
		SÚRAO TZ 333/2018

4.4.3.2 C-14 PMMA method (University of Helsinki)

The samples were first dried at 105°C for 12 days. The impregnation of the C-14 PMMA was performed in a vacuum, following which the samples were placed in a refrigerator and stored there for 26 days. The volume of the C-14-MMA used for each sample was 210 ml and the specific activity 340 kBq ml⁻¹. All the samples were immersed in C-14-MMA until polymerisation, which was performed via heating. The indicator solution contained 0.25 wt% azobisisobutyronitrile (AIBN) as the polymerisation thermal initiator. Polymerisation was carried out in a water bath using an optimised heating procedure. The samples were then cut and polished with silicon carbide.

Autoradiography was performed using Kodak Biomax film over an exposure period of 22 days. Digitalised images of the porosity distribution in the samples are shown in Fig. 16–

 SÚRAO	Radionuclide migration processes in a crystalline rock environment. Final report.	Evidenční označení:
		SÚRAO TZ 333/2018

; the images were subsequently used for the development of the μ DFN models (see Section 4.4.3.3).

In addition, the porosity of the samples was measured at Helsinki University using the gravimetric determination method (Melnik and Skeet 1986).

The results of the C-14 PMMA porosity determination and a comparison with values obtained via the gravimetric method are provided in Tab. 9. The resulting porosity distribution is provided in Appendix 4.

Tab. 9 Measurement of porosity (%) by means of two methods (C-14 PMMA, gravimetric method at Helsinki University and ÚJV)

	D2_2/3 3517_2_3	PZV1_97 A 2016_1	TIV1_90B 2116_2	B2_1B 816_2	B3_3A 3517_2_3
PMMA porosity (%)	0.61	0.6	0.69	0.23	0.37
Helsinki University porosity gravimetric (%)	0.98	0.77	0.58	0.66	0.45
ÚJV porosity gravimetric (%)	0.50	0.39	0.27	0.47	0.22

The table illustrates that the results of the C-14 PMMA determination of porosity are not consistent with those of either of the gravimetric testing series. Both of the gravimetric methods, however, do evince a certain level of interdependence (see Fig. 21), which has also been observed in other projects. This procedure is highly dependent on the procedure and equipment used and the person who performs the testing. The ÚJV values can be seen to be consistently lower than those determined by the University of Helsinki. However, the porosity values as determined by the C-14 PMMA method, at least approximately, correspond to the D_e values obtained for the given samples via the penetration diffusion experiments (Chapter 6; see Fig. 22).

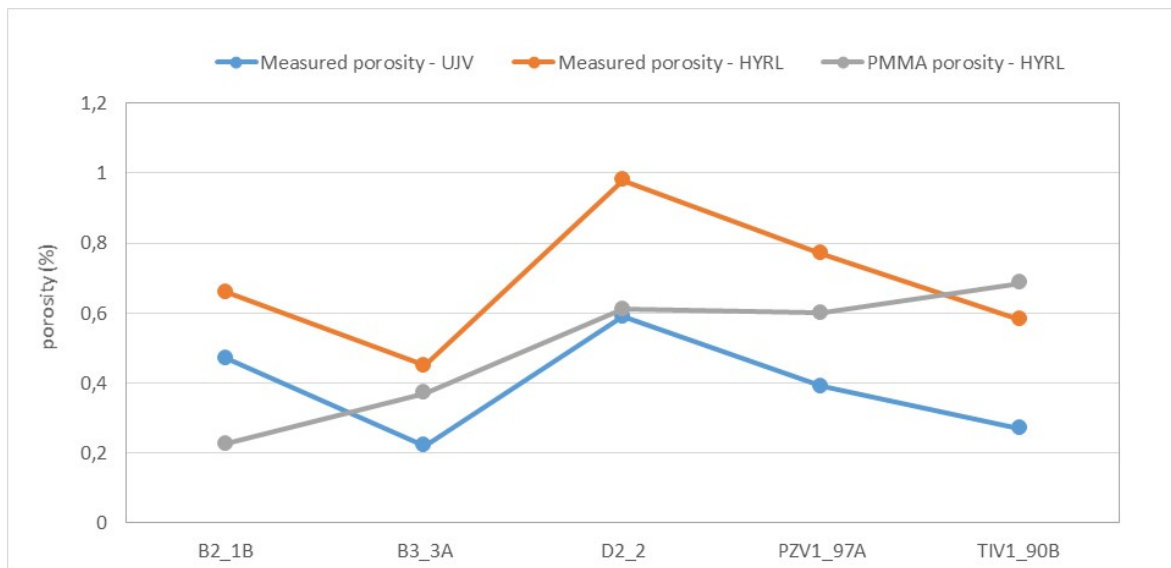


Fig. 21 Porosity values as measured via the two methods (C-14 PMMA and gravimetrically at UniHelsinki and at ÚJV Řež, a. s.)

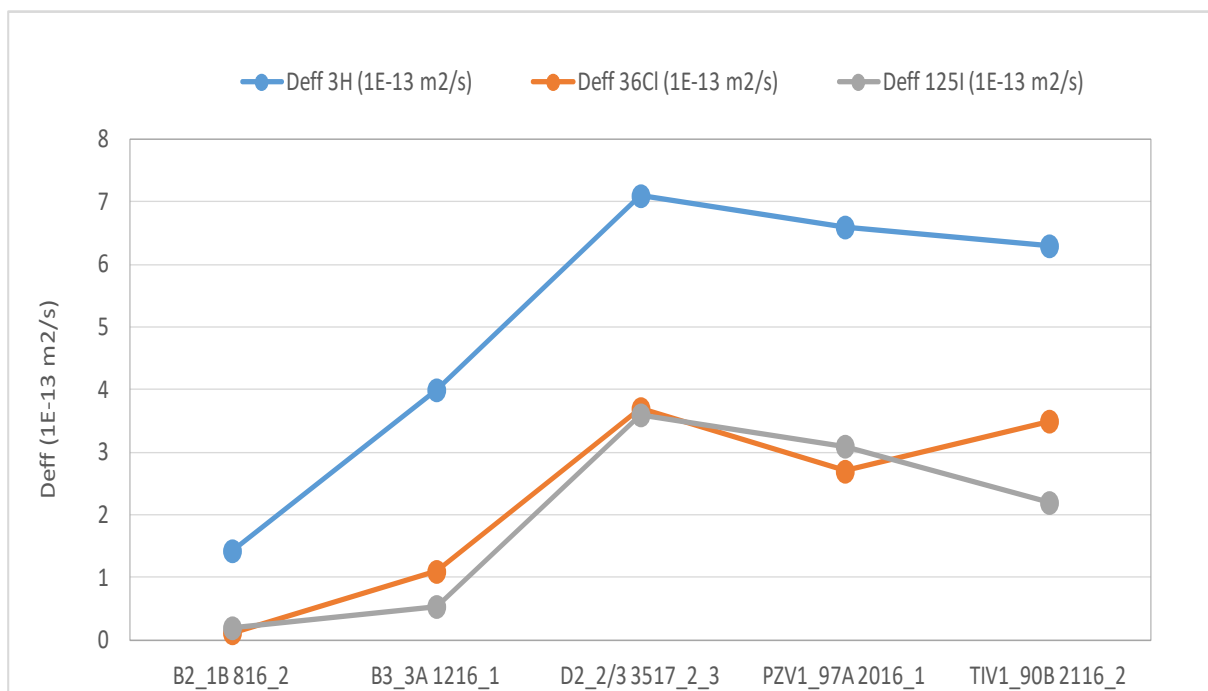


Fig. 22 D_e values ($m^2 s^{-1}$) for HTO, ^{36}Cl and ^{125}I , measured for the rock samples via the penetration diffusion method

Fig. 23 highlights clear differences with respect to the representation of individual pixel porosity for the metamorphic and igneous rocks. The metamorphic samples (B2_1B, B3_3A) evince a higher proportion of pixels with lower porosity and the magmatic rocks exhibit a larger proportion of pixels with higher porosity, i.e. up to 10%. The TIV1 sample, which has a lower proportion of pixels with lower porosity and, conversely, a higher proportion of pixels with higher porosity, is an extreme case. This also provides a potential reason for the anion

exclusion being more pronounced for the metamorphic rocks (see Chapter 6 – with respect to the metamorphic samples (B2_1B and B3_3), 90% of the pixels have a porosity of less than 1%, while for the igneous rocks this indicator is just 60% (D2 and PZV1) and 45% (TIV1). The remainder of the pixels have a porosity of greater than 1. Concerning the TIV1 sample, more than 10% of the pixels exhibited a porosity of more than 10%. However, as shown in Fig. 22, the highest D_e values did not refer to this sample. Rather, sample D2 (see also Chapter 6 and Fig. 54) evinced an ambiguous relationship between the total porosity value and the D_e .

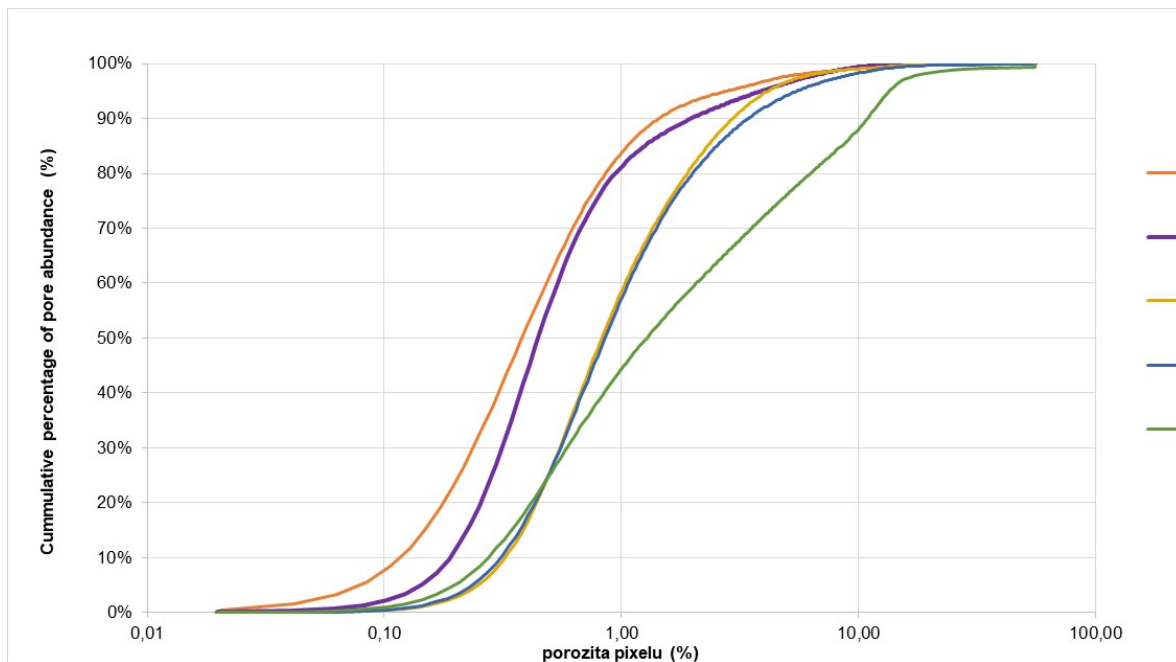


Fig. 23 Cumulative pixel porosity for the various samples (B2_1B orange, B3_3A purple; D2 yellow, pZV1 blue and TIV1 green)

4.4.3.3 μ DFN simulation methodology

Simulations based on the CPM concept realised at the rock matrix microscale were used for the modelled assessment of the diffusion experiments. The Modflow and MT3DMS modelling tools were used for the numerical solution.

The digitalised images obtained via the autoradiography method employing ^{14}C -PMMA (polymethylmethacrylate supplemented with unstable ^{14}C) were used as the primary input information. In the digital format, the images had 8-bit depth and the porosity was described using a scale of 256 discrete values. The resolution of the images was approximately $21.3 \mu\text{m}$ and the model discretisation was determined identically - the simulated space in the horizontal direction consisted of a regular network of model elements with dimensions of $21.3 \times 21.3 \mu\text{m}$. Each pixel of the scanned radiographic images was represented by one model cell, thus ensuring the maximum fidelity of the information when transferred to the simulation. With average sample diameters of around 50 mm, each sample was represented by a total of around $4 \cdot 10^6$ discrete porosity values. Thus, while the radiographic images provided relatively

 SÚRAO	Radionuclide migration processes in a crystalline rock environment. Final report.	Evidenční označení:
		SÚRAO TZ 333/2018

detailed information on the porosity distribution, it was limited to the immediate vicinity of the section plane. Since the partial aims of the modelled assessment included the analysis of the images and the evaluation of faults (microfractures and micropores) in the sample volume based on 2D information obtained from the radiographic images, the samples were modelled in two variants (Fig. 24):

- 2D simulation – the assessment of the intensity of diffusion on two-dimensional elements selected from the studied samples,
- 3D simulation – modelled assessment employing the assumed distribution of porosity in the sample volume.

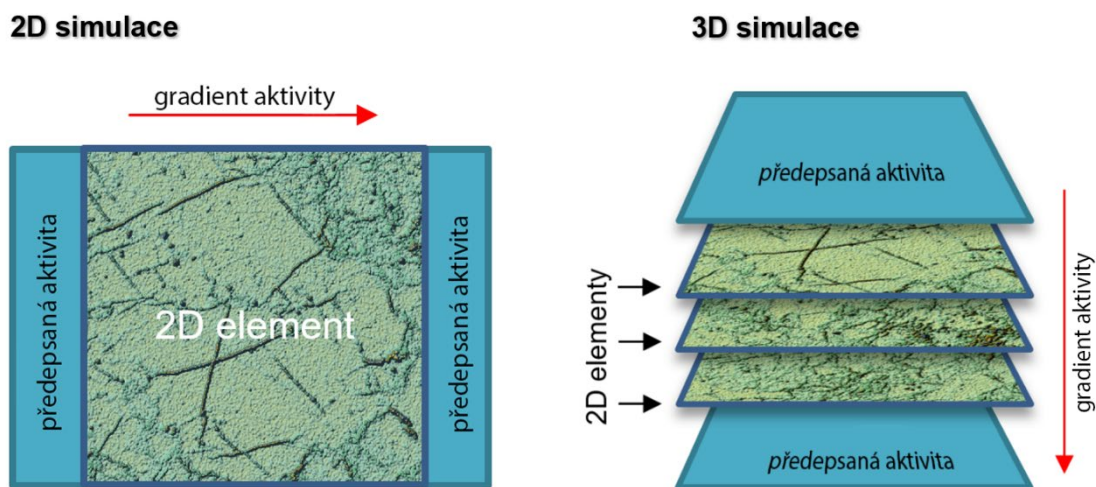


Fig. 24 Schematic representation of the 2D (left) and 3D (right) microCPM models

The digitalised autoradiographic images were processed according to the methodology provided in Sardini et al. 2014, i.e. the conversion of the image information (the level of exposure to radioactive radiation due to ^{14}C β -decay) to the corresponding porosity values using equations (4.1)–(4.3):

$$OD = -\log_{10} \frac{I}{I_0} \quad (4.1)$$

$$A = -\frac{1}{k} \times \ln \left(\frac{OD - OD_0}{OD_{max}} \right) \quad (4.2)$$

$$n = \frac{\beta}{1 + (\beta - 1) \times \frac{A}{A_0}} \times \frac{A}{A_0} \quad (4.3)$$

where OD is the optical density, I is the intensity of a given pixel, I_0 is the background intensity, OD_{max} is the optical density at media saturation, OD_0 is the optical density at background intensity, A is the activity of the pixel, A_0 is the initial PMMA activity and β is the sample density to PMMA ratio.

 SÚRAO	Radionuclide migration processes in a crystalline rock environment. Final report.	Evidenční označení:
		SÚRAO TZ 333/2018

The modelled assessment of the effective diffusion coefficient of the sample based on the experiments was numerically addressed using the analogy between the flow and the diffusion flow in the steady state, see equations (4.4) and (4.5).

$$Q = K \cdot A \cdot \frac{\Delta H}{\Delta L} \quad (4.4)$$

$$J = D_{eff} \cdot A \cdot \frac{\Delta C}{\Delta L} \quad (4.5)$$

where Q is the flow ($m^3 s^{-1}$), J is the diffusion flow ($Bq s^{-1}$), D_e the effective diffusion coefficient ($m^2 s^{-1}$), K the hydraulic conductivity ($m s^{-1}$), A the sample area (m^2) and n the porosity (-).

The calibration of the model according to the results of the diffusion experiments was addressed by means of a series of realisations with various model parameters - effective porosity. Due to the significantly higher computational complexity of the transient simulation of the spread of substances, the procedure presented above was used for the solution, i.e. analogous diffusion and advective flow in the steady state (the numerical solution consists of the conversion of the diffusion transport of the tracer through the variable porosity environment to advection flow through the environment with variable hydraulic conductivity). The applicability of this concept was verified by comparing it with the results of the transient transport simulations. The comparison confirmed that the differences between the results (the D_e value for a given sample) of the two procedures lie at the level of error inherent in the numerical solution, i.e. at an order of magnitude lower than the changes that occur during the calibration process.

The diffusion coefficient values in water for the various tracers were taken from Hofmanová (2018) and are summarised in Tab. 10.

Tab. 10 Diffusion coefficient values used in the modelled assessment (Hofmanová 2018)

Diffusing tracer	HTO	$^{36}Cl^-$	$^{125}I^-$
$D_w (\times 10^{-9} m^2 s^{-1})$	2.44	2.03	2.05

Model solution

2D simulation

The primary purpose of performing 2D simulations was to describe the behaviour of the model in the areas of the samples that exhibited differing porosity characteristics and to determine a methodological procedure for the more complex 3D calibration of the model as described in Chapter 4.4.3.3.

3–4 elements of 1×1 cm were selected for each of the five samples to be subjected to examination, representing areas of average, minimum and maximum porosity. Thus, the model elements had dimensions approximately equal to the thickness of the samples. One of the basic assumptions consisted of the isotropic nature of porosity, which enables the usability of radiographic images taken in a plane perpendicular to the direction of the applied activity

gradient. Selected elements can then be considered to be representative in terms of fracture connectivity as well as in the direction of the activity gradient during the diffusion experiments. A graphical overview of the areas from which the square model elements were selected for the 2D simulations is provided in Fig. 25.

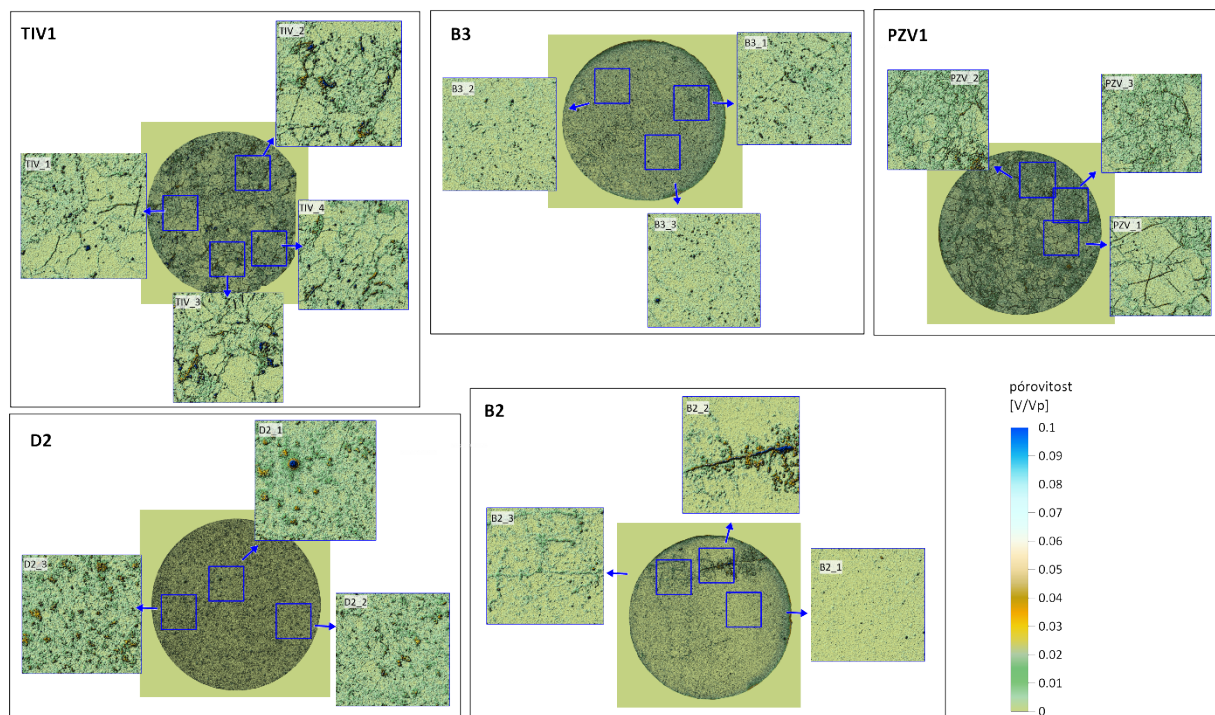


Fig. 25 Locations of selected elements that represent the characteristic areas of the samples

Although two-dimensional simulations can generally be expected to evince lower connectivity (and, consequently, a lower D_e) compared to real conditions, the 2D simulation results using porosity directly as derived from radiographic images showed higher D_e values than those recorded during the diffusion experiments. The modelled D_e is also overestimated in the case of the simulation of elements selected from areas with minimal porosity. Thus, it can be concluded that only a certain proportion of the fracture structures that were detected by the autoradiographic method were involved in the transport of substances. A further possibility concerns the in reality higher tortuosity of the microstructures captured in the image - the tortuosity value was not entered into the modelled simulations (or was accorded a value of 1); the curvature of the transport pathways was reflected in the model by the detailed discretisation of the computed network.

The determination of that part of the fractures involved in the diffusion dissemination of substances was then subjected to the calibration of the modelled values of the porosity of the individual computational cells (pixels). This process was based on the gradual increase in the porosity limit value, which enabled the diffusive transport of substances in the model solution. This resulted in the gradual elimination of areas and fractures with low porosity which resulted, in turn, in transport being concentrated in a network of more prominent and interconnected microstructures. The increasing threshold level was accompanied by a decrease in both the porosity value and the interconnectivity of the fractures. The procedure for increasing the effective porosity threshold values is shown for selected elements of the samples in Fig. 26.

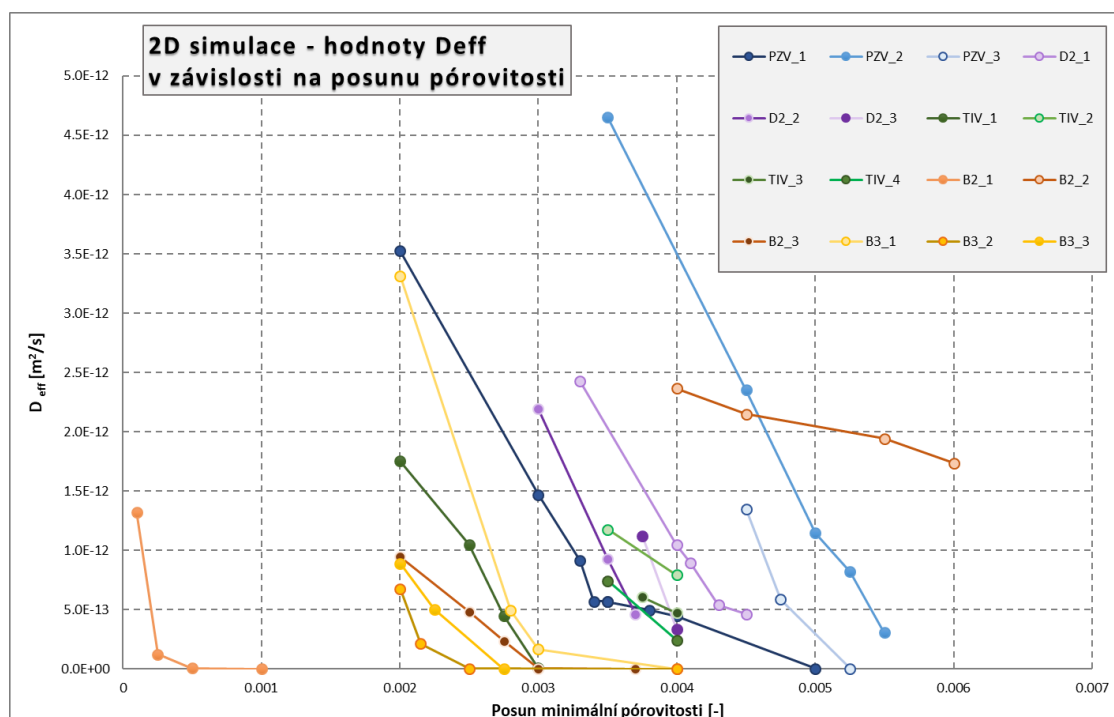


Fig. 26 Effective ^3H diffusion values depending on the minimum porosity involved in the transport

The results of the 2D simulations indicate that decreasing porosity is accompanied by a decrease in the effective diffusion coefficient. With an adequate reduction in the porosity threshold value, model results were obtained comparable to the measured D_e values for all the studied samples. At the same time, it is apparent that the level at which the D_e was attained/exceeded decreased to very low to zero values as a result of the complete closure of the (up to that time) interconnected transport routes.

The level of fracture connectivity that led to a D_e comparable to the measured values with respect to the simulation of selected TIV and PZV sample elements is illustrated via the particle tracking method in Fig. 27.

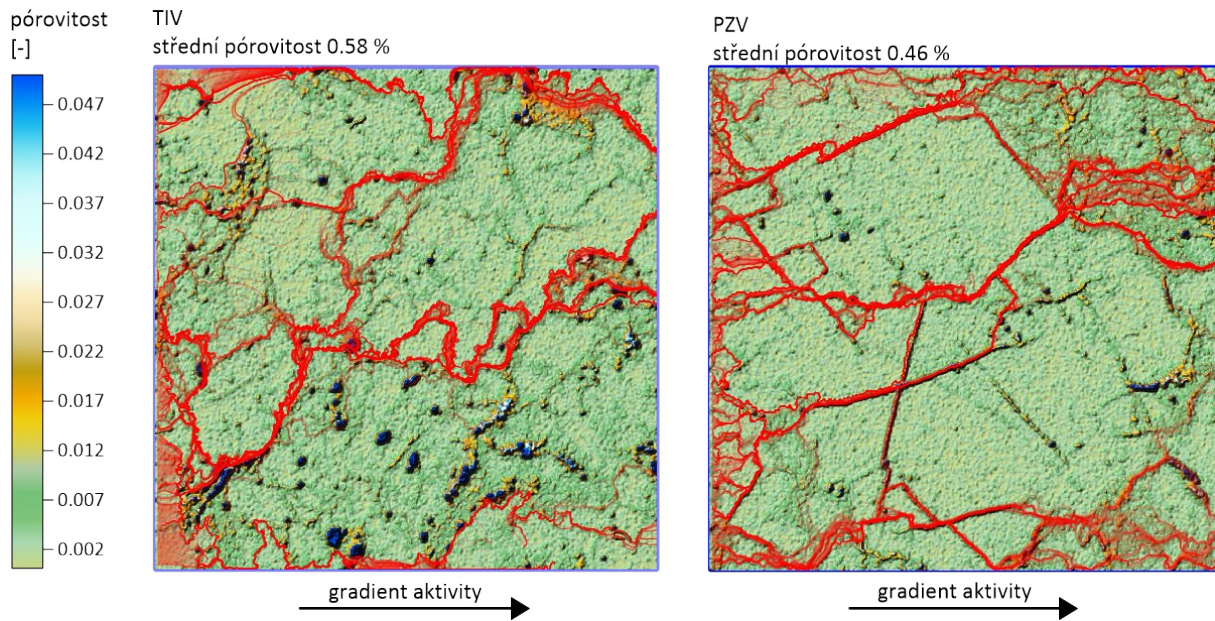


Fig. 27 Analytical particle trajectories suggesting the character of the fracture interconnections in the 2D simulations

It is apparent from the above images that, with respect to the 2D simulations, the transport of substances occurred primarily via a network of significant interconnected fractures (model areas, i.e. images showing high porosity). At the same time, it is possible to identify areas in the model elements that, despite higher porosity values, did not participate in the transport of substances since they did not form part of the interconnected network.

Tab. 11 Results of the 2D simulation of elements selected from individual samples for ^3H testing

	Mean porosity of the whole sample (%)	Mean porosity of selected element (%)	Reduction of the porosity threshold (%)	Average porosity of the selected element after reduction (%)	Ratio	Modelled D_e ($\times 10^{-13} \text{ m}^2 \text{ s}^{-1}$)	D_e measurement interval ($\times 10^{-13} \text{ m}^2 \text{ s}^{-1}$)
PZV1	0.623	0.463	0.300	0.227	49%	6.19	6.0–7.1
PZV2		0.675	0.450	0.304	45%	6.18	
PZV3		0.599	0.400	0.262	44%	6.69	
D2_1	0.628	0.664	0.350	0.360	54%	7.04	6.3–7.8
D2_2		0.542	0.300	0.281	52%	6.54	
D2_3		0.719	0.340	0.424	59%	5.84	
TIV_4	0.652	0.588	0.275	0.361	61%	5.58	6.0–6.6
TIV_1		0.423	0.210	0.257	61%	7.23	

 SÚRAO	Radionuclide migration processes in a crystalline rock environment. Final report.	Evidenční označení:
		SÚRAO TZ 333/2018

TIV_2		0.700	0.310	0.446	64%	6.51	
TIV_3		0.705	0.300	0.484	69%	6.06	
B2_3	0.284	0.293	0.250	0.129	44%	1.71	1.2–1.7
B2_2		0.423	0.710	0.314	74%	2.59	
B2_1		0.113	0.020	0.093	83%	1.17	
B3_3	0.410	0.317	0.180	0.164	52%	3.47	2.7–5.3
B3_2		0.290	0.170	0.139	48%	4.43	
B3_1		0.429	0.240	0.218	51%	4.44	

A summary of the results of the 2D simulation of the ^3H tracer diffusion is presented in Tab. 11. Although it concerned primarily the testing of the responses of various simulated elements, D_e model values were achieved within the porosity calibration that were comparable to the results of the diffusion experiments. With the exception of sample B2, it is evident that all the samples exhibited relatively balanced porosity characteristics (at the individual element scale). Approximately the same porosity reduction, i.e. around 50%, was required with respect to the calibration of the various elements to achieve the D_e measurement. Higher porosity reduction ratios of over 60% were calibrated for the TIV sample.

Compared to the other samples, sample B2 was relatively variable, i.e. it consisted of a region with a dominant fracture that was included in the B2_2 element, together with an area with a minimum of detected fractures (minimum average porosity) in the B2_3 element. Due to the significant differences compared to the predominant character of the sample, the dominant fracture area was not included in the 3D simulations.

3D simulation

Following the verification of the concept by means of the results of the 2D simulations, 3D models were created for the various samples. One of the basic tasks with concern to 3D modelling consists of the determination of the adequate spatial representation of porosity based on two-dimensional information provided by autoradiographic images. The direct extrapolation of porosity as measured in the image plane to the thickness of the whole sample would lead to the direct connection of the upper and lower walls of the sample (the diffusion measurement would be perpendicular to the image plane) which, clearly, does not correspond to the conditions of the real samples. Hence, model discretisation in the vertical direction was applied to layers with a thickness corresponding to the “characteristic” size of the fractures. Due to the different origins of the various samples, the vertical thickness (and number of layers) was specific to each of the five samples analysed. The determination of the thickness of the model layers was performed employing a combination of the visual assessment of the nature of the porosity distribution of the samples and analysis using variograms. The variograms provided information on the spatial correlation of the analysed samples and the magnitude of the fractures. The standardised variograms for the various samples together with the indicated thicknesses of the model layers are shown in Fig. 28.

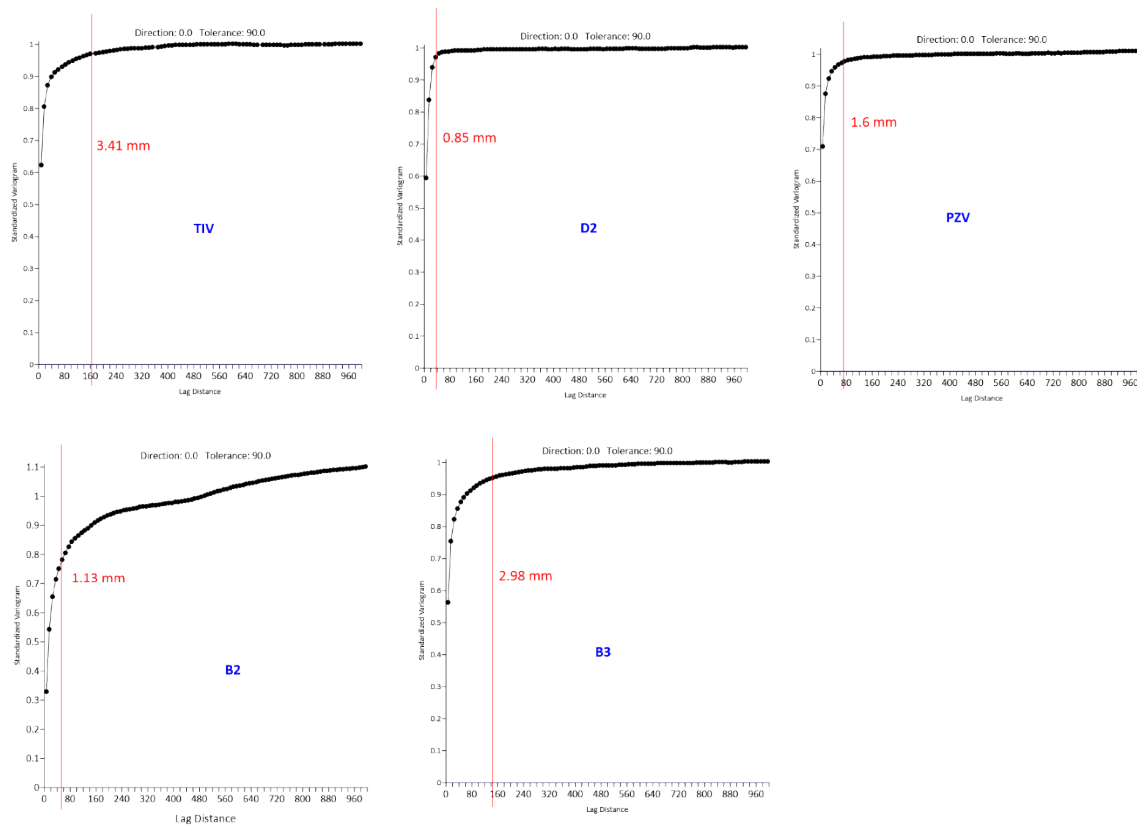


Fig. 28 Standardised variograms of the simulated samples

The thickness of the model layers was based on the position of the so-called sill, i.e. the position beyond which the variability does not increase with increasing distance. The determination of this value was not conclusive for all the samples (e.g. the PZV sample) and was performed in connection with the analysis of the directional variograms and the manual identification of fracture dimensions. The resulting vertical discretisation divided the 10 mm samples into between 3 (TIV) and 12 (D2) layers (Fig. 28). The porosity of the individual layers was taken from randomly selected elements, dimensionally identical to the 2D simulations (10 × 10 mm). The resulting models thus described cube-shaped spaces with edges of 10 mm. The option of employing randomly selected elements is based on the selection of layers with thicknesses that exceed the characteristic dimensions of the fractures. The discretisation of the individual elements (and the whole of the 3D models) in the horizontal direction was the same as in the 2D simulations, i.e. networks of 470 × 472 cells.

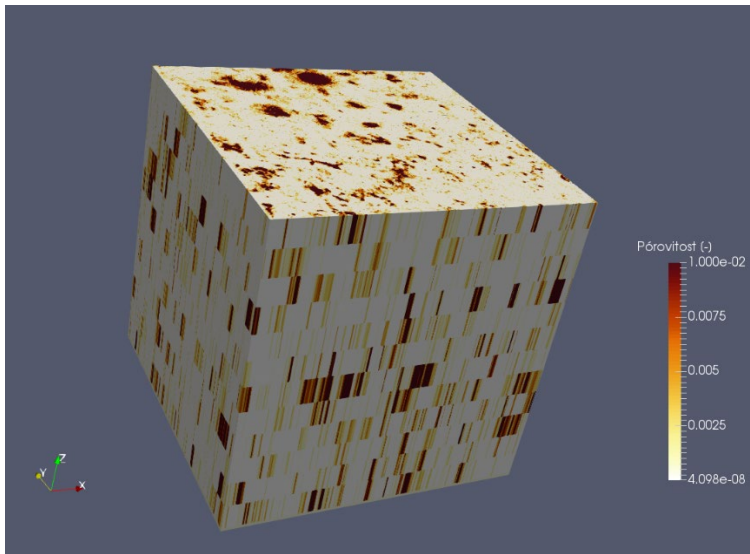


Fig. 29 3D model of sample D2

In order to verify the dependence of the model results (modelled D_e) on the selection of individual elements, variant solutions were determined for selected samples. Fig. 30 shows a selection of various elements for the construction of 2 models of the B2 sample together with the number of the layer under which they were included in the models. The results of the two models and a related discussion are included in the assessment together with the results of all the samples. Due to the significantly different characteristics of the dominant fractures and the uncertainty of their influence on the samples on which the diffusion experiments were conducted, the area with fractures was not included in the selection of elements for the 3D simulation of the B2 sample.

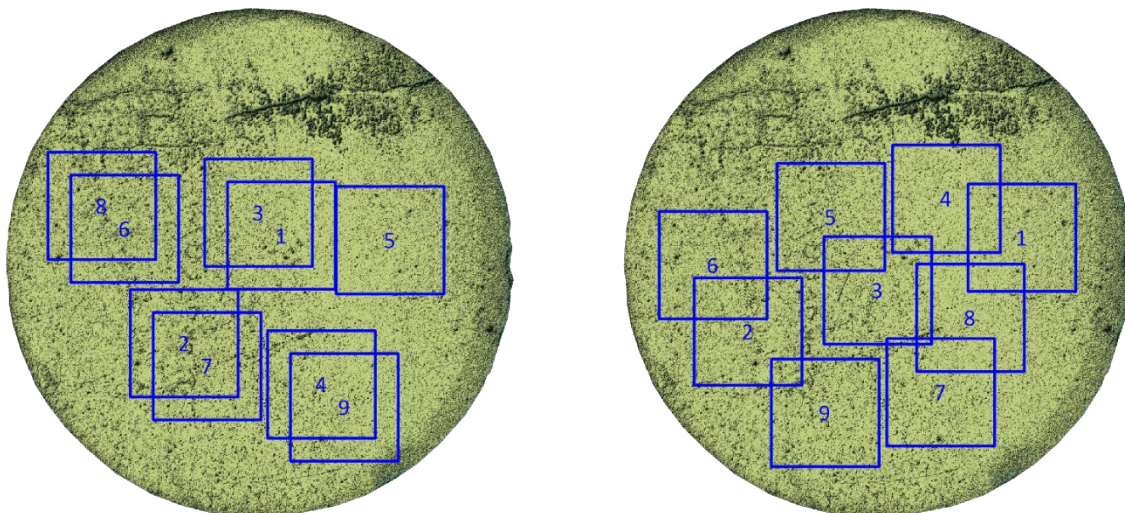


Fig. 30 Selection of the elements and their order in the 3D model layers in various versions

The calibration process, as in the case of the 2D simulations, consisted of determining the porosity at which the intensity of the modelled diffusion transport was comparable to the

 SÚRAO	Radionuclide migration processes in a crystalline rock environment. Final report.	Evidenční označení:
		SÚRAO TZ 333/2018

experimental value. This was performed via lowering the porosity threshold value below which lower porosity fractures were no longer involved in the transport process. The changes in the porosity of individual samples were introduced consistently with respect to all the modelled layers – i.e. the same porosity thresholds were determined for all the layers, despite their consisting of different elements. The assessment of the diffusion transport for all the tracers that were evaluated (Tab. 10) was performed in the same way. A summary of the results of the calibration of the models is provided in Tab. 12.

Tab. 12 Results of the calibrated 3D models for the various samples

		B2_1B 816_2	B3_3A 1216_1	D2_2/3 3517_2_3	PZV1_97 A 2016_1	TIV1_90B 2116_2
	PMMA porosity - HYRL	0.23	0.37	0.61	0.6	0.69
	PMMA porosity - PROGEO	0.24	0.35	0.63	0.63	0.65
	measured porosity - HYRL	0.66	0.45	0.98	0.77	0.58
	measured porosity - UJV	0.47	0.22	0.59	0.39	0.27
	number of model layers	9	9	12	6	3
³ H	porosity - 3D model (%)	0.187*	0.182	0.256	0.236	0.337
	porosity threshold value (%)	0.0015	0.0030	0.0048	0.0054	0.0050
	measured D_e ($\times 10^{-13} \text{ m}^2 \text{ s}^{-1}$)**	1.7	2.7	7.1	6.6	6.3
	modelled D_e ($\times 10^{-13} \text{ m}^2 \text{ s}^{-1}$)	1.79	2.67	7.26	6.64	6.33
³⁶ Cl	porosity - 3D model (%)	0.147*	0.153	0.229	0.198	0.317
	porosity threshold value (%)	0.0025	0.0037	0.0054	0.0065	0.0057
	measured D_e ($\times 10^{-13} \text{ m}^2 \text{ s}^{-1}$)**	0.14	0.58	3.7	2.7	3.5
	modelled D_e ($\times 10^{-13} \text{ m}^2 \text{ s}^{-1}$)	0.141	0.572	3.45	2.77	3.59
¹²⁵ I	porosity - 3D model (%)	0.151*	0.149	0.229	0.204	0.291
	porosity threshold value (%)	0.0024	0.0038	0.0054	0.0063	0.0068
	measured D_e ($\times 10^{-13} \text{ m}^2 \text{ s}^{-1}$)**	0.2	0.54	3.6	3.1	2.2
	modelled D_e ($\times 10^{-13} \text{ m}^2 \text{ s}^{-1}$)	0.2	0.506	3.50	3.18	2.19

* model B2 was considered without the inclusion of the “dominant” fracture

 SÚRAO	Radionuclide migration processes in a crystalline rock environment. Final report.	Evidenční označení:
		SÚRAO TZ 333/2018

** the D_e measurements are stated by the value determined via the nearest analysed sample or via the average value of all the measurements (via the “nearest” sample if no measurement was available)

In general, it can be stated that in all cases a good match was attained between the modelled D_e and the measured values. Compared to the 2D simulations the calibration using the 3D simulations required a significant reduction in porosity as a result of the overall lower interconnectivity of the fractures in the 2D models.

In order to verify the sensitivity of the model results on the selection of the specific elements that determined the distribution of porosity in the individual layers, two solutions were considered for samples with differing porosity distributions, i.e. B2 (with the marking of the respective layers in Fig. 31) and TIV1. The process consisted of the selection of different layers at the same porosity threshold. In the case of sample B2 a change in the D_e of around 7% was evident (decrease to $1.68 \times 10^{-13} \text{ m}^2 \text{ s}^{-1}$), while the average porosity of the individual elements remained essentially identical (0.0678% and 0.0681%). The alternative solution for the TIV1 sample revealed an increase of 13% ($D_e = 7.17 \times 10^{-13} \text{ m}^2 \text{ s}^{-1}$) with a change in the average porosity of the model layers from 0.25% to 0.29%. Due to small changes in the average porosity of the elements, the main cause of the changes in the D_e between the individual solutions was attributed to the differing connectivity of the individual model layers.

An overview of the ratios of the calibrated porosity to the values determined from the radiographic images is provided in Tab. 13.

Tab. 13 Relative porosity of the calibrated 3D models relative to the initial porosity determined via the ^{14}C -PMMA method

	B2	B3	D2	PZV1	TIV1
calibrated porosity - ^3H	78%	52%	41%	37%	52%
calibrated porosity - ^{36}Cl	61%	44%	36%	31%	49%
calibrated porosity - ^{125}I	63%	43%	36%	32%	45%

The results of the calibrated 3D model showed (in a similar way to the results of the 2D models) that in order to attain the measured D_e value, it was necessary to reduce the effective porosity in all the assessed samples. The effective porosity for the ^3H calibrated model ranged from 37% to 78% of the initial value depending on the specific sample. According to the model results, the most significant decrease in the effective porosity could be expected in the case of the PZV1 sample due to its microstructure, concerning which transport was primarily concentrated in significant fractures with high porosity. This led to the requirement for a significant reduction in the effective porosity so as to attain a comparable reduction in the D_e to that of the samples with more evenly distributed porosity. This applied, for example, to sample B2, concerning which the model calibration predicted the lowest reduction in porosity. Since sample B2 was processed without including the dominant fractures, the character of all the model layers was relatively homogeneous in terms of porosity (see element B2_1 in Fig. 30).

 SÚRAO	Radionuclide migration processes in a crystalline rock environment. Final report.	Evidenční označení:
		SÚRAO TZ 333/2018

An additional reduction in the effective porosity was required when calibrating the model for the ^{36}Cl and ^{125}I tracers. The decrease in the porosity threshold value in this case reflected the lower D_e values recorded in the diffusion experiments. The lower effective porosity can be interpreted as the influence of anion exclusion. The predicted character of the effects of anion exclusion was consistent with the principle of the calibration procedure in which the smallest fractures are eliminated via increasing the porosity threshold. The modelled results were comparable in terms of the effective porosity for both the tracer groups (^{36}Cl and ^{125}I). The most significant decrease in the effective porosity in terms of both the evaluated and total porosity was evident in the case of sample B2 while, conversely, the smallest decrease in the effective porosity was assumed by the model for the TIV1 sample.

The distributions of the reduced effective porosity values determined via the model calibrations are presented in Fig. 31. The porosity of the samples shown was reduced by the threshold value that was used in the calibration of the layers of the models (Tab. 12). Zero porosity and below threshold values are indicated in white. At a given level of porosity reduction, the non-uniform distribution of values is clearly evident, with apparently higher average porosity at the sample edges. Since this was most likely the result of the sensing method employed, these areas were not included in the assessment. In all cases, it is apparent that only a limited area of the sample was involved in the diffusion transport of substances, which is concentrated in the higher porosity fracture areas. This is particularly evident in the case of the TIV1, PZV1 and B3 samples, where visually evident networks of still interconnected fractures remain active. The same change in porosity (reduction in values during model calibration) occurred with respect to samples B2 and D2; however, the resulting networks exhibited different characters corresponding to the differing initial distribution of the fractures in these samples.

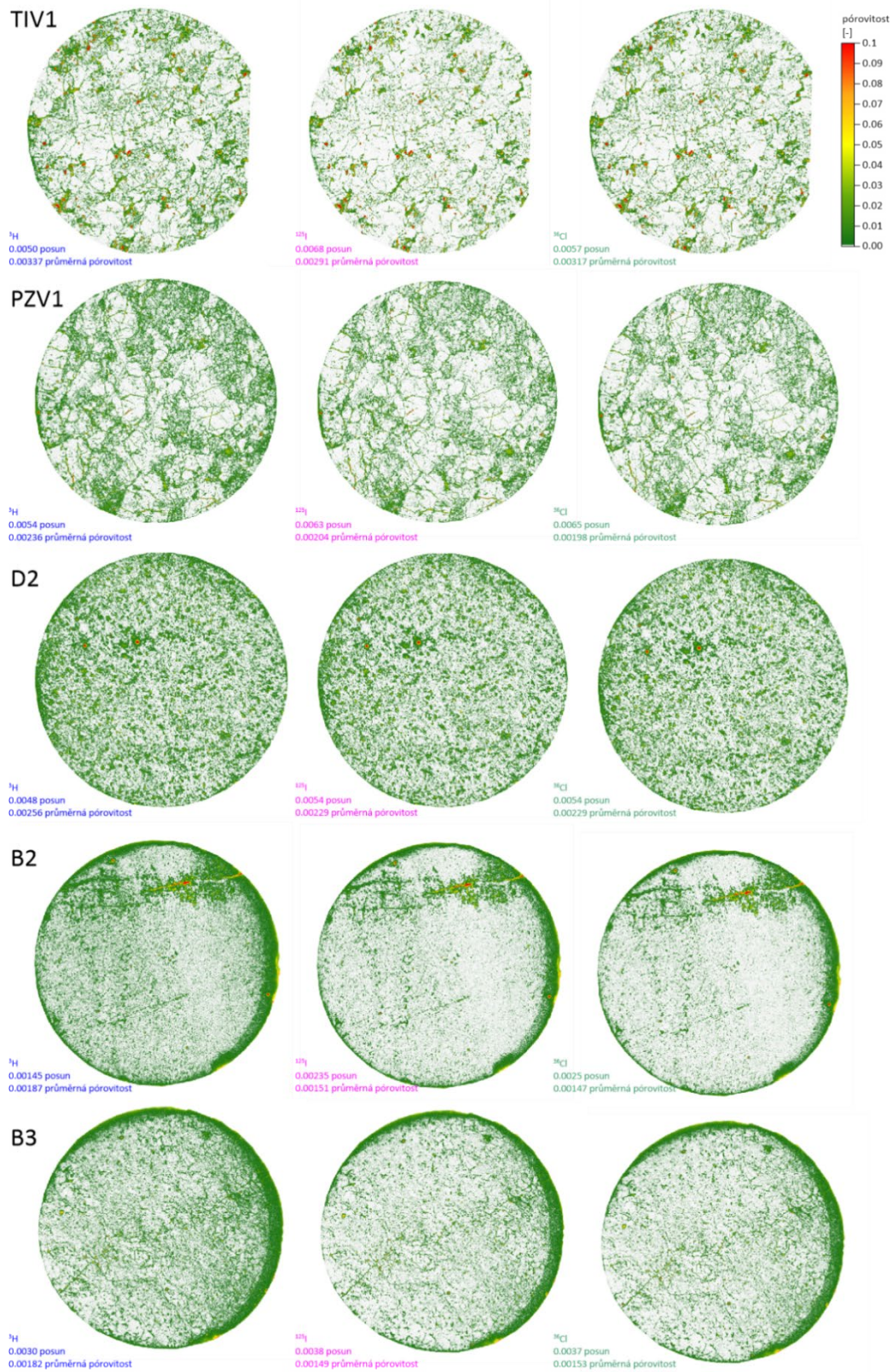


Fig. 31 Porosity distribution of the calibrated models for the various samples and tracers

 SÚRAO	Radionuclide migration processes in a crystalline rock environment. Final report.	Evidenční označení:
		SÚRAO TZ 333/2018

4.4.3.4 Summary

MicroCPM models were constructed in both the 2D and 3D variants for all the analysed samples based on ^{14}C -PMMA autoradiographic images. Due to the problem of assembling representative 3D models based only on surface images, the sensitivity of the models was also assessed via 2D simulations in relation to the selection of areas with differing average porosity values. Multiple-layer 3D models were then assembled based on the 2D model results. The thickness of the layers was specific to each sample and was based on the dimensions of the fractures that were determined on the basis of the variogram analysis. The porosity distribution in the individual layers and its initial value were taken from randomly selected areas of the autoradiographic images. The calibration itself was performed by increasing the porosity threshold values until the modelled effective diffusion coefficient achieved acceptable compliance with the diffusion test results. The reduction in the total effective porosity was in the range of around 37% to 78% of the initial ^3H tracer value. The decrease in the modelled porosity value was explained by the limited fracture connectivity in the direction perpendicular to the image plane.

Moreover, according to the results of the calibrated models, an additional reduction in the effective porosity was attained via the use of ^{36}Cl and ^{125}I . **This can be interpreted as the influence of anion exclusion, where not all the pores that allowed the diffusion of ^3H participated in the diffusion transport process.**

The detailed modelled assessment indicated that the porosity determined via the ^{14}C -PMMA autoradiographic method may exhibit systemic errors (bias). This may be the result of, for example, the overestimation of the influence of larger fractures or, conversely, the suppression of the importance of fractures with dimensions below the resolution of the images employed. The relatively large differences between the porosity determined gravimetrically and that determined via the autoradiographic ^{14}C -PMMA analysis provide space for discussion concerning the representativeness of both methods. One of the most important parameters that influences the relationship between the ^{14}C -PMMA-determined porosity and the actual porosity of the sample consists of the background pixel intensity - this value is specific to each image and each measurement, and basically defines the borders at which the pixels exhibit non-zero porosity, i.e. non-zero diffusion values. With respect particularly to the samples with low porosity values (e.g. B2), the determined background intensity exerts a significant influence on the overall porosity as assessed from the images. Any error in the input values entered into the model is then directly transmitted to the model results and the subsequent assessment.

With concern to the determination of porosity and its spatial distribution via the ^{14}C -PMMA method, the image resolution of the autoradiographic images represents a limiting factor - due to lower microfracture aperture values in the order of magnitudes (up to 1–2 μm) compared to the size of the pixels (21 μm), we recommend the verification of the results via the microscopy of the samples at a higher resolution by means of an optical or electron microscope (for a comparison of fracture size via both methods, see Fig. 32).

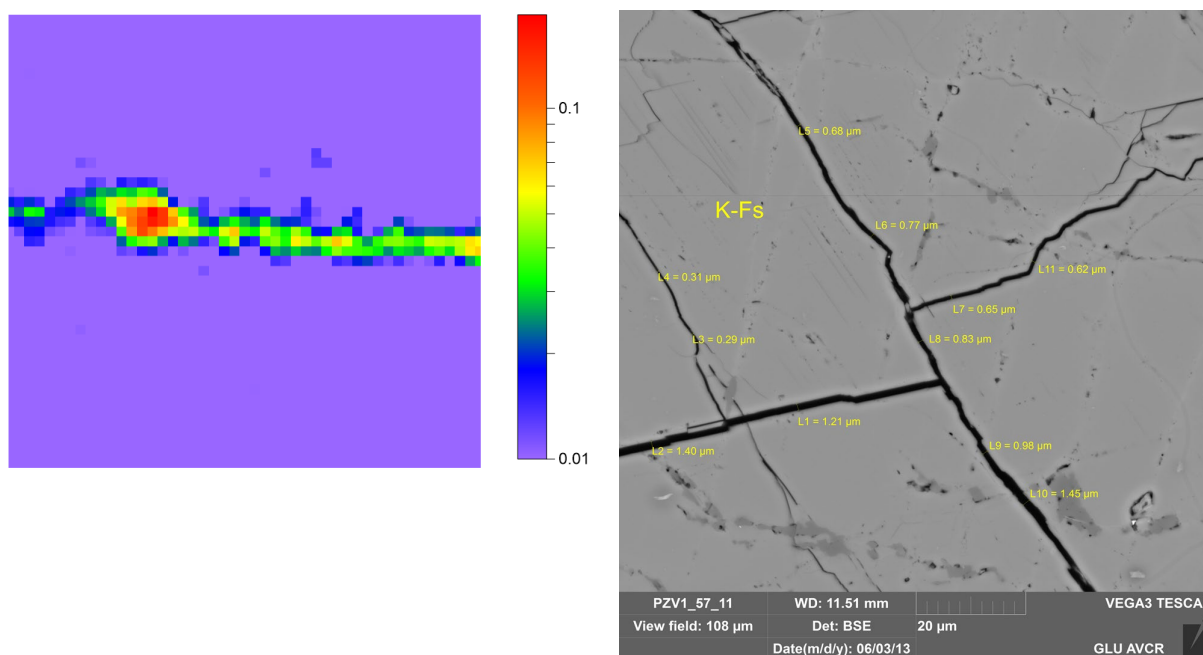


Fig. 32 Left: PZV1 – microfracture from a C14-PMMA image - selection 1×1 mm (47×47 pixels), 1 pixel = $21 \mu\text{m}$. (47×47 pixels), 1 pixel = $21 \mu\text{m}$. Right: PZV1_57_11 - scanning electron microscopy

The results of these studies were published in the form of an oral presentation at the Migration 2019 conference in Kyoto, 16–21 September 2019.

4.5 Determination of the cation exchange capacity of the rock

The assessment of the cation exchange capacity of the rock material provides relevant information on the sorption of radionuclides on granitic rocks, e.g. information on the radionuclide sorption mechanism and the dominant sorbents in the rock matrix structure. Significant sorbents in rock materials consist of e.g. layered minerals, so-called phyllosilicates (mica, clays), which are characterised by several types of sorption sites. Sorption on such sites may occur via ion exchange, which is indicated by a high cation exchange capacity value.

4.5.1 The rock samples and their treatment

The cation exchange capacity (CEC) was determined for selected rock samples, which differed significantly in terms of the content of phyllosilicates, as well as for samples of altered parts of the rock and fracture fillings. The following samples were selected, representing certain types of rock materials in order to highlight the mechanism governing the sorption of cations on the individual minerals contained in the rock: durbachite PZV1 (Horka site) with high mica and potassium feldspar contents, TIV1 granite (Čertovka site) with high potassium feldspar and low mica contents, PDV1 granite with high quartz and higher muscovite contents, S3-3 granite (Bukov URF) with low feldspar and mica contents, but with higher hornblende and plagioclase contents, and 2S4-4 granite (Bukov URF) with 50 wt% of magnesio-hornblende and 35 wt%

 SÚRAO	Radionuclide migration processes in a crystalline rock environment. Final report.	Evidenční označení:
		SÚRAO TZ 333/2018

of plagioclase. The determination of the cation exchange capacity was performed for all the samples selected for the study of fractures and altered nuclei. An overview of the samples is provided in Tab. 2 and Tab. 3. Prior to the determination of the cation exchange capacity, defined amounts of crushed rock samples were leached in deionised water for two months so as to wash out any impurities as well as those cations that were not firmly bound to the rock structure. During the leaching process, the entire volume of the liquid phase was removed regularly and fresh deionised water was added to the rock samples so as to allow continued leaching. The removed liquid phases were subjected to the determination of the content of basic cations (Na^+ , K^+ , Mg^{2+} , Ca^{2+}) via the atomic absorption spectrometry (AAS) as to allow for the monitoring of the decrease in the cation concentration up to the point where the cation concentration was constant and ranged in the order of hundredths of mg l^{-1} . Prolonged leaching aimed at attaining a concentration of cations in the liquid phase below the detection limit was not possible due to the potential risk of the dissolution of the phyllosilicates. The concentration of cations in the liquid phase was subsequently recalculated to the total amount of cations released from the rock matrix, see Tab. 14.

Tab. 14 Results of the leaching of the rock samples prior to the determination of the CEC

Sample	Weight (g)	Total amount of leached cations (mg)			
		Na^+	K^+	Mg^{2+}	Ca^{2+}
PZV1	10.0469	0.110	1.325	0.687	0.548
TIV1	18.0329	0.261	1.361	0.024	0.143
PDV1	13.4819	0.165	1.299	0.066	0.118
S3-3	7.1545	0.115	1.506	0.302	0.489
2S4-4	13.0622	0.285	0.510	0.366	1.086

4.5.2 Determination of the CEC

4.5.2.1 Rock samples

The CEC and cation content at the exchange sites were determined based on certified methodology no. SÚJB/ONRV/15452/2014 (Červinka 2014). The Cu(II)triethylenetetramine complex (abbreviated to Cu(II)-trien) was used in the methodology to exchange the cations in the interlayer of phyllosilicates for Cu^{2+} cations. The results of the determination consisted of a rock material CEC value (in $\text{meq } 100 \text{ g}^{-1}$) which corresponded to the amount of copper that was bound (i.e. exchanged for cations) to the rock material, and the CEC_{sum} value (in $\text{meq } 100 \text{ g}^{-1}$) which corresponded to the total amount of exchanged cations. These two values should be in balance.

This procedure is employed routinely to determine the cation exchange capacity of clay materials (bentonites), concerning which the CEC values, depending on the properties of the particular bentonite, are in the order of tens of $\text{meq } 100 \text{ g}^{-1}$. The CECs of selected bentonites were determined e.g. as part of the TIP project. By way of illustration, the CEC determined for Rokle bentonite was $80 \text{ meq } 100 \text{ g}^{-1}$; for B75 bentonite $56.8 \text{ meq } 100 \text{ g}^{-1}$ and for S65 bentonite $71.5 \text{ meq } 100 \text{ g}^{-1}$ (Gondolli et al. 2013).

 SÚRAO	Radionuclide migration processes in a crystalline rock environment. Final report.	Evidenční označení:
		SÚRAO TZ 333/2018

The resulting CEC values of the rock samples are provided in Tab. 15. As can be seen, the CEC is very low for all the samples, i.e. in the order of tenths of meq 100 g⁻¹, which is two orders of magnitude lower than the values determined for the above-mentioned bentonite materials. Such low CEC values were due to the low content of cation exchange minerals, e.g. layered silicates (biotite, muscovite, smectite, kaolinite, chlorite, etc.). Despite the low CEC values, a certain trend could be observed in the resulting data. The highest CEC was determined for the PZV1 sample which contained the highest amount of biotite. Conversely, the presence of potassium feldspars, plagioclase and magnesio-hornblende did not lead to higher cation exchange capacities. Moreover, the balance between the exchanged CEC_{sum} and copper CECs was approximately in equilibrium with respect solely to the PZV1 sample (0.45 meq 100 g⁻¹ cations versus 0.38 meq 100 g⁻¹ copper), see Tab. 15. Regarding the other samples, where the CEC was one order of magnitude lower, no balance was determined between the exchanged cations and the copper.

The reason consisted of the low exchange capacity of the materials, concerning which the determination of such CEC values suffer from such margins of error that no dependable conclusions can be drawn. Therefore, we do not recommend considering the applicability of the Cu(II)-trien method for the determination of low CEC rocks. For comparison purposes, CEC values for Czech bentonites ranged from 56.8 to 71.5 mmol 100 g⁻¹ (Červinka et al. 2018).

Tab. 15 CEC values of the rock samples determined via the Cu (II)-trien method

Rock	Fraction	CEC (meq 100 g ⁻¹)	CEC _{sum} (meq 100 g ⁻¹)	Mica content ^a (wt%)
PZV1	B	0.38	0.45	13
TIV1	C	0.07	0.13	5.5
PDV1	C	0.09	0.18	7
D2	C	n.a.	n.a.	5.5
S3-3	C	0.27	0.43	4
S3-4	C	n.a.	n.a.	4
S4-3	C	n.a.	n.a.	4.5
2S4-2	C	n.a.	n.a.	11
2S4-4	C	0.07	0.25	< LOD

a) total biotite and muscovite content

n.a. not applicable/was not determined

4.5.2.2 Altered rock and fracture filling samples

Following the investigation of the rock samples, the CEC analysis of samples of selected fracture fillings was performed. The results presented in Fig. 33 reveal that the fracture filling and altered rock samples evinced the highest CEC_{Cu} values of all the studied samples. The highest cation exchange capacity values were obtained from a sample from the BZ-XIIJ fault zone, i.e. sample BZ_317m, concerning which the recorded value was one order of magnitude higher than those of the rock samples. The higher values were most probably related to the higher levels of layered silicates, mainly kaolinite (6.5 wt%), muscovite (10.5 wt%) and chlorite (5 wt%), with higher Fe contents.

 SÚRAO	Radionuclide migration processes in a crystalline rock environment. Final report.	Evidenční označení:
		SÚRAO TZ 333/2018

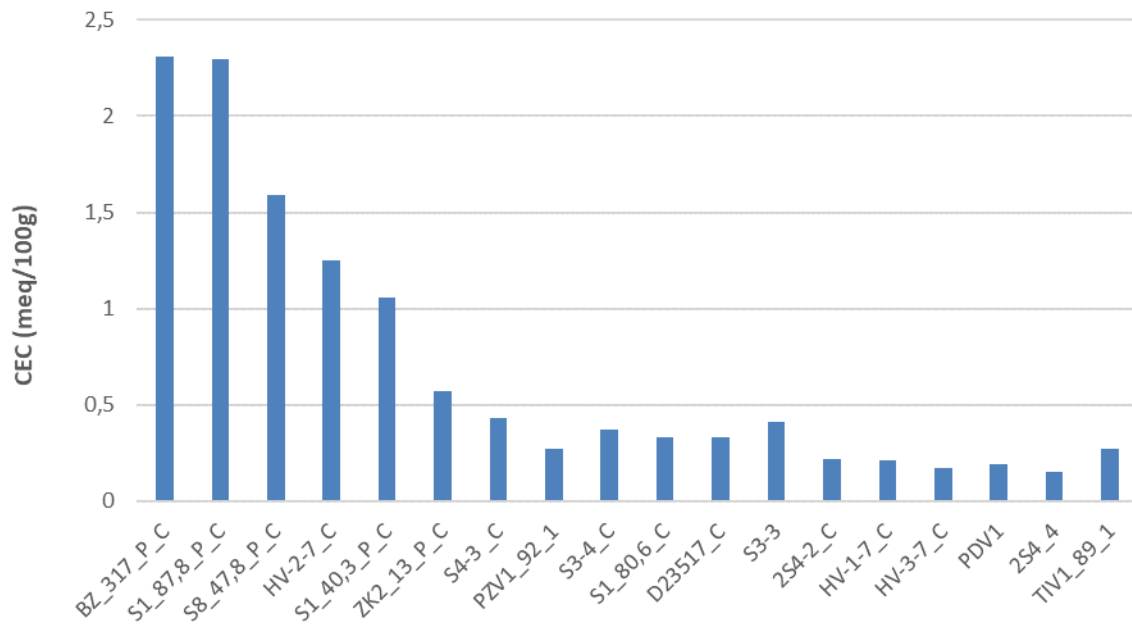


Fig. 33 CEC values of the rock and fracture filling samples determined via the Cu(II)-trien method

4.5.3 CEC verification using sorption isotherms

In order to verify the CEC values obtained via the Cu(II)-trien method, the CECs of the rock samples were determined by means of sorption experiments using the ^{137}Cs radioactive tracer and assessment involving the Langmuir isotherm:

$$q_k = \frac{K_L \cdot C_k \cdot Q_{\max}}{(1 + K_L \cdot C_k)}, \quad (4-5)$$

where q_k is the solid phase radionuclide concentration, C_k is the liquid phase radionuclide concentration, K_L is the Langmuir isotherm coefficient (equilibrium reaction of the addition reaction equation) and Q_{\max} is the Langmuir isotherm coefficient (maximum achievable concentration of the monitored substances in the solid phase).

The Langmuir isotherm provides a typical example of a non-linear isotherm from above a concave shape and is derived on the condition that the sorption is conducted via an addition reaction. The Langmuir isotherm coefficient Q_{\max} (in mmol g^{-1}) quantifies the maximum achievable solid phase concentration of the monitored substances and provides an equivalent value to the cation exchange capacity (CEC) of the given material with respect to the ion exchange sorption of the radionuclide (Štamberg 1998).

For reasons of clarity, the following text will refer to the cation exchange capacity determined by the Langmuir isotherm as Q_{\max} (in mmol g^{-1}). This method was also employed, for example, in the TIP project, where the cation exchange capacities using sorption isotherms were determined for various S65 and B75 modified bentonites. By way of illustration, the resulting Q_{\max} value for B75 bentonite was 0.68 mmol g^{-1} and for S65 bentonite 0.71 mmol g^{-1} (Gondolli et al. 2013).

The rock isotherms were created in a caesium concentration range of $1 \cdot 10^{-5}$ – $9 \cdot 10^{-3}$ mol l⁻¹ per fraction C of all the studied samples. The only exception concerned the PZV1 material, where the sorption isotherm was created on fraction B. The smaller rock fraction was finally chosen due to the problem of the assessment of the sorption experiments and their isotherms on fraction C. Due to the heterogeneity of the composition of the solid phase on fraction C, it was not possible to represent the resulting isotherm points via the Langmuir equation. As in the study of the sorption of radionuclides on the rock samples, solid phase weights of 0.5 g and liquid phase volumes of 5 ml were used in the experiments, which lasted 7 days. For illustration purposes, Fig. 34 shows the resulting sorption isotherm of caesium on the PZV1 material.

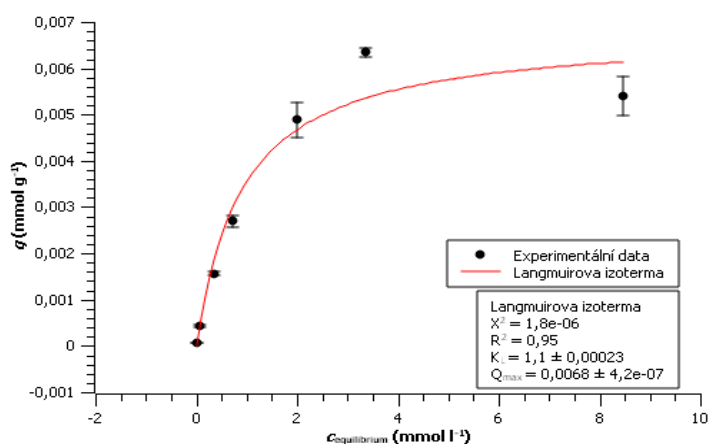


Fig. 34 Sorption of the caesium isotherm on sample PZV1, $c(\text{Cs}) = 1 \cdot 10^{-5}$ – $9 \cdot 10^{-3}$ mol l⁻¹, fraction B: 0.125–0.063 mm

The resulting Q_{max} of the studied rocks are shown in Tab. 16. The very low values result from the mineralogical composition of the rock samples, i.e. the low content of cation exchange minerals. For reasons of comparison, the table also shows the CEC values obtained via the Cu(II)-trien method and converted to units of mmol g⁻¹. The results show that although both values, i.e. the Q_{max} and CEC describe the cation exchange capacity of the rock material (and should, therefore, be identical), they differ from each other. However, it is also evident that they follow the same trend, i.e. both methods determined the highest exchange capacity values with respect to the PZV1 material with high mica content (Fig. 35). The differences between the Q_{max} and CEC values were probably due to the ability of Cs to bind to sorption sites (or exchange with K⁺) from sites that are most likely inaccessible for the Cu(II)-trien molecule (due to the organic nature of this compound, a large molecule size can be assumed).

As with the comparison of the CECs of the rocks and bentonites, the Q_{max} values of the rocks are two orders of magnitude lower than those of the selected bentonites (see above).

Tab. 16 Cation exchange capacity values of the rocks as calculated from the Langmuir isotherm (Q_{max}) and the Cu(II)-trien method (CEC)

Rock	Fraction	Q_{max} (mmol g ⁻¹)	CEC (mmol g ⁻¹)
------	----------	---	--------------------------------

 SÚRAO	Radionuclide migration processes in a crystalline rock environment. Final report.	Evidenční označení:
		SÚRAO TZ 333/2018

PZV1	B	0.0068	0.0019
TIV1	C	0.0012	0.0003
PDV1	C	0.0031	0.0005
D2	C	0.0033	n.a.
S3-3	C	0.0061	0.0014
S3-4	C	0.0046	n.a.
S4-3	C	0.0045	n.a.
2S4-2	C	0.0036	n.a.
2S4-4	C	0.0049	0.0004

n.a. not applicable/not determined

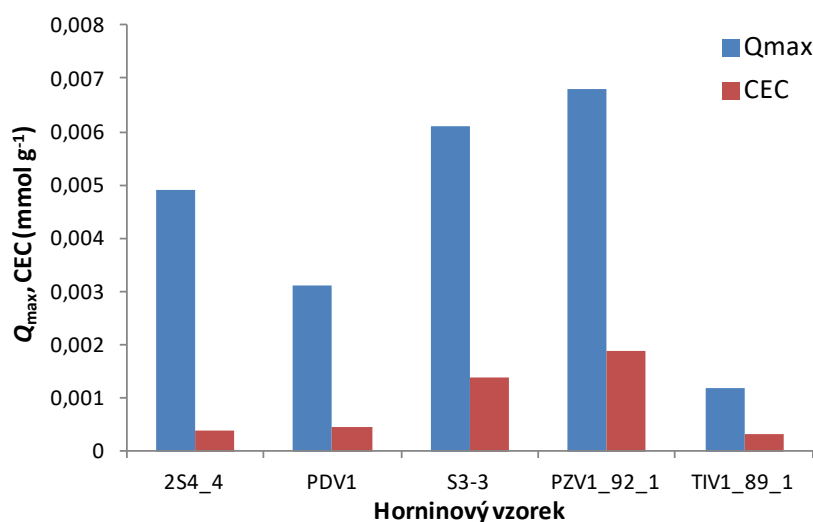


Fig. 35 Cation exchange capacity values of the rocks as calculated from the Langmuir isotherm (Q_{max}) and the Cu(II)-trien method (CEC)

The results imply that the sorption of radionuclides via the ion exchange mechanism occurs only at the sorption sites of the layered silicates, which have a minority representation in the rock structure, and that sorption on other minerals (plagioclase, hornblende, etc.) appears to be the formation of surface complexes. The results also show that the determination of the cation exchange capacities of rock samples is problematic and that none of the methods used is wholly suitable for the accurate determination of low exchange capacity values.

4.5.4 Determination of the specific surface area and mercury porosity

The specific surface was measured on prepared samples of altered rocks and fracture fillings of fraction C, which was also used in the sorption experiments. The measurement of the pore distribution and the specific surface area was performed at the University of Chemistry and Technology, Prague on Micromeritics 3Flex and ASAP 2020 equipment, which is used mainly for the measurement of the N₂ adsorption isotherm (adsorption isotherm – the dependence of

 SÚRAO	Radionuclide migration processes in a crystalline rock environment. Final report.	Evidenční označení:
		SÚRAO TZ 333/2018

the adsorbed amount of a component on its pressure over the solid substance at a constant temperature). The specific surface of the mesopores is then obtained from this dependence employing, for example, the BET method. Krypton is used as the adsorption gas for the measurement of small surfaces (around $1 \text{ m}^2 \text{ g}^{-1}$). The specific surface areas of the various samples was determined according to the BET method from both nitrogen and krypton measurements. The results are shown in Tab. 17.

Tab. 17 – Specific surface area values ($\text{m}^2 \text{ g}^{-1}$) measured via (N_2 , Kr), porosity values determined by Hg porosimetry and cation exchange capacity (CEC_{Cu}) for the fracture filling and rock matrix materials (in grey)

Sample	Specific surface ($\text{m}^2 \text{ g}^{-1}$) measured by N_2	Specific surface ($\text{m}^2 \text{ g}^{-1}$) measured by Kr	Hg porosity (%)	CEC (meq 100 g^{-1}) Cu(II)-trien
BZ_317m_fraction C	9.1314	-	6.05	2.31
S1_87.8m_fraction C	3.5327	4.6146	3.77	2.29
S8_47.8m_fraction C	1.5748	1.8329	3.84	1.58
ZK2_13m_fraction C	1.1479	1.4287	3.47	0.57
S1_40.3m fraction C	1.1216	1.5059	2.11	1.06
S1_80.6 m				0.33
D2 3517, fraction C	0.197	0.2176	1.93	0.33
D2-3, sample piece	0.0878	0.0871	0.19	

The Kr and N_2 specific surface measurement results were similar, i.e. at around $1 \text{ m}^2 \text{ g}^{-1}$. In general, it is possible to state that since the krypton measurements indicated higher surface areas, the agreement between the nitrogen and krypton measurements will decline with increasing surface areas. The S1-87.8m fraction C sample evinced a specific surface area as measured by nitrogen of $3.533 \text{ m}^2 \text{ g}^{-1}$ and by krypton of $4.615 \text{ m}^2 \text{ g}^{-1}$. Since krypton measurement indicates larger specific surface areas, the specific surface value measured by nitrogen can be assumed to be more accurate of the two approaches. The BZ_317m sample evinced a specific surface area measured by nitrogen of $9.1314 \text{ m}^2 \text{ g}^{-1}$; the surface area was not measured using krypton since it was already too high for the application of this method. The lowest specific surface areas were recorded for the carbonate-quartz vein ZK2_13 m sample ($1.4 \text{ m}^2 \text{ g}^{-1}$; Kr) and the leucogranite S1_40.3m sample ($1.51 \text{ m}^2 \text{ g}^{-1}$; Kr).

A sample from the Deštná site (D2) was investigated for the comparison of intact healthy rock (granite) and the prepared C fraction of the same rock. A specific surface area value of around $0.087 \text{ m}^2 \text{ g}^{-1}$ (Kr) was recorded for the intact rock ($7 \times 7 \times 20 \text{ mm}$ block) whereas, in contrast, the prepared C fraction of the same sample (D2) evinced a specific surface area value of around $0.22 \text{ m}^2 \text{ g}^{-1}$ (Kr).

In addition, Hg porosimetry was performed on the same samples. The measured porosity values were found to correlate closely with both the specific surface values and the CEC_{Cu} values (Tab. 17). The highest porosity (6.1%) was recorded for hydrothermally altered gneiss from a fault zone (BZ_317m). The other porosity values (fraction C) ranged between 3.77% (S1_87.8m) and 2.11% (S1_40.3m). The porosity of the non-affected granite from the Čihadlo site (D2) was determined at 0.19%, which increased to 1.93% following the grinding of the sample.

The investigated samples contained both micropores and smaller mesopores. The largest pore representation was between 0.1 and 1 μm . The pore size distribution in the samples is shown graphically in Fig. 36.

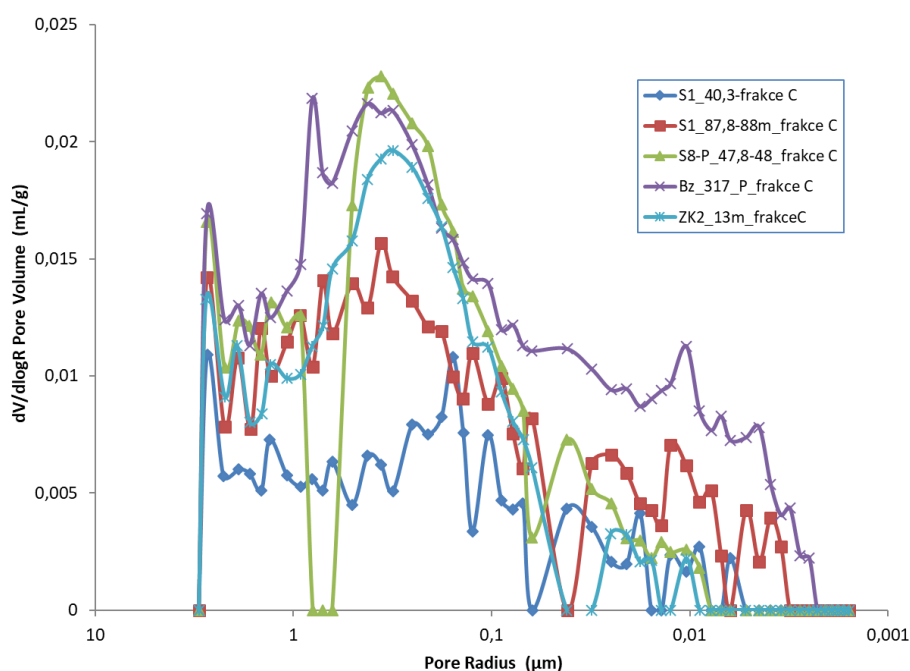


Fig. 36 Pore size distribution in the studied fracture filling samples

The cumulative curve indicates that most of the pores were filled in the low pressure section and contained mainly larger pores. The highest representation of pores was recorded for the BZ_317m sample and the lowest for the carbonate-quartz vein ZK2_13m sample (Fig. 37).

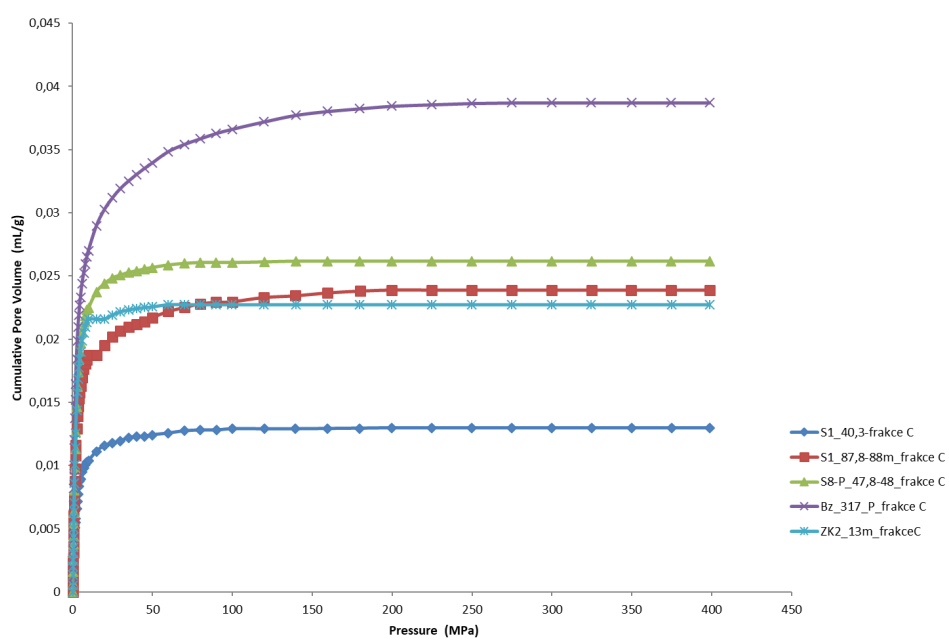


Fig. 37 Cumulative pore distribution curves of the studied fracture filling samples

 SÚRAO	Radionuclide migration processes in a crystalline rock environment. Final report.	Evidenční označení:
		SÚRAO TZ 333/2018

5 Sorption of radionuclides on granitic rocks

5.1 Methodology

The principle of the static sorption experiment consists of the interaction of a known amount of the solid phase (sorbent) m (g) and a known volume of the liquid phase V (l) with a given initial concentration c_0 (mol l⁻¹) or volume activity A_0 (Bq l⁻¹; cpm, etc.) of the radionuclide under study. The reaction mixture, containing the solid phase, the liquid phase and the radionuclide, is placed for a pre-determined time in a sealable sample tube (tube, flask, vial, etc.) and is stirred regularly. Mixing is conducted continuously on a shaker or manually periodically (e.g. 1 × per day). Following the given time interval, the solid and liquid phases are separated and the concentration (activity) of the radionuclide c (or A) in the liquid phase is determined. The interaction of the studied radionuclide is described by the values of the distribution coefficient R_d and the sorption yield η_{sorpce} , which are given by:

$$R_d = \frac{(c_0 - c) \cdot V}{c \cdot m}, \quad (5-1)$$

$$\eta_{\text{sorpce}} = \frac{(c_0 - c)}{c_0} \cdot 100, \quad (5-2)$$

where c_0 is the initial concentration of the monitored substance (mol l⁻¹), c is the concentration of the monitored substance in the aqueous phase (mol l⁻¹), V is the volume of the liquid phase (l) and m is the mass of the solid phase (g).

With respect to this experiment, the ratio of the solid (g) to the liquid phase (ml) was: s : l = 1 : 10 and the weight of the rock material was 0.5 g. The sorption experiment lasted 7 days and radionuclide sorption was monitored after 0.04, 0.31, 1, 2, 4 and 7 days of phase contact.

The sorption of the following species of radionuclides was studied on selected rock samples:

- ¹³⁷Cs; CsCl ($c = 2 \cdot 10^{-5}$ mol l⁻¹) labelled ¹³⁷CsCl ($A_0 \sim 800$ Bq ml⁻¹)
- ⁸⁵Sr; SrCl₂ ($c = 2 \cdot 10^{-5}$ mol l⁻¹) labelled ⁸⁵SrCl₂ ($A_0 \sim 800$ Bq ml⁻¹)
- SeO₃²⁻ in the form of Na₂SeO₃ ($c = 2 \cdot 10^{-5}$ mol l⁻¹)
- UO₂²⁺ in the form of UO₂(NO₃)₂ ($c = 2.6 \cdot 10^{-4}$ mol l⁻¹)
- ³⁶Cl; NaCl ($c = 1.1 \cdot 10^{-4}$ mol l⁻¹) labelled Na³⁶Cl ($A_0 \sim 800$ Bq ml⁻¹)
- ¹²⁵I; CaI₂ ($c = 2 \cdot 10^{-5}$ mol l⁻¹) labelled Na¹²⁵I ($A_0 \sim 800$ Bq ml⁻¹)
- ¹⁵²Eu; EuNO₃ ($c = 2 \cdot 10^{-5}$ mol l⁻¹) labelled ¹⁵²EuCl₃ ($A_0 \sim 800$ Bq ml⁻¹)

Caesium is one of a group of critical radionuclides that occurs exclusively as a cation (Cs(I)), which does not form complexes in solution. Whereas the sorption of Cs(I) to hydroxyl groups of given minerals is prevented by its large size and low charge, its sorption to mica minerals via cation exchange and surface complexation is highly effective (Söderlund et al. 2014).

 SÚRAO	Radionuclide migration processes in a crystalline rock environment. Final report.	Evidenční označení:
		SÚRAO TZ 333/2018

Strontium is one of a group of cationically weakly-sorbing critical radionuclides. It occurs in the form of Sr (II) and forms carbonate complexes and hydroxo-complexes at pH > 9 or in the presence of carbonates. The main sorption mechanism in the rock environment consists of ion exchange, wherein sorption is determined principally by the cation exchange capacity (CEC) values and the pH (Carbol and Engkvist 1997).

Selenium is one of a group of redox-sensitive anionic critical radionuclides. It is characterised by complicated chemistry - under oxidation conditions it occurs as selenite (SeO_3^{2-}) and selenate (SeO_4^{2-}) and under mildly reducing conditions as elemental Se; under reducing conditions the dominant species is selenide (HSe^{2-}). Selenium in the form SeO_3^{2-} was chosen for the experiments since it is able to sorb on rock materials under given conditions. In contrast, SeO_4^{2-} behaves as a non-sorbing radionuclide in crystalline rock environments (Havlová et al. 2013).

Uranium is one of a group of redox-sensitive critical radionuclides; it occurs in the geosphere predominantly in two oxidation stages: U(IV) and U(VI). Its sorption on rocks depends on the pH of the system; under low pH, uranyl ions (UO_2^{2+}) are sorbed via cation exchange, while with increasing pH, uranyl sorption decreases as a result of the formation of non-sorbing U(VI)-carbonate complexes (Hakanen et al. 2014).

Iodine and chlorine are two of the most important radionuclides in terms of their contribution to the total dose per member of the representative population as considered in the long-term safety assessments of deep geological repositories (DGR). Since the capture of even small amounts of these radionuclides would make an important contribution to reducing their effects, the study included the assessment of the capture of these radionuclides on fracture filling materials.

Chlorine is present in groundwater in the form of Cl^- , and this chloride ion is one of the most conservative ions present in the geosphere. Its unwillingness to sorb and the increased concentration of the chloride in deep groundwater predetermines it for low sorption on granitic rocks (Carbol and Engkvist 1997). With respect to deep disposal, the most important isotope is ^{36}Cl , whose half-life is $3.01 \cdot 10^5$ years. It is produced by the capture of neutrons by stable ^{35}Cl , which is present in trace amounts (i.e. as an impurity) in various materials present in nuclear reactors (Sheppard 1996).

Iodine is a redox-sensitive element that occurs in groundwater in the form of I^- . In surface waters, a part of the presence of iodine may consist of IO_3^- (Hakanen et al. 2014). Iodine is present in nuclear waste in the form of a fission product. Iodine has several isotopes, most of which have short half-lives (in days). However, the most problematic isotope consists of ^{129}I , which has a half-life of $1.57 \cdot 10^7$ years (β radiation) (Carbol and Engkvist 1997). Due to the anionic character of iodine, low sorption on granitic rocks can be predicted (Havlová et al. 2015a).

The project was expanded to include the consideration of europium, a chemical analogue of americium. Americium will be present in spent nuclear fuel in the form of the ^{243}Am isotope, which is formed via multi-stage neutron capture on ^{238}U , the properties of which rank it as one of the group of critical radionuclides (alpha emitter, $T_{1/2} \sim 7400$ years). The use of europium as a chemical analogue of americium is commonly considered in practice, either in separation (extraction, elution methods) or in other chemical processes. ^{152}Eu is a redox-sensitive radionuclide with a ready tendency to hydrolyse at a pH of 8–9 and, therefore, exhibits strong

 SÚRAO	Radionuclide migration processes in a crystalline rock environment. Final report.	Evidenční označení:
		SÚRAO TZ 333/2018

sorption on mineral surfaces (Baes and Mesmer 1976). In terms of the lanthanide series, the trivalent valency state is dominant.

5.1.1 Description of the solid and liquid phases

5.1.1.1 Description of the solid phase (characterisation of the rock fractions used)

The sorption of radionuclides was monitored on selected rock samples taken from candidate DGR sites, an overview and the characterisation of which are provided in Tab. 2.

Five grain fractions were prepared from each of the rock samples (A: < 0.063 mm, B: 0.125–0.063 mm, C: 0.63–0.125 mm, D: 0.8–0.63 mm and E: > 0.8 mm), which were subsequently analysed via X-ray diffraction on a powder diffractometer. The mineralogical composition of the individual fractions is shown in Tab. 5.

The fractions selected for the sorption experiments (C: 0.63–0.125 mm and D: 0.8–0.63 mm) were subsequently washed with SGW2 synthetic granitic water, air dried and submitted to sorption experimentation. The weight of the rock materials was 0.5 g.

5.1.1.2 Properties of the solutions used

Synthetic granitic water designated SGW2 (Červinka and Gondolli 2016) was used for the sorption experiments, the composition of which is shown in Tab. 18.

Tab. 18 Chemical composition and pH of the SGW2 synthetic granitic water (Červinka and Gondolli 2016)

Species	SGW2 (mg l ⁻¹)
Na ⁺	16.5
K ⁺	2.14
Ca ²⁺	37.3
Mg ²⁺	8.32
Cl ⁻	3.49
SO ₄ ²⁻	21.9
HCO ₃ ⁻	168.7
pH	8.2

5.2 Results and evaluation

5.2.1 Caesium

The resulting caesium R_d values for the studied rock samples are shown in Fig. 38 and in Tab. 19 and Tab. 20. The R_d values ranged from 9–111 ml g⁻¹ for fraction C and 8–135 ml g⁻¹ for fraction D. Low values were obtained with concern to both fractions on TIV1 granite (Čertovka

 SÚRAO	Radionuclide migration processes in a crystalline rock environment. Final report.	Evidenční označení:
		SÚRAO TZ 333/2018

site) and the highest R_d values related to the PZV1 durbachite sample (Horka site). These two rock samples differed significantly in terms of their mineralogical composition (see Tab. 5). The TIV1 granite (Čertovka site) contained almost 50 wt% of quartz (the PZV1 sample contained 25 wt% of quartz) and the PZV1 durbachite (Horka site) contained a significantly higher amount of biotite (19.5 wt% for fraction C). The content of other minerals was comparable (see Tab. 5).

Low R_d values of around 10 ml g^{-1} were recorded for both fractions for the D2, 2S4-4 and GRB samples, all of which were characterised by low (D2 granite - Čihadlo site, GRB granulite - Kraví hora site) or no (2S4-4 amphibolite - Bukov URF/Kraví hora) biotite contents and a 50 wt% content of magnesio-hornblende (2S4-4 amphibolite – Bukov URF/Kraví hora). With respect to the granodiorite BT sample (Březový potok site) and GB granite (Hrádek site), the final R_d value was in the range $22\text{--}32 \text{ ml g}^{-1}$. These two samples were characterised by relatively low biotite contents (below 10 wt%) and relatively high proportions of plagioclase (30–42 wt%).

The R_d values of the remaining rock samples, i.e. samples from the Bukov URF (S3-3, S3-4, S4-3 and 2S4-2) were determined at between $30\text{--}40 \text{ ml g}^{-1}$ for fraction C and $70\text{--}110 \text{ ml g}^{-1}$ for fraction D. While the mica mineral contents in these samples were lower than in the PZV1 durbachite sample (Horka site), the samples were interesting in terms of their content of hornblende amphibolic minerals and high contents of plagioclase (around 50 wt%). With concern to the Bukov URF samples, roughly twice the sorption was observed on fraction D (larger grain size) than on fraction C, the reason for which was unclear. The C and D fractions did not differ significantly in terms of their mineralogical composition, thus no enrichment of certain minerals occurred in either fraction due to crushing and sieving that might have resulted in the higher capture of caesium. A different situation was observed, for example, concerning the PZV1 durbachite sample (Horka site), where a higher level of sorption was observed on fraction C, the biotite content of which was 50% higher than that of fraction D (see Tab. 5). Since higher caesium capture levels were observed for fraction D concerning the Bukov URF samples, sorption was not influenced by the sorption surface, which was considered for the smaller C grain fraction. Since the other experimental conditions were very similar for both fractions, no differences were observed regarding the pH (pH ~ 8.5) and E_h ($E_h \sim 400 \text{ mV}$) electrochemical parameters.

The R_d values of the C fractions of the rock samples (ZK2 13m, S1 40.3m, S1 80.6m, S1 87.8m, S8 47.8m and BZ 317m) with fracture fillings (labelled P), which were examined in the context of the expansion of the project varied in the range $8\text{--}362 \text{ ml g}^{-1}$. For illustration purposes, sorption experiments performed on the D fractions of three selected fractures revealed R_d values in the range $6\text{--}91 \text{ ml g}^{-1}$.

The highest fraction C sorption level was recorded for sample BZ 317 (362 ml g^{-1}), which contained the highest amounts of kaolinite (6.5 wt%) and mica (10.5 wt%) compared to the other investigated rocks with fractures. Other significant sorption levels were recorded for the S1 87.8m (213 ml g^{-1}) and S8 47.8m (150 ml g^{-1}) materials, which differed significantly in terms of their composition, i.e. both biotite (19 wt%) and kaolinite (4 wt%) were present in the S1 87.8m sample (213 ml g^{-1}), while sample S8 47.8 m (150 ml g^{-1}) contained hornblende (3.5 wt%), chlorite (12 wt%) and a small amount of mica (0.5 wt%).

 SÚRAO	Radionuclide migration processes in a crystalline rock environment. Final report.	Evidenční označení:
		SÚRAO TZ 333/2018

The resulting distribution coefficient values show that of all the studied samples caesium is sorbed particularly on rocks that contain mica, plagioclase and amphibolite. Mica, a member of the phyllosilicates group, and amphibolites, that belong to the inosilicates group, retain caesium via the ion exchange mechanism. Further information on the mechanism governing the capture of caesium on rocks and minerals is available in a report by Havlová et al. (2017).

	Radionuclide migration processes in a crystalline rock environment. Final report.	Evidenční označení:
		SÚRAO TZ 333/2018

Tab. 19 Caesium R_d values, including their expanded standard uncertainties, of the C fractions of rock samples from candidate DGR sites, $c(\text{Cs}) = 2 \cdot 10^{-5} \text{ mol l}^{-1}$, fraction C: 0.63–0.125 mm

Rock sample	Time of sorption (days)					
	0.04	0.31	1	2	4	7
PZV1-C	6.4 ± 1.2	7.4 ± 1.2	22.9 ± 2.4	13.1 ± 1.6	74.1 ± 6.5	129 ± 11
TIV1-C	2.4 ± 0.9	3.1 ± 1.0	2.7 ± 0.9	4.7 ± 1.1	5.1 ± 1.1	9.0 ± 1.3
PDV1-C	2.9 ± 1.0	3.5 ± 1.0	4.4 ± 1.0	10.2 ± 1.4	12.8 ± 1.6	25.2 ± 2.6
D2-C	4.8 ± 1.1	6.2 ± 1.1	6.0 ± 1.1	6.7 ± 1.2	7.2 ± 1.2	10.3 ± 1.4
S3-3-C	7.4 ± 1.2	10.6 ± 1.4	15.2 ± 1.8	25.9 ± 2.6	28.6 ± 2.8	36.6 ± 3.4
S3-4-C	5.4 ± 1.1	7.9 ± 1.3	14.1 ± 1.7	16.7 ± 1.9	24.6 ± 2.6	41.1 ± 3.9
S4-3-C	4.4 ± 1.0	6.0 ± 1.1	6.0 ± 1.1	15.2 ± 1.8	14.5 ± 1.7	29.1 ± 2.9
2S4-2-C	6.2 ± 1.2	8.3 ± 1.3	7.4 ± 1.6	15.4 ± 1.8	13.7 ± 2.4	42.0 ± 3.2
2S4-4-C	4.6 ± 1.1	4.0 ± 1.0	7.3 ± 1.2	7.5 ± 1.2	9.2 ± 1.4	9.3 ± 1.4
GRB-C	6.6 ± 1.2	10.2 ± 1.4	10.0 ± 1.4	12.8 ± 1.6	12.5 ± 1.6	12.7 ± 1.6
BT-C	9.6 ± 1.4	13.3 ± 1.6	15.6 ± 1.8	21.0 ± 2.7	24.5 ± 3.1	29.1 ± 3.5
GB-C	7.9 ± 1.3	14.1 ± 1.7	17.2 ± 1.9	22.9 ± 2.4	21.5 ± 2.3	22.3 ± 2.3
Fracture fillings						
ZK2 13m_P	4.9 ±	5.5 ± 1.1	6.7 ± 1.1	6.3 ± 1.2	7.5 ± 1.2	8.2 ± 1.3
S1 40.3m_P	14.0 ± 1.5	11.7 ± 1.5	21.5 ± 2.3	22.2 ± 2.3	24.4 ± 2.5	29.3 ± 2.7
S1_80.6m_P	16.8 ± 1.9	27.7 ± 2.9	40.0 ± 3.7	39.9 ± 3.7	61.6 ± 5.8	133.1 ± 11.1
S1 87.8m_P	74.0 ± 6.0	79.1 ± 6.8	102.9 ± 9.2	141.2 ± 10.6	102.2 ± 8.7	213.4 ± 15.6
S8 47.8m_P	20.3 ± 2.2	85.9 ± 7.3	56.9 ± 5.1	110.1 ± 9.4	140.0 ± 11.7	150.1 ± 12.5
BZ_317_P	197.0 ± 16.3	284.4 ± 23.3	198.8 ± 18.8	241.8 ± 20.3	281.7 ± 23.2	361.8 ± 29.5

Tab. 20 Caesium R_d values, including their expanded standard uncertainties, of the D fractions of rock samples from candidate DGR sites, $c(\text{Cs}) = 2 \cdot 10^{-5} \text{ mol l}^{-1}$, fraction D: 0.8–0.63 mm

Rock sample	Time of sorption (days)					
	0.04	0.31	1	2	4	7
PZV1-D	4.1 ± 1.0	7.4 ± 1.3	30.0 ± 3.3	51.7 ± 4.7	111 ± 10	104 ± 9.0
TIV1-D	1.3 ± 0.9	2.4 ± 0.9	2.0 ± 0.9	3.8 ± 1.0	8.9 ± 1.3	10.6 ± 1.5
PDV1-D	2.1 ± 0.9	3.3 ± 1.0	6.0 ± 1.1	12.9 ± 1.6	19.9 ± 2.2	30.7 ± 2.9
D2-D	2.4 ± 0.9	4.0 ± 1.0	5.3 ± 1.1	5.3 ± 1.1	7.9 ± 1.3	9.7 ± 1.4
S3-3-D	4.4 ± 1.0	7.2 ± 1.4	19.9 ± 1.9	12.3 ± 2.4	38.5 ± 3.6	71.0 ± 6.2

S3-4-D	4.1 ± 1.0	4.5 ± 1.0	3.9 ± 1.2	48.4 ± 3.8	41.3 ± 3.3	89.1 ± 6.5
S4-3-D	3.0 ± 1.0	5.9 ± 1.1	9.4 ± 1.4	20.9 ± 2.0	34.2 ± 3.3	72.0 ± 6.7
2S4-2-D	1.9 ± 0.9	3.3 ± 1.0	15.0 ± 1.6	17.6 ± 1.7	26.9 ± 3.8	111 ± 12
2S4-4-D	2.3 ± 0.9	4.0 ± 1.0	6.0 ± 1.1	6.2 ± 1.1	7.7 ± 1.2	8.4 ± 1.3
GRB-D	3.0 ± 1.0	7.3 ± 1.2	11.1 ± 1.5	11.3 ± 1.5	12.2 ± 1.6	12.8 ± 1.6
BT-D	4.1 ± 1.0	8.2 ± 1.3	10.7 ± 1.5	15.8 ± 2.2	29.2 ± 3.5	32.7 ± 3.8
GB-D	4.5 ± 1.0	11.0 ± 1.5	13.0 ± 1.6	14.6 ± 1.7	16.4 ± 1.9	22.2 ± 2.3
Fracture fillings						
ZK2 13m P	3.4 ± 1.0	4.0 ± 1.0	6.7 ± 1.2	6.3 ± 1.2	5.7 ± 1.1	6.1 ± 1.3
S1 40.3m P	8.8 ± 1.2	13.9 ± 1.9	18.1 ± 2.0	19.0 ± 2.1	21.7 ± 2.3	21.4 ± 2.2
S1 87.8m P	31.3 ± 3.1	51.6 ± 4.2	68.7 ± 6.6	121.5 ± 9.3	83.4 ± 7.2	90.9 ± 11.8

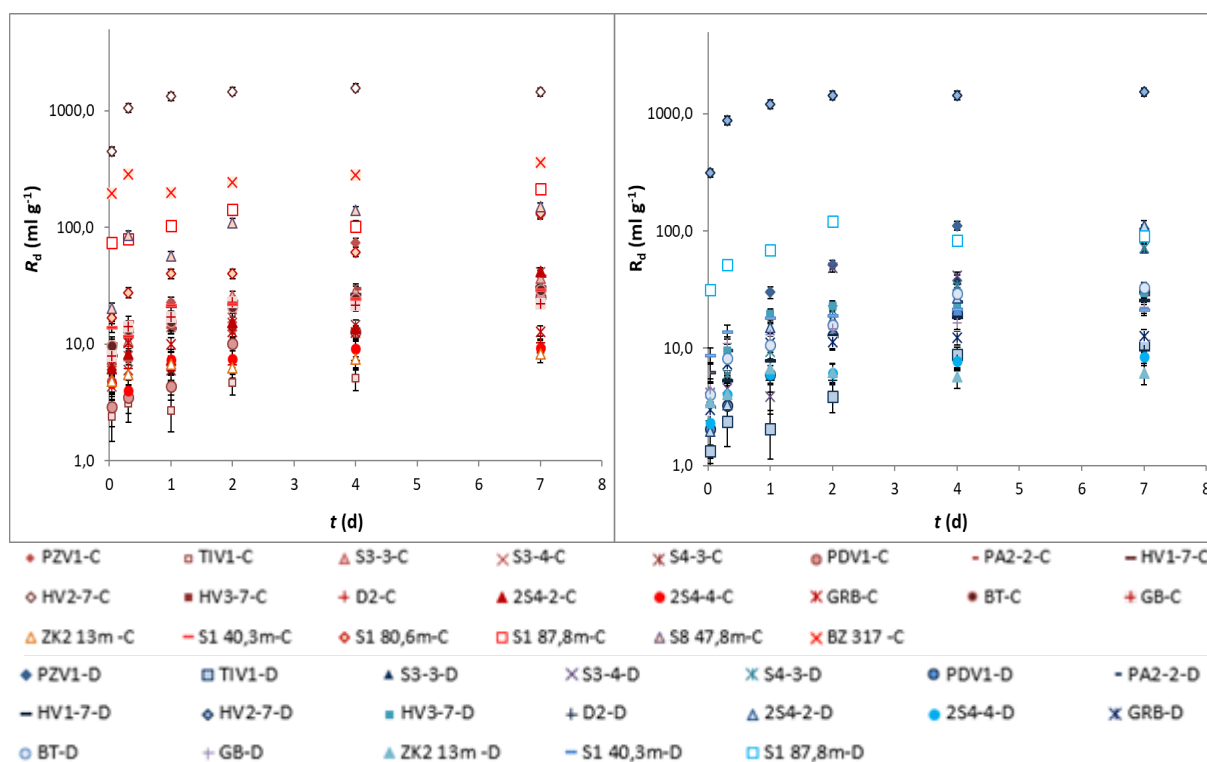


Fig. 38 Caesium R_d values, including their expanded standard uncertainties of rock samples from the candidate sites, left: fraction C (0.63–0.125 mm), right: fraction D (0.8–0.63 mm), $c(\text{Cs}) = 2 \cdot 10^{-5} \text{ mol l}^{-1}$

 SÚRAO	Radionuclide migration processes in a crystalline rock environment. Final report.	Evidenční označení:
		SÚRAO TZ 333/2018

5.2.2 Strontium

The resulting strontium R_d values of the samples are shown in Fig. 39 and in Tab. 21 and. The R_d values are one order of magnitude lower than in the case of caesium, with only slightly higher R_d values being attained with respect to the C rock fractions of all the studied materials. The strontium fraction C R_d of the samples ranged from 2.2 to 7.0 ml g⁻¹, while the R_d of the D fractions ranged from 1.2 to 5.9 ml g⁻¹. For both fractions, the lowest R_d values were recorded for the TIV1 (granite, Čertovka site) and the PDV1 (granite, Panské Dubenky site) samples, with higher values being recorded for the fraction samples from the Bukov site (S3-3, S4-3 and S3-4) and the GB sample (granite, Hrádek site). The highest R_d values for both fractions were determined for the BT sample (granodiorite, Březový potok site) which contained 9 wt% of biotite and nearly 40 wt% of plagioclase.

As can be seen from the above results, a higher biotite content does not necessarily lead to a higher degree of strontium capture (PZV1, Horka site) (Fig. 39 in chapter 5.2.8 **Chyba! Nenalezen zdroj odkazů.**), rather, with respect to the sorption of this radionuclide, the presence of amphibolites should be considered, e.g. in the Bukov URF samples (Ticknor et al. 1989). Nevertheless, since higher R_d values were also obtained for the samples with an almost 50 wt% content of plagioclase, the importance of the function of this series of minerals in crystalline rocks should not be neglected.

The results show that the smaller grain fraction of the studied rocks led to a higher R_d value with respect only to the migmatite 2S4-2 sample (Bukov URF/Kraví hora site; 4.8 ml g⁻¹ versus 1.6 ml g⁻¹). The R_d values of the other materials were either identical or differed in terms of just single units for the two fractions, which corresponded to the expanded standard uncertainty of the determination of R_d .

Strontium in crystalline rocks preferentially sorbs on hornblende and mica minerals, while quartz and feldspars are characterised by a low level of strontium capture (Tricknor et al. 1989). Crawford (Crawford et al. 2006) identified reversible ion exchange as the main strontium sorption mechanism on crystalline rocks in groundwater environments, and the sorption intensity is given by the solid phase CEC value. Further information on the mechanism governing the capture of strontium on rocks and minerals is available in a report by Havlová et al. (2017).

Tab. 21 Strontium R_d values, including their expanded standard uncertainties, of the C fractions of rock samples from candidate DGR sites, $c(\text{Sr}) = 2 \cdot 10^{-5} \text{ mol l}^{-1}$, fraction C: 0.63–0.125 mm

Rock sample	Time of sorption (days)					
	0.04	0.31	1	2	4	7
PZV1-C	2.7 ± 0.9	2.7 ± 0.9	2.8 ± 1.0	3.8 ± 1.0	4.0 ± 1.0	4.0 ± 1.0
TIV1-C	< 0.8	1.2 ± 0.9	1.3 ± 0.9	1.5 ± 0.9	2.1 ± 0.9	2.2 ± 0.9
PDV1-C	1.7 ± 0.9	1.9 ± 0.9	1.8 ± 0.9	2.1 ± 0.9	2.3 ± 0.9	2.7 ± 0.9
D2-C	1.9 ± 0.9	2.6 ± 0.9	3.8 ± 1.0	5.4 ± 1.1	6.0 ± 1.1	5.9 ± 1.1

Rock sample	Time of sorption (days)					
	0.04	0.31	1	2	4	7
S3-3-C	3.2 ± 1.0	4.1 ± 1.0	4.6 ± 1.1	4.8 ± 1.1	5.7 ± 1.1	5.8 ± 1.1
S3-4-C	2.7 ± 0.9	3.4 ± 1.0	4.0 ± 1.0	4.0 ± 1.0	4.5 ± 1.0	5.4 ± 1.1
S4-3-C	3.3 ± 1.0	4.0 ± 1.0	4.5 ± 1.0	5.3 ± 1.1	4.8 ± 1.1	6.7 ± 1.2
2S4-2-C	2.7 ± 0.9	3.0 ± 1.0	3.2 ± 1.0	3.7 ± 1.0	3.8 ± 1.0	4.8 ± 1.1
2S4-4-C	2.0 ± 0.9	2.6 ± 0.9	3.4 ± 1.0	4.2 ± 1.0	3.5 ± 1.0	3.6 ± 1.0
GRB-C	2.3 ± 0.9	2.4 ± 0.9	2.4 ± 0.9	2.8 ± 0.9	2.6 ± 0.9	3.0 ± 1.0
BT-C	5.3 ± 1.1	6.3 ± 1.2	6.7 ± 1.2	7.0 ± 1.5	7.0 ± 1.5	7.0 ± 1.5
GB-C	3.8 ± 1.0	5.1 ± 1.1	5.0 ± 1.1	5.3 ± 1.1	5.6 ± 1.1	5.5 ± 1.1

Tab. 22 Strontium R_d values, including their expanded standard uncertainties, of the D fractions of rock samples from candidate DGR sites, $c(\text{Sr}) = 2 \cdot 10^{-5} \text{ mol l}^{-1}$, fraction D: 0.8–0.63 mm

Rock sample	Time of sorption (days)					
	0.04	0.31	1	2	4	7
PZV1-D	1.3 ± 0.9	1.7 ± 0.9	1.8 ± 0.9	2.0 ± 0.9	3.0 ± 1.0	3.7 ± 1.0
TIV1-D	< 0.8	1.0 ± 0.9	< 0.8	1.0 ± 0.9	1.0 ± 0.9	1.2 ± 0.9
PDV1-D	1.3 ± 0.9	1.6 ± 0.9	1.7 ± 0.9	1.8 ± 0.9	1.9 ± 0.9	2.3 ± 0.9
D2-D	1.4 ± 0.9	2.2 ± 0.9	2.7 ± 0.9	3.1 ± 1.0	3.4 ± 1.0	4.5 ± 1.1
S3-3-D	2.3 ± 0.9	2.7 ± 0.9	3.3 ± 1.0	3.6 ± 1.0	4.3 ± 1.0	4.3 ± 1.0
S3-4-D	1.7 ± 0.9	2.3 ± 0.9	2.9 ± 1.0	2.6 ± 0.9	3.8 ± 1.0	3.7 ± 1.0
S4-3-D	2.4 ± 0.9	2.8 ± 1.0	3.0 ± 1.0	3.2 ± 1.0	4.0 ± 1.0	4.4 ± 1.0
2S4-2-D	0.9 ± 0.9	1.0 ± 0.9	1.1 ± 0.9	1.5 ± 0.9	1.5 ± 0.9	1.6 ± 0.9
2S4-4-D	3.0 ± 1.0	4.1 ± 1.0	4.5 ± 1.0	4.4 ± 1.0	4.8 ± 1.1	5.0 ± 1.1
GRB-D	1.4 ± 0.9	2.2 ± 0.9	2.4 ± 0.9	2.6 ± 0.9	2.4 ± 0.9	2.7 ± 0.9
BT-D	2.6 ± 0.9	3.9 ± 1.0	4.8 ± 1.1	4.8 ± 1.3	5.6 ± 1.4	5.9 ± 1.4
GB-D	2.3 ± 0.9	3.4 ± 1.0	3.7 ± 1.0	4.1 ± 1.0	4.1 ± 1.0	4.1 ± 1.0

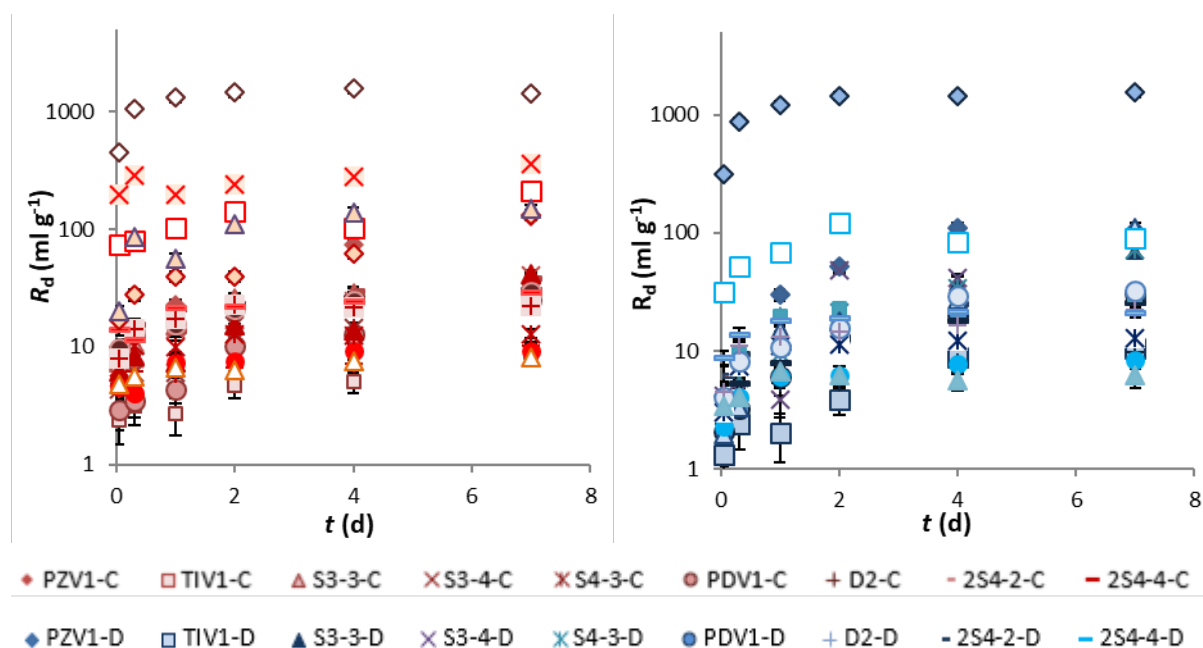


Fig. 39 Strontium R_d values, including their expanded standard uncertainties, of rock samples from the candidate sites, left: fraction C (0.63–0.125 mm), right: fraction D (0.8–0.63 mm), $c(\text{Sr}) = 2 \cdot 10^{-5} \text{ mol l}^{-1}$

5.2.3 Selenium

The final selenite R_d values for the samples studied are shown in Fig. 40 and in Tab. 23 and Tab. 24. The R_d values for the rocks of the candidate sites were determined to be in the range 0.2–12 ml g^{-1} in the case of fraction C and 0.3 to 5 ml g^{-1} for fraction D; thus, the slightly higher sorption of selenite was evident for the C fractions of the studied rocks. The only exception concerned the D2 granite sample (Čihadlo locality), the R_d values of which were 12.3 ml g^{-1} for fraction C and 4.7 ml g^{-1} for fraction D, i.e. in both cases significantly higher than for the other rocks studied. The question therefore is what led to the higher sorption of selenium on this sample? Its mineralogy implied that it did not contain a significantly higher content of “interesting” minerals than did the other rock samples; the contents of biotite, muscovite and kaolinite were in the order of single units of percent. With respect to a number of rock samples, a minimum change was evident that was less than the level of measurement uncertainty (for $R_d \sim 0 \text{ ml g}^{-1}$, $U_{R_d} < 0.8 \text{ ml g}^{-1}$). Due to the insufficient evidence of sorption on these materials, the R_d distribution coefficient results are not included in Tab. 23 and Tab. 24.

Furthermore, the study of selenite sorption was performed for the samples with fracture fillings, the R_d values for which are shown in Tab. 23 and Tab. 24, i.e. the R_d ranged between 1.4–5.6 ml g^{-1} for fraction C and around 1 ml g^{-1} for fraction D. Since the investigation of the D fractions of the sorption material was not considered to be of interest in terms of the expansion of the project, only two fracture samples were subjected to experimentation. The sorption of selenite on the selected fractured rocks was found to be higher than that of the granitic rock samples, i.e. in neither case were the R_d values determined to be below the level of measurement uncertainty ($U_{R_d} < 0.8 \text{ ml g}^{-1}$). The higher sorption may have been due to the presence of calcite in all the fracture samples. Furthermore, all the samples, except for the S1 87.8m sample (Bukov URF site), contained chlorite, i.e. an Fe-mineral characterised by the capture

 SÚRAO	Radionuclide migration processes in a crystalline rock environment. Final report.	Evidenční označení:
		SÚRAO TZ 333/2018

of selenite. The highest sorption in this series of samples concerned the ZK 13 m sample (Bukov URF site), which contained the highest amounts of both chlorite (13.5 wt%) and calcite (34 wt%).

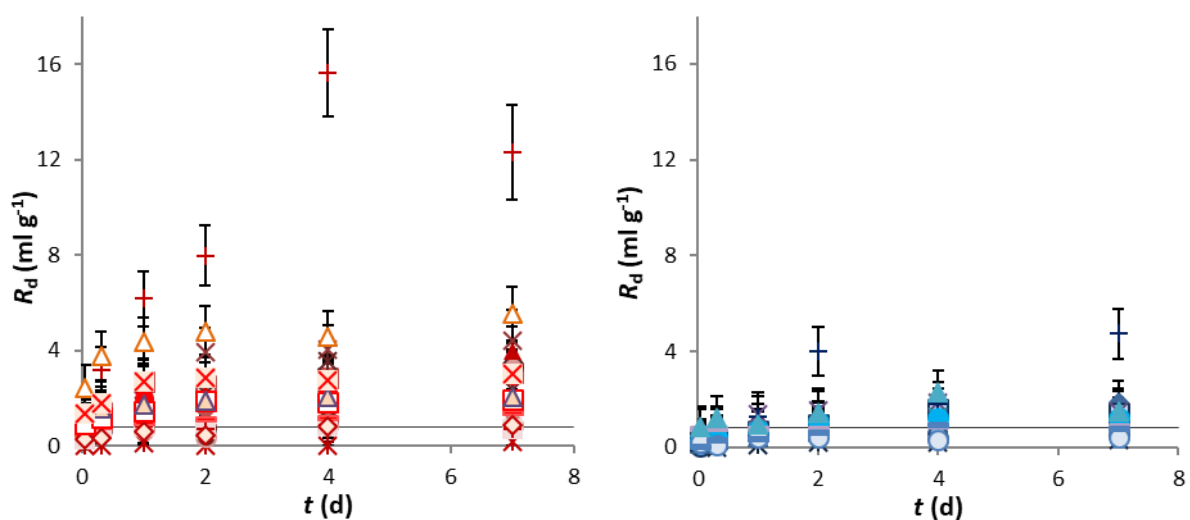
Selenite can be sorbed onto rock materials via the ligand exchange mechanism, with sorption evincing a pH dependency where the capture of selenite on Fe-hydroxides occurs at $\text{pH} < 9$ and sorption on iron-containing silicate minerals (e.g. biotite and chlorite) occurs at $\text{pH} < 8$. A further potential selenium sorption mechanism consists of the reduction of selenite to Se^0 and Se^{-II} , which may occur in the presence of iron sulphides in conjunction with so-called green rust or microbial activity. Based on the mineralogical analysis of the studied rock samples, it is reasonable to state that of the range of potential selenium sorbents, mica minerals and their products (e.g. chlorite) were present in the studied rocks. The sorption of selenium on biotite is due to the presence of FeII-rich biotite, which is capable of reducing SeO_3^{2-} to Se^0 . Hornblende has not been reported to be a potential selenium sorbent (Söderlund et al. 2016). Further information on the mechanism governing the capture of selenite on rocks and minerals is available in a report by Havlová et al. (2017).

Tab. 23 Selenite R_d values, including their expanded standard uncertainties, of the C fractions of rock samples from candidate DGR sites, $c(\text{Se}) = 2 \cdot 10^{-5} \text{ mol l}^{-1}$, fraction C: 0.63–0.125 mm

Rock sample	Time of sorption (days)					
	0.04	0.31	1	2	4	7
PZV1-C	< 0.8	< 0.8	1.2 ± 0.9	1.5 ± 0.9	1.8 ± 0.9	1.4 ± 0.9
TIV1-C	< 0.8	1.4 ± 0.9	2.7 ± 0.9	2.6 ± 0.9	2.8 ± 1.0	3.1 ± 1.0
PDV1-C	< 0.8	< 0.8	0.9 ± 0.8	0.8 ± 0.8	1.1 ± 0.9	3.4 ± 1.0
D2-C	1.1 ± 0.9	3.2 ± 1.0	6.2 ± 1.2	8.0 ± 1.3	15.7 ± 1.8	12.3 ± 2.0
S3-3-C	0.8 ± 0.8	1.2 ± 0.9	1.8 ± 0.9	2.9 ± 1.0	2.7 ± 0.9	3.4 ± 1.0
S3-4-C	< 0.8	1.2 ± 0.9	2.0 ± 0.9	3.9 ± 1.0	4.1 ± 1.0	4.4 ± 1.3
S4-3-C	< 0.8	1.0 ± 0.9	1.7 ± 0.9	2.2 ± 0.9	3.6 ± 1.0	2.4 ± 0.9
2S4-2-C	0.8 ± 0.8	1.5 ± 0.9	2.5 ± 0.9	2.2 ± 0.9	2.9 ± 1.0	4.0 ± 1.0
2S4-4-C	0.9 ± 0.9	1.4 ± 0.9	2.0 ± 0.9	1.9 ± 0.9	2.5 ± 0.9	3.0 ± 1.0
GRB-C	< 0.8	< 0.8	< 0.8	< 0.8	< 0.8	< 0.8
BT-C	< 0.8	< 0.8	< 0.8	< 0.8	0.9 ± 0.9	0.9 ± 0.9
GB-C	< 0.8	< 0.8	0.8 ± 0.9	0.7 ± 0.9	0.9 ± 0.9	< 0.8
Fracture fillings						
ZK2 13m_P	2.4 ± 0.9	3.8 ± 1.0	4.4 ± 1.0	4.8 ± 1.1	4.6 ± 1.1	5.5 ± 1.1
S1 40.3m_P	< 0.8	< 0.8	1.0 ± 0.9	1.1 ± 0.9	1.2 ± 0.9	1.4 ± 0.9
S1_80.6m_P	< 0.8	< 0.8	< 0.8	< 0.8	< 0.8	0.9 ± 0.9
S1 87.8m_P	0.9 ± 0.9	1.2 ± 0.9	1.5 ± 0.9	1.9 ± 0.9	1.8 ± 0.9	2.0 ± 0.9
S8 47.8m_P	1.4 ± 0.9	1.6 ± 0.9	1.7 ± 0.9	1.9 ± 0.9	2.1 ± 0.9	2.1 ± 0.9
BZ_317_P	1.4 ± 0.9	1.8 ± 0.9	2.7 ± 0.9	2.9 ± 1.0	2.8 ± 0.9	3.0 ± 1.0

Tab. 24 Selenite R_d values (ml g^{-1}), including their expanded standard uncertainties, of the D fractions of rock samples from candidate DGR sites, $c(\text{Se}) = 2 \cdot 10^{-5} \text{ mol l}^{-1}$, fraction D: 0.8–0.63 mm

Rock sample	Time of sorption (days)					
	0.04	0.31	1	2	4	7
PZV1-D	< 0.8	0.8 ± 0.9	< 0.8	< 0.8	< 0.8	1.9 ± 0.9
TIV1-D	< 0.8	< 0.8	< 0.8	1.0 ± 0.9	1.6 ± 0.9	1.5 ± 0.9
PDV1-D	< 0.8	< 0.8	< 0.8	0.9 ± 0.9	< 0.8	< 0.8
D2-D	< 0.8	< 0.8	1.3 ± 0.9	4.0 ± 1.0	1.8 ± 1.4	4.7 ± 1.1
S3-3-D	< 0.8	< 0.8	0.8 ± 0.8	< 0.8	1.0 ± 0.9	1.2 ± 0.9
S3-4-D	< 0.8	< 0.8	1.4 ± 0.9	1.6 ± 0.9	1.9 ± 0.9	1.5 ± 0.9
S4-3-D	< 0.8	< 0.8	< 0.8	< 0.8	1.3 ± 0.9	< 0.8
2S4-2-D	< 0.8	< 0.8	< 0.8	< 0.8	0.9 ± 0.9	1.1 ± 0.9
2S4-4-D	< 0.8	< 0.8	< 0.8	1.1 ± 0.9	1.2 ± 0.9	1.2 ± 0.9
GRB-D	< 0.8	< 0.8	< 0.8	< 0.8	< 0.8	< 0.8
BT-D	< 0.8	< 0.8	< 0.8	< 0.8	< 0.8	< 0.8
GB-D	< 0.8	< 0.8	< 0.8	< 0.8	0.9 ± 0.9	0.8 ± 0.9
Fracture fillings						
ZK2 13m P	0.9 ± 0.9	1.2 ± 0.9	1.0 ± 0.9	1.5 ± 0.9	2.3 ± 0.9	1.5 ± 0.9
S1 40.3m P	< 0.8	< 0.8	< 0.8	< 0.8	1.0 ± 0.9	< 0.8



 SÚRAO	Radionuclide migration processes in a crystalline rock environment. Final report.	Evidenční označení:
		SÚRAO TZ 333/2018

◆ PZV1-C	◻ TIV1-C	▲ S3-3-C	× S3-4-C	× S4-3-C	● PDV1-C	- PA2-2-C	- HV1-7-C
◇ HV2-7-C	■ HV3-7-C	+ D2-C	▲ 254-2-C	● 254-4-C	× GRB-C	● BT-C	+ GB-C
▲ ZK2 13m-C	- S1 40,3m-C	◇ S1 80,6m-C	□ S1 87,8m-C	▲ S8 47,8m-C	× BZ 317-C		
◆ PZV1-D	◻ TIV1-D	▲ S3-3-D	× S3-4-D	× S4-3-D	● PDV1-D	+ D2-D	▲ 254-2-D
● 254-4-D	× GRB-D	○ BT-D	- GB-D	▲ ZK2 13m-D	- S1 40,3m-D	— u (Rd)	

Fig. 40 Selenite R_d values of rock samples from the candidate sites, left: fraction C (0.63–0.125 mm), right: fraction D (0.8–0.63 mm), $c(\text{Se}) = 2 \cdot 10^{-5} \text{ mol l}^{-1}$

5.2.4 Uranium

The resulting uranium R_d values for the studied samples are shown in Fig. 41 and Tab. 25 and

 SÚRAO	Radionuclide migration processes in a crystalline rock environment. Final report.	Evidenční označení:
		SÚRAO TZ 333/2018

Tab. 26. The R_d values after 7 days of experimentation attained values of around 1 ml g^{-1} for both rock fractions, thus indicating the negligible sorption of uranyl on all the studied samples regardless of the differences in the mineralogical composition of the various rocks. In many cases, the resulting R_d values were less than the level of measurement uncertainty (for $R_d \sim 0 \text{ ml g}^{-1}$, $U_{R_d} < 1,6 \text{ ml g}^{-1}$), see

Tab. 25 and

 SÚRAO	Radionuclide migration processes in a crystalline rock environment. Final report.	Evidenční označení:
		SÚRAO TZ 333/2018

Tab. 26. At the same time, no effect of fraction size on the capture of uranyl was observed. As in the case of selenite, higher R_d values were observed with concern to the D2 granite (Čihadlo site) and GB (granulite, Hrádek site) samples; despite the very low uranium capture values, higher sorption was evident for these samples than for the other rocks studied (see Fig. 41).

Under the experimental pH (pH ~ 7.9) and E_h (E_h ~ 145 mV) conditions, uranium was present in the oxidation state (+IV) in the SGW2 environment as a mixture of the $UO_2(CO_3)_3^{4-}$, $UO_2(CO_3)_2^{2-}$, $(UO_2)_2CO_3(OH)_3^-$ and $UO_2(OH)_2$ species, with the dominant species in the studied system consisting of Ca-uranyl-carbonate complexes. These species have been reported as being the main species present in the system at pH > 7.5 and are characterised by their non-sorbing behaviour (Hakanen et al. 2014). For more information on the uranium capture mechanism on rocks and minerals, see a report by Havlová et al. (2017).

Tab. 25 Uranium R_d values ($ml\ g^{-1}$), including their expanded standard uncertainties, of the C fractions of rock samples from candidate DGR sites, $c(U) = 2.6 \cdot 10^{-4}\ mol\ l^{-1}$, fraction C: 0.63–0.125 mm

Rock sample	Time of sorption (days)					
	0.04	0.31	1	2	4	7
PZV1-C	< 1.6	< 1.6	< 1.6	< 1.6	< 1.6	< 1.6
TIV1-C	< 1.6	< 1.6	< 1.6	< 1.6	< 1.6	< 1.6
PDV1-C	< 1.6	< 1.6	< 1.6	< 1.6	< 1.6	< 1.6
D2-C	< 1.6	< 1.6	< 1.6	1.9 ± 1.8	2.3 ± 1.8	2.1 ± 1.8
S3-3-C	< 1.6	< 1.6	< 1.6	< 1.6	< 1.6	< 1.6
S3-4-C	< 1.6	< 1.6	< 1.6	< 1.6	< 1.6	< 1.6
S4-3-C	< 1.6	< 1.6	< 1.6	< 1.6	< 1.6	< 1.6
2S4-2-C	< 1.6	< 1.6	< 1.6	< 1.6	< 1.6	< 1.6
2S4-4-C	< 1.6	< 1.6	< 1.6	< 1.6	< 1.6	< 1.6
GRB-C	< 1.6	< 1.6	< 1.6	< 1.6	< 1.6	< 1.6
BT-C	< 1.6	< 1.6	< 1.6	< 1.6	< 1.6	< 1.6
GB-C	1.9 ± 1.8	2.0 ± 1.8	3.3 ± 2.0	4.0 ± 2.0	3.3 ± 2.0	3.3 ± 2.0
Fracture fillings						
ZK2 13m_P	< 1.6	< 1.6	< 1.6	< 1.6	< 1.6	< 1.6
S1 40.3m_P	< 1.6	< 1.6	< 1.6	< 1.6	< 1.6	< 1.6

Tab. 26 Uranium R_d values (ml g^{-1}), including their expanded standard uncertainties, of the D fractions of rock samples from candidate DGR sites, $c(U) = 2.6 \cdot 10^{-4} \text{ mol l}^{-1}$, fraction D: 0.8–0.63 mm

Rock sample	Time of sorption (days)					
	0.04	0.31	1	2	4	7
PZV1-D	< 1.6	< 1.6	< 1.6	< 1.6	< 1.6	< 1.6
TIV1-D	< 1.6	< 1.6	< 1.6	< 1.6	< 1.6	< 1.6
PDV1-D	< 1.6	< 1.6	< 1.6	< 1.6	< 1.6	< 1.6
D2-D	< 1.6	< 1.6	< 1.6	< 1.6	< 1.6	< 1.6
S3-3-D	< 1.6	< 1.6	< 1.6	< 1.6	< 1.6	< 1.6
S3-4-D	< 1.6	< 1.6	< 1.6	< 1.6	< 1.6	< 1.6
S4-3-D	< 1.6	< 1.6	< 1.6	< 1.6	< 1.6	< 1.6
2S4-2-D	< 1.6	< 1.6	< 1.6	< 1.6	< 1.6	< 1.6
2S4-4-D	< 1.6	< 1.6	< 1.6	< 1.6	< 1.6	< 1.6
GRB-D	< 1.6	< 1.6	< 1.6	< 1.6	< 1.6	< 1.6
BT-D	< 1.6	< 1.6	< 1.6	< 1.6	< 1.6	< 1.6
GB-D	< 1.6	1.9 ± 1.8	2.2 ± 1.8	2.3 ± 1.8	2.4 ± 1.9	2.4 ± 1.8
Fracture fillings						
ZK2 13m P	< 1.6	< 1.6	< 1.6	< 1.6	< 1.6	< 1.6
S1 40.3m P	< 1.6	< 1.6	< 1.6	< 1.6	< 1.6	< 1.6

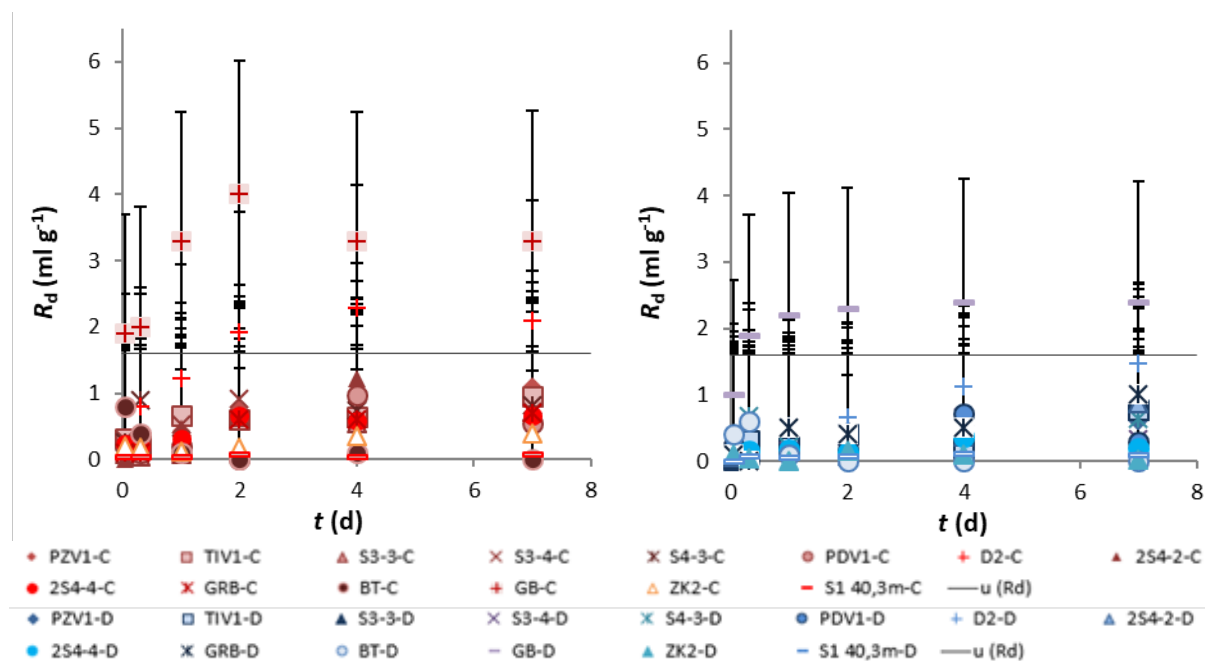


Fig. 41 Uranium R_d values of rock samples from the candidate sites, left: fraction C (0.63–0.125 mm), right: fraction D (0.8–0.63 mm), $c(U) = 2.6 \cdot 10^{-4} \text{ mol l}^{-1}$

5.2.5 Chlorine

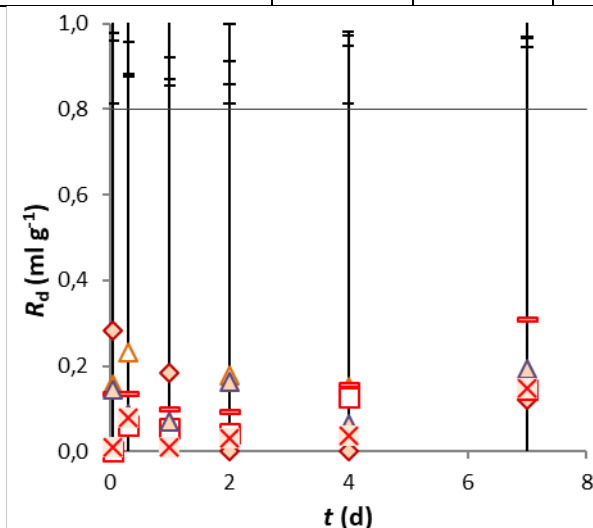
The experiments were performed with the Na^{36}Cl radionuclide in 0.1 mol l^{-1} HCl, an aliquot of which was added to the SGW2 synthetic granitic water. The addition of the radionuclide source solution was so small that no significant effect on the pH of the resulting ^{36}Cl solution was recorded in the SGW2 (pH ~ 8.2).

The resulting values of the chloride R_d distribution coefficient for selected fracture filling samples are shown in Fig. 42 and in Tab. 27. Minimal chlorine capture was observed during experimentation and the resulting R_d values did not exceed the level of measurement uncertainty (for $R_d \sim 0 \text{ ml g}^{-1}$, $U_{R_d} < 0.8 \text{ ml g}^{-1}$).

The minimum levels of sorption for the given fracture materials are in accordance with information provided in the literature, where chloride is listed as a non-reactive ion that behaves very conservatively in the given geological environment (Carbol and Engkvist 1997).

Tab. 27 Chlorine R_d values, including their expanded standard uncertainties, of the C fractions of rock samples from candidate DGR sites, $c(\text{Cl}) = 2 \cdot 10^{-4} \text{ mol l}^{-1}$, fraction C: 0.63–0.125 mm; for the fracture filling samples

Rock sample	Time of sorption (days)					
	0.04	0.31	1	2	4	7
ZK2 13m_P	< 0.8	< 0.8	< 0.8	< 0.8	< 0.8	< 0.8
S1 40.3m_P	< 0.8	< 0.8	< 0.8	< 0.8	< 0.8	< 0.8
S1_80.6m_P	< 0.8	< 0.8	< 0.8	< 0.8	< 0.8	< 0.8
S1 87.8m_P	< 0.8	< 0.8	< 0.8	< 0.8	< 0.8	< 0.8
S8 47.8m_P	< 0.8	< 0.8	< 0.8	< 0.8	< 0.8	< 0.8
BZ_317_P	< 0.8	< 0.8	< 0.8	< 0.8	< 0.8	< 0.8



 SÚRAO	Radionuclide migration processes in a crystalline rock environment. Final report.	Evidenční označení:
		SÚRAO TZ 333/2018

△ ZK2 13m
 - S1 40,3m
 ◇ S1 80,6m
 □ S1 87,8m
 △ S8 47,8m
 × BZ 317
 — u (Rd)

Fig. 42 Chlorine R_d values of the fracture filling rock samples from the candidate sites, fraction C (0.63–0.125 mm), $c(\text{Cl}) = 2.1 \cdot 10^{-4} \text{ mol l}^{-1}$

5.2.6 Iodine

Na^{125}I in 0.04 mol l^{-1} NaOH was selected as the iodine source, an aliquot of which was reductively treated with sodium thiosulphate and added to SGW2 synthetic granitic water so that the resulting solution did not contain potentially oxidised ^{125}I forms. CaI_2 was also added to the SGW2 at a concentration of $\sim 2 \cdot 10^{-4} \text{ mol l}^{-1}$.

The iodine R_d values obtained from the sorption experiments conducted on selected fracture materials are shown in Tab. 28 **Chyba! Nenalezen zdroj odkazů.** and Fig. 43. Minimum sorption was observed with respect to all the materials studied, i.e. R_d values were determined of less than the level of measurement uncertainty (for $R_d \sim 0 \text{ ml g}^{-1}$, $U_{R_d} < 0.8 \text{ ml g}^{-1}$). This confirms the afore-mentioned information on the sorption of iodine on granitic rocks where, due to the anionic character of iodine, no significant sorption was expected on the given materials; the R_d values mentioned in other studies are around $0\text{--}1 \text{ ml g}^{-1}$ (Havlová et al. 2015a). Furthermore, the sorption rate may be significantly influenced by the pH; increasing pH is accompanied by decreasing sorption and, hence, lower R_d values (Hakanen et al. 2014).

Tab. 28 Iodine R_d values (ml g^{-1}), including their expanded standard uncertainties, of the C fractions of rock samples from candidate DGR sites, $c(\text{I}) = 2 \cdot 10^{-5} \text{ mol l}^{-1}$, fraction C: 0.63–0.125 mm; for the fracture filling samples

Rock sample	Time of sorption (days)					
	0.04	0.31	1	2	4	7
ZK2 13m_P	< 0.8	< 0.8	< 0.8	< 0.8	< 0.8	< 0.8
S1 40.3m_P	< 0.8	< 0.8	< 0.8	< 0.8	< 0.8	< 0.8
S1_80.6m_P	< 0.8	< 0.8	< 0.8	< 0.8	< 0.8	< 0.8
S1 87.8m_P	< 0.8	< 0.8	< 0.8	< 0.8	< 0.8	< 0.8
S8_P 47.8m_P	< 0.8	< 0.8	< 0.8	< 0.8	< 0.8	< 0.8
BZ_317_P	< 0.8	< 0.8	< 0.8	< 0.8	< 0.8	< 0.8

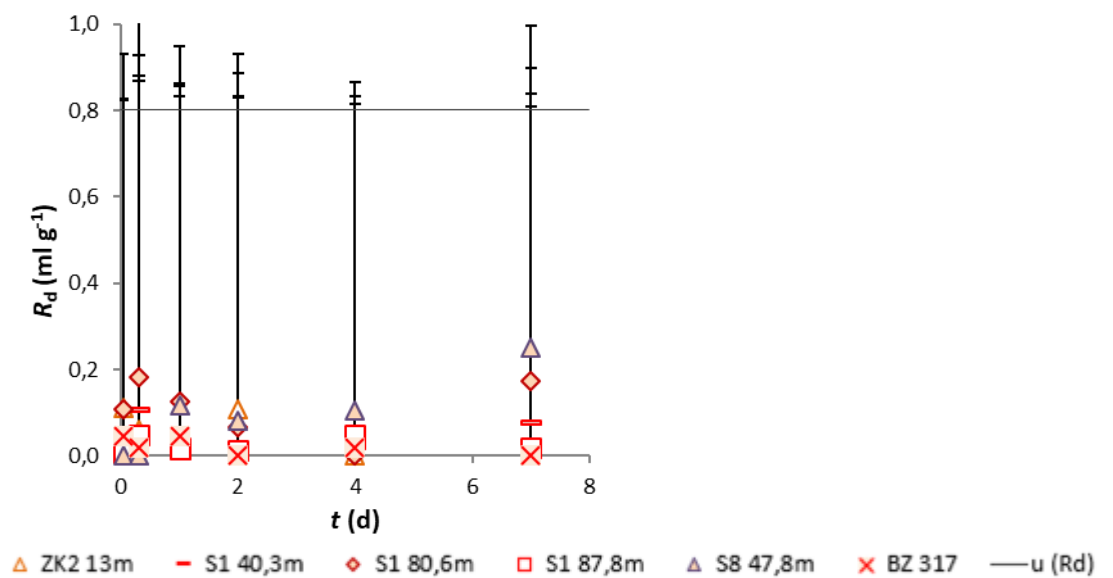


Fig. 43 Iodine R_d values of the fracture filling rock samples from the candidate sites, fraction C (0.63–0.125 mm), $c(l) = 2 \cdot 10^{-5} \text{ mol l}^{-1}$

5.2.7 Europium

In the context of the expansion of the project, the sorption of europium was studied on altered and fractured rocks. Two orientation sorption experiments series were performed on these rocks. Samples were selected that exhibited the highest and lowest sorption in the previous experiments (BZ_317m and S1_80.6m). A number of complications that arose during experimentation are mentioned below.

An experimental solution of $2 \cdot 10^{-5} \text{ mol l}^{-1} \text{ Eu}(\text{NO}_3)_3$ and SGW2 synthetic granitic water was prepared, labelled ^{152}Eu , via the addition of a source solution of $^{152}\text{EuCl}_3$ in $0.1 \text{ mol l}^{-1} \text{ HCl}$. Although measurement using a Gamma Spectrometer Wizard determined that the experimental solution did not exhibit the expected activity, it was decided that it could still be used for further orientation experiments on the BZ 317m (biotitic gneiss, Bukov URF) and S1 80.6m (migmatite, Bukov URF) rock samples. Following the start of the orientation sorption experiments and after the first sampling campaign, it was evident that there was a significant decrease in radionuclide activity not only in the samples containing the studied rocks (i.e. the sorption of europium was evident on the rock material), but also in the control samples, i.e. the so-called blanks, that should not have exhibited any change in composition during experimentation. This indicated the possibility of the sorption of radionuclides on the walls of the reaction equipment (PP tube, PE cap). Moreover, the BZ 317m experiment led to the production of a thin rusty layer at the liquid-solid interface (Fig. 44). Since the rock contained iron, the occurrence of the cationic exchange of trivalent europium for iron was assumed.

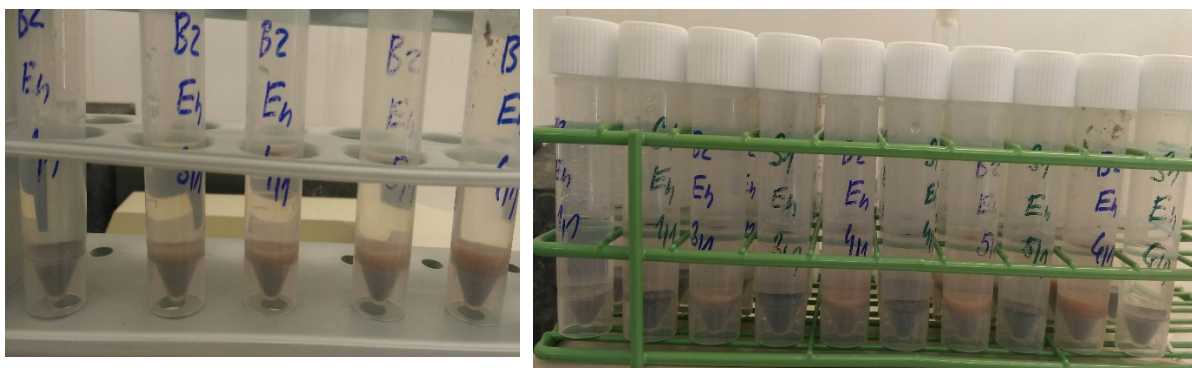


Fig. 44 Sorption of Eu on selected rocks (the formation of Fe-hydroxide rust layers)

The next part of the research involved the performance of desorption experiments on the already sorbed europium on the rock and reaction equipment cover materials. Two series of samples were selected (experiments after 24 h and after 2 days) from both of the rocks (4 series in total). One series of samples contained three reaction devices (1 reaction device with the rock - designated A, 1 reaction device after sorption on the rock but without the rock - designated B, and 1 reaction device after the blank control sample - designated C). All the original experimental solution/rock was selected from all the reaction devices and the cover material/rock was subsequently washed several times with distilled water in order to thoroughly rinse the original experimental solution from the system. For reasons of clarity, Tab. 29 provides a list of the designations of the various reaction devices. 0.1 mol l⁻¹ HCl was added to the reaction devices thus prepared. After one week, samples were taken and measured. The results obtained from the sorption to the given material and the subsequent desorption are shown in Tab. 30.

Tab. 29 Overview of the designated reaction devices for the sorption and desorption of Eu

Designation	Sorption	Desorption
A	Cover + rock	Cover + rock
B	Cover + rock	Cover
C	Cover + blank	Cover

Tab. 30 Sorption and desorption of Eu on the fractured rock samples

BZ_317m_P			
	Sorption (%)	Desorption (%)	Missing following desorption (%)
1 A	86	46	54
1 B	85	6	94
1 C	78	24	76
4A	96	67	33

 SÚRAO	Radionuclide migration processes in a crystalline rock environment. Final report.	Evidenční označení:
		SÚRAO TZ 333/2018

4B	98	9	91
4C	85	52	48
S1 80.6m			
	Sorption (%)	Desorption (%)	Missing following desorption (%)
1A	87	9	91
1B	87	4	96
1C	78	36	64
4A	99	8	92
4B	99	2	98
4C	72	80	20

The results show that the radionuclide was not effectively desorbed from either the rock or the cover material of the reaction equipment. Thus, it was not possible to determine the proportion of sorption on a given rock compared to the rate of sorption on the cover material.

The next step consisted of the conducting of test experiments that focused on the materials that made up the reaction equipment (glass/plastic) and the pH of the solution (acidity/alkalinity of the medium) and, subsequently, the composition of the experimental solution (SWG2/distilled water). The data obtained is listed in Tab. 31, which shows that there was a significant loss of radionuclide activity in the experimental solution. The SGW2 solution, which was acidified to pH ~ 3, exhibited the lowest loss and, after three days, partial desorption was evident from the walls of the material back into the solution. Conversely, the SGW2 solution that was not acidified (so as to maintain the original pH of the SGW2) witnessed significant losses that continued throughout the experiment.

Tab. 31 Sorption of europium on the device materials ($2 \cdot 10^{-5} \text{ mol l}^{-1} \text{ Eu}(\text{NO}_3)_3$)

Solution	Material	Residual activity in the solution	
		After 2.5 h (%)	After 3 days (%)
SGW2 pH ~ 3	Plastic	32.6	110
	Glass	33.5	53.4
SGW2 pH ~ 8.3	Plastic	21.6	7.5
	Glass	14.6	11.6
Distilled water pH ~ 7	Plastic	26.8	26.7
	Glass	24.5	22.5

 SÚRAO	Radionuclide migration processes in a crystalline rock environment. Final report.	Evidenční označení:
		SÚRAO TZ 333/2018

In order to clarify the issue, the potential for the simulation of the given environment was considered via the application of computer programs. The PHREEQC hydrogeochemical program was selected for simulation purposes and the Thermochimie eDH database was selected for the modelling of Eu species in the SGW2 synthetic granitic water ($\text{pH} = 8.20$, $T = 25^\circ\text{C}$). Three different concentrations of $\text{Eu}(\text{NO}_3)_3$ were modelled: $2 \cdot 10^{-3} \text{ mol l}^{-1}$, $2 \cdot 10^{-5} \text{ mol l}^{-1}$ and $2 \cdot 10^{-8} \text{ mol l}^{-1}$ (Tab. 32, Tab. 33). Tab. 32 and Tab. 33 show that almost all the Eu species are in the form of complexes or the solid phase and that the soluble form of Eu^{3+} is virtually absent in the solution.

Tab. 32 Results of the modelling of Eu speciation in SGW2 and demineralised water

	Demineralised water	SGW2	SGW2	SGW2
<i>pH</i>	7	8.3	8.3	8.3
<i>Concentration (mol l⁻¹) of Eu as Eu(NO₃)₃</i>	$2 \cdot 10^{-5}$	$2 \cdot 10^{-5}$	$2 \cdot 10^{-3}$	$2 \cdot 10^{-8}$
<i>Eu speciation (s)</i>				
<i>Eu(OH)₃</i>	x	x	x	x
<i>Eu(CO₃)(OH)</i>		x	x	
<i>Eu(CO₃)(OH):0.5H₂O</i>		x	x	
<i>Eu₂(CO₃)₃:3H₂O</i>		x	x	

Tab. 33 Results of the modelling of Eu speciation in SGW2

C_{Eu} (mol l ⁻¹)	$\text{Eu}(\text{CO}_3)^+$	$\text{Eu}(\text{CO}_3)_2^-$	$\text{Eu}(\text{OH})_2^+$	$\text{Eu}(\text{OH})^{+2}$	$\text{Eu}(\text{CO}_3)_3^-$	Eu^{+3}
$2 \cdot 10^{-3}$	74.3	22.3	1.6	1.0	-	0.6
$2 \cdot 10^{-5}$	35.1	64.5	0.1	0.1	0.2	-
$2 \cdot 10^{-8}$	34.8	64.8	0.1	0.1	0.2	-

A further option considered the use of distilled water as the solvent, concerning which the problem of the alkaline environment of the SWG2 was solved via NaHCO_3 and Na_2CO_3 , which leads to strong Eu hydrolysis and the formation of $\text{Eu}(\text{OH})_3$ precipitates (Palágyi and Štamberg 2013). Consequently, the next step consisted of the modelling of the Eu species at the three concentrations mentioned above ($2 \cdot 10^{-3} \text{ mol l}^{-1}$, $2 \cdot 10^{-5} \text{ mol l}^{-1}$ a $2 \cdot 10^{-8} \text{ mol l}^{-1}$); however, this time distilled water (DW) was used as the solvent ($\text{pH} = 7$, $T = 25^\circ\text{C}$). The Eu specie in this case occurred predominantly in the soluble form of the Eu^{3+} trivalent cation and the solid phase was in the form $\text{Eu}(\text{OH})_3$, where it was represented in a significantly smaller amount than when the SGW2 was used as the solvent.

 SÚRAO	Radionuclide migration processes in a crystalline rock environment. Final report.	Evidenční označení:
		SÚRAO TZ 333/2018

Tab. 34 Results of the modelling of Eu speciation in distilled water

c_{Fe} (mol l ⁻¹)	Eu ⁺³	Eu(OH) ⁺²	Eu(OH) ₂ ⁺	Eu(NO ₃) ⁺²
$2 \cdot 10^{-3}$	86.0	8.6	0.8	4.7
$2 \cdot 10^{-5}$	85.6	12.8	1.6	-
$2 \cdot 10^{-8}$	84.9	13.4	1.9	-

The data obtained via modelling with the PHREEQC hydrogeochemical program suggests that the composition of the solution as well as its pH exerts a significant influence on the presence of the soluble form of Eu, as confirmed by the scientific literature that addresses europium (see below). The next step consisted of the modelling of the E_h-pH diagrams of the Eu in the SGW2 (Fig. 45) and DW (Fig. 46) using Geochemist Work Bench Professional 10.0.10 (GWB) for a concentration of $2 \cdot 10^{-5}$ mol l⁻¹ Eu(NO₃)₃. The concentration was chosen with respect to that used in the experiments. The results correspond to the previous modelling of speciation, where the Eu species is present predominantly in the form of Eu(CO₃)₃ in the pH range of the SGW2 synthetic granitic water used (pH ~ 8.2).

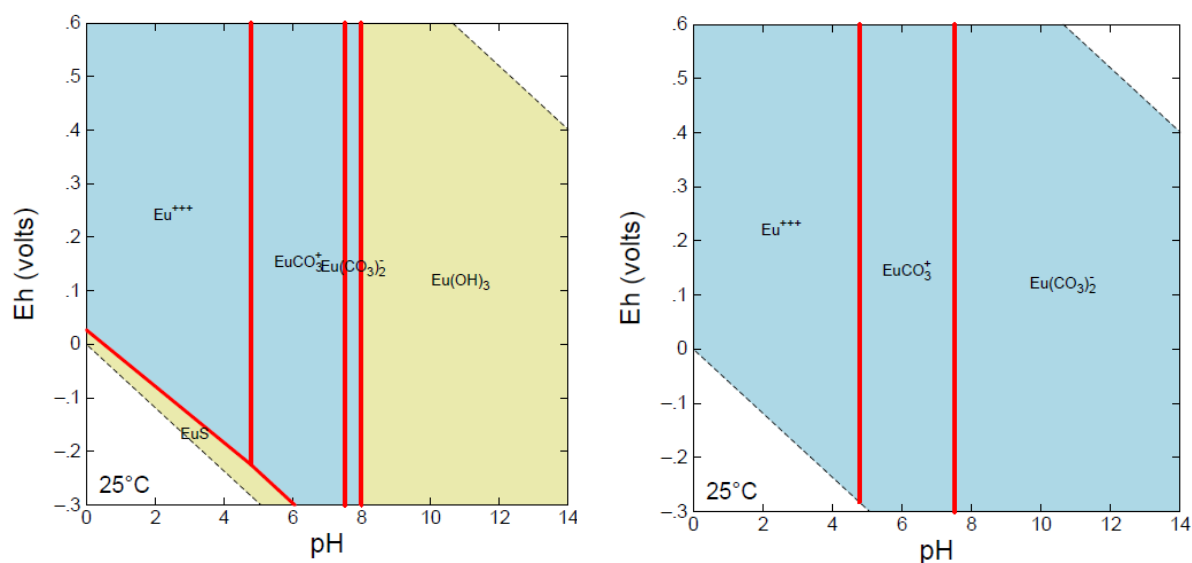


Fig. 45 E_h -pH diagrams of Eu in the SGW2 a) with solid phases, b) without solid phases

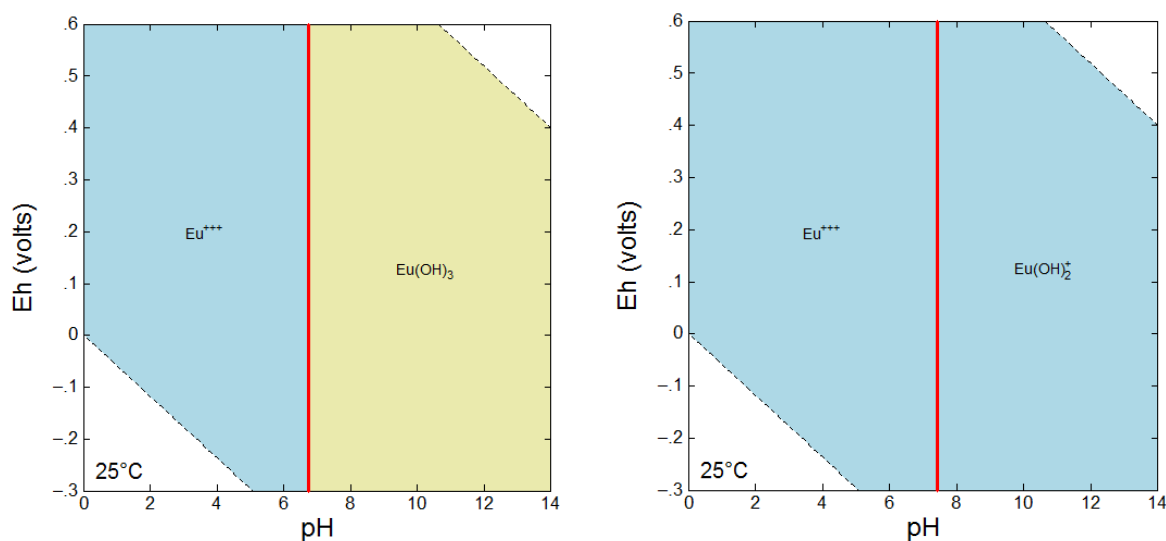


Fig. 46 E_h -pH diagrams of Eu in the DW a) with solid phases, b) without solid phases

Following the formation of a rust band in the sorption experiments mentioned above, the effect of iron on the Eu species was also considered via modelling in the PHREEQC hydrogeochemical program under the same conditions as those mentioned above (3 concentrations of $\text{Eu}(\text{NO}_3)_3$; 2 solutions). In neither case was the influence of Fe observed on the Eu species in the solution or the creation of the solid phase.

The findings were followed by the study of the literature that addresses the issue of europium. Certain studies have suggested that maintaining the dissolved form of europium in a given solution is problematic (Palágyi et al. 2009, 2010; Holgersson 2013). As mentioned above, Palágyi et al. (2009) refer to the problem of alkaline environments which contain NaHCO_3 and Na_2CO_3 where Eu^{3+} is strongly hydrolysed and an insoluble $\text{Eu}(\text{OH})_3$ precipitate is formed. They also mention the formation of colloidal complexes which may be complexed with e.g. humic substances. Conference contributions from Becker and Lippold (Becker and Lippold 2016) mention the need to adjust the pH of the Eu solution to $\text{pH} \sim 3$ in order to prevent colloid formation and sorption on the walls of the material. The issue of europium sorption is addressed in detail in Holgersson (2013), in which the author discusses the sorption procedures of two independent institutions, each of which determined differing results with respect to the sorption of europium on rocks. The study highlights the problem of the composition of the sorption solution, its pH, s: l ratio during sorption, etc. and confirms all the aspects that were addressed in this part of the report.

Based on data obtained from the expert literature and the modelling and experimental verification of sorption, it can be stated that the study of the sorption of europium is a complex issue that should be studied in more detail in a separate study. The data obtained indicates that the composition of the solution and its pH significantly influence the chemical form of the Eu species in the solution. Since the aim of this project was not to address the issue of europium in detail, these effects were not studied extensively. Moreover, the sorption of europium on rock materials was not addressed experimentally since a previous study indicated that it would have been necessary to select an acidic environment and thus adjust the composition of the experimental solution, which would have been in contradiction to the

 SÚRAO	Radionuclide migration processes in a crystalline rock environment. Final report.	Evidenční označení:
		SÚRAO TZ 333/2018

composition of the groundwater and hence the synthetic SGW2 that was used in all the other experiments conducted in the context of this project. Moreover, it would also have been necessary to modify the methodology applied in the project. The modification of the various parameters would have led to significant complications in terms of the data interpretation and would have complicated the potential mutual comparison of the results obtained. On the basis of the information obtained and following agreement with the Client, it was decided not to continue the consideration of the sorption of Eu on the other samples.

5.2.8 Summary of the results

Tab. 35 and Fig. 47 provide summaries of the results of the sorption experiments on two fractions of twelve samples from selected candidate sites involving Cs(I), Sr(II), Se(IV) and U(VI). Furthermore, the tables also summarise the results of sorption experiments on six altered rock and fracture samples involving the above-mentioned species as well as the sorption of Cl(-I) and I(-I). The results revealed that the sorption of individual radionuclides differs significantly as does the sorption of the various radionuclides on the studied rock samples.

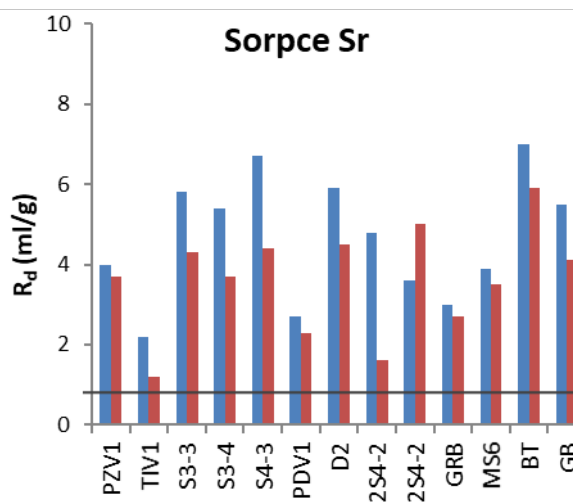
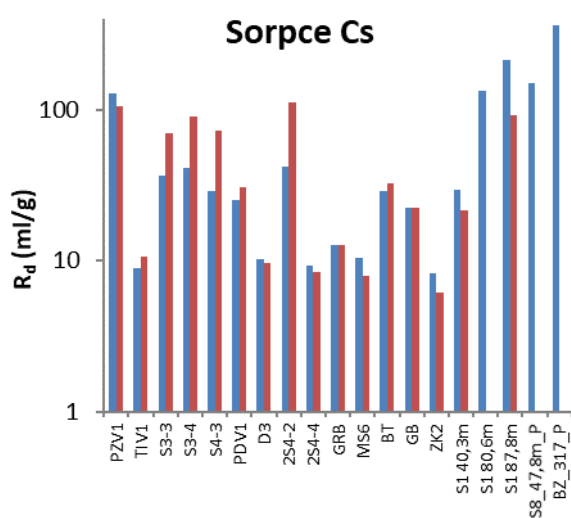
Tab. 35 and Fig. 47 do not show the results of the sorption of europium on certain fracture samples. Following the initial testing of the sorption of Eu and subsequent agreement with the Client (SÚRAO), the testing of Eu sorption was discontinued. The various issues surrounding this species are very specific; the conclusions obtained are presented in the previous chapter (see 5.2.7 Europium).

With respect to the sorption behaviour of radionuclides, it can be stated that caesium is strongly sorbed on rock materials and that strontium exhibits only a slight sorbing character. Selenite, uranium U(VI), chloride and iodide can be classified as non-sorbing radionuclides. The mineralogical composition of the rock samples constituted an important factor in terms of radionuclide behaviour. In the case of the cationic radionuclides Cs(I) and Sr(II), the most important sorbents consisted of layered minerals (in this case mica), in the case of radionuclides which may be present in solution in the form of anions, e.g. selenium, the decisive factor was the presence of Fe-minerals and selected cation complexes, which are able to enhance the sorption of selenium to rock materials via a number of mechanisms. That said, the content of Fe was low in the rocks subjected to study.

Tab. 35 R_d results for selected radionuclides in the form of the C and D fractions of rock samples from the candidate sites, phase ratio 1 : 10, 7 days, fraction C: 0.63–0.125 mm, fraction D: 0.8–0.63 mm

Sample	Cs		Sr		Se		U		Cl	I
	Fraction C	Fraction D	Fraction C	Fraction C						
PZV1	128.8	104.2	4.0	3.7	1.4	1.9	< 1.6	< 1.6	n.a.	n.a.
TIV1	9.0	10.6	2.2	1.2	3.1	1.5	< 1.6	< 1.6	n.a.	n.a.
PDV1	25.2	30.7	2.7	2.3	3.4	< 0.8	< 1.6	< 1.6	n.a.	n.a.
D2	10.3	9.7	5.9	4.5	12.3	4.7	2.1	< 1.6	n.a.	n.a.
S3-3	36.6	70.4	5.8	4.3	3.4	1.2	< 1.6	< 1.6	n.a.	n.a.

S3-4	41.1	89.1	5.4	3.7	4.4	1.5	< 1.6	< 1.6	n.a.	n.a.
S4-3	29.1	72.0	6.7	4.4	2.4	< 0.8	< 1.6	< 1.6	n.a.	n.a.
2S4-2	42.0	110.5	4.8	1.6	4.0	1.1	< 1.6	< 1.6	n.a.	n.a.
2S4-4	9.3	8.4	3.6	5.0	3.0	1.2	< 1.6	< 1.6	n.a.	n.a.
GRB	12.7	12.8	3.0	2.7	< 0.8	< 0.8	< 1.6	< 1.6	n.a.	n.a.
BT	29.1	32.7	7.0	5.9	< 0.8	< 0.8	< 1.6	< 1.6	n.a.	n.a.
GB	22.3	22.2	5.5	4.1	< 0.8	< 0.8	3.3	2.4	n.a.	n.a.
<i>Fracture fillings</i>										
ZK2 13m P	8.2	6.1	n.a.	n.a.	5.6	1.5	< 1.6	< 1.6	< 0.8	< 0.8
S1 40.3m P	29.3	21.4	n.a.	n.a.	1.4	< 0.8	< 1.6	< 1.6	< 0.8	< 0.8
S1_80.6 m P	133.1	n.a.	n.a.	n.a.	0.9	n.a.	n.a.	n.a.	< 0.8	< 0.8
S1 87.8m P	213.4	90.9	n.a.	n.a.	2.0	n.a.	n.a.	n.a.	< 0.8	< 0.8
S8 47.8m P	150.1	n.a.	n.a.	n.a.	2.1	n.a.	n.a.	n.a.	< 0.8	< 0.8
BZ_317 m P	361.8	n.a.	n.a.	n.a.	3.0	n.a.	n.a.	n.a.	< 0.8	< 0.8



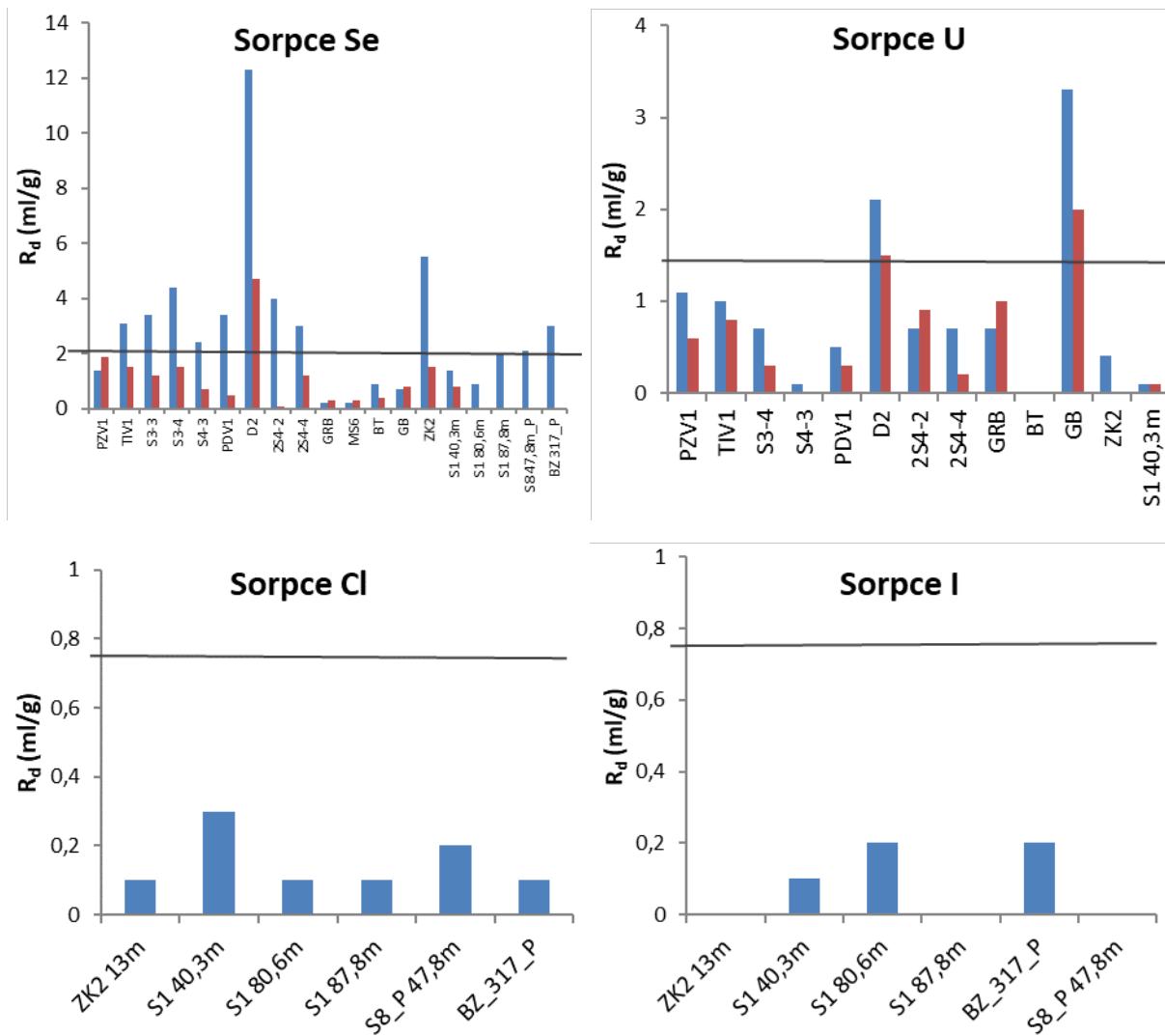


Fig. 47 Sorption of selected radionuclides on the rock samples (Cs, Sr, Se, U) and fracture filling samples (Cs, Sr, Se, U, Cl, I) ■ fraction C: 0.63–0.125 mm, ■ fraction D: 0.8–0.63 mm

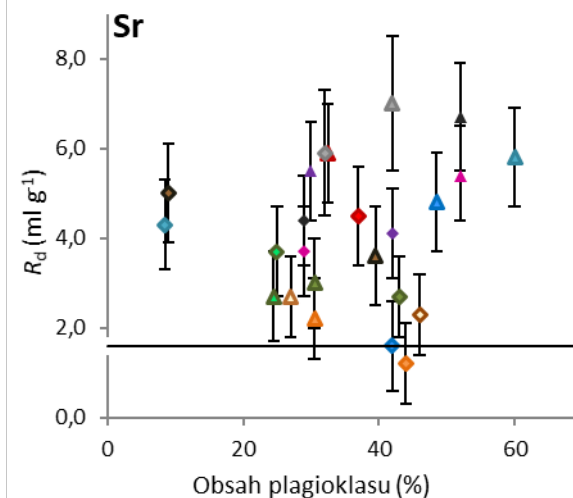
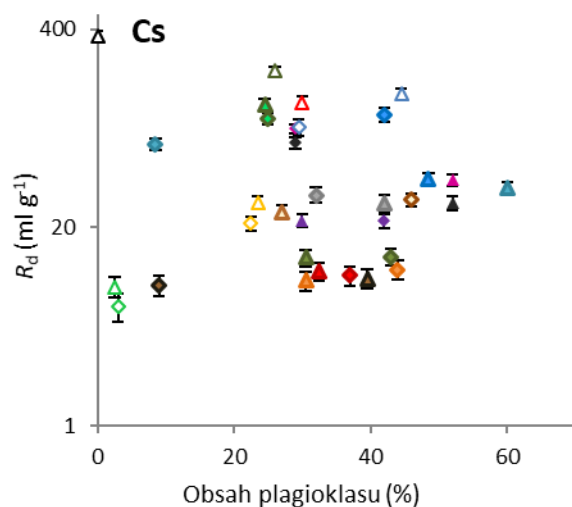
As previously mentioned, phyllosilicates (mica) and inosilicates (amphiboles) were considered to be potential sorbents of the selected radionuclides with concern to the granitic rocks subjected to study (see Tab. 36). However, the professional literature also mentions the influence of plagioclase on radionuclide sorption (Muuri et al. 2016; Ebong and Evans 2011; Stumpf et al. 2006; Ticknor et al. 1989; Andersson and Allard 1983). Plagioclase is one of a number of tectosilicates that contain $(\text{SiO}_4)^{4-}$ tetrahedra in which the isomorphous substitution of silicon Si(IV) for aluminium Al(III) is able to occur and thus the presence of a negative charge in the crystallographic system is compensated by cations. Due to the negative charge on the surface of plagioclase, it is, therefore, possible to predict the capture of positively-charged radionuclides via electrostatic forces (Muuri et al. 2016). An increase in the R_d values of cationic radionuclides with increasing plagioclase content in the rock samples was also observed for the rocks from the candidate sites (see caesium and strontium in Fig. 48). Conversely, the influence of plagioclase on the capture of selenium is negligible (Ticknor et al. 1989) and the sorption of uranyl was not significantly affected by the presence of plagioclase

(see Fig. 48). The presence of plagioclase and biotite did not affect the sorption rate of the other negatively-charged radionuclides such as iodide and chloride on the selected fracture samples (Fig. 48, Fig. 49).

The samples from the Bukov URF contained around 50% of plagioclase (see Fig. 48) and, with concern to these samples, the influence of the grain size on caesium sorption was evident, i.e. higher sorption was observed on the larger rock fraction (see Cs in Fig. 48). The question therefore arises as to whether the crushing and treatment of samples with higher contents of plagioclase and amphibolites (S3-3, S3-4, S4-3 and 2S4-2) negatively affected the sorption properties of the rock material.

Tab. 36 Comparison of the relative sorption capacities of minerals contained in granitic rocks (Ticknor et al. 1989)

Radionuclide	Relative sorption capacity
^{137}Cs	Hornblende ~ biotite ~ kaolinite ~ laumontite >> actinolite ~ epidote ~ plagioclase ~ silica
^{75}Se	Chlorite ~ serpentinite > orthopyroxene > olivine >> plagioclase
^{85}Sr	Hornblende ~ biotite = kaolinite ~ laumontite ~ epidote > actinolite >> plagioclase ~ silica



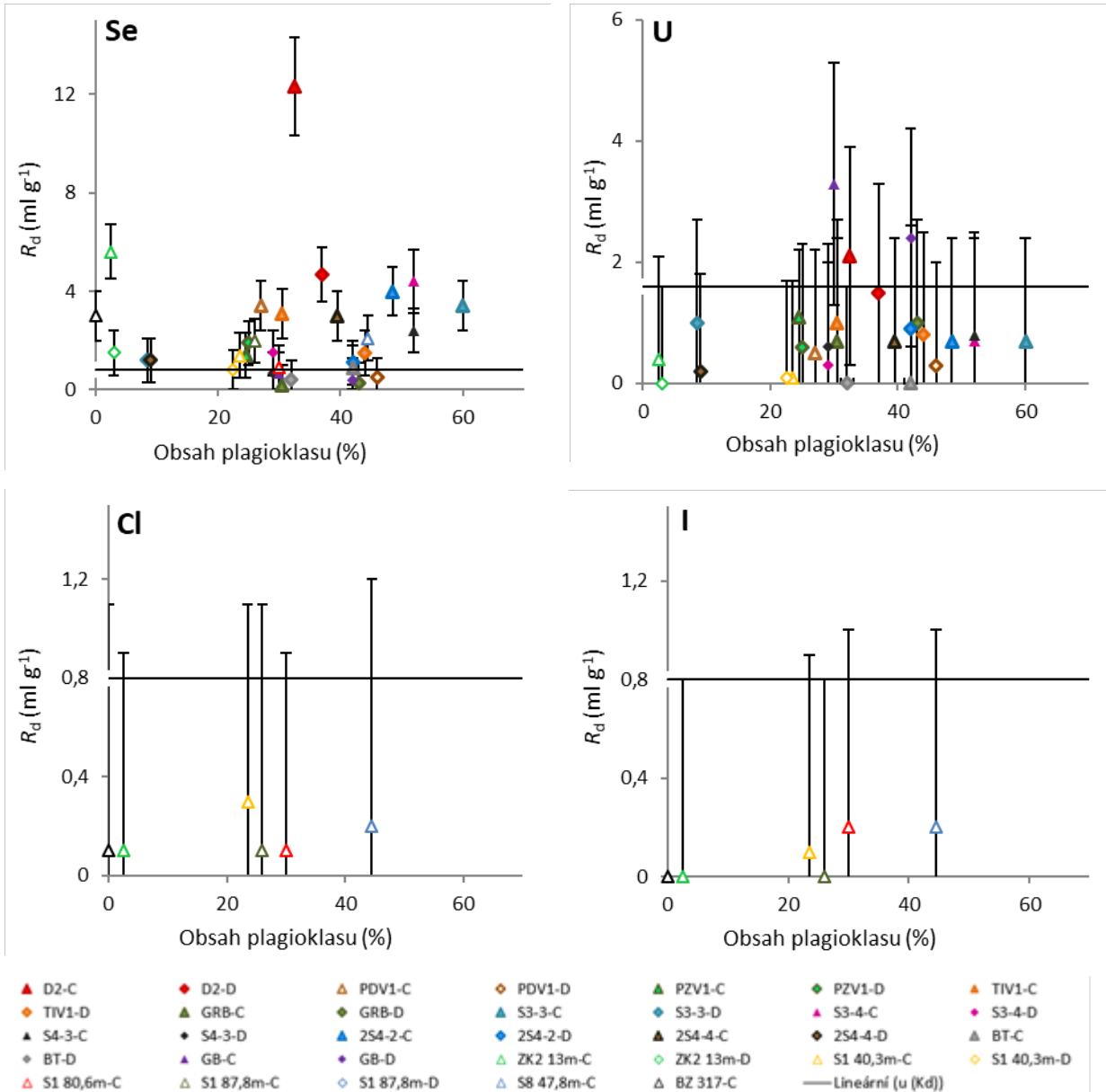
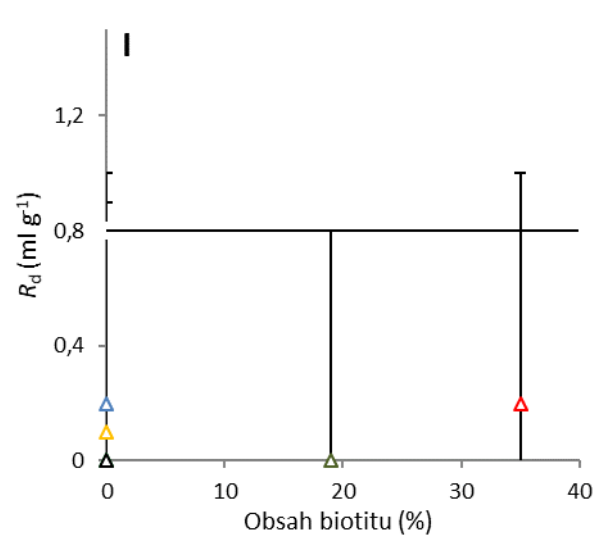
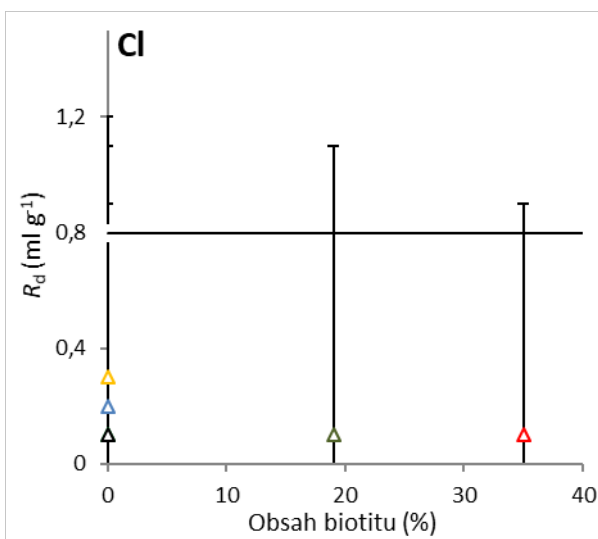
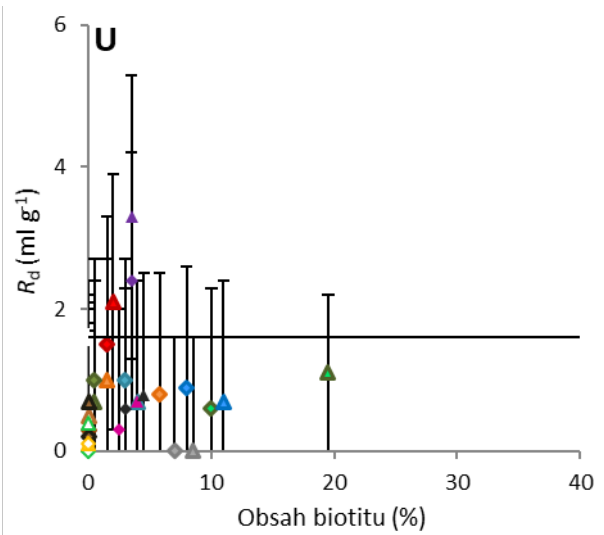
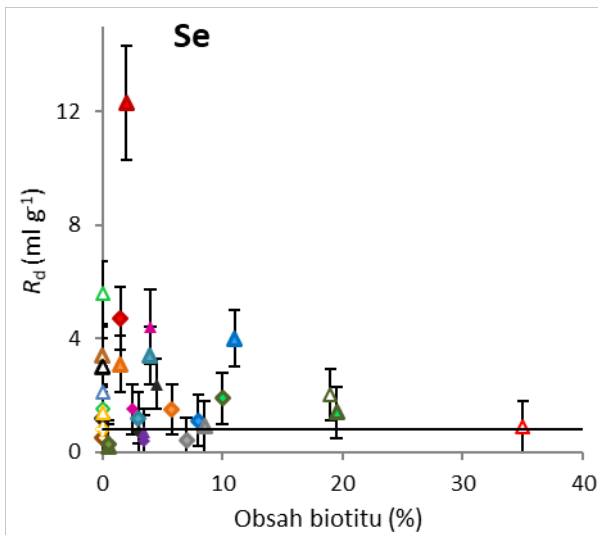
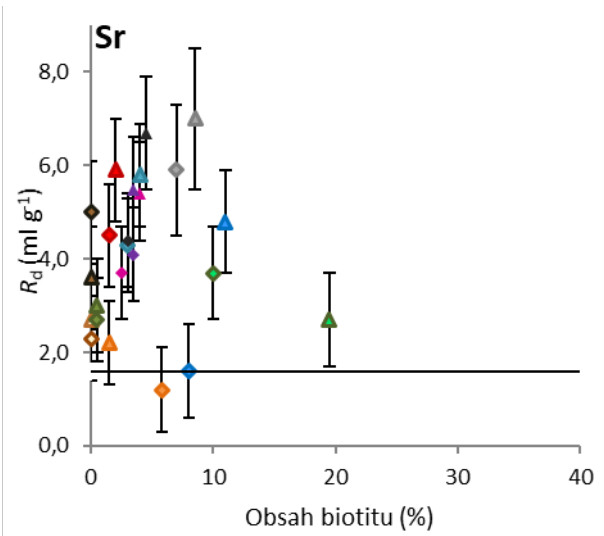
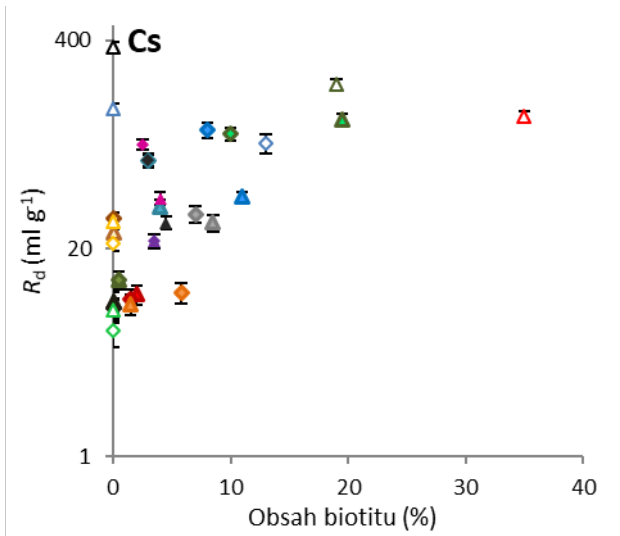


Fig. 48 Dependence of the R_d values of the radionuclides on the plagioclase content of the rock samples for the studied radionuclides: Cs graph - fractions C and D; Sr graph - fraction C; Se graph - fraction C; U graph - fraction C. Fraction C: 0.63–0.125 mm, fraction D: 0.8–0.63 mm (note: the Cs graph does not show the R_d value of the PZV1 durbachite, the high sorption of which on PZV1 was due to the higher biotite content in the sample)



 SÚRAO	Radionuclide migration processes in a crystalline rock environment. Final report.	Evidenční označení:
		SÚRAO TZ 333/2018

Fig. 49 Dependence of the R_d values of the radionuclides on the biotite content of the rock samples for the studied radionuclides: Cs graph - fractions C and D; Sr graph - fraction C; Se graph - fraction C; U graph - fraction C. Fraction C: 0.63–0.125 mm, fraction D: 0.8–0.63 mm (note: the Cs graph does not show the R_d value of the PZV1 durbachite, the high sorption of which on PZV1 was due to the higher biotite content in the sample)

When processing the results of the sorption experiments performed via the batch method, it was necessary to bear in mind that we were working with sample fractions that did not fully correspond to the real environment in the respected rock masses. An SKB report (Crawford et al. 2006) provides a summary of international experience regarding the estimation of reliable K_d distribution coefficients in experiments employing crystalline samples. The report suggests that the artefacts in such experiments cannot be controlled unless variables such as the pH are monitored during the sorption experiment and the specific BET surface area is measured before and after the sorption experiments which, unfortunately, is rarely reported in the literature. It further states that the distribution coefficients should not be reported as K_d values normalised to the weight of the sample, but rather as K_a values normalised to the BET surface area. Only through the use of normalised BET values is it possible to extrapolate the measured values to samples of similar rock types (Crawford et al. 2006). Thus, BET values normalised from other crystalline formations without correction were used in the safety analysis of the Swedish crystalline rock repository. In cases where the BETs were not normalised, the available values were corrected by means of the I scaling coefficient to reflect the associated uncertainties (Crawford et al. 2006). The report also states that BET surface area measurements are reasonably well representative, which seems to be more important than the rock type in terms of determining sorption properties.

Crawford et al. (2006) recommend that laboratory estimates of the K_d derived from crushed crystalline sample experiments be rounded down by a factor of at least 10 and possibly up to 100 for safety assessment purposes so as to ensure that the retention properties are not overestimated. According to this report, a tenfold reduction in the grain size of the crystalline material results in a corresponding increase in the BET surface area. Moreover, the data suggests that the significance of the BET specific surface area declines for grain sizes above 1 mm, which can be demonstrated by the extrapolation of laboratory estimates of the K_d for corresponding material fractions to intact rock (Crawford et al. 2006).

These conclusions must be taken into account when evaluating and applying the data obtained from sorption experiments on Czech crystalline rocks.

 SÚRAO	Radionuclide migration processes in a crystalline rock environment. Final report.	Evidenční označení:
		SÚRAO TZ 333/2018

6 Diffusion of radionuclides in granite rock environments

6.1 Methodology

Fick's laws are used to describe the diffusion of substances (tracers, contaminants) through the pores of materials; these laws are mentioned below in the section that addresses the evaluation of the results of the penetration diffusion experiments. The geometric properties of the transport pores and the retardation processes of the contaminants in the pore environment have been described in detail in previous reports, e.g. in Bukovská et al. 2017.

6.2 Arrangement of the Experimental Apparatus at ÚJV Řež

The diffusion coefficient in the equilibrium state of the system is usually determined via the conducting of so-called penetration diffusion experiments, especially in the case of non- or weakly-sorbing tracers (^3H in the form of tritiated water, ^{36}Cl in the form of chloride, ^{125}I in the form of iodide). The typical arrangement of the cells in the penetration (*through diffusion*) experiment is shown in the following figure (Löfgren 2004) (Fig. 50).

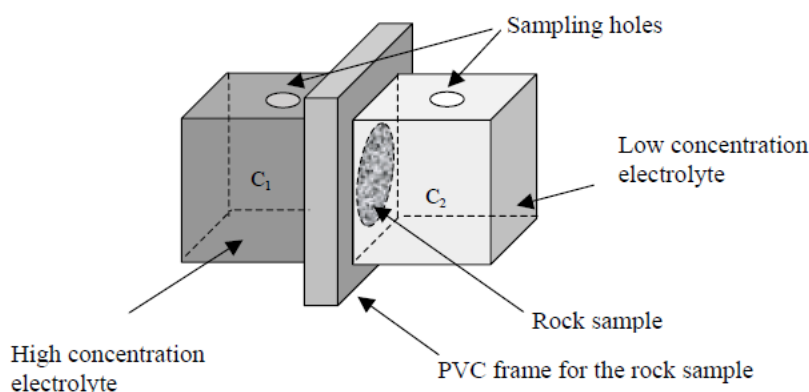


Fig. 50 Basic arrangement of the cells for the laboratory diffusion experiments (from left): inlet tank - sample - outlet tank (Löfgren 2004)

The methodology of the diffusion experiments conducted at ÚJV Řež is based on the 2402.04 partial project workflow. The diffusion cells used in the Fuel Cycle Chemistry department were inspired by a design from Helsinki University. The diffusion cell design is shown in Fig. 51.



Fig. 51 Diffusion cell for the penetration diffusion experiments: ÚJV Řež design with various reservoir sizes

The diffusion cell is made of polymethyl methacrylate (PMMA) with a silicone rubber seal placed in the middle. The sample is placed in the seal so as to ensure that the solutions do not mix. One side of the sample is in contact with the solution containing the tracer in the inlet reservoir, while the other side of the sample is in contact with the unlabelled solution in the outlet reservoir (usually synthetic groundwater of a given composition). The crystalline rock sample is in the form of a disc with a diameter of 42–50 mm and a thickness of 8–10 mm. The volume of the input reservoir is 160–165 ml, while, due to the low diffusivity of the rock samples, the output reservoirs have a lower volume (55–59 ml).

The activity in the source tank is not maintained at a constant value and is left unchanged. The activity decreases as the tracer diffuses through the sample in the direction of the alignment of the concentration gradient. Due to the volume of the input reservoir, which is around three times greater than that of the output reservoir, and the generally small amount of the diffused tracer, the activity decrease in the input reservoir is not noticeable in most cases and it can be used as a constant source for the analytical solution of the diffusion equations (including the time-lag method), see below. The increase in the tracer concentration is monitored in the output reservoir throughout the experiment. Both tanks are sampled and measured at regular intervals (7–14 days) according to the type of tracer. The penetration curve is evaluated and the diffusion coefficient calculated based on the increase in the tracer activity in the output reservoir.

6.2.1 Evaluation of the results of the penetration diffusion experiments

The results were evaluated by means of the fitting of the total diffused activity (or amount of the substance) dependent on time t (s) using the analytical solution in Fick's 2nd Law:

$$\frac{\partial C}{\partial t} = \frac{D_e}{\alpha} \left(\frac{\partial^2 C}{\partial x^2} \right), \quad (6-1)$$

where C (mol m^{-3} or Bq m^{-3}) is the concentration or volume activity in the pore water, D_e ($\text{m}^2 \text{s}^{-1}$) is the effective diffusion coefficient and α is the rock capacity factor, defined as:

 SÚRAO	Radionuclide migration processes in a crystalline rock environment. Final report.	Evidenční označení:
		SÚRAO TZ 333/2018

$$\alpha = \varepsilon + \rho_d \cdot K_d, \quad (6-2)$$

with porosity ε (-), bulk density ρ_d (kg m^{-3}) and the equilibrium distribution coefficient K_d ($\text{m}^3 \text{kg}^{-1}$).

For non-sorbing species, the capacity factor is equal to the transport porosity. The initial and boundary conditions are given as follows:

- $C(x,t) = 0$ $t = 0;$ $x \neq 0,$
- $C(x, t) = C_0$ $x = 0;$ $t \geq 0,$
- $C(L, t) = 0$ $x = L;$ $t > 0,$

where L (m) is the sample thickness and C_0 (mol m^{-3} or Bq m^{-3}) is the (initial) concentration (or activity concentration) in the inlet reservoir.

The analytical solution of the through diffusion (TD) experiment is given by the solution of equation (6-1) with the initial and boundary conditions given above and assuming that the tracer flux J ($\text{mol m}^{-2} \text{s}^{-1}$ or $\text{Bq m}^{-2} \text{s}^{-1}$) in the output reservoir at the end of the sample ($x = L$) is given by the relationship:

$$J(L, t) = -D_e \cdot \left. \frac{\partial C}{\partial x} \right|_{x=L}. \quad (6-3)$$

The calculation of the effective diffusion coefficient and porosity is then given by the analytical solution (Crank 1975, Jakob 2004):

$$Q(t) = S \cdot L \cdot C_0 \cdot \left[\frac{D_e \cdot t}{L^2} - \frac{\alpha}{6} - \frac{2\alpha}{\pi^2} \sum_{n=1}^{\infty} \frac{(-1)^n}{n^2} \cdot \exp\left(-\frac{D_e \cdot n^2 \cdot \pi^2 \cdot t}{L^2 \cdot \alpha}\right) \right], \quad (6-4)$$

where $Q(t)$ (mol or Bq) is the amount of the diffused substance (or activity) at time t through a sample of thickness L and area S , C_0 is the initial concentration (or volume activity) of the monitored substance, which is kept constant during the experiment.

Provided that the diffusion flux attains the steady state ($t \rightarrow \infty$), then the equation is reduced to the form:

$$\frac{Q(t)}{S \cdot C_0} = \frac{D_e \cdot t}{L} - \frac{\alpha \cdot L}{6} \quad (6-5)$$

where the diffusion coefficient D_e can be determined from the dependency of $Q(t) / (S \cdot C_0)$ on time and from the section of the capacity factor α .

This evaluation method is known as the time-lag method. A more detailed description of the evaluation of penetration diffusion experiments and the limits of the various evaluation methods can be found in Červinka et al. 2015 or Van Loon et al. 2003.

Such data evaluation methods are commonly used even when the above-mentioned boundary conditions are not strictly observed. In general, conditions are accepted for the application of these methods if the inlet C_0 concentration does not fall below 95% of the initial C_0 concentration ($t = 0, x = 0$) and no more than 5% of the initial source concentration diffuses into the target reservoir (García-Gutierrez et al. 2003). These conditions were met with respect

 SÚRAO	Radionuclide migration processes in a crystalline rock environment. Final report.	Evidenční označení:
		SÚRAO TZ 333/2018

to almost all the experiments performed (the maximum source decrease was 7% of the initial concentration). Occasional non-systematic deviations in the measured values can be attributed to inaccuracies in the determination of the activity in the solutions.

The search for the optimal values of D_e and α was performed via the fitting of the experimental data to the model analytical solution (6-4) by means of the least squares method. In order to simplify the fitting, the porosity ε was set at a constant value along the diffusion path as determined by the progressive drying method (see chapter 4.4); the only unknown (fitting) parameter was the effective diffusion coefficient D_e . By means of further simple adjustments (see below) we were able to calculate the other parameters (the geometric factor G (-) and the rock formation factor F_f (-)) via information from table values of reference diffusivities D_w ($\text{m}^2 \text{s}^{-1}$) for infinite dilution ($D_w = 2.44 \cdot 10^{-9} \text{m}^2 \text{s}^{-1}$ for HTO, $D_w = 2.30 \cdot 10^{-9} \text{m}^2 \text{s}^{-1}$ for iodide and $D_w = 2.03 \cdot 10^{-9} \text{m}^2 \text{s}^{-1}$ for chloride).

$$D_e = \varepsilon \cdot D_p = \varepsilon \cdot D_w \cdot G = F_f \cdot D_w \quad (6-6)$$

6.3 Properties of the rock samples

Diffusion experiments were performed on samples from the following sites: Čihadlo (D2), Čertovka (TIV), Horka (PZV), Panské Dubenky (PDV), Kraví hora (GRB and 2S3), Březový potok (Defurovy Lažany quarry - samples BT3 and BT8) and Hrádek (Borsov quarry - samples GB2 and GB4; Bromberg quarry - sample GC3). A summary of the samples including their dimensions is provided in Tab. 37 based on the list of samples provided in Tab. 2.

Tab. 37 List of the diffusion experiment samples with their dimensions

Sample designation	BT8_1	BT8_2	BT3_2	BT3_3	GB2_1	GB2_2	GB4_1	GB4_3
Thickness L (mm)	9.9	9.9	9.9	10.6	10.3	10.6	9.3	10.4
Diameter d (mm)	47.9	47.9	47.5	47.5	47.8	47.8	47.8	47.8
Sample designation	GC3_2	D2_1/4	D2_2/1	D2_2/2	TIV1_68 A	TIV1_68 C	PZV1_90 B	PZV1_90 C
Thickness L (mm)	9.9	10.3	10.4	10.6	9.6	9.6	10.0	10.7
Diameter d (mm)	47.8	49.9	49.9	49.9	47.8	47.8	47.7	47.7
Sample designation	PDV1_89C	PDV1_97 A	GRB_1_1	GRB_1_2	GRB_3_1	GRB_3_2	2S3_2_1	2S3_2_3
Thickness L (mm)	10.6	10.7	10.4	9.5	10.8	10.2	9.9	10.2

 SÚRAO	Radionuclide migration processes in a crystalline rock environment. Final report.	Evidenční označení:
		SÚRAO TZ 333/2018

Diameter d (mm)	47.6	47.6	50.1	50.2	50.3	50.3	49.0	49.1
----------------------	------	------	------	------	------	------	------	------

6.4 Properties of the solutions

SGW2 synthetic granitic water (Červinka and Gondolli 2016) was used in all the diffusion experiments. The average chemical composition of the SGW2 synthetic granitic water is shown in Tab. 18.

In order to monitor the transport behaviour of the samples, two types of source solutions in SGW2 synthetic granitic water were used for the diffusion experiments on rock samples from the candidate sites with:

- 1) A mixture of ^3H and ^{36}Cl tracers, in which the approximate activity of the ^3H tracer ($T_{1/2} = 12.32$ years) was 4 kBq ml^{-1} and of the ^{36}Cl tracer ($T_{1/2} = 301300$ years) approximately 2.5 kBq ml^{-1} with a carrier preparation in the form of NaCl (concentration of approximately 0.016 mol l^{-1}), with the detection of β^- conversions via the liquid scintillation calculation on a Hidex 300 SL device (Hidex Oy).
- 2) Firstly, a solution with only the ^3H tracer followed by the replacement of the source solution with a ^{125}I tracer solution in the form of NaI ($T_{1/2} = 59.4$ days) with an approximate activity of $1.1\text{--}2.0 \text{ kBq ml}^{-1}$ with the detection of the emitted photons originating from electron capture on a thallium-activated NaI detector on a 1480 WIZARD 3" device (Wallac Oy). A CaI_2 carrier with a concentration of $5 \cdot 10^{-6} \text{ mol l}^{-1}$ (resulting in an iodide concentration of $10^{-5} \text{ mol l}^{-1}$) and $\text{Na}_2\text{S}_2\text{O}_3$ solution to eliminate iodide oxidation were added to the SGW2 solution.

6.5 Results and evaluation

Despite the various sample sizes (diameters $d = 47.5\text{--}50.3$ mm and thicknesses $L = 9.3\text{--}10.8$ mm) and solution contents in the reservoirs, a comparison of all the penetration curves is provided in Fig. 52 for illustration and for the purpose of the comparison of the tritium and anionic tracers.

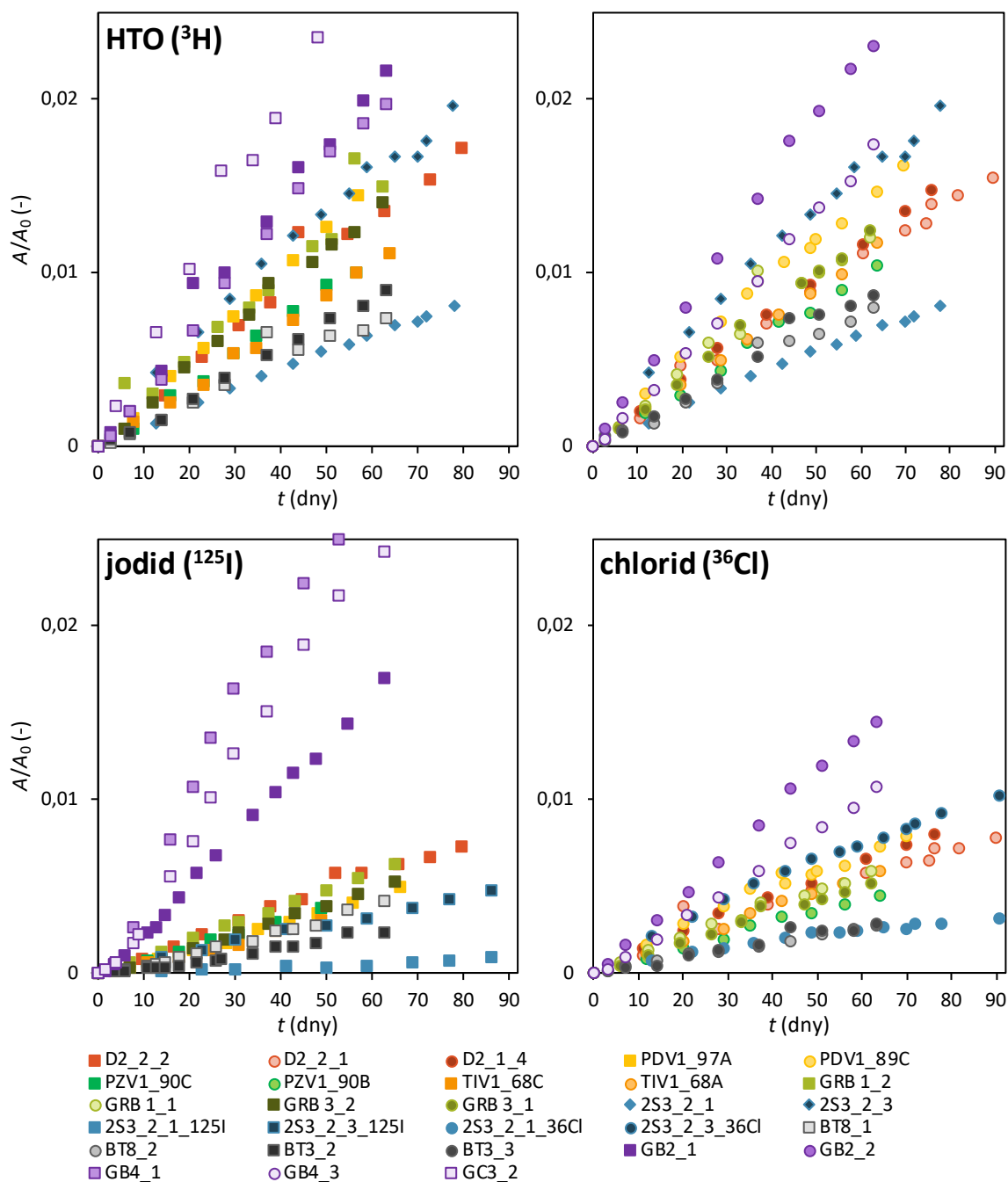


Fig. 52 Penetration curves (the development of relative volumetric activity in the outlet reservoirs) for the diffusion experiments with tritium (^3H), iodide (^{125}I) and chloride (^{36}Cl)

It is clear from Fig. 52 that the highest diffusivity of all the tracers considered concerns the samples from the Hrádek site (the GB samples), while the lowest values were determined for the samples from the Březový potok (BT) site. The results of the sample from the Bukov URF/Kraví hora site (drill core 2S3) were, in terms of the results of parallel experiments and despite the samples in both test series having the same porosity (determined in Chapter 4.4), very inconsistent in the case both of the diffusion of tritium and both anions; thus, the sample was not considered in the comparison. The effective diffusion coefficient values for the samples are listed according to site in Tab. 38 to Tab. 45 with the corresponding uncertainty at a significance level of 0.05 (i.e. $1.96 \cdot \sigma$). At this point it should be noted that the measured

volume activity signal in the output reservoirs was only slightly above the detection limit with acceptable measurement uncertainty (i.e. three to four times the measured background) in some of the diffusion experiments, even after extended experimentation times. Therefore, it was considered better to consider all the effective diffusion coefficient values of less than $2 \cdot 10^{-13} \text{ m}^2 \text{ s}^{-1}$ as less than or equal to $2 \cdot 10^{-13} \text{ m}^2 \text{ s}^{-1}$ and the values shown in Tab. 43 and Tab. 44 as mere estimates.

A comparison of Fig. 52 with the effective diffusion coefficients values in Tab. 38 to Tab. 45 highlights the lower diffusivity of the anions than that of tritium, which can be attributed to anion exclusion due to repulsive electrostatic forces between the negatively-charged anionic tracer and the surface of the transport pores of the rock samples. The GB4_1 sample (granulite, Kraví hora) evinced higher iodide (^{125}I) than tritium (^3H) diffusivity due to the probable occurrence of a fracture in the sample, which minimised the exclusion effect. The ratio of the effective diffusion coefficients between the tritium and anions is further illustrated in Fig. 53.

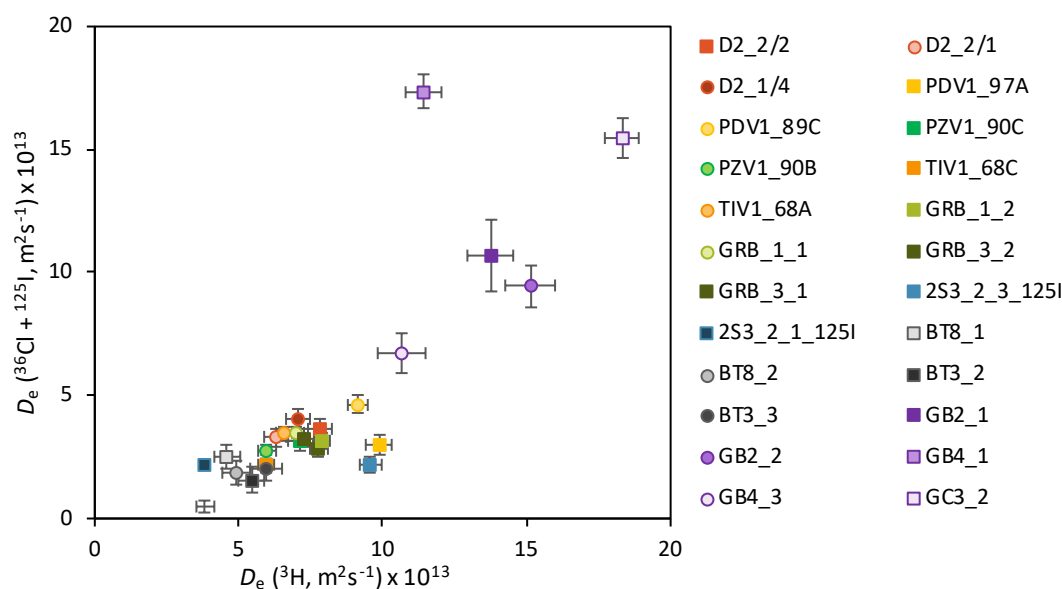


Fig. 53 Effective diffusion coefficient values (analytical solution) of tritium (^3H) versus anions (chloride ^{36}Cl , iodide ^{125}I)

Fig. 54 further illustrates the influence of porosity on the effective diffusion coefficient of tritium (^3H , HTO). Despite the higher porosity of the samples from the Březový potok site compared to the Čertovka, Horka and Panské Dubenky sites, the effective diffusion coefficients are significantly lower and, thus, no connection can be determined between these quantities. If the porosity determined by the drying method (see Chapter 4.4) is equal to the transport porosity, the interpretation of the geometric diffusion pathway according to (6-6) is a geometric factor equal to $G = 0.03\text{--}0.11$ (assuming that the D_w table values at infinite dilution influenced by the solution (electrolyte) and carrier tracer do not change). The uncertainty of the interpretation according to (6-6) in the geometric factor is enhanced e.g. by the 2S3 core (Kraví hora), concerning which the calculated values differ by more than 100% ($G = 0.03\text{--}0.08$). This discrepancy is partially explained in the discussion of the drill core below; however, a smaller discrepancy is evident with regard to a further TIV drill core (Čertovka) with $G = 0.09\text{--}0.11$, despite the fact that the samples are almost adjacent (separated by sample TIV_68B). Despite

these uncertainties (the size G , D_w and transport porosity, i.e. the determination of the uncertainty of total porosity via the drying method described above), which we are not able to demonstrate properly, effective diffusion coefficients can be considered decisive in terms of the description of the diffusion experiments of non-interacting species on rocks.

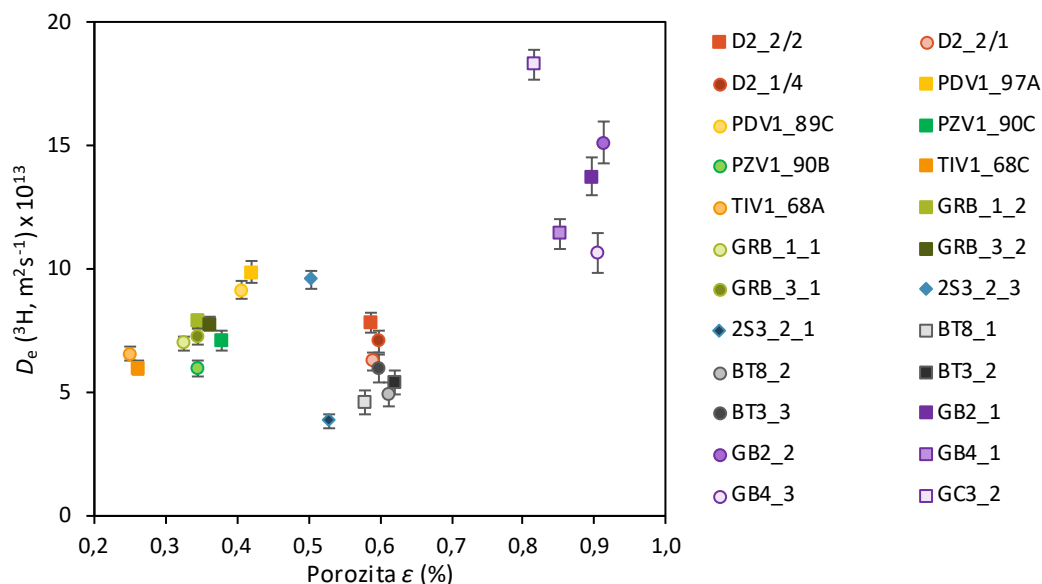


Fig. 54 Effective diffusion coefficient values (analytical solution) of tritium (^3H) depending on the porosity of the sample (determined by the drying method)

130 Čihadlo site – Deštná (drill core D2)

The samples originated from the surface sampling of fresh quarry stone. Granite is the predominant rock type.

Tab. 38 Evaluation of the effective diffusion coefficients for the D2 core samples

Sample designation	ϵ %	D_e (^3H) $\cdot 10^{-13} \text{ m}^2 \text{ s}^{-1}$	D_e (^{36}Cl) $\cdot 10^{-13} \text{ m}^2 \text{ s}^{-1}$	D_e (^{125}I) $\cdot 10^{-13} \text{ m}^2 \text{ s}^{-1}$	Ratio of D_e anion/ ^3H	Evaluation
D2_2/2	0.59	7.8 ± 0.4		3.6 ± 0.4	0.46 ± 0.06	analytical solution
		7.5 ± 0.3		3.3 ± 0.3	0.44 ± 0.04	time-lag
D2_2/1	0.59	6.3 ± 0.4	3.3 ± 0.3		0.53 ± 0.06	analytical solution
		6.0 ± 0.3	2.9 ± 0.2		0.49 ± 0.05	time-lag

 SÚRAO	Radionuclide migration processes in a crystalline rock environment. Final report.	Evidenční označení:
		SÚRAO TZ 333/2018

Sample designation	ε %	D_e (^3H) $\cdot 10^{-13} \text{ m}^2 \text{ s}^{-1}$	D_e (^{36}Cl) $\cdot 10^{-13} \text{ m}^2 \text{ s}^{-1}$	D_e (^{125}I) $\cdot 10^{-13} \text{ m}^2 \text{ s}^{-1}$	Ratio of D_e anion/ ^3H	Evaluation
D2_1/4	0.60	7.1 ± 0.4	4.1 ± 0.4		0.57 ± 0.07	analytical solution
		6.8 ± 0.1	3.5 ± 0.1		0.52 ± 0.02	<i>time-lag</i>

120 Čertovka site – Tis u Blatna (drill core TIV1)

The samples were taken from an archived drill core from a depth of 68 m. Granite is the predominant rock type.

Tab. 39 Evaluation of the effective diffusion coefficients for the TIV1 core samples

Sample designation	ε %	D_e (^3H) $\cdot 10^{-13} \text{ m}^2 \text{ s}^{-1}$	D_e (^{36}Cl) $\cdot 10^{-13} \text{ m}^2 \text{ s}^{-1}$	D_e (^{125}I) $\cdot 10^{-13} \text{ m}^2 \text{ s}^{-1}$	Ratio of D_e anion/ ^3H	Evaluation
TIV1_68C	0.26	6.0 ± 0.3		2.2 ± 0.3	0.36 ± 0.05	analytical solution
		6.0 ± 0.3		2.2 ± 0.1	0.36 ± 0.03	<i>time-lag</i>
TIV1_68A	0.25	6.6 ± 0.3	3.5 ± 0.3		0.53 ± 0.05	analytical solution
		6.5 ± 0.2	3.3 ± 0.2		0.51 ± 0.04	<i>time-lag</i>

140 Horka site – Pozdátky (drill core PZV1)

The samples were taken from an archived drill core from a depth of 90 m. Syenite is the predominant rock type.

Tab. 40 Evaluation of the effective diffusion coefficients for the PZV1 core samples

Sample designation	ε %	D_e (^3H) $\cdot 10^{-13} \text{ m}^2 \text{ s}^{-1}$	D_e (^{36}Cl) $\cdot 10^{-13} \text{ m}^2 \text{ s}^{-1}$	D_e (^{125}I) $\cdot 10^{-13} \text{ m}^2 \text{ s}^{-1}$	Ratio of D_e anion/ ^3H	Evaluation
PZV1_90C	0.38	7.1 ± 0.4		3.1 ± 0.4	0.44 ± 0.06	analytical solution
		7.1 ± 0.4		3.1 ± 0.1	0.43 ± 0.03	<i>time-lag</i>

 SÚRAO	Radionuclide migration processes in a crystalline rock environment. Final report.	Evidenční označení:
		SÚRAO TZ 333/2018

Sample designation	ϵ %	D_e (^3H) $\cdot 10^{-13} \text{ m}^2 \text{ s}^{-1}$	D_e (^{36}Cl) $\cdot 10^{-13} \text{ m}^2 \text{ s}^{-1}$	D_e (^{125}I) $\cdot 10^{-13} \text{ m}^2 \text{ s}^{-1}$	Ratio of D_e anion/ ^3H	Evaluation
PZV1_90B	0.34	6.0 ± 0.3	2.7 ± 0.3		0.46 ± 0.05	analytical solution
		6.0 ± 0.4	2.5 ± 0.2		0.42 ± 0.05	<i>time-lag</i>

Panské Dubenky site (drill core PDV1)

The samples were taken from an archived drill core from depths of 89 and 97 m. Granite is the predominant rock type.

Tab. 41 Evaluation of the effective diffusion coefficients for the PDV1 core samples

Sample designation	ϵ %	D_e (^3H) $\cdot 10^{-13} \text{ m}^2 \text{ s}^{-1}$	D_e (^{36}Cl) $\cdot 10^{-13} \text{ m}^2 \text{ s}^{-1}$	D_e (^{125}I) $\cdot 10^{-13} \text{ m}^2 \text{ s}^{-1}$	Ratio of D_e anion/ ^3H	Evaluation
PDV1_97A	0.42	9.9 ± 0.5		3.0 ± 0.4	0.30 ± 0.04	analytical solution
		9.9 ± 0.2		3.0 ± 0.1	0.30 ± 0.01	<i>time-lag</i>
PDV1_89C	0.41	9.2 ± 0.3	4.5 ± 0.3		0.51 ± 0.04	analytical solution
		8.4 ± 1.1	3.9 ± 0.4		0.46 ± 0.08	<i>time-lag</i>

170 Kraví hora site – Horní Bory (drill cores GRB 1 and GRB 3)

The samples originate from the surface sampling of fresh quarry stone. Felsic granulite is the predominant rock type. The GRB_1 samples were drilled in parallel with foliation and the GRB_3 samples perpendicular to foliation. As can be seen from the results provided in Tab. 42, the direction of the samples evinced no statistically significant effect on the effective diffusion coefficient values for any of the tracers.

 SÚRAO	Radionuclide migration processes in a crystalline rock environment. Final report.	Evidenční označení:
		SÚRAO TZ 333/2018

Tab. 42 Evaluation of the effective diffusion coefficients for the GRB core samples

Sample designation	ε %	D_e (^3H) $\cdot 10^{-13} \text{ m}^2 \text{ s}^{-1}$	D_e (^{36}Cl) $\cdot 10^{-13} \text{ m}^2 \text{ s}^{-1}$	D_e (^{125}I) $\cdot 10^{-13} \text{ m}^2 \text{ s}^{-1}$	Ratio of D_e anion/ ^3H	Evaluation
GRB_1_2	0.35	7.9 ± 0.3		3.2 ± 0.3	0.40 ± 0.04	analytical solution
		7.6 ± 0.9		3.1 ± 0.1	0.41 ± 0.05	<i>time-lag</i>
GRB_1_1	0.33	7.0 ± 0.3	3.5 ± 0.3		0.49 ± 0.05	analytical solution
		6.7 ± 0.4	3.1 ± 0.2		0.48 ± 0.09	<i>time-lag</i>
GRB_3_2	0.36	7.8 ± 0.3		2.8 ± 0.3	0.36 ± 0.04	analytical solution
		7.7 ± 0.5		2.9 ± 0.1	0.38 ± 0.03	<i>time-lag</i>
GRB_3_1	0.35	7.3 ± 0.3	3.3 ± 0.3		0.45 ± 0.05	analytical solution
		7.3 ± 0.9	3.0 ± 0.3		0.41 ± 0.07	<i>time-lag</i>

Kraví hora site – Bukov (drill core 2S3)

The samples were taken from an archived drill core from a depth of 78 m. Migmatite is the predominant rock type.

Due to the non-standard development of activity in the target reservoirs (the concave shape of the penetration curve) for both samples from the 2S3 drill core, it was not possible to provide a meaningful evaluation of the diffusion experiment with the ^{36}Cl analytical solution. The diffusion coefficients were calculated via the determination of the diffusion flux between the samples (experimental points).

In this case, and in contrast to the samples from the other sites, diffusion experiments with ^{125}I were conducted on the samples following the experiments employing a mixture of the $^3\text{H} + ^{36}\text{Cl}$ tracers (i.e. all three tracers were used on the two samples). The resulting D_e values for ^{125}I were found to be comparable in both cases.

Samples 2S3_2_1 and 2S3_2_3 evinced considerably different effective diffusion coefficient values despite their originating from the same drill core and being almost adjacent samples. Upon closer inspection of the discs, an area in which the rock was visibly more disturbed than on the rest of the sample was determined on the 2S3_2_3 sample (for which higher D_e values were determined). In addition, a portion of the edge of the sample was found to be chipped in this area which created a preferential diffusion pathway and which, in turn, most likely led to

 SÚRAO	Radionuclide migration processes in a crystalline rock environment. Final report.	Evidenční označení:
		SÚRAO TZ 333/2018

the higher diffusion coefficient values. A comparison of the results with previous results from the neighbouring S3 drill core (see the Final Report by Bukovská et al. 2017) confirmed this hypothesis. The effective diffusion coefficient values for ^3H ranged from $1.6\text{--}3.0 \cdot 10^{-13} \text{ m}^2 \text{ s}^{-1}$, and for ^{36}Cl from $0.4\text{--}0.8 \cdot 10^{-13} \text{ m}^2 \text{ s}^{-1}$.

Tab. 43 Evaluation of the effective diffusion coefficients for the 2S3 core samples

Sample designation	ε %	$D_e (^3\text{H})$ $\cdot 10^{-13} \text{ m}^2 \text{ s}^{-1}$	$D_e (^{36}\text{Cl})$ $\cdot 10^{-13} \text{ m}^2 \text{ s}^{-1}$	$D_e (^{125}\text{I})$ $\cdot 10^{-13} \text{ m}^2 \text{ s}^{-1}$	Ratio of D_e anion/ ^3H	Evaluation
2S3_2_1	0.53	3.8 ± 0.3	X*	0.5 ± 0.3	0.12 ± 0.07	analytical solution
		3.5 ± 0.1		0.4 ± 0.1	0.10 ± 0.03	time-lag
			1.0 ± 0.8		0.29 ± 0.24	time-lag
2S3_2_3	0.50	9.6 ± 0.4	X*	2.2 ± 0.3	0.23 ± 0.03	analytical solution
		8.7 ± 0.5		1.8 ± 0.1	0.21 ± 0.02	time-lag
			3.7 ± 1.3		0.43 ± 0.15	time-lag

*) The samples could not be evaluated via the analytical solution

Březový potok site – Defurovy Lažany (drill cores BT8 and BT3)

Tab. 44 Evaluation of the effective diffusion coefficients for the BT core samples

Sample designation	ε %	$D_e (^3\text{H})$ $\cdot 10^{-13} \text{ m}^2 \text{ s}^{-1}$	$D_e (^{36}\text{Cl})$ $\cdot 10^{-13} \text{ m}^2 \text{ s}^{-1}$	$D_e (^{125}\text{I})$ $\cdot 10^{-13} \text{ m}^2 \text{ s}^{-1}$	Ratio of D_e anion/ ^3H	Evaluation
BT8_1	0.58	4.6 ± 0.5		2.5 ± 0.5	0.55 ± 0.12	analytical solution
		3.8 ± 1.7		2.6 ± 0.2	0.67 ± 0.20	time-lag
BT8_2	0.61	4.9 ± 0.5	1.9 ± 0.5		0.38 ± 0.10	analytical solution
		4.8 ± 1.1	1.5 ± 0.1		0.31 ± 0.08	time-lag

 SÚRAO	Radionuclide migration processes in a crystalline rock environment. Final report.	Evidenční označení:
		SÚRAO TZ 333/2018

Sample designation	ϵ %	D_e (^3H) $\cdot 10^{-13} \text{ m}^2 \text{ s}^{-1}$	D_e (^{36}Cl) $\cdot 10^{-13} \text{ m}^2 \text{ s}^{-1}$	D_e (^{125}I) $\cdot 10^{-13} \text{ m}^2 \text{ s}^{-1}$	Ratio of D_e anion/ ^3H	Evaluation
BT3_2	0.62	5.4 ± 0.5		1.6 ± 0.5	0.29 ± 0.10	analytical solution
		5.5 ± 0.2		1.4 ± 0.2	0.25 ± 0.03	<i>time-lag</i>
BT3_3	0.60	6.0 ± 0.6	2.1 ± 0.5		0.35 ± 0.09	analytical solution
		5.8 ± 1.1	1.7 ± 0.6		0.30 ± 0.11	<i>time-lag</i>

Hrádek – Boršov (drill cores GB2 and GB4) and Bromberg sites (drill core GC3)

Tab. 45 Evaluation of the effective diffusion coefficients for the GB and GC core samples

Sample designation	ϵ %	D_e (^3H) $\cdot 10^{-13} \text{ m}^2 \text{ s}^{-1}$	D_e (^{36}Cl) $\cdot 10^{-13} \text{ m}^2 \text{ s}^{-1}$	D_e (^{125}I) $\cdot 10^{-13} \text{ m}^2 \text{ s}^{-1}$	Ratio of D_e anion/ ^3H	Evaluation
GB2_1	0.90	13.8 ± 0.8		10.7 ± 1.4	0.77 ± 0.11	analytical solution
		12.5 ± 1.3		10.6 ± 0.4	0.84 ± 0.08	<i>time-lag</i>
GB2_2	0.91	15.1 ± 0.9	9.4 ± 0.8		0.62 ± 0.07	analytical solution
		14.0 ± 1.0	9.1 ± 0.4		0.65 ± 0.05	<i>time-lag</i>
GB4_1	0.85	11.4 ± 0.6		17.3 ± 0.7	1.52 ± 0.10	analytical solution
		10.7 ± 0.8		13.5 ± 2.4	1.41 ± 0.16	<i>time-lag</i>
GB4_3	0.91	10.7 ± 0.8	6.7 ± 0.8		0.63 ± 0.09	analytical solution
		10.8 ± 0.6	6.7 ± 0.4		0.62 ± 0.05	<i>time-lag</i>

 SÚRAO	Radionuclide migration processes in a crystalline rock environment. Final report.	Evidenční označení:
		SÚRAO TZ 333/2018

Sample designation	ϵ %	D_e (^3H) $\cdot 10^{-13} \text{ m}^2 \text{ s}^{-1}$	D_e (^{36}Cl) $\cdot 10^{-13} \text{ m}^2 \text{ s}^{-1}$	D_e (^{125}I) $\cdot 10^{-13} \text{ m}^2 \text{ s}^{-1}$	Ratio of D_e anion/ ^3H	Evaluation
GC3_2	0.82	18.3 ± 0.6		15.5 ± 0.8	0.84 ± 0.05	analytical solution
		17.0 ± 1.7		13.8 ± 1.5	0.81 ± 0.11	<i>time-lag</i>

6.6 Discussion

Although the samples originated from different localities across the Czech Republic and consisted of different rock types, and despite some of the samples originating from surface quarries and the others from drill cores, the effective diffusion coefficients obtained lay in a relatively narrow range: for ^3H $(4\text{--}10) \cdot 10^{-13} \text{ m}^2 \text{ s}^{-1}$, for ^{36}Cl $(1\text{--}10) \cdot 10^{-13} \text{ m}^2 \text{ s}^{-1}$ and for ^{125}I $(1\text{--}4) \cdot 10^{-13} \text{ m}^2 \text{ s}^{-1}$; values below $2 \cdot 10^{-13} \text{ m}^2 \text{ s}^{-1}$ are merely estimates within the determination limit based on the detection limits.

With respect to the Bukov URF metamorphic rocks, anion exclusion was proven (to a greater extent than in igneous/magmatic rocks) caused by greater anion repulsion in the pore space than the diffusion of non-interacting ^3H , thus resulting in lower D_e values for ^{36}Cl and ^{125}I . Metamorphic rocks generally exhibit lower porosity with smaller and less interconnected pores. The range of mean D_e values for ^3H , ^{36}Cl and ^{125}I for metamorphic and igneous/magmatic rocks is shown in the following figure (Fig. 55).

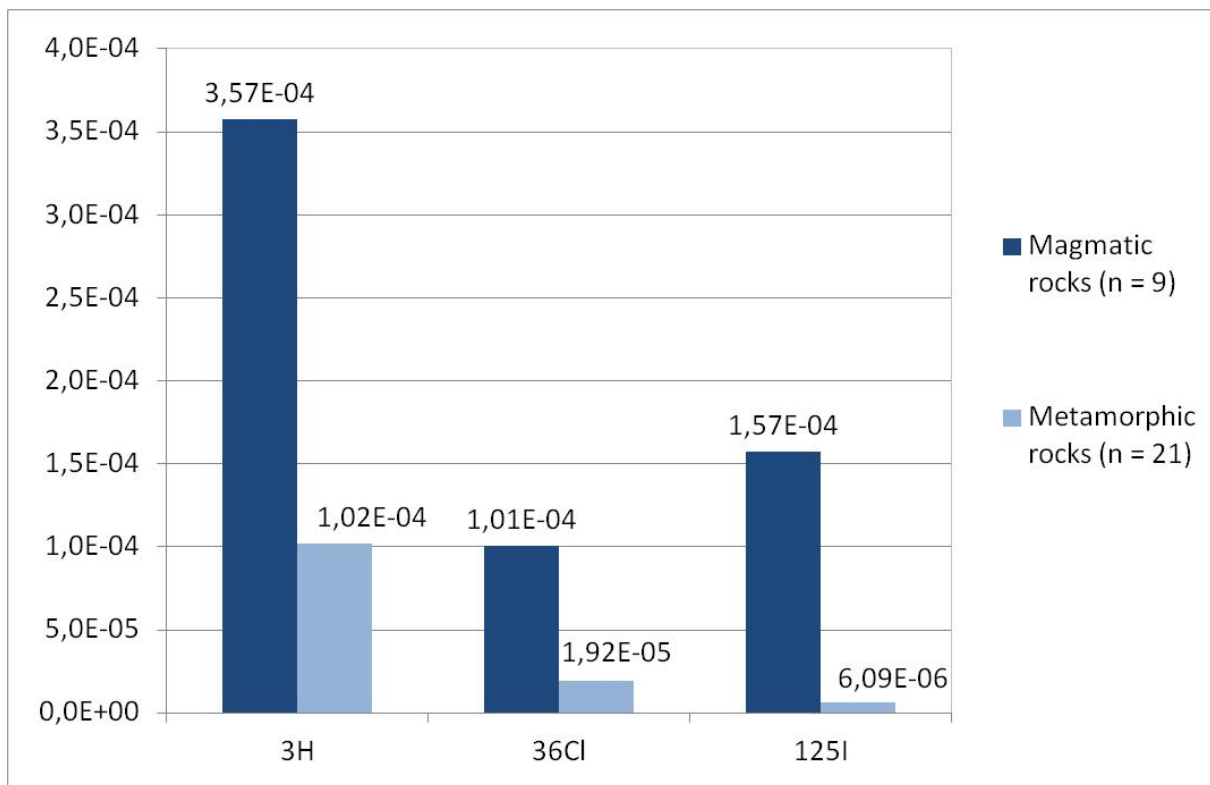


Fig. 55 Average D_e values for ^3H , ^{36}Cl and ^{125}I for igneous and metamorphic rocks

 SÚRAO	Radionuclide migration processes in a crystalline rock environment. Final report.	Evidenční označení:
		SÚRAO TZ 333/2018

7 Hydrochemistry of the groundwater at the Bukov URF

7.1 Composition of the water in granitic rock massifs

The basic properties of the water in granitic massifs and the candidate sites has been assessed in reports by Havlová et al. (2015a) and Červinka and Gondolli (2016).

A detailed knowledge of the groundwater composition constitutes an elementary input requirement for a number of DGR safety areas. The first Czech experimental research was based on the average composition of groundwater from the Melechov massif (Buňatová et al. 1995) and reference groundwater from the Příbram site (Háje, underground gas storage). A more comprehensive assessment and overview of the groundwater composition of the Bohemian Massif was subsequently conducted by Rukavičková et al. (2009). According to the analysis performed, the groundwaters were divided into three types: groundwater from granites at depths of more than 30 m, fossil water and mineral water affected by the intake of deep CO₂. The chemical composition of the groundwater at the candidate DGR sites was discussed in Havlová et al. (2015a). The basic chemical compositions of selected groundwaters used for the preparation of synthetic groundwater or recommended as the reference groundwater are provided in Tab. 46.

Tab. 46 Basic chemical composition of the groundwater 1) Melechov massif - average, SGW preparation (Buňatová et al. 1995), 2) Háje u Příbrami site, underground gas reservoir, seepage P-6, years 1990–1996 - average, 3) Bohemian Massif - median (Rukavičková et al. 2009), 4) Bohemian Massif, mineral waters - median (Rukavičková et al. 2009), 5) Bohemian Massif, fossil water - median (Rukavičková et al. 2009), 6) Jáchymov, source Běhounek, borehole HG-1, 7) Čertovka site, borehole TIV-1 (Havlová et al. 2015a), 8) Magdaléna site, borehole N-2 (Havlová et al. 2015a), 9) Horka site, borehole NT-2 (Havlová et al. 2015a), 10) Čihadlo site, borehole DE-2 (Havlová et al. 2015a), 11) Březový potok site, borehole HV-5 (Havlová et al. 2015a), 12) Hrádek site, borehole DC-1 (Havlová et al. 2015a), 13) Kraví Hora site, borehole S-1, Bukov URF (Havlová et al. 2015a), 14) Bukov URF (600 m) - average, SGW2 preparation, 15) Rožná Mine (1000 m) - average, SGW3 preparation

No.	Depth (m)	pH	I (mol l ⁻¹)	Na (mg l ⁻¹)	K (mg l ⁻¹)	Ca (mg l ⁻¹)	Mg (mg l ⁻¹)	Cl (mg l ⁻¹)	HCO ₃ (mg l ⁻¹)	SO ₄ (mg l ⁻¹)	TDS (mg l ⁻¹)	Balance Cat/an %
1	-	8.3	0.003	10.6	1.8	27.0	6.4	42.4	30.4	27.7	152.8	0.0
2	900	9.1	0.002	75.9	0.5	3.9	0.6	14.9	137.6	18.3	114.1	0.1
3	-	-	0.003	11.4	2.3	30.1	8.0	11.7	85.4	34.1	183.0	5.3
4	-	-	0.020	501.5	25.5	60.9	28.7	92.6	1220.5	162.5	2092.2	3.5
5	-	-	0.020	1050.0	52.5	55.9	22.0	644.0	863.0	26.3	2713.7	22.2
6	-	-	0.006	141.0	8.5	23.6	5.5	52.4	442.0	15.6	690.0	-6.3
7	100	6.7	0.003	7.2	9.2	15.6	8.1	4.3	100.7	16.6	161.8	-3.1
8	70	7.5	0.004	12.5	3.6	24.1	10.8	12.1	95.8	33.6	203.7	2.1
9	80	7.9	0.006	5.1	4.2	30.0	27.0	20.0	143.0	40.0	286.0	0.3
10	80	6.9	0.004	10.7	1.5	29.6	8.8	8.2	112.9	33.6	213.0	-1.5

11	60	7	0.005	14.0	2.5	43.8	8.4	13.6	162.0	49.0	293.6	-6.8
12	90	7	0.003	6.5	1.7	25.1	6.1	5.3	91.5	15.9	170.4	0.6
13	600	8.6	0.004	14.7	2.5	33.6	7.8	2.9	155.6	13.9	264.8	1.4
14	600	8.2	0.004	16.5	2.1	34.6	8.3	3.3	168.7	21.0	287.5	-1.7
15	1000	9.2	0.004	89.4	0.7	1.3	0.1	18.7	163.5	10.5	319.3	0.4

The basic chemical compositions of the groundwaters described in Tab. 46 were plotted in the form of a Piper diagram (see Fig. 56). Put simply, the Ca-Mg-HCO₃ composition dominates with respect to the groundwater at the candidate DGR sites (sampling depths up to 100 m, with the exception of the Bukov URF - sampling depth 600 m). The median of the groundwaters in the granites of the Bohemian Massif at similar depth correspond very well. The average water composition of the Melechov massif, which is used for the preparation of synthetic granitic water (ÚJV), differs in terms of an increased content of chlorides. The generic representative consists of the average composition of the groundwater from the Bukov URF (600 m) and labelled SGW2. Deeper groundwaters, represented by the analysis of waters from the Háje underground gas reservoir (Příbram), the Běhounek spring (borehole HG-1, Jáchymov) and the median of the fossil and mineral waters of the Bohemian Massif, are distinguished by a pronounced Na content with dominant HCO₃⁻ or Cl⁻ anions. Whereas it is likely that as the depth increases, the sodium content in the groundwater increases, this does not correspond, for example, to the analysis from the Bukov URF (depths of around 600 m). The generic representative consists of the average composition of groundwater from the Rožná mine (1000 m), labelled SGW3.

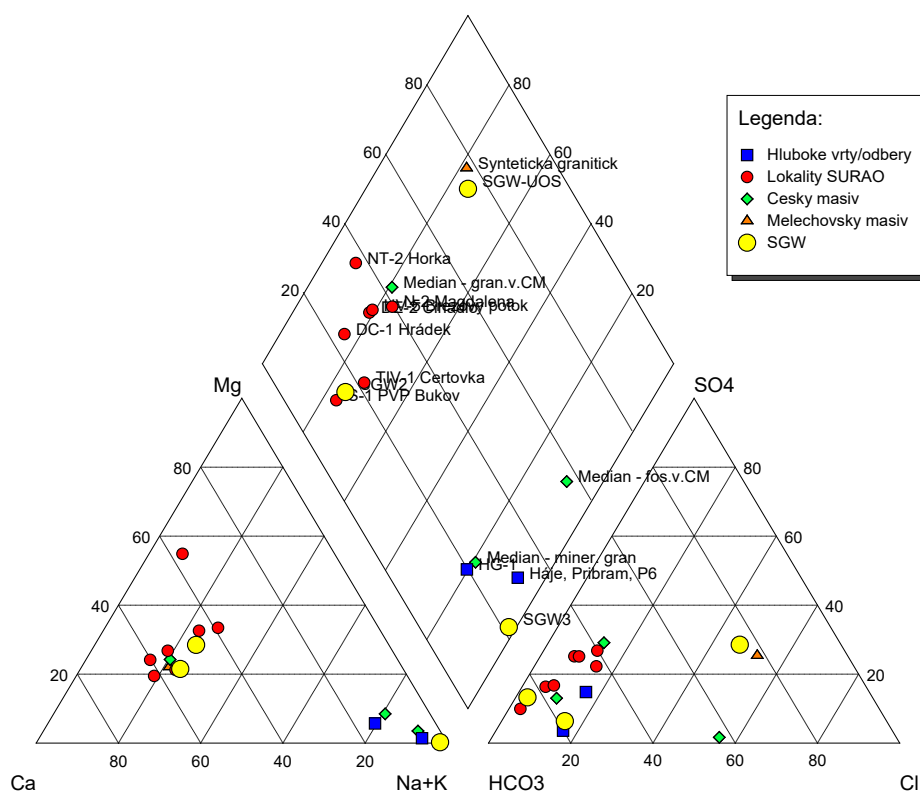


Fig. 56 Piper diagram of the groundwater composition according to Tab. 46

 SÚRAO	Radionuclide migration processes in a crystalline rock environment. Final report.	Evidenční označení:
		SÚRAO TZ 333/2018

The depth interval of the groundwater transition from type Ca-HCO₃ to Na-HCO₃ is not known precisely since insufficient analysis has been conducted to date of the groundwater at deeper horizons corresponding to the planned depth of the DGR (500 m) either for the candidate sites or crystalline rocks in general (especially granitic plutons). The explanation for the lack of groundwater analysis is simple: granitic plutons are homogeneous rocks with an extensive depth reach and are generally of little interest in terms of wider geological research. Given the current state of knowledge and the availability of data, the most practical approach is to prepare two generic synthetic groundwaters, one that corresponds to type Ca-HCO₃ and the other to type Na-HCO₃ so as to cover both basic types of water. While these waters are generally representative for all the candidate sites, minor variations in the chemical compositions of the various waters are inevitable. For example, the Horka site is characterised by an elevated content of magnesium. However, such differences in the chemical composition of the waters of the various sites should not exert a significant impact on the monitored processes and the values obtained for safety analysis purposes. Based on a professional discussion (hosted by SÚRAO on 2 March 2016), the analyses from the Bukov URF and the Rožná mine, both of which are located near the Kraví hora site, were selected for the preparation of the two basic water types. These groundwaters were chosen as the reference waters for further experimental and modelling research purposes.

SGW2 – this water is based on the analysis of groundwater at the Bukov URF (southern part of the Rožná uranium mine, level 12, approx. 600 m below the surface). Its composition represents shallow circulation groundwater in a fracture environment of crystalline rocks of the Bohemian Massif, Ca-HCO₃ type (Červinka and Gondolli 2016), see Tab. 47.

SGW3 – this water is based on the analysis of groundwater at the Rožná Mine (levels 22 to 24, approx. 1000 m below the surface). Its composition represents deep circulation groundwater in a fracture environment of crystalline rocks of the Bohemian Massif; Na-HCO₃ type, see Tab. 47.

Tab. 47 Suggested chemical composition of the SGW2 and SGW3 groundwaters based on the real analysis of groundwater from the Bukov URF and Rožná mine

Water	pH	Concentration (mg l ⁻¹)								TYPE	meq l ⁻¹		Balance
		Na ⁺	K ⁺	Ca ²⁺	Mg ²⁺	F ⁻	Cl ⁻	SO ₄ ²⁻	HCO ₃ ⁻		Cat.	An.	
SGW2	8.2	16.5	2.1	34.6	8.3	-	3.3	21.0	168.7	Ca-HCO ₃	3.18	3.32	-2.10%
SGW3	9.2	89.4	0.7	1.3	0.1	9.9	18.7	10.5	163.5	Na-HCO ₃	3.98	3.95	0.40%

Note: for SGW2, the balance difference can be compensated for by reducing the sulphate concentration, for SGW3 by reducing the sodium concentration

 SÚRAO	Radionuclide migration processes in a crystalline rock environment. Final report.	Evidenční označení:
		SÚRAO TZ 333/2018

7.2 Measurement of the hydrochemical parameters in borehole S-18

A detailed knowledge of the hydrochemical parameters, especially the E_h (ORP) value and the amount of dissolved oxygen in dependence on depth within the rock massif as well as the monitoring of the steady-state conditions in boreholes, is important in terms of experiments planned at the Bukov URF.

Borehole S18 in the ZK-3S adit (Bukov URF, level 12) was selected for the study of the vertical distribution of the measured parameters. The measurement of selected hydrochemical parameters (pH, redox potential (ORP), dissolved oxygen content (LDO), electrical conductivity (EC) and water temperature) was performed at a depth interval of 0–48 m using a MS5 fy OTT multiparametric probe with continuous data recording.

7.2.1 Instrumentation

A Minisonde 5 - MS5 fy OTT multiparametric probe (Fig. 57) was used for the measurement of the hydrochemical parameters. This in-situ probe is particularly suitable for the long-term measurement of electrochemical quantities (dissolved oxygen (LDO), pH, E_h (ORP), electrical conductivity, total dissolved solutes (TDS), temperature and water level). The depth of the probe was determined by a built-in pressure sensor. Due to its size and, especially, its diameter, it is suitable for use in small-diameter boreholes. The probe is intended for both short-term measurements and profiling (direct connection to a computer) and long-term in-situ measurements (the option of suspending the probe in the borehole). The interface between the probe and the computer consisted of a standard RS232, SDI-12, RS485 interface.

Prior to measurement, the Minisonde 5 - MS5 was calibrated to all the measured values by means of WTW standards (O_2 - saturated distilled water with oxygen, pH - standard phthalate buffer: pH = 4 and phosphate buffer: pH = 7, WTW, E_h - ZoBell solution at the given temperature, conductivity - KCl solution at the given temperature). The automatic conversion of the ORP values to the standard hydrogen electrode $E_h(\text{SHE})$ (mV) = ORP (mV) + 197 (mV) was set in the measuring probe. The pressure sensor was calibrated according to the metreage of the embedded probe.



Fig. 57 Minisonde 5 - MS5 fy OTT multiparametric probe, packer with cable bushing

Samples were taken from selected depths by means of a Gigant pump for chemical analysis in the laboratory. The samples were collected in HDPE samplers and the hydrochemical parameters (T, pH, ORP, LDO, electrical conductivity) measured on site using a WTW Multi 3630 IDS device (WTW, Germany). The following electrodes were used for the measurements: an ORP-T 900P platinum electrode (WTW, Germany), a SenTix 940P pH electrode (WTW, Germany) and an FDO 925P oxygen electrode (WTW, Germany). Conductivity and temperature measurements were taken using a TetraCon 925-P electrode (WTW, Germany). Prior to each measurement, calibration was performed on standard solutions, pH (WTW, TEC 4,7,10), ORP (WTW, RH 28 redox-buffer), conductivity (WTW, E-SET Trace 0.01 mol l⁻¹ KCl) and LDO (single-point calibration in 100% oxygen saturated water; the zero point check was performed using a sodium sulphite solution according to DIN EN 25814/ISO 5814).

7.2.2 Measurement procedure

Hydrochemical profiling (0–48 m) was performed in the borehole followed by the recording of steady state measurements at selected depths (3, 5, 10 m) (Tab. 48). Prior to measurement, the probe was embedded at a depth of 0.5 m and left fixed in position for approx. 15 min. The first measurements were taken accompanied by continuous recording during both the insertion and retraction of the probe. The probe was manually activated at a speed of around 0.8 m min⁻¹ with automatic data recording after 1 second. Probe depth calibration checks were performed during measurement.

 SÚRAO	Radionuclide migration processes in a crystalline rock environment. Final report.	Evidenční označení:
		SÚRAO TZ 333/2018

Tab. 48 Overview of the measurements in borehole S18 (ZK3-S)

Profiling (0–48 m)	Steady-state measurement (long-term measurement)	Depth (m)	Notes
8. 8. 2018	8. 8.–12. 9. 2018	5	
12. 9. 2018			Probe removal, not packed
17. 10. 2018	17. 10. –15. 11. 18	10	new packer
15. 11. 2018	15. 11. –13. 12. 18	3	
9. 1. 19			Probe removal, unpacked

Following the profiling process, a water sample was drawn by means of pumping from the selected level, and the probe was then embedded at the selected depth level (3, 5 and 10 m). The small-diameter borehole was packed using a stainless obturator, which allowed for both the sealing of the borehole and access for the cable of the probe (with data download capability). The simple obturator used for the taking of the initial measurements was unfortunately “drowned” due to careless handling by an external contractor and was replaced by a new modified stainless steel packer. The measurement process was terminated after around 1 month and the measurement of the profile was repeated.

7.2.3 Results of the hydrochemical measurement of borehole S-18 (vertical profiling)

Dissolved oxygen content (LDO)

The highest dissolved oxygen content was measured during the first measurement campaign on 8 August 2018, when the borehole was opened (without packing). Oxygen concentration levels of up to around 1.5 mg l⁻¹ were observed (corresponding to 15% saturation) in the subsurface layer. Subsequently, the dissolved oxygen concentration was observed to decrease rapidly. From a depth of around 20 m, the concentration was practically zero (at a probe detection and accuracy limit of 0.1 mg l⁻¹). Following the packing of the borehole, a decrease in the oxygen concentration was observed at the mouth of the well (oxygen content of around 0.2 mg l⁻¹) with a rapid decrease to zero dissolved oxygen content. Slightly higher dissolved oxygen values were measured at a depth of 0–15 m (0.1–0.2 mg l⁻¹) during profiling on 17 October 2018, corresponding to the fact that at that time the borehole had been packed for around 14 days (Fig. 58). Similar developments were reported by Rukavičková et al. (2017).

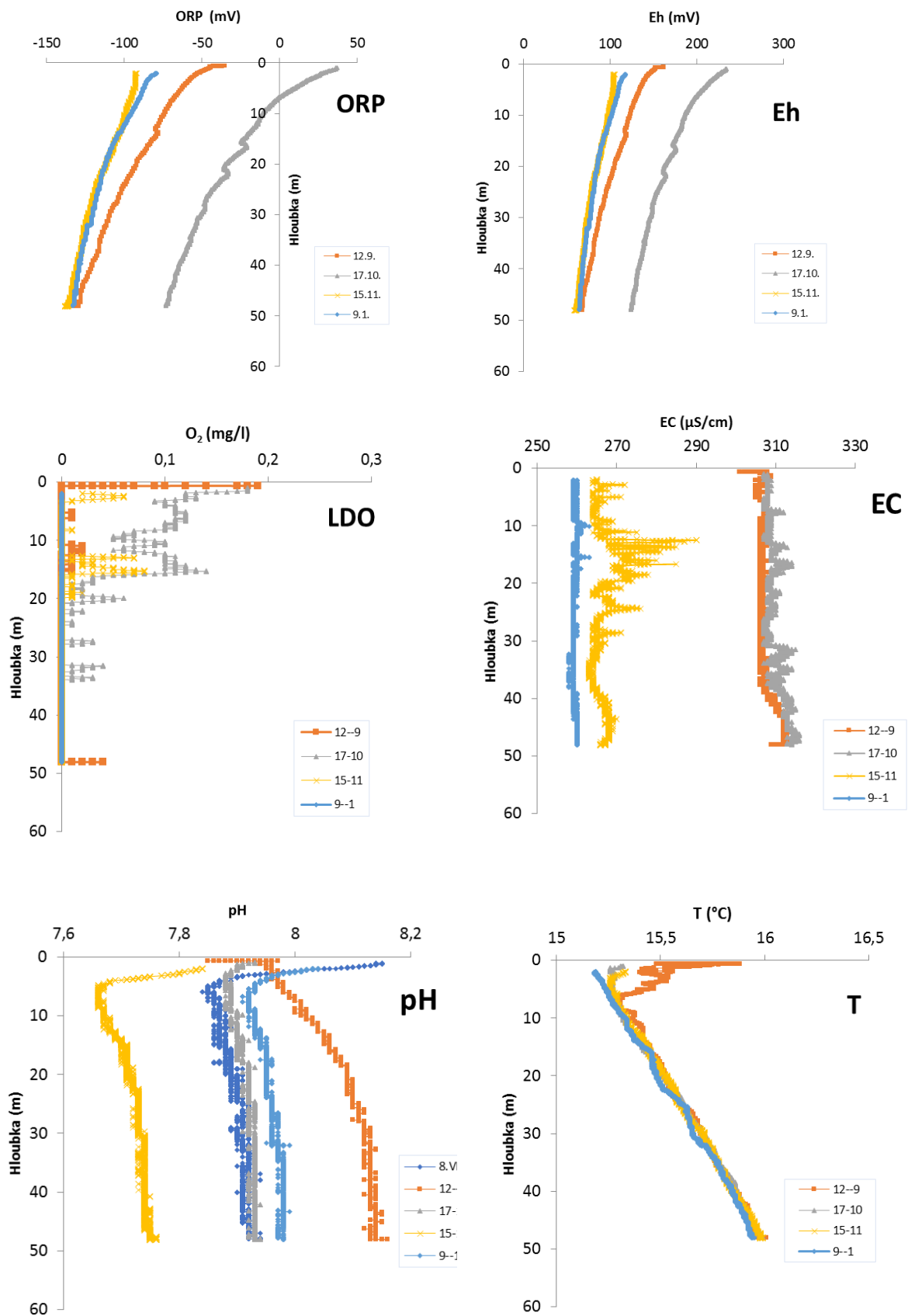


Fig. 58 Parameter development (ORP/Eh, LDO, EC, pH, T) in the S18 borehole (0–48 m)

 SÚRAO	Radionuclide migration processes in a crystalline rock environment. Final report.	Evidenční označení:
		SÚRAO TZ 333/2018

Redox potential (ORP)

The redox potential values in the borehole ranged from -50 mV at its mouth to around -140 mV at a depth of 48 m (Fig. 58). The exception concerned the reading of 17 October, when the values ranged from 36 mV to -74 mV, which was probably caused by testing in the borehole during which an external contractor managed to “drown” the packer, which necessitated the opening of the borehole from 1–17 October 2018. On 4 October, the packer was retrieved thus further influencing the water in the profile. A similar increase was observed with respect to the oxygen content.

Following subsequent packing with a new packer and the sealing of the disturbed section in the upper 30 cm of the borehole, the conditions in the profile stabilised and from 15 November the values ranged from -92 mV to -140 mV.

The redox potential values were based on a normal hydrogen electrode and indicated the qualitative character of the development of E_h with depth.

pH

Most of the measured pH values ranged from 7.8 to 8.1, while higher pH values were measured at the top of the borehole, possibly due to leaching from concrete. The deeper profile stabilised at a value of around 7.9. A graph showing the development of pH with depth is provided in Fig. 58.

Electric conductivity (EC)

The highest conductivity values were recorded in the first months of measurement, at which time the conductivity values in the upper part of the profile were around $330 \mu\text{S cm}^{-1}$ (8 August 2018) with subsequent measurements of around $310 \mu\text{S cm}^{-1}$ (12 September and 17 October 2018). Following the installation of the new packer, which sealed a failure in the top part of the borehole at a depth of 0–35 cm, an overall decrease in conductivity was apparent, eventually attaining a steady state value of around $260 \mu\text{S cm}^{-1}$. A possible explanation related to the sealing of seepage from the concrete at the top of the borehole. This was confirmed by the higher conductivity values recorded in the upper part of the borehole (up to around $523 \mu\text{S cm}^{-1}$) in 2017 prior to sealing (Rukavičková et al. 2017).

Temperature

The temperature development of all the measurements was consistent and the temperature gradient corresponded to $0.016 \text{ }^\circ\text{C m}^{-1}$. Higher temperatures were detected at the mouth of the borehole (temperature influence of the adit environment); at around 4 m depth the temperature was around $15.2 \text{ }^\circ\text{C}$ and at a depth of 48 m the maximum temperature was around $15.94 \text{ }^\circ\text{C}$. The development of temperature is shown in Fig. 58.

7.2.4 Groundwater sampling

Following the measurement of the hydrochemical parameters in the profile, water samples were taken from the studied depths (3 and 10 m) by means of a Gigant pump. In addition, an indicative recharge test was performed following the pumping of the water surface to the

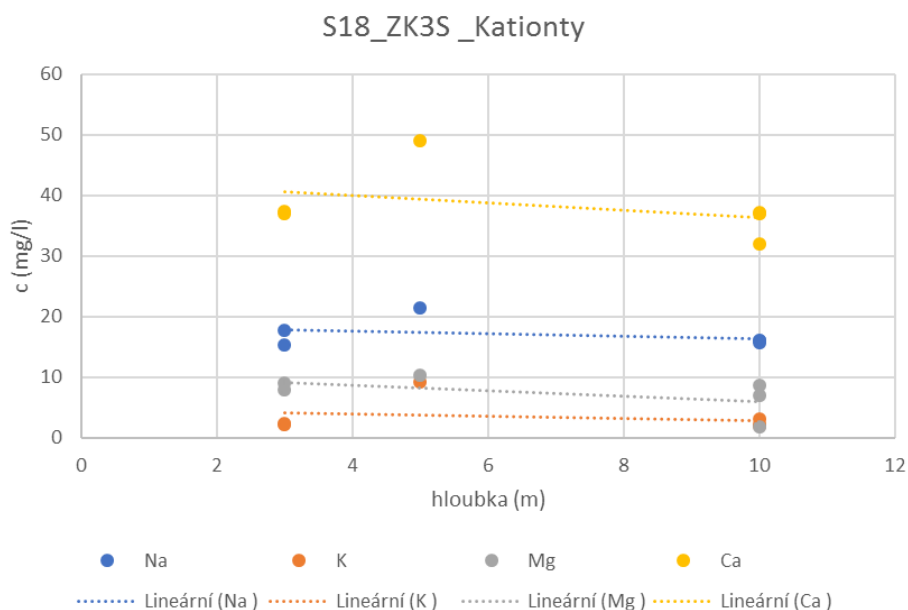
required level and the samples were subjected to the analysis of their hydrochemical parameters. The samples were then transported to the laboratory for analysis. Subsequently, the probe was embedded at the selected depth level, the head of the borehole was sealed with a packer and data recording commenced.

The samples were analysed at the ÚJV Řež laboratories using atomic absorption spectrometry (AAS) on a GBC SavantAA spectrometer. Selected samples from depths of 3 and 10 m were also measured at the ALS a. s. accredited laboratory mainly with respect to $\text{Fe}^{2+}/\text{Fe}^{3+}$ for the determination of the main redox pairs. The results of the analyses of the two laboratories were in good agreement (see Tab. 49).

Tab. 49 Contents of the main cations in samples taken from borehole S-18 (from depths of 3, 5 and 10 m)

Sampling date	Depth (m)	Measured by	Na^+	K^+	Mg^{2+}	Ca^{2+}	Mn^{2+}	Fe	Fe^{2+}	Fe^{3+}
8. 8. 2018	5	UJV (mg l^{-1})	21.43	9.297	10.25	48.99		3.646		
17. 10. 2018	10	UJV (mg l^{-1})	15.66	2.125	1.84	37.05		0.249		
15. 11. 2018	10	UJV (mg l^{-1})	16.01	2.018	8.707	37.21		< LOD		
15. 11. 2018	10	ALS (mg l^{-1})	16.1	3.03	6.96	32	0.008	0.0494	0.944	< 0.010
9. 1. 2019	3	UJV (mg l^{-1})	15.3	2.237	9.04	37.06		0.103		
9. 1. 2019	3	ALS (mg l^{-1})	17.7	2.32	7.94	37.4	0.0042	0.0932	0.713	< 0.010

The values obtained from the samples taken from the various depth levels, i.e. 3, 5 and 10 m were balanced in the profile; only at a depth of 5 m was a slight increase in the contents of the studied elements observed (Fig. 59 and Fig. 60).



 SÚRAO	Radionuclide migration processes in a crystalline rock environment. Final report.	Evidenční označení:
		SÚRAO TZ 333/2018

Fig. 59 Concentrations of Na, K, Mg, Ca in samples from depths of 3.5 and 10 m in borehole S18 (ZK3-S, Bukov URF)

The main anions were measured at ÚJV Řež. The analysis results are shown in Tab. 50 and Fig. 60.

Tab. 50 Content of anions in the samples taken from borehole S-18 (from depths of 3, 5 and 10 m)

Sampling date	Depth (m)	Measured by	Cl ⁻	SO ₄ ²⁻	NO ₃ ⁻	F ⁻	CO ₃ ²⁻	HCO ₃ ⁻
8. 8. 2018	5	UJV (mg l ⁻¹)	10.49	53.56	1.83			
17. 10. 2018	10	UJV (mg l ⁻¹)	6.89	37.87	2.08			
15. 11. 2018	10	UJV (mg l ⁻¹)	6.61	36.21	0.73			
15. 11. 2018	10	ALS (mg l ⁻¹)	6.06	35.60	< 2.0	0.21	0.00	142.00
9. 1. 2019	3	UJV (mg l ⁻¹)	10.15	32.40	0.00	0.21		
9. 1. 2019	3	ALS (mg l ⁻¹)	6.34	34.40	< 2.0	< 0.200	0.00	136.00

The contents of the measured anions (Cl⁻, SO₄²⁻, NO₃⁻, F⁻) were stable and no significant differences in terms of concentration were observed at the various depths (Fig. 60).

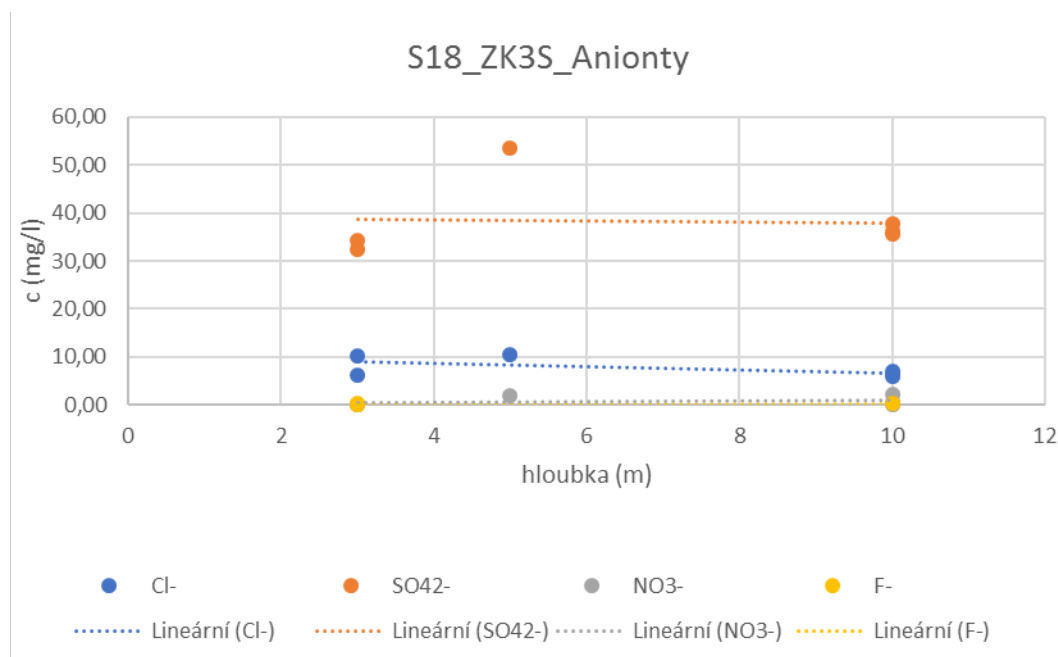


Fig. 60 Concentrations of Cl⁻, SO₄²⁻, NO₃⁻, F⁻ in the S18 borehole at depths of 3, 5 and 10 m

The values recorded for the samples from depths of 3, 5 and 10 m depth corresponded to the values obtained at the Bukov URF. The waters are of the Ca-Na-HCO₃-SO₄ type. No significant

differences in the composition were recorded at the various depth levels. The results of the chemical analysis of the groundwater from borehole S18 are shown in Durov and Piper diagram form (Fig. 61) in comparison with water taken from the Bukov URF (Bukovská et al. 2017).

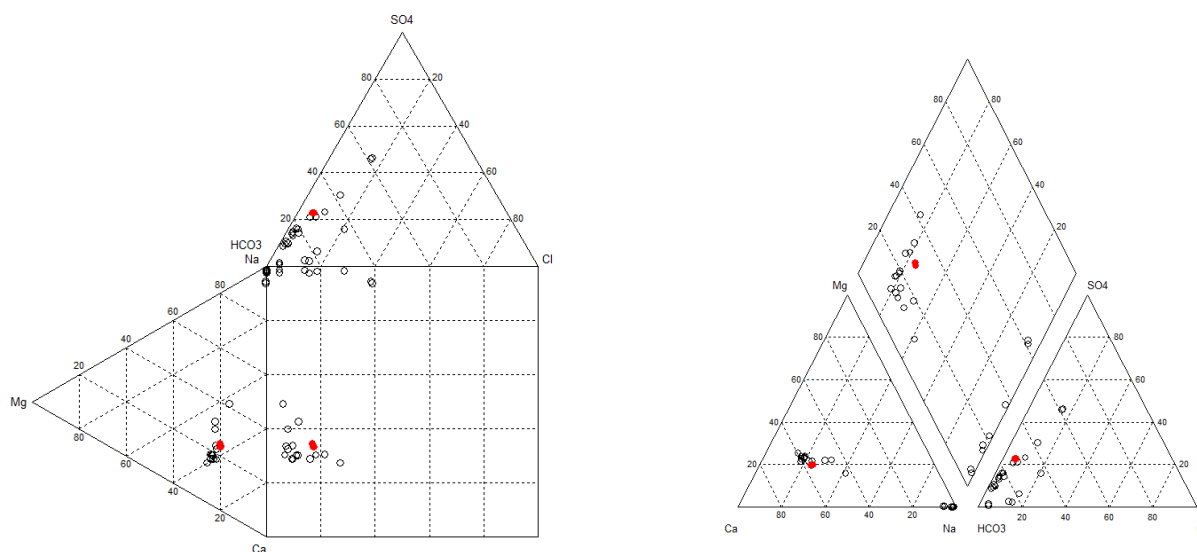


Fig. 61 Results of the chemical analysis of the groundwater from borehole S18 (samples from depths of 3, 5 and 10 m) plotted in the form of Durov and Piper diagrams - red points, grey points - comparative analysis of water from the Bukov URF (Bukovská et al. 2017)

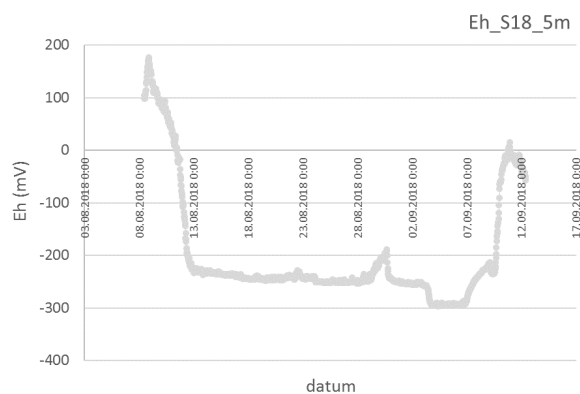
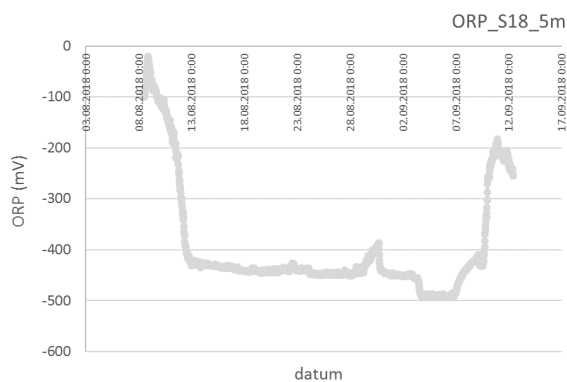
7.2.5 Long-term measurement of the electrochemical quantities in borehole S18 (ZK-3S)

Following the conducting of hydrochemical profiling, the MS 5 probe was embedded at the selected depth level and the head of the borehole was sealed with a mechanical packer (Fig. 62). The resulting values were recorded after 20 minutes. The first measurement was performed at a depth of 5 m and subsequently 10 m. With regard to the experiments planned at the Bukov URF, the originally planned depth of 20 m was replaced by the measurement of the electrochemical parameters in the subsurface layer at a depth of 3 m.



Fig. 62 Mechanical packer for a) borehole sealing b) sealing of the packer cable

The initial measurement was taken at a depth of 5 m (8 August–12 September 2018). The E_h (SHE) values gradually decreased and stabilised (around 4 days) from around 98 mV to -250 mV. The most rapid decreases were observed for the oxygen content, where after around 1 day a decrease in the oxygen content was observed to values close to zero (below the detection limit) and the dissolved oxygen values remained below the detection limit throughout the whole of the measurement period. The pH values ranged between 8 and 8.3. The temperature ($\sim 15.2\text{ }^\circ\text{C}$) and conductivity ($\sim 300\ \mu\text{S cm}^{-1}$) values were stable during the measurement period (Fig. 63).



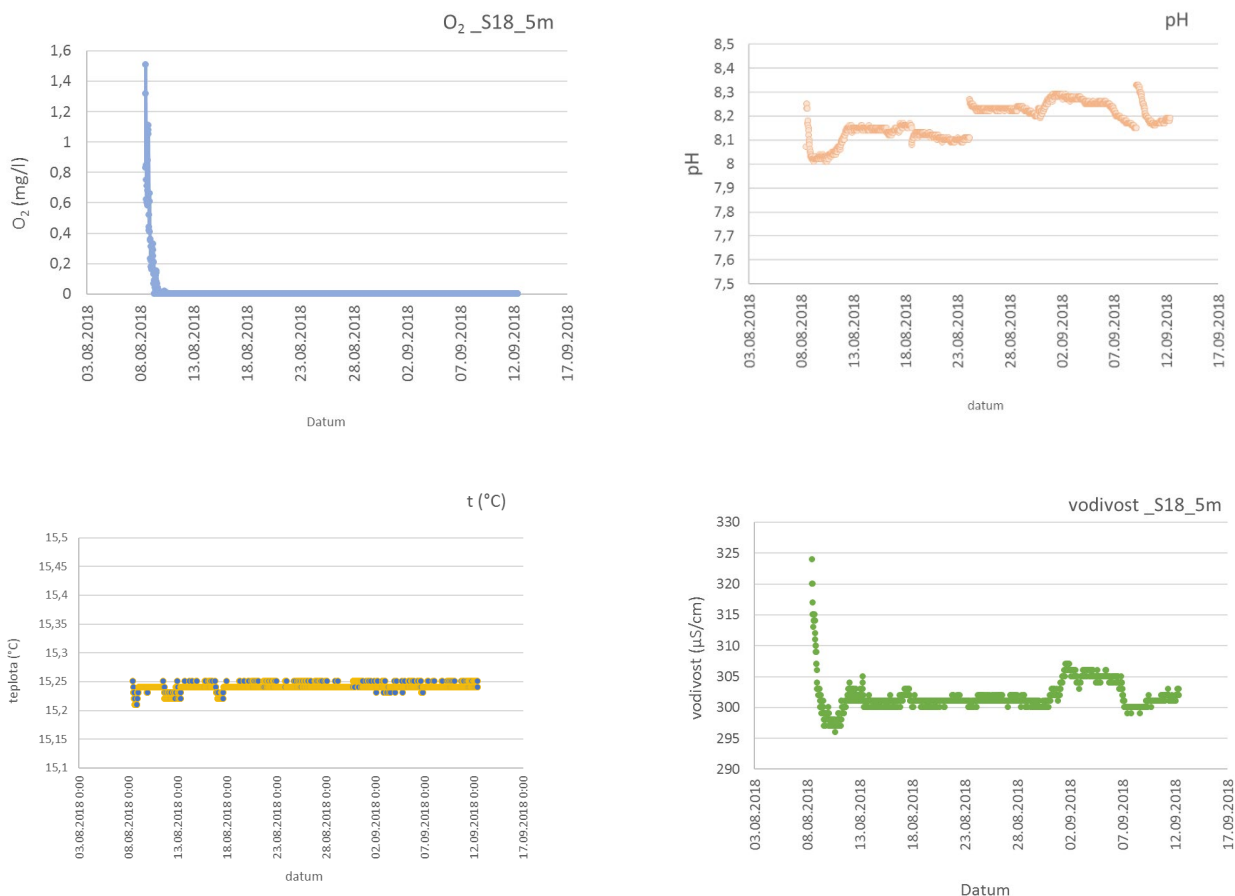


Fig. 63 Measurement of the electrochemical quantities (ORP / E_h , O_2 , pH, temperature, EC) in borehole S18 (ZK3-S) at a depth of 5 m (8. 8.–12. 9. 2018)

Careless handling of the packer by an external contractor led to the accidental release of the packer, which fell to the bottom of the borehole. Since it was considered that this may have partially affected the conditions in the borehole, measurement at a depth of 10 m was shifted to 17 October–15 November 2018. The original packer was replaced by a new packer that was modified so as to allow for the deeper sealing of the device thus preventing the inflow of concrete leachates. The E_h (SHE) values stabilised at around -216 mV within approx. 6 days. The measurement results recorded an apparent increase in the E_h value, which was probably due to drilling work conducted in the adit for the installation of thermometers (3 boreholes) (see SÚRAO information). The dissolved oxygen content decreased very rapidly from a concentration of 0.7 mg l^{-1} to practically zero and remained unchanged throughout the measurement period. The pH values were in the range 8.0–8.25. The development of temperature over time was constant at 15.3°C and the conductivity was stable at around $306 \text{ }\mu\text{S cm}^{-1}$ (Fig. 64).

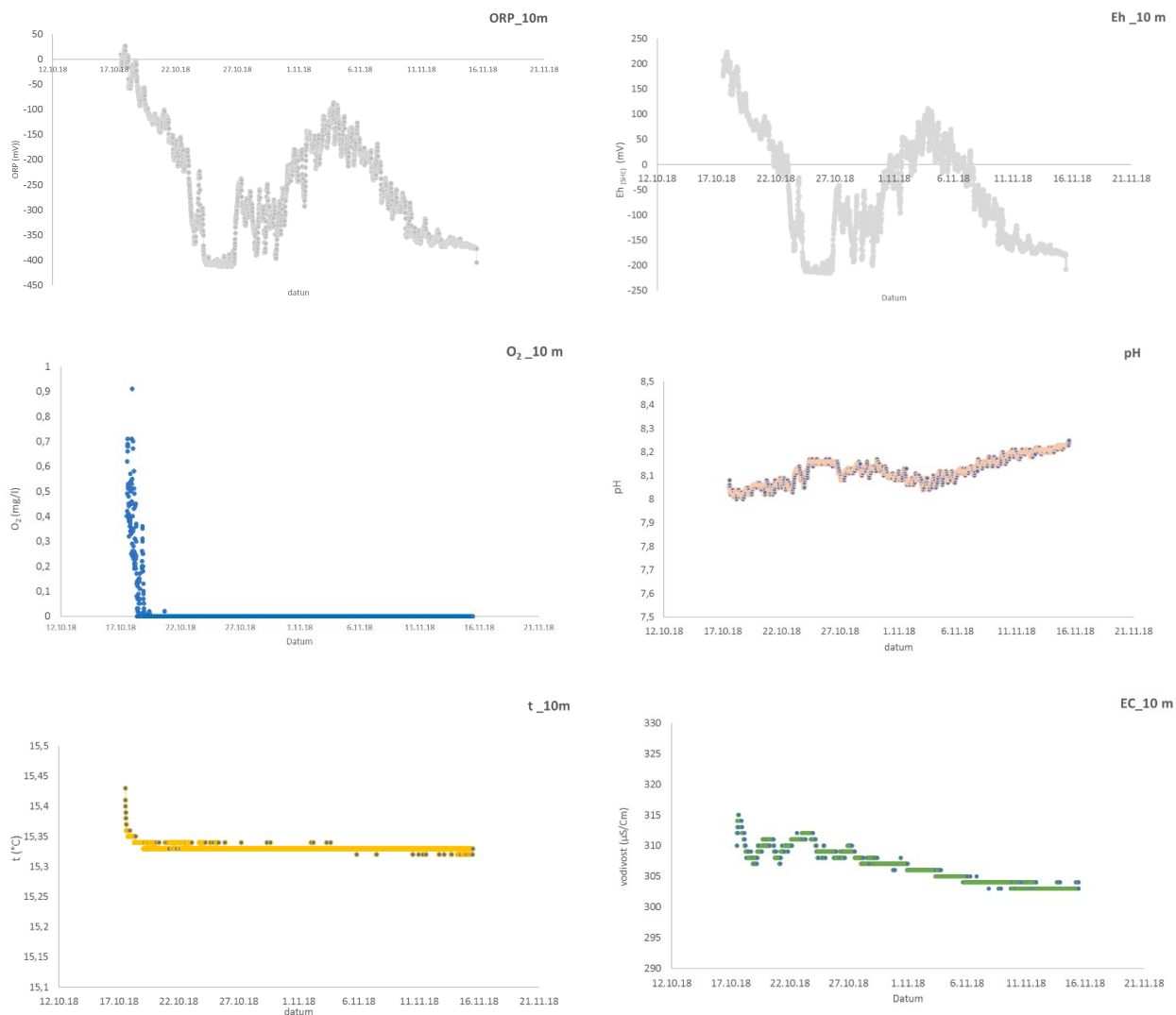


Fig. 64 Measurement of the electrochemical quantities (ORP / E_h , O_2 , pH, temperature, EC) in borehole S18 (ZK3-S) at a depth of 10 m (17. 10.–15. 11. 2018)

Due to the requirement to investigate the E_h conditions in the subsurface layer, the final measurements were taken at a depth of 3 m (15 November–13 December 2018). The development of the various parameters was stable during the measurement process, i.e. no significant changes were observed. The steady state values of E_h (SHE) were around -250 mV. As with the previous measurements, the steady state dissolved oxygen concentrations was below the detection limit of the probe, i.e. $< 0.1 \text{ mg l}^{-1}$. The pH values exhibited the same trend and were in the range 7.9–8.2. The temperature at a depth of 3 m was stable at $\sim 15.2 \text{ }^\circ\text{C}$. The observed water conductivity value of around $265 \text{ } \mu\text{S cm}^{-1}$ was lower than those recorded in the previous measurement campaigns, which probably reflected the lower inflow of concrete leachates (following the installation of the new packer) (Fig. 65).

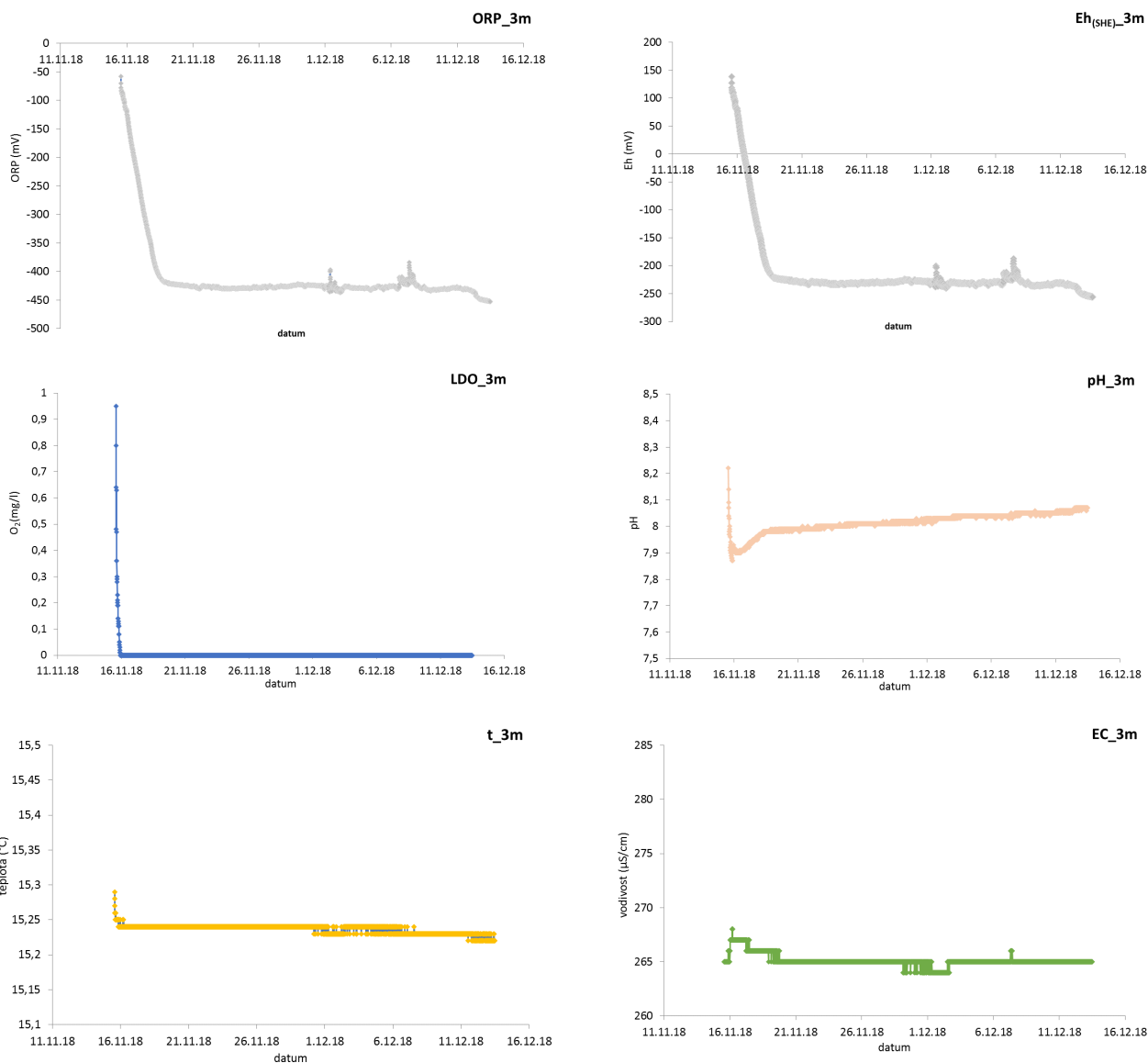


Fig. 65 Measurement of the electrochemical quantities (ORP / E_h , O_2 , pH, temperature, EC) in borehole S18 (ZK3-S) at a depth of 3 m (15. 11.–13. 12. 2018)

7.2.6 Inflows to borehole S18 - recharge tests

Since a weak overflow was observed in the borehole, recharge testing was conducted in order to determine the inflows to its upper part. Prior to testing (8 August 2018), the surface of the water in the borehole was pumped to a level of around 5 m depth. The calculated inflow to the borehole was determined at 363 ml min^{-1} (level increase of 8 cm min^{-1}). A further test was performed on 17 October involving the pumping of the water in the borehole to a level of around 10.6 m depth. In this case, the recharge test indicated an inflow of 418 ml min^{-1} (level increase of 9.22 cm min^{-1}). The slight increase in the yield in the borehole indicated the presence of

groundwater inflow at a depth of between 5 and 10 m. The results of the recharge tests are shown in Fig. 66 and Fig. 67.

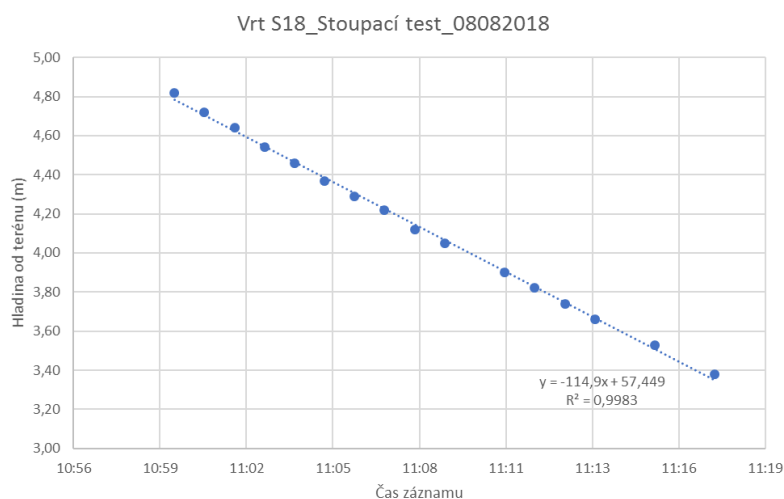


Fig. 66 Development of the recharge test on 8. 8. 2018 at a depth of 5 m

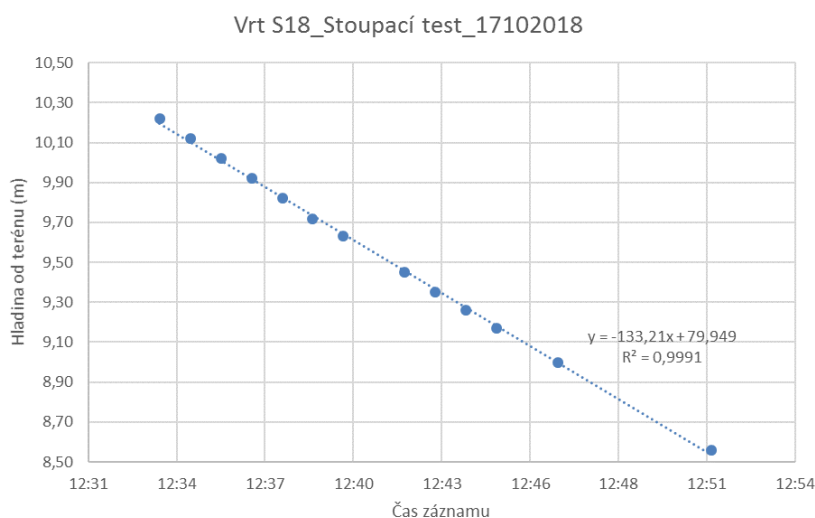


Fig. 67 Development of the recharge test on 17. 10. 2018 at a depth of 10 m

7.2.7 Evaluation

The redox potential values recalculated to the standard E_h (SHE) hydrogen electrode stabilised between -200 to -250 mV at a pH of 8 and a temperature of 15.2 to 15.4°C at the studied depths of 3, 5 and 10 m. In addition, groundwater samples were taken from borehole S-18 in order to determine the main redox pairs (especially Fe^{2+}/Fe^{3+}). While the Fe^{2+} contents were determined in two samples at 0.013 and 0.017 mmol l⁻¹, the Fe^{3+} contents were below the detection limit ($< 2 \cdot 10^{-4}$ mmol l⁻¹). Calculations conducted using the PHREEQC geochemical program (Parkhurst and Appelo 2013) with the phreeqc.dat database indicated that the Fe^{3+}

content should be around $1 \cdot 10^{-8} \text{ mmol l}^{-1}$ for the measured redox potential. The $\text{Fe}^{2+}/\text{Fe}(\text{OH})_3(\text{s})$ redox pair best corresponded to the measured redox potential. The recorded values correspond to those of groundwater from deep rock environments (see Fig. 68).

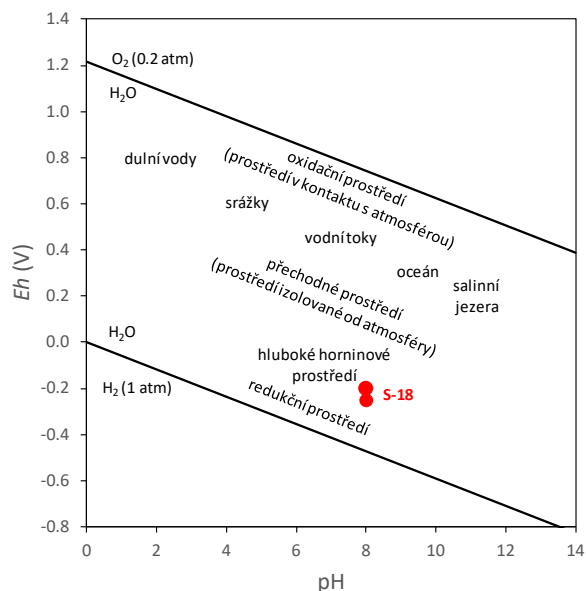
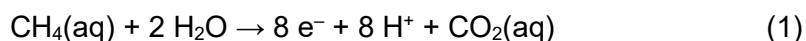


Fig. 68 pH condition and redox potential areas in the natural rock environment, the red values relate to the S-18 borehole

Finally, it was possible to compare an analysis of gases recorded at the BK18 (S-1) sampling point in 2016 (CGS). The partial pressure of carbon dioxide gas was determined at 0.075 and methane at 0.036. Methane plays a major role in reduction reactions in the rock environment and can be expressed by the equation (1):



From the representation of these gases and from equation (1), the oxidation reduction potential was calculated using the Nernst equation at around -300 mV at pH 8.

In general, the measured values were in line with the values determined from the Rožná mine and the Bukov URF, e.g. Červinka et al. (2018).

 SÚRAO	Radionuclide migration processes in a crystalline rock environment. Final report.	Evidenční označení:
		SÚRAO TZ 333/2018

8 Conclusion

This report provides a summary of the results of the determination of the transport parameters of the granitic and metamorphic rocks (and their fractures) from the Bohemian Massif that is considered in the Transport 1 Final Report and, partly, in the Characterisation of the Bukov URF study. It focused primarily on the determination of the sorption and diffusion properties that are important in terms of radionuclide migration and the determination of related properties such as the mineralogical composition, porosity, density and cation exchange capacity, without which the results of the determination of the sorption and diffusion properties would not have adequate informative value.

With concern to the diffusion characteristics (the effective diffusion coefficient D_e), it can be stated that although the samples originated from different sites located throughout the Czech Republic and consisted of different rock types, the diffusion efficiency coefficients obtained lay in a relatively narrow range: for ^3H $(4-10) \cdot 10^{-13} \text{ m}^2 \text{ s}^{-1}$, for ^{36}Cl $(1-10) \cdot 10^{-13} \text{ m}^2 \text{ s}^{-1}$ and for ^{125}I $(1-4) \cdot 10^{-13} \text{ m}^2 \text{ s}^{-1}$; values below $2 \cdot 10^{-13} \text{ m}^2 \text{ s}^{-1}$ were considered to be merely estimates that were on the limit of determination based on the detection limits. Anion exclusion was detected in the metamorphic rock samples that resulted in a lower D_e for the ^{36}Cl and ^{125}I values compared to the ^3H value.

The measurement of the porosity of rocks with a porosity of below 1% is particularly problematic. None of the methods is 100% certain and each method has its advantages and disadvantages. The gravimetric method is strongly dependent on the equipment and procedure employed, while the Hg porosimetry method requires adjustments to the instrumentation and the measurement procedures in order to ensure representative results. The C-14 PMMA method suffers from the potential overestimation of the porosity values due to the low resolution of individual pixels. Moreover, the μDFN model is unable to reliably and comprehensively respond to whether the pore size (aperture) or their interconnection (connectivity) is behind anion exclusion. In such cases, it is always advisable to supplement the measurement of porosity with the study of pore size and interconnection via visualisation methods (e.g. SEM), which are able to quantify the pore network to a sufficient extent.

From the point of view of the sorption behaviour of radionuclides, it can be stated that caesium is strongly sorbed on rock materials, strontium exhibits a slight sorption character and selenite and uranium U(VI) can be classified as non-sorbing radionuclides. The mineralogical composition of the rock samples was an important factor in terms of influencing the behaviour of radionuclides. In the case of the cationic radionuclides Cs(I) and Sr(II), the important sorbents consisted of layered minerals (in this case mica and secondary minerals of the kaolinite type).

In addition to the work with the rock matrix material, the sorption experiments also focused on the sorption of the above-mentioned radionuclides on selected fracture fillings (containing chlorite carbonates and kaolinite), which was supplemented with the application of ^{125}I , ^{36}Cl and Eu nuclides. Here again, it was confirmed that Cs is sorbed most intensively and that Se, U, Cl and U behave as non-absorbing radionuclides under the given conditions due to their occurrence in the anionic form.

With respect to the processing of the results of sorption experiments performed via the batch sorption experimental method, it is important to note that we worked with samples that did not

 SÚRAO	Radionuclide migration processes in a crystalline rock environment. Final report.	Evidenční označení:
		SÚRAO TZ 333/2018

fully correspond to the real environment in the rock mass. Clearly, such experiments involve uncertainties that cannot be controlled unless variables such as the pH are monitored during the sorption experiments and the specific BET surface area measured before and after the conducting of such experiments which, unfortunately, is rarely reported in the literature. Distribution coefficients should not be reported as K_d values normalised to the sample weight, but rather as K_a values normalised to the BET surface area.

In the interest of assuming a conservative approach to the given data, it is appropriate to round down the data for safety assessment purposes by a factor of at least 10 and possibly up to 100 in order to ensure that the retention properties are not overestimated.

The geochemical conditions at the site are very important in terms of the migration of radionuclides in the rock environment, especially the pH and E_h , the O_2 and CO_2 content in the water, the presence of complexing substances, etc. The measurement of the hydrochemical parameters of the groundwater in-situ (Bukov URF) was carried out in the form of hydrochemical profiling and the long-term measurement of parameters for the monitoring of the development of the E_h in an environment corresponding to that of the future DGR. The redox potential measured relative to the standard hydrogen electrode $E_h(SHE)$ ranged from -200 to -250 mV at a pH of around 8 and a temperature of 15.2 to 15.4 °C. The Fe^{2+} content was determined in two samples at 0.013 and 0.017 mmol l⁻¹. However, the Fe^{3+} contents were below the detection limit ($< 2 \cdot 10^{-4}$ mmol l⁻¹). According to the results of calculations in the PHREEQC geochemical program (Parkhurst and Appelo 2013) with the phreeqc.dat database, the Fe^{3+} content should be around $1 \cdot 10^{-8}$ mmol l⁻¹ for the measured redox potential. The redox pair $Fe^{2+}/Fe(OH)_3(s)$ best corresponded to the measured redox potential. The measured values were found to correspond to those of groundwater from a deep rock environment.

 SÚRAO	Radionuclide migration processes in a crystalline rock environment. Final report.	Evidenční označení:
		SÚRAO TZ 333/2018

9 Literature

- ANDERSSON K., ALLARD B. (1983): Sorption of radionuclides on geologic media – A literature survey. I: Fission Products. Report 83-07. – SKB, Stockholm, Sweden.
- AROMAA H., VOUTILAINEN M., IKONEN J., YLI-KAILA M., POTERI A., SIITARI-KAUPPI M. (2019): Through diffusion experiments to study the diffusion and sorption of HTO, ³⁶Cl, ¹³³Ba and ¹³⁴Cs in crystalline rock. *Journal of Contaminant Hydrology*, 222, pp. 101-111.
- BAES C. AND MESMER R. S. (1976): *The Hydrolysis of Cations*. John Wiley & Sons, New York, London, Sydney, Toronto 1976. 489 pp.
- BECKER M., LIPPOLD H. (2016): Complexation and Adsorption of [¹⁵²Eu]Eu to Superplasticizers and Bentonite at Variable Salt Concentrations, 2nd Petrus-OPERA Conference on Radioactive Waste Management and Geological Disposal, 23-24.
- BRUKER AXS (2014): Topas 5. Karlsruhe, Germany.
- BRUKER AXS (2015): Diffrac.Eva, 4.1. Karlsruhe, Germany.
- BUKOVSKÁ Z, VERNER K, BRÁZDA L., BURIÁNEK D., DOBEŠ P., DUDÍKOVÁ SCHULMANNOVÁ P., ERBAN V., FRANĚK J., HALODOVÁ P., HANÁK J., HAVLOVÁ V., HOLEČEK J., JAČKOVÁ I., JELÉNEK J., KAŠPAR V., KOLOMÁ K., KOPAČKOVÁ V., KOUČKA L., KUČERA P., LAUFEK F., LNĚNIČKOVÁ Z., KOČERGINA J., MYŠKA O., NAHODILOVÁ R., NOVOTNÁ I., PERTOLDOVÁ J., RUKAVIČKOVÁ L., SOEJONO I., ŠVAGERA O., TOMEK F., VESELOVSKÝ F., ZUNA M. (2017): Komplexní geologická charakterizace prostorů PVP Bukov, závěrečná zpráva. Technická zpráva č. 191/2017, SÚRAO, Praha, 2017.
- BUŇATOVÁ V., JELÍNEK E., KUČERA J., ŘANDA Z. (1995): Interakce štěpných produktů s horninami. - Zpráva grantu GA ČR 205/93/0702. PřF UK Praha.
- CARBOL P., ENGVIST I. (1997): Compilation of radionuclide sorption coefficients for performance assessment. SKB rapport R-97-13. – SKB, Stockholm, Sweden.
- CRANK J. (1975): *The Mathematics of diffusion*. Second edition. Oxford university press. ISBN 0198533446.
- CRAWFORD J., NERETNIEKS I., MALMSTRÖM M. (2006): Data and uncertainty assessment for radionuclide Kd partitioning coefficients in granitic rock for use in SR-Can calculations. Report R-06-75. – SKB, Stockholm, Sweden.
- ČERNÝ P., DOMEČKA K., MAREK K., KRÍŽOVÁ H., RŮŽIČKA J. (1998): Závěrečná zpráva geologického průzkumu lokality Panské Dubenky, okr. Jihlava. Stavební geologie geotechnika, Praha.
- ČERVINKA R. (2014): Stanovení kationtové výměnné kapacity (CEC) a výměnných kationtů pomocí metody s Cu(II)triethylentetraminem. Certifikovaná metodika. Č.j. SÚJB/ONRV/15452/2014.
- ČERVINKA R. A GONDOLLI J. (2016): Výběr reprezentativních podzemních vod a příprava jejich syntetických ekvivalentů. - TZ 41/2016. SÚRAO, Praha, 122 str
- ČERVINKA R., VEČERNÍK P., KAŠPAR V., VAŠIČEK R. (2018): Kompletní charakterizace bentonitu BCV 2017. Samostatná příloha 3. průběžné zprávy. TZ pro SÚRAO, v procesu schvalování. SÚRAO, Praha, 2018.
- ČERVINKA R., VOPÁLKA D., ADAM R., BRÁZDA L., DRTINOVÁ B., HOFMANOVÁ E., KITNEROVÁ J., RAMEŠOVÁ L., REIMITZ D., ŠIMÚTHOVÁ Z., ŠTAMBERG K., VETEŠNÍK A. (2015): Transport

 SÚRAO	Radionuclide migration processes in a crystalline rock environment. Final report.	Evidenční označení:
		SÚRAO TZ 333/2018

radionuklidů z úložiště / vstupní parametry a procesní modely pro hodnocení transportu radionuklidů přes inženýrské bariéry, 1. průběžná zpráva. Technická zpráva č. 2015/18, SÚRAO, Praha, 2015.

- ČERVINKA R., GONDOLLI J., KLAJMON M., RUKAVIČKOVÁ VENCELIDES Z., ZEMAN J. (2018): chování horninového prostředí / příprava geochemického modelu úložiště – geochemické výpočty a model reakčního transportu, závěrečná zpráva. technická zpráva číslo 271/2018. SÚRAO, Praha, 127 str.
- EBONG F. S., EVANS N. (2011): Sorption of Ni And Eu in a Multi-element System. – J. Mat. Sci. Engin., B1, 504–515.
- FIZ (2015): ICSD Database, Karlsruhe, Germany.
- FR-TI1/367 - Výzkum vlivu mezizrnné propustnosti granitů na bezpečnost hlubinného ukládání do geologických formací a vývoj metodiky a měřicí aparatury (2009–2015)
- GARCÍA-GUTIÉRREZ M., CORMENZANA J. L., MISSANA T., MINGARRO M., MOLINERO J. (2003): Overview of laboratory methods employed for obtaining diffusion coefficients in FEBEX compacted bentonite. – J.of Iberian Geology 32 , 37-53.
- GONDOLLI J., BRYNYCH V., DRTINOVÁ B., HOFMANOVÁ E., VEČERNÍK P., VIDENSKÁ K., VOPÁLKA D. (2013): Výzkum interakčních procesů vybraných radionuklidů s materiály inženýrských bariér, Zpráva 14270, projekt TIP FR-TI1/362, SÚRAO, Praha, 2013.
- HAKANEN M., ERVANNE H., PUUKKO E. (2014): Safety Case for the Disposal of Spent Nuclear Fuel at Oikiluoto. POSIVA 2012-41. – Posiva Oy, Eurajoki, Finland.
- HANÁK J., CHLUPÁČOVÁ M., ONDRA P., HROUDA F., SOSNA K., ŽIŽKA J., KAŠPAREC I., DĚDEČEK P. (2017): Stanovení petrofyzikálních charakteristik horninového prostředí pro území potenciálních lokalit HÚ. Závěrečná zpráva číslo 103/2017, SÚRAO, Praha, 2017.
- HAVLOVÁ V., KOLOMÁ K., BRÁZDA L., RUKAVIČKOVÁ L. (2017): Odhad hodnot transportní charakteristiky krystalinických hornin Českého masivu. - TZ 102/2017. SÚRAO Praha, 2017.
- HAVLOVÁ V., VIDENSKÁ K., GONDOLLI J., MILICKÝ M., GVOŽDÍK L., KRÁLOVCOVÁ J., RUKAVIČKOVÁ L. (2015a): Migrační procesy radionuklidů v prostředí krystalických hornin a migrační parametry hornin Českého masivu. TZ 13/2015. SÚRAO, Praha, 2015.
- HAVLOVÁ V., VIDENSKÁ K., HOFMANOVÁ E., PALÁGYI Š., ŠTAMBERG K., VEČERNÍK P., VOPÁLKA D. (2013): Laboratorní výzkum vybraných vzorků horninového prostředí, Zpráva 14060, projekt TIP FR-TI1/362, SÚRAO, Praha, 2013.
- HELLMUTH K.H., SIITARI-KAUPPI M., LINDBERG A. (1993): Study of porosity and migration pathways in crystalline rocks by impregnation with ¹⁴C-polymethylmethacrylate. J. Contam. Hydrol. 13, 403–418.
- HOFMANOVÁ E. (2018): Diffusion of Anionic Species in Compacted Bentonite. PhD. Thesis. Faculty of Nuclear Science and Physical Engineering, Czech Technical University, Prague, 2018.
- HOLGERSSON S. (2013): Studies on Batch Sorption Methodologies – Eu Sorption Onto Kivetty Granite, Working Report 2013-06.
- IRAOLA A., TRINCHERO P., VOUTILAINEN M., GYLLING B., SELROOS J.-O., MOLINERO J., SVENSSON U., BOSBACH D., DEISSMANN G. (2017): Microtomography-based Inter-Granular Network for the simulation of radionuclide diffusion and sorption in a granitic rock. Journal of Contaminant Hydrology, 207, pp. 8-16.

 SÚRAO	Radionuclide migration processes in a crystalline rock environment. Final report.	Evidenční označení:
		SÚRAO TZ 333/2018

- JAKOB A. (2004): Matrix diffusion for performance assessment - experimental evidence, modelling assumptions and open issues. PSI Report Nr. 04-08.
- KLAJMON M., ČERVINKA R., HAVLOVÁ V., KOLOMÁ K., RUKAVIČKOVÁ L. (2017): Migrační procesy radionuklidů v prostředí krystalických hornin a migrační parametry hornin českého masivu. Tz 104/2017. SÚRAO, Praha, 2017.
- KUVA J., VOUTILAINEN M., KEKÄLÄINEN P., SIITARI-KAUPPI M., TIMONEN J., KOSKINEN L. (2015a): Gas Phase Measurements of Porosity, Diffusion Coefficient, and Permeability in Rock Samples from Olkiluoto Bedrock, Finland. *Transport in Porous Media*, 107 (1), pp. 187-204.
- KUVA J., VOUTILAINEN M., LINDBERG A., PARKKONEN J., SIITARI-KAUPPI M., TIMONEN J. (2015b): Pore and mineral structure of rock using nano-tomographic paging *Materials Research Society Symposium Proceedings*, 1744, pp. 235-240.
- LÖFGREN M. (2004): Diffusive properties of granitic rock as measured by in-situ electrical methods. PhD theses. Department of Chemical Engineering and Technology Royal Institute of Technology (KTH) Stockholm, Sweden
- MELNYK T. W., SKEET A. (1986): An improved technique for determination of rock porosity. – *Can. J. Earth Sci.* 23, 1068 - 1074.
- MÍSAŘ Z. (1983): *Geologie ČSSR I. Český masív*. Praha, 333 str.
- MUURI E., IKONEN J., MATARA-AHO M., LINDBERG A., HOLGERSSON S., VOUTILAINEN M., SIITARI-KAUPPI M., MARTIN A. (2016): Behavior of Cs in Grimsel granodiorite: sorption on main minerals and crushed rock. – *Radiochim. Acta*, 104, 575–582.
- NENONEN V., SAMMALJÄRVI J., JOHANSON B., VOUTILAINEN M., L'HÔPITAL E., DICK P., SIITARI-KAUPPI M. (2018): Porosity distribution in a heterogeneous clay-rich fault core by image processing of ¹⁴C-PMMA autoradiographs and Scanning Electron Microscopy. *MRS Advances*, 3 (21), pp. 1167-1173.
- PALÁGYI Š., VODIČKOVÁ H. (2009A): SORPTION AND DESORPTION OF ¹²⁵I⁻, ¹³⁷Cs⁺, ⁸⁵Sr²⁺ AND ¹⁵²,¹⁵⁴Eu³⁺ ON DISTURBED SOILS UNDER DYNAMIC FLOW AND STATIC BATCH CONDITIONS. *Journal of Radioanalytical and Nuclear Chemistry*, 280, 3-14.
- PALÁGYI Š., VODIČKOVÁ H., LANDA J., PALAGYIOVÁ, LACIOK A. (2009B): MIGRATION AND SORPTION OF ¹³⁷Cs AND ¹⁵²,¹⁵⁴Eu IN CRUSHED CRYSTALLINE ROCKS UNDER DYNAMIC CONDITIONS. *JOURNAL OF RADIOANALYTICAL AND NUCLEAR CHEMISTRY*,. 295, 431 - 441
- PALÁGYI Š., ŠTAMBERG K. (2013): Sorption of ¹²⁵I⁻, ¹³⁷Cs⁺, ⁸⁵Sr²⁺ and ¹⁵²,¹⁵⁴Eu³⁺ during their transport in undisturbed vertical and horizontal soil cores under dynamic flow conditions, *Journal of Radioanalytical and Nuclear Chemistry* 279, 1447-1458,.
- PARKHURST D.L., APPELO C.A.J. (2013): Description of input and examples for PHREEQC version 3—A computer program for speciation, batch-reaction, one-dimensional transport, and inverse geochemical calculations: U.S. Geological Survey Techniques and Methods, book 6, chap. A43, 497 p., available only at z: <http://pubs.usgs.gov/tm/06/a43/>.
- POST J.E., BISH D.L. (1989): Rietveld refinement of crystal structures using powder X-ray diffraction data. In: Bish, D.L. and Post, J.E. (Eds), *Reviews in Mineralogy - Modern Powder Diffraction*, Mineralogical Society of America, 20, 277-308.
- RUKAVIČKOVÁ L., BREITER K., HOLEČEK J., PAČES T., PROCHÁZKA J., HANÁK J., DOBEŠ P., HAVLOVÁ V., VEČERNÍK P., HERCÍK M. (2009): Výzkum vlivu mezizrné propustnosti granitů

 SÚRAO	Radionuclide migration processes in a crystalline rock environment. Final report.	Evidenční označení:
		SÚRAO TZ 333/2018

- na bezpečnost hlubinného ukládání do geologických formací a vývoj metodiky a měřicí aparatury. Etapová zpráva o řešení projektu v roce 2009. Archív společnosti ISATech s.r.o.
- RUKAVIČKOVÁ L., HOLEČEK J., BREITER K., MAŇÁK L., DOBEŠ P., PACHEROVÁ P., PAČES T., HANÁK J., HANŽL P., NAJSER J., HAVLOVÁ V., ZÁRUBA J., BLÁHA V., MYŠKA O., ROJOVSKÝ M. (2011): Výzkum vlivu mezizrnné propustnosti granitů na bezpečnost hlubinného ukládání do geologických formací a vývoj metodiky a měřicí aparatury. Vývoj metodiky terénního výzkumu hydrochemických parametrů na srovnávacích vrtech. – Závěrečná zpráva, 193 s. MS ČGS Praha.
- RUKAVIČKOVÁ ET AL. 2017
- SAMMALJÄRVI J., LINDBERG A., IKONEN J., VOUTILAINEN M., SIITARI-KAUPPI M., KOSKINEN L. (2019): Investigation of mineralogy, porosity and pore structure of Olkiluoto bedrock. Materials Research Society Symposium Proceedings, 1665, pp. 31-37.
- SAMMALJÄRVI J., LINDBERG A., VOUTILAINEN M., IKONEN J., SIITARI-KAUPPI M., PITKÄNEN P., KOSKINEN L. (2017): Multi-scale study of the mineral porosity of veined gneiss and pegmatitic granite from Olkiluoto, Western Finland. Journal of Radioanalytical and Nuclear Chemistry, 314 (3), pp. 1557-1575.

 SÚRAO	Radionuclide migration processes in a crystalline rock environment. Final report.	Evidenční označení:
		SÚRAO TZ 333/2018

- SARDINI, P.; KUVVA; SIITARI-KAUPPI, M.; HELLMUTH, K.-H. (2014): A simplified simulation approach for estimating crack aperture using ¹⁴C-PMMA method. *Journal of Coupled Systems and Multiscale Dynamics*, Volume 2, Number 4, December 2014, pp. 244-255(12).
- SHEPPARD S.C., JOHNSON L.H. (1996): Chlorine-36 in nuclear waste disposal—1. Assessment results for used fuel with comparison to ¹²⁹I and ¹⁴C, *Waste management*, 16, 607-614.
- SIITARI-KAUPPI M. (2002): Development of ¹⁴C-polymethylmethacrylate method for the characterisation of low porosity media. Application to rocks in geological barriers of nuclear waste storage. PhD thesis, Universities of Helsinki and Poitiers.
- SIITARI-KAUPPI M., MARCOS N., KLOBES P., GOEBBELS J., TIMONEN J., HELLMUTH K.H. (2003): The Palmottu Natural Project. Physical Rock Matrix Characterisation. Geological Survey of Finland, Report YST-118.
- SKAGIUS K., NERETNIEKS I. (1986): Porosities and diffusivities of some non-sorbing species in crystalline rocks. *Water Resour. Res.* 22, 389–397.
- SÖDERLUND M., LUSA M., VIRTANEN S., VÄLIMAA I., HAKANEN M., LEHTO J., LAHDENPERÄ A-M. (2014): Distribution Coefficients of Caesium, Chlorine, Iodine, Niobium, Selenium and Technetium on Olkiluoto Soils. Working Report 2013-68. – Posiva Oy, Eurajoki, Finland.
- SÖDERLUND M., VIRKANEN J., HOLGERSSON S., LEHTO J. (2016): Sorption and speciation of selenium in boreal forest soil. – *J. Environ. Radioact.*, 164, 220–231.
- STUMPF S., STUMPF T., WALTHER C., BOSBACH D., FANGHÄNEL T. (2006): Sorption of Cm(III) onto different Feldspar surfaces: a TRLFS study. – *Radiochim. Acta*, 94, 243–248.
- ŠTAMBERG K. (1998): Modelování migračních procesů v životním prostředí. – Vydavatelství ČVUT, Praha.
- TICKNOR K. V., VANDERGRAAF T. T. (1989): Radionuclide sorption on primary and fracture-filling minerals from the East Bull Lake pluton, Massey, Ontario, Canada. – *Appl. Geochem.*, 4, 163–176.
- VAN LOON L. R., SOLER J. M., JAKOB A., BRADBURY M. H. (2003): Effect of confining pressure on the diffusion of HTO, ³⁶Cl- and ¹²⁵I- in a layered argillaceous rock (Opalinus Clay): diffusion perpendicular to the fabric. *Applied Geogemistry* 18, 1653-1662.
- VOKÁL A., HAVLOVÁ V., HERCÍK M., LANDA J., LUKIN D., VEJSADA J. (2009): Aktualizace referenčního projektu hlubinného úložiště radioaktivních odpadů v hypotetické lokalitě. I. etapa - Analýza vstupních předpokladů řešení. 2.dílčí zpráva – Bezpečnostní aspekty a screeningové výpočty. - ÚJV Řež, a.s. pro SÚRAO.
- VOUTILAINEN M., KEKÄLÄINEN P., POTERI A., SIITARI-KAUPPI M., HELARIUTTA K., ANDERSSON P., NILSSON K., BYEGÅRD J., SKÅLBERG M., YLI-KAILA M., KOSKINEN L. (2019a): Comparison of water phase diffusion experiments in laboratory and in situ conditions. *Journal of Hydrology*, 575, pp. 716-729.
- VOUTILAINEN M., MIETTINEN A., SARDINI P., PARKKONEN J., SAMMALJÄRVI J., GYLLING B., SELROOS J.-O., YLI-KAILA M., KOSKINEN L., SIITARI-KAUPPI M. (2019b): Characterization of spatial porosity and mineral distribution of crystalline rock using X-ray micro computed tomography, C-14-PMMA autoradiography and scanning electron microscopy. *Applied Geochemistry*, 101, pp. 50-61.
- VOUTILAINEN M., KEKÄLÄINEN P., SIITARI-KAUPPI M., SARDINI P., MUURI E., TIMONEN J., MARTIN A. (2017): Modeling Transport of Cesium in Grimsel Granodiorite With Micrometer Scale

 SÚRAO	Radionuclide migration processes in a crystalline rock environment. Final report.	Evidenční označení:
		SÚRAO TZ 333/2018

Heterogeneities and Dynamic Update of Kd. *Water Resources Research*, 53 (11), pp. 9245-9265.

VOUTILAINEN M., LAMMINMÄKI S., TIMONEN J., SIITARI-KAUPPI M., BREITNER D. (2009): Physical rock matrix characterization: Structural and mineralogical heterogeneities in granite. *Materials Research Society Symposium Proceedings*, 1124, pp. 555-560.

VOUTILAINEN M., SAMMALJÄRVI J., MUURI E., DONNARD J., DUVAL S., SIITARI-KAUPPI M. (2018): Digital autoradiography on C-14-labelled PMMA impregnated rock samples using the BeaverTM. *MRS Advances*, 3 (21), pp. 1161-1166.

VOUTILAINEN M., SIITARI-KAUPPI M., SARDINI P., LINDBERG A., TIMONEN J. (2012): Pore-space characterization of an altered tonalite by X-ray computed microtomography and the ¹⁴C-labeled-polymethylmethacrylate method. *Journal of Geophysical Research: Solid Earth*, 117 (1), art. no. B01201.

 SÚRAO	Radionuclide migration processes in a crystalline rock environment. Final report.	Evidenční označení:
		SÚRAO TZ 333/2018

10 Appendices

Appendix 1 Overview of the results of the determination of porosity and density via the water saturation method for samples from the sites

Tab. 51 Results of the determination of the porosity (%) and density of the samples from the candidate sites

Sample code	Porosity (%)	Bulk density (kg m ⁻³)	Mineralogical density (kg m ⁻³)	Site	Rock	Sampling point
BT8-1	0.58	2646	2661	110 Březový potok	amph. - biot. granodiorite	Defurovy Lažany
BT8-2	0.61	2649	2665	110 Březový potok	amph. - biot. granodiorite	Defurovy Lažany
BT8-3	0.59	2647	2663	110 Březový potok	amph. - biot. granodiorite	Defurovy Lažany
BT3-1	0.62	2653	2670	110 Březový potok	amph. - biot. granodiorite	Defurovy Lažany
BT3-2	0.62	2647	2663	110 Březový potok	amph. - biot. granodiorite	Defurovy Lažany
BT3-3	0.60	2651	2667	110 Březový potok	amph. - biot. granodiorite	Defurovy Lažany
TIV1_68A	0.25	2624	2631	120 Čertovka	coarse-grained biot. granite	Tis u Blatna
TIV1_68C	0.26	2634	2641	120 Čertovka	coarse-grained biot. granite	Tis u Blatna
TIV_90A	0.24	2616	2622	120 Čertovka	coarse-grained biot. granite	Tis u Blatna
TIV_90B	0.27	2614	2621	120 Čertovka	coarse-grained biot. granite	Tis u Blatna
TIV_90C	0.26	2617	2624	120 Čertovka	coarse-grained biot. granite	Tis u Blatna
TG3-1	0.38	2634	2644	120 Čertovka	coarse-grained biot. granite	Tis u Blatna
TG3-2	0.44	2628	2640	120 Čertovka	coarse-grained biot. granite	Tis u Blatna
TG3-3	0.49	2623	2636	120 Čertovka	coarse-grained biot. granite	Tis u Blatna
D2-2-1	0.59	2605	2620	130 Čihadlo	granite	Deštná

D2-2-2	0.59	2609	2624	130 Čihadlo	granite	Deštná
D2-2-3	0.59	2595	2611	130 Čihadlo	granite	Deštná
D2-1-4	0.60	2607	2622	130 Čihadlo	granite	Deštná
D2-1-5	0.60	2605	2620	130 Čihadlo	granite	Deštná
PZV1_97A	0.39	2743	2754	140 Horka	amph. - biot. melasyenite	Pozďátky
PZV1_90A	0.37	2774	2784	140 Horka	amph. - biot. melasyenite	Pozďátky
PZV1_90B	0.34	2749	2759	140 Horka	amph. - biot. melasyenite	Pozďátky
PZV1_90C	0.38	2752	2762	140 Horka	amph. - biot. melasyenite	Pozďátky
S6-1	0.51	2791	2805	140 Horka	amph.+biot granite - syenite	Oslavička
S6-2	0.57	2790	2806	140 Horka	amph.+biot granite - syenite	Oslavička
S6-3	0.62	2754	2771	140 Horka	amph.+biot granite - syenite	Oslavička
GC3-1	0.87	2610	2633	150 Hrádek	Čeřínek granite	Bromberg
GC3-2	0.82	2613	2634	150 Hrádek	Čeřínek granite	Bromberg
GC3-3	0.83	2601	2623	150 Hrádek	Čeřínek granite	Bromberg
GB2-1	0.90	2596	2619	150 Hrádek	muscovite-biotitic granite /granodiorite	Boršov
GB2-2	0.91	2599	2623	150 Hrádek	muscovite-biotitic granite /granodiorite	Boršov
GB2-3	0.87	2604	2627	150 Hrádek	muscovite-biotitic granite /granodiorite	Boršov
GB4-1	0.85	2593	2615	150 Hrádek	muscovite-biotitic granite /granodiorite	Boršov
GB4-2	0.89	2598	2622	150 Hrádek	muscovite-biotitic granite /granodiorite	Boršov
GB4-3	0.91	2586	2610	150 Hrádek	muscovite-biotitic granite /granodiorite	Boršov
TT6-1	0.73	2738	2758	160 Magdaléna	syenite	Klokoty -tábor
TT6-2	0.67	2743	2761	160 Magdaléna	syenite_	Klokoty -tábor
TT6-3	0.70	2744	2763	160 Magdaléna	syenite_	Klokoty -tábor

 SÚRAO	Radionuclide migration processes in a crystalline rock environment. Final report.			Evidenční označení:	
				SÚRAO TZ 333/2018	

GRB-1-1	0.33	2635	2644	170 Kraví hora	granulite	Dolní Bory
GRB-1-2	0.35	2632	2632	170 Kraví hora	granulite	Dolní Bory
GRB-2-1	0.36	2636	2646	170 Kraví hora	granulite	Dolní Bory
GRB-2-2	0.36	2636	2646	170 Kraví hora	granulite	Dolní Bory
GRB-3-1	0.35	2637	2646	170 Kraví hora	granulite	Dolní Bory
GRB-3-2	0.36	2628	2638	170 Kraví hora	granulite	Dolní Bory
GRB-3-3	0.34	2630	2639	170 Kraví hora	granulite	Dolní Bory
G5-1	0.60	2641	2657	170 Kraví hora	biotitic granulite	Moravské Pavlovice
G5-2	0.46	2650	2662	170 Kraví hora	biotitic granulite	Moravské Pavlovice
G5-3	0.45	2646	2658	170 Kraví hora	biotitic granulite	Moravské Pavlovice
PDV1_89A	0.41	2620	2631	Panské Dubenky	porphyritic two-mica granite	Panské Dubenky
PDV1_89B	0.4	2620	2630	Panské Dubenky	porphyritic two-mica granite	Panské Dubenky
PDV1_89C	0.41	2609	2620	Panské Dubenky	porphyritic two-mica granite	Panské Dubenky
PDV1_97A	0.42	2617	2628	Panské Dubenky	porphyritic two-mica granite	Panské Dubenky
PDV1_30A	0.84	2601	2623	Panské Dubenky	porphyritic two-mica granite	Panské Dubenky
PDV1_30B	0.83	2605	2627	Panské Dubenky	porphyritic two-mica granite	Panské Dubenky
PDV1_51A	0.76	2601	2620	Panské Dubenky	porphyritic two-mica granite	Panské Dubenky
PDV1_51B	0.81	2601	2621	Panské Dubenky	porphyritic two-mica granite	Panské Dubenky
PDV1_72A	0.52	2616	2630	Panské Dubenky	porphyritic two-mica granite	Panské Dubenky
PDV1_79A	0.46	2624	2636	Panské Dubenky	porphyritic two-mica granite	Panské Dubenky

Overview of the results of the determination of porosity and density via the application of the water saturation method on samples from the Bukov URF - 170 Kraví Hora site (Tab. 52).

 SÚRAO	Radionuclide migration processes in a crystalline rock environment. Final report.	Evidenční označení:
		SÚRAO TZ 333/2018

Tab. 52 Results of the determination of the porosity (%) and density of samples from the Bukov URF - 170 Kraví Hora site

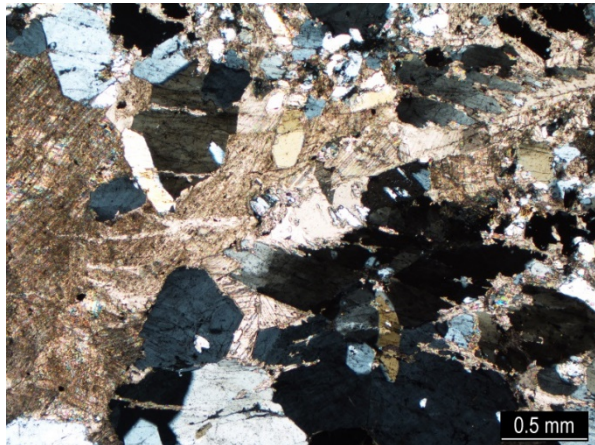
Sample code	Porosity %	Bulk density (kg m ⁻³)	Mineralogical density (kg m ⁻³)	Rock
S3-3/1	0.29	2895	2904	Migmatized amphibolic amphibolite
S3-3/2	0.26	2894	2902	Migmatized amphibolic amphibolite
S3-3/3	0.31	2893	2902	Migmatized amphibolic amphibolite
S3-4/1	0.42	2866	2878	Banded amphibolic gneiss with biotite
S3-4/2	0.33	2810	2819	Banded amphibolic gneiss with biotite
S3-4/3	0.39	2788	2799	Banded amphibolic gneiss with biotite
S4-3/1	0.30	2809	2818	Amph. gneiss, recrystallised
S4-3/2	0.23	2799	2805	Amph. gneiss, recrystallised
S4-3/3	0.28	2794	2801	Amph. gneiss, recrystallised
S4-2/1	0.18	2722	2727	Migmatite, Leukosome
S4-2/3	0.14	2716	2720	Migmatite, Leukosome
S4-2/4	0.18	2726	2731	Migmatite, Leukosome
S4-4/2	0.45	2937	2950	Amphibolite
S4-4/3	0.58	2889	2906	Amphibolite

 SÚRAO	Radionuclide migration processes in a crystalline rock environment. Final report.	Evidenční označení:
		SÚRAO TZ 333/2018

 SÚRAO	Radionuclide migration processes in a crystalline rock environment. Final report.	Evidenční označení:
		SÚRAO TZ 333/2018

Appendix 2 Petrographic description of the fracture and altered rock samples

Sample: ZU_2_13m (ZK213m) carbonate-quartz hydrothermal vein (thickness of 25 mm)	
Description: hydrothermal vein	
Cutting orientation: perpendicular to the edge vein	
Rock: carbonate-quartz hydrothermal vein (thickness of 25 mm)	
Construction: hypidiomorphic, in places cataclastic	
Grain size: medium grained (1-3 mm)	
<p>Description: The vein is composed of idiomorphic to hypidiomorphic quartz crystals and xenomorphic carbonate crystals. The edges feature a substantial zone of up to 1 mm thick consisting of fine-grained calcite, quartz and chlorite; moreover, this zone is annealed by coarse-grained quartz crystals surrounded by carbonate. Sometimes the quartz features undulose extinction. Carbonate grains often fill the voids between the crystallised quartz and are significantly doubled. The deformation bending of the lamellae is noticeable locally in the carbonates. Sometimes the carbonates may be penetrated by younger carbonate veins. The quartz crystals and carbonates contain abundant primary-secondary to secondary fluid inclusions. In rare cases, fan-shaped chlorite aggregates can be observed in the carbonates or on the contact between quartz and carbonate crystals. Larger amounts of chlorite in association with muscovite and opaque minerals are present at the edge of the vein in contact with the surrounding rock.</p>	
<p>Secondary transformations and alterations: The vein is locally affected by deformation that manifested itself via the crushing of quartz crystals. During deformation the carbonates mostly behaved plastically, but in places they have been penetrated by small veins of carbonate (up to 0.01 mm).</p>	
	<p><i>The edge of the carbonate-quartz hydrothermal veins, quartz crystals that abundantly close primary-secondary to secondary fluid inclusions and have been disrupted by younger fractures can easily be observed. The quartz is surrounded by calcite and a zone containing fan-shaped chlorite aggregates near the vein edge (PPL) is visible on the left side of the image.</i></p>



Predominantly plastically deformed carbonate and brittle-deformed quartz have been penetrated by calcite veins (XPL).

Sample: S1_40.3m (muscovite-biotite leucogranite)

Description: unaltered rock mass; the described sample is limited on both sides by areas covered with chlorite (probably a vein with a thickness of around 3 cm)

Cutting orientation: perpendicular to the vein orientation

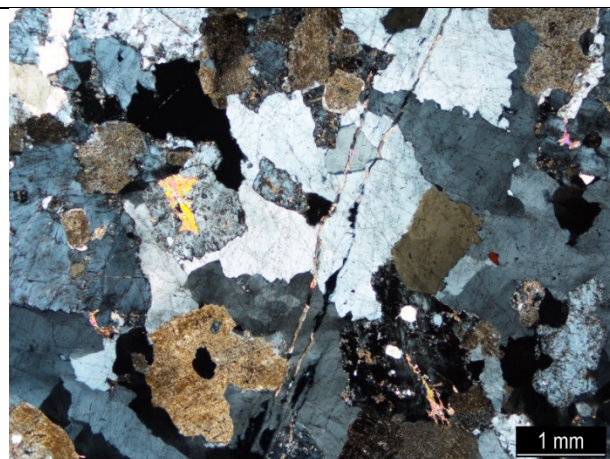
Rock: muscovite-biotite leucogranite

Construction: hypidiomorphic

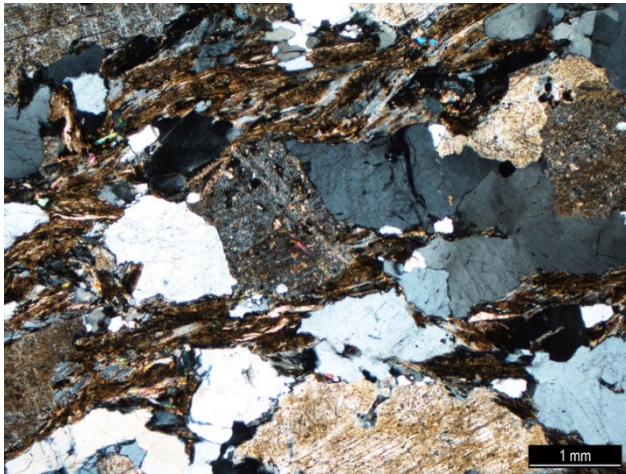
Grain size: medium grained (1-3 mm)

Description: The leucogranite is mainly composed of hypidiomorphic plagioclase (31 mod.%), hypidiomorphic to xenomorphic potassium feldspar (29 mod.%) and xenomorphic quartz (26 mod.%). The biotite (8 mod.%) is almost completely replaced by chlorite and occurs mainly at the edges of the vein. The quartz extringuishes undulosely and contains abundant secondary fluid inclusions. Small muscovite flakes (6 mod.%) appear together with biotite or are suppressed by feldspar. The accessory minerals consist of apatite, zirconium and opaque minerals.

Secondary transformations and alterations: The plagioclase is affected by sericitisation and kaolinisation. These transformations did not affect the albite rims around some of the plagioclases. Biotite is often oriented parallel to the vein edge and is completely replaced by chlorite or affected by baueritisation. Conversions to clay minerals are also abundant. Minerals such as plagioclase and biotite are sometimes suppressed by carbonates. The leucogranite is fragmented by a network of sub-parallel fractures that are oriented perpendicular to the vein edge. These fractures are often healed with carbonate (the thickness of the carbonate veins does not usually exceed 0.01 mm). Secondary carbonate occurs in the form of small grains localised along the edges and cleavage micro fractures of the plagioclase.



Leucogranite penetrated by thin carbonate veins and, in places, secondary muscovites in altered plagioclase (XPL) are apparent.



Intensely hydrothermally altered biotite, converted to a mixture of chlorite, clay minerals and carbonate. The plagioclases are clouded by clay minerals and are sericitised (XPL).

Sample: S1_87.8m (migmatitised biotite gneiss)

Description: the migmatitised biotite gneiss is locally disturbed by chlorite shear zones

Cutting orientation: perpendicular to the foliation

Rock: migmatitised biotite gneiss

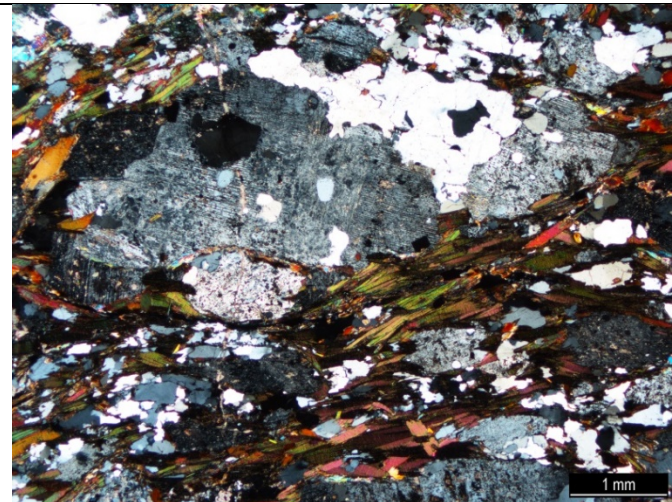
Construction: lepido-granoblastic

Grain size: medium grained (1-2 mm)

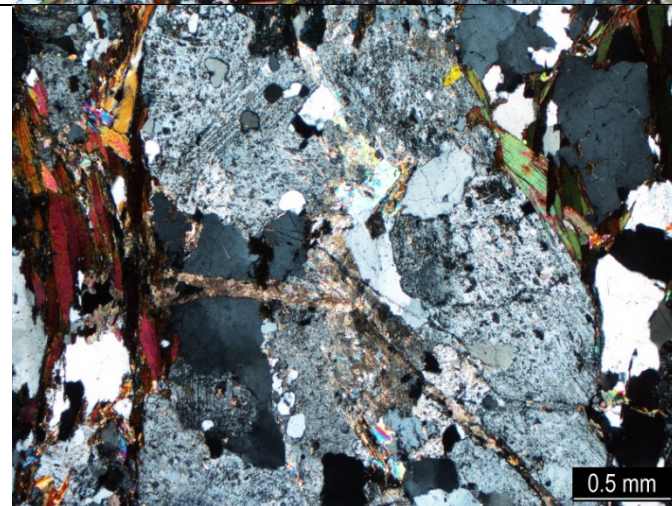
Description: The studied sample represents the biotite-rich position of migmatite. The rock contains hypidioblastic plagioclase, hypidioblastic to xenoblastic potassium feldspar, xenoblastic quartz and flakes of biotite. The metamorphic foliation is defined by the preferred biotite arrangement. The biotite is free of significant changes and contains pleochroic grains around radioactive minerals (zircon).

Muscovite is also present in the accessory volume (often suppressing feldspars). The plagioclases often occlude oval quartz inclusions as well as (rarely) xenomorphic garnets. Apatite, monazite and zircon are present as accessory minerals.

Secondary transformations and alterations: The plagioclase and potassium feldspar are affected by poor sericitisation. There are rare occurrences of 0.03 mm thick carbonate veins which break through the rock perpendicular to the foliation. Carbonate also suppresses the plagioclase, especially near to calcite veins. Overall, the degree of alteration of this sample is relatively low.



Metamorphic foliation is defined by the preferred biotite arrangement (XPL).



Sericitised plagioclase penetrated by a carbonate vein (XPL).

Sample: S1_80.6m

Description: The stromatitic migmatite contains up to 0.4 cm thick leucosome lenses; however, melanosome bands, usually several mm thick, dominate.

Cutting orientation: perpendicular to the foliation

Rock: biotitic migmatite

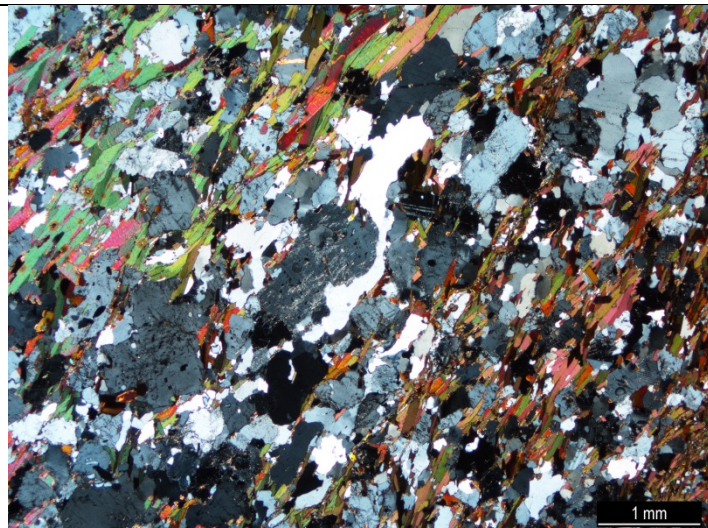
Construction: lepto-granoblastic

Grain size: medium grained (1-2 mm)

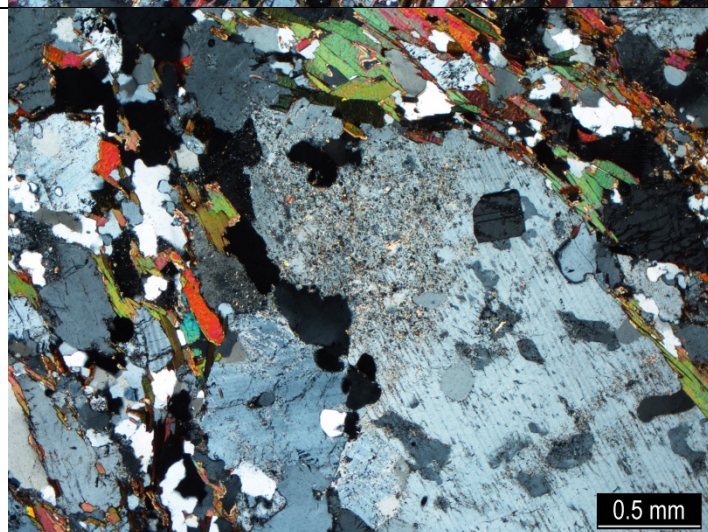
Description: Biotite is represented along with plagioclase and quartz in dark melanosome positions. The biotite is free of secondary transformations and contains pleochroic grains around radioactive minerals. Leucosome is sharply separated from the melanosome and hypidioblastic plagioclase (sometimes in the form of larger porphyroblasts of up to 2 mm), hypidioblastic to xenoblastic potassium feldspar (sometimes with minor inclusions

of plagioclase and quartz) and xenoblastic quartz prevail within it. Larger flakes of secondary muscovite appear rarely. Apatite, monazite and zirconium are present as accessory minerals.

Secondary transformations and alterations: Plagioclase and potassium feldspar are affected by poor sericitisation, which affects only some parts of the grain. Carbonate coatings (up to 0.01 mm thick) appear rarely on plagioclase cleavage micro cracks.



Contact between the melanosome and the leucosome (XPL).



Weakly sericitised plagioclase (XPL).

Sample: S8_47.3m

Description: massive dark rock strongly affected by alteration

Cutting orientation: multi-directionally grained rock

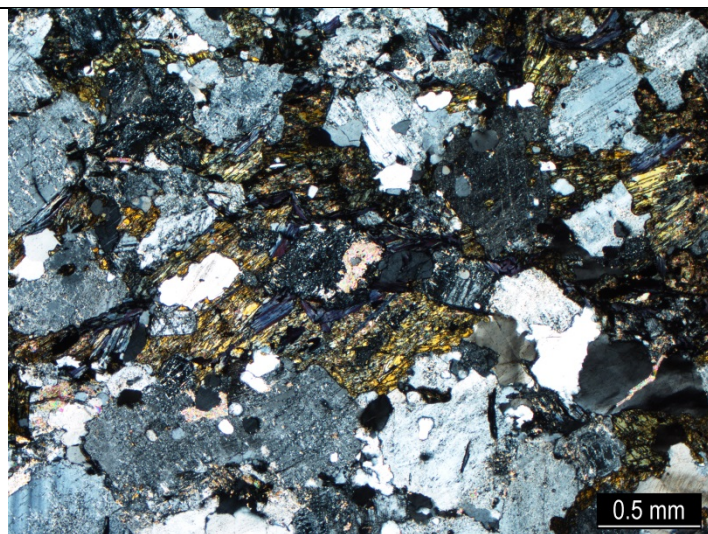
Rock: biotitic amphibolite (apparently located in migmatite)

Construction: nemato-granoblastic

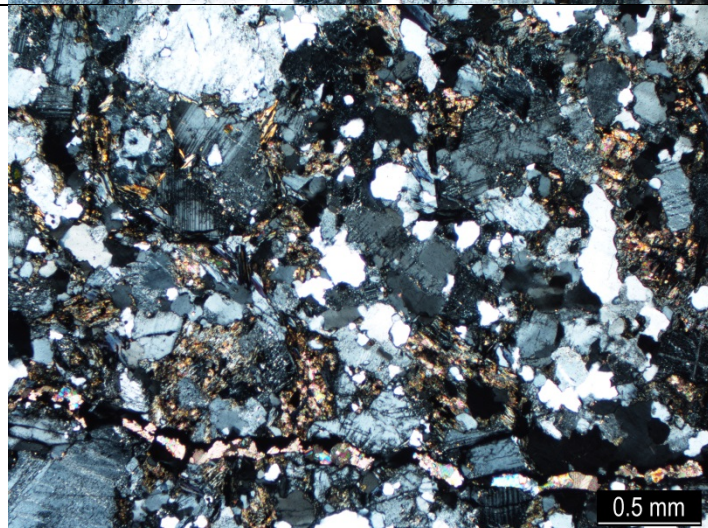
Grain size: medium grained (1-2 mm)

Description: The rock consists of amphibole, plagioclase and biotite. All these minerals are significantly affected by secondary changes. The plagioclase is hypidioblastic to xenoblastic and polysynthetically doubled. Xenoblastic quartz is relatively abundant. Idioblastic to hypidioblastic amphibole is sealed by minor plagioclase inclusions. Accessory minerals consist of apatite and opaque minerals.

Secondary transformations and alterations: The plagioclases are affected by intensive sericitisation. Biotite flakes have been replaced by chlorite. Moreover, amphibole has often been partially or completely replaced by chlorite (sometimes together with calcite). Hairline micro fractures/cracks filled with calcite are present locally, and calcite is also crystallised in places as fine grains at the edges of plagioclase crystals or along cleaved micro fractures/cracks of plagioclase.



Amphibole is partially suppressed by chlorite, and the plagioclases are sericitised and clouded by clay minerals (XPL).



A calcite vein intrudes upon chlorite and sericitised plagioclase (XPL).

Sample: BZ_317_P

Description: massive dark rock containing up to 3 mm-thick hydrothermal carbonate veins

Cutting orientation: perpendicular to the foliation

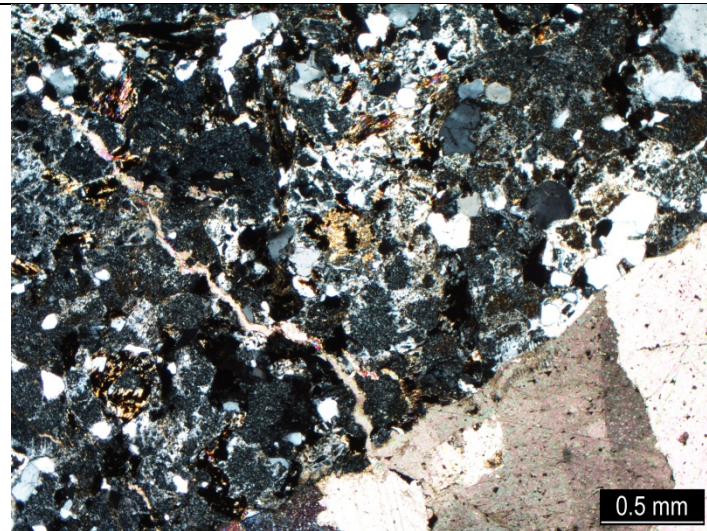
Rock: hydrothermally altered biotitic gneiss (melanosome from migmatite)

Construction: lepido-granoblastic

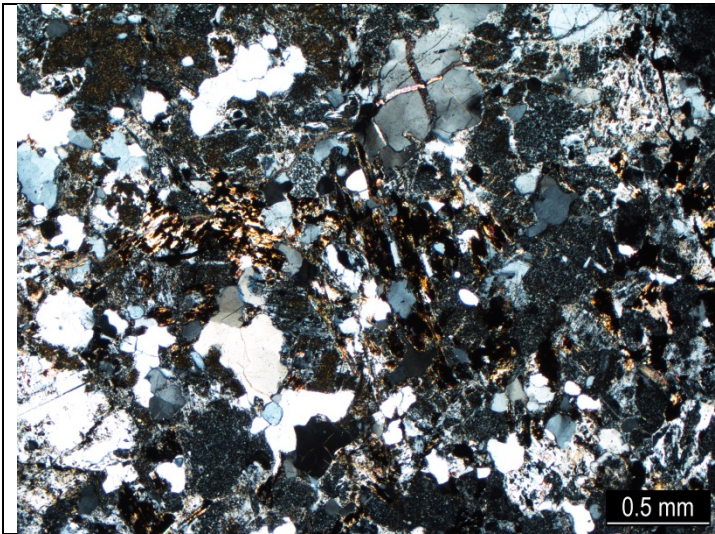
Grain size: medium grained (1-2 mm)

Description: The rock consists mainly of hypidioblastic plagioclase, xenoblastic quartz and biotite. The plagioclase and biotite are significantly affected by secondary transformations. Apatite and zirconium are present as accessory minerals.

Secondary transformations and alterations: The plagioclase is affected by intensive sericitisation and clouded by clay minerals. The biotite is chloritised and often also baueritised. The rock is penetrated by carbonate veins. Moreover, carbonates also locally suppress the plagioclase. Irregular carbonate grains are abundant in the intergranular spaces between the plagioclase.



Hydrothermal calcite veins (XPL).



Intensely altered rock containing feldspars affected by intensive sericitisation and kaolinisation. The biotites are baueritised and chloritised (XPL).

 SÚRAO	Radionuclide migration processes in a crystalline rock environment. Final report.	Evidenční označení:
		SÚRAO TZ 333/2018

Appendix 3 Recommended procedure for determining the Hg porosimetry of rock samples

Sample preparation

- Use an accurate diamond saw for formatting - accurate sample preparation aimed at filling as much of the space in the penetrometer as possible
- always take (macro) photos of the samples prior to analysis
- ideally: SEM photos of the surfaces of the samples for the justification of readings for apertures larger than (100/10/1 μm), pore gap calibration
- dry at ≤ 40 °C for approx. 24–48 h; this can be monitored via accurate weighing and the subsequent adjustment of the time for similar samples
 - this reduces the probability of thermal damage to the sample due to the differing thermal expansion of the various minerals (quartz versus the rest)
 - the disadvantage may be a larger moisture balance in the sample, which will result in the longer emptying time of the sample by the porosimeter prior to the commencement of the analysis
 - however, since it empties to a predetermined pressure value, there is no risk that the quality of the analysis will be adversely affected by the lower drying temperature

Settings and experimental conditions

- the same experimental conditions for all the samples
- specimen holder, device, lab
 - penetrometer - use one specific device
 - mercury temperature during the experiment: air-conditioned room, recording of the results, inputs to the calculation
- experimental conditions
 - pressure increments, i.e. the size intervals of the apertures
 - equalisation time between each increment (high pressure part): 3 minutes recommended
 - blank run correction, see below
 - mercury wetting angle 130°–140°, recommended 130° (more common), in any case, the same for all
- blank run correction, preferably on the basis of the analysis of a non-porous steel cylinder with a volume similar to that of the samples (or it is possible to use already measured samples with Hg-filled pores; it reacts more realistically depending on the mineralogical composition)
 - the same experimental settings as for the sample analysis including the penetrometer and all the experimental conditions
- re-intrusion - reduce to atmospheric pressure once maximum pressure is attained and then once more increase to the maximum
 - only the “free porosity”, i.e. the cracks are filled during re-intrusion
 - provides information for the interpretation of the ratio of the cracks to total porosity
 - reset the pressure increment steps and equalisation time in the same way as for intrusion
- recommended: the custom manufacturing of the penetrometer with a non-standard low probe for increased accuracy at low porosities

 SÚRAO	Radionuclide migration processes in a crystalline rock environment. Final report.	Evidenční označení:
		SÚRAO TZ 333/2018

- manufacturer recommended minimum 10-20%, optimally around 50%

Recording of the results

- always in tabular form (excel, txt, ...)
- to allow for the compilation of auxiliary graphs
- containing (Micromeritics) all the parametric data obtained from the experiment, so it is more easily usable than (customer) .pdf
- include the “volumetric median pore size” in the statistics of the results
- the unimodal aperture size distribution is best described by the characteristic aperture size
- allow for manual adjustments
- allow for processing for any purpose

 SÚRAO	Radionuclide migration processes in a crystalline rock environment. Final report.	Evidenční označení:
		SÚRAO TZ 333/2018

Appendix 4 Helsinki University “Report on the Determination of the Porosity of Samples via the C14.PMMA Method”

TECHNICAL NOTE HYRL 1_2019

January 2019

C-14-PMMA impregnations of Czech granite samples

Juuso Sammaljärvi, Ville Nenonen, Jussi Ikonen & Maikki Siitari-Kauppi

Radiochemistry, Department of Chemistry, University of Helsinki, Finland

C-14-PMMA impregnations of five Czech granite samples

Five granite samples were impregnated with C-14-PMMA for porosity analyses in University of Helsinki.

The samples were sent to HYRL in September 2018. The samples are listed in Table 1 below.

Table 1. Overview of samples sent by Věnda Havlova, Nuclear Research Institute, Prague, Czech Republic (UJV).

Sample code	location site	place	depth m	diameter cm thickness mm	description	note
2016_1 PZV1_97A	Pozdátky 140 Horka	PZV1	97-98	47 5	durbachite amphibol biotic syenite	drill core 76mm
1216_1 B3_3_A	Rozná-PVP Bukov 171 Kravi Hora	ZK1	550	47 5	migmatite	oriented sampling

 SÚRAO	Radionuclide migration processes in a crystalline rock environment. Final report.	Evidenční označení:
		SÚRAO TZ 333/2018

816_2 B2_1_B	Rozná-PVP Bukov PVP Bukov	ZK1	550	47 5	amphibolite	oriented sampling
1916_2 TIV1_90B	Tisu u Blatna 120Certovka	TIV1	90,17- 91,0	47 5	biotic granite slight alteration	drill core 76mm
3517_2_3 D2_2/3	Destná 130 Cihadlo	quarry Destná	30	47 5	granite	drill from rock block

The samples were Czech granites; diameter of 47 mm and thickness of about 5 mm from different locations of the country.

Drying

All samples were dried in oven at 105 °C for 12 days. The samples were placed into plastic vials which were placed to the aluminium chambers and kept at room temperature (21 ± 2 °C) under vacuum before impregnation.

Impregnation

Impregnation was done under vacuum and thereafter the samples were placed in refrigerator, and held there for 26 days. The C-14-MMA volume for each sample was 210 ml and the specific activity was 340 kBq/ml. All the samples were immersed in C-14-MMA until the polymerisation that was done by heating polymerization.

Polymerisation

The tracer solution contained 0.25 % (w/w) of azobisisobutyronitrile (AIBN) as a thermal initiator for polymerization. Polymerisation was carried out in a water bath using optimized heating polymerization procedure.

Sample handling

 SÚRAO	Radionuclide migration processes in a crystalline rock environment. Final report.	Evidenční označení:
		SÚRAO TZ 333/2018

The samples cutting and polishing was done in University of Helsinki, Department of Chemistry (HYRL).

Polishing was done with silicon carbide powder and using water as the polishing liquid.

 SÚRAO	Radionuclide migration processes in a crystalline rock environment. Final report.	Evidenční označení:
		SÚRAO TZ 333/2018

Autoradiography

Autoradiography was performed at HYRL with Kodak Biomax films using an exposure time of 22 days. The preliminary results are shown in this technical note. The porosities provided by autoradiography are absolute porosity values. The porosity results are tabulated in Table 2.

Table 2 HYRL porosity results, 10% uncertainty

Sample name	Porosity by film autoradiography (HYRL)	Porosity by water gravimetry (HYRL)
B2_1B 816_2	0,44	0,66
B3_3A 1216_1	0,67	0,45
D2_2/3 3517_2_3	0,83	0,98
PZV1_97A 2016_1	0,87	0,77
TIV1_90B 2116_2	0,94	0,58

The Figures 1-5 show the samples that were sent for C-14 PMMA impregnation. C-14-MMA intruded thoroughly into all five granite samples and the C-14 PMMA autoradiography revealed the pore structures of the studied samples.

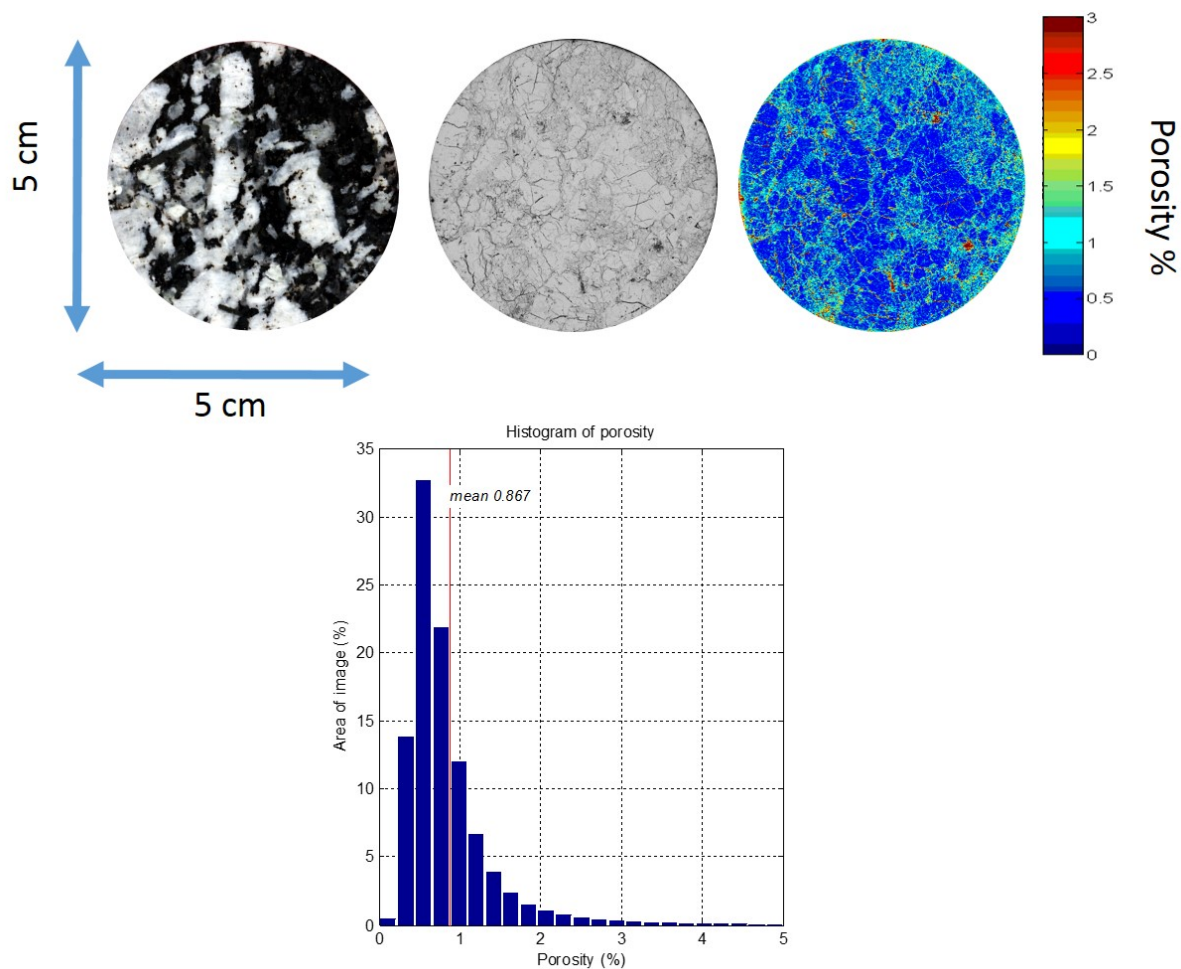


Figure 1. Surface scan (left), autoradiogram (right) and porosity histogram of sample PZV1_97A.

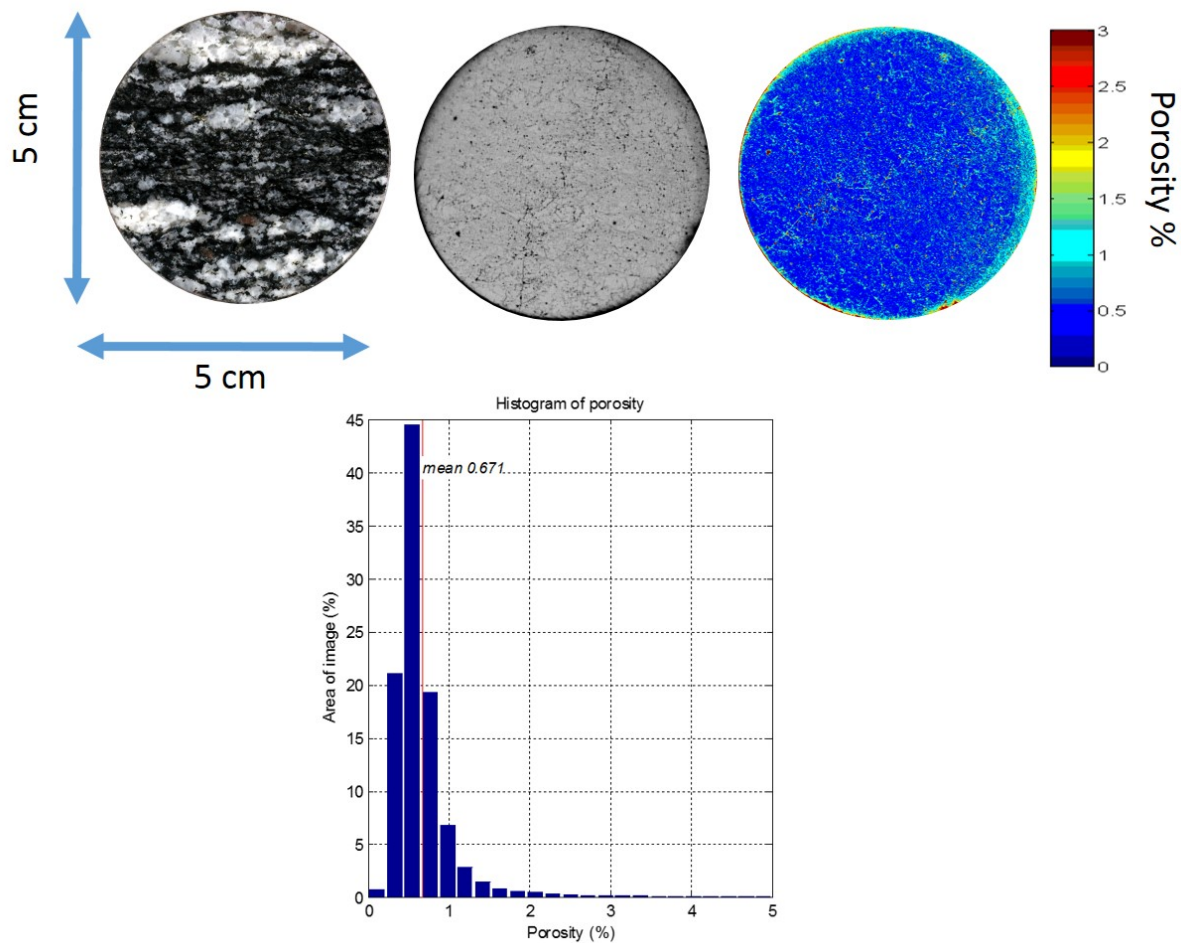


Figure 2. Surface scan (left), autoradiogram (right) and porosity histogram of sample B3_3_A.

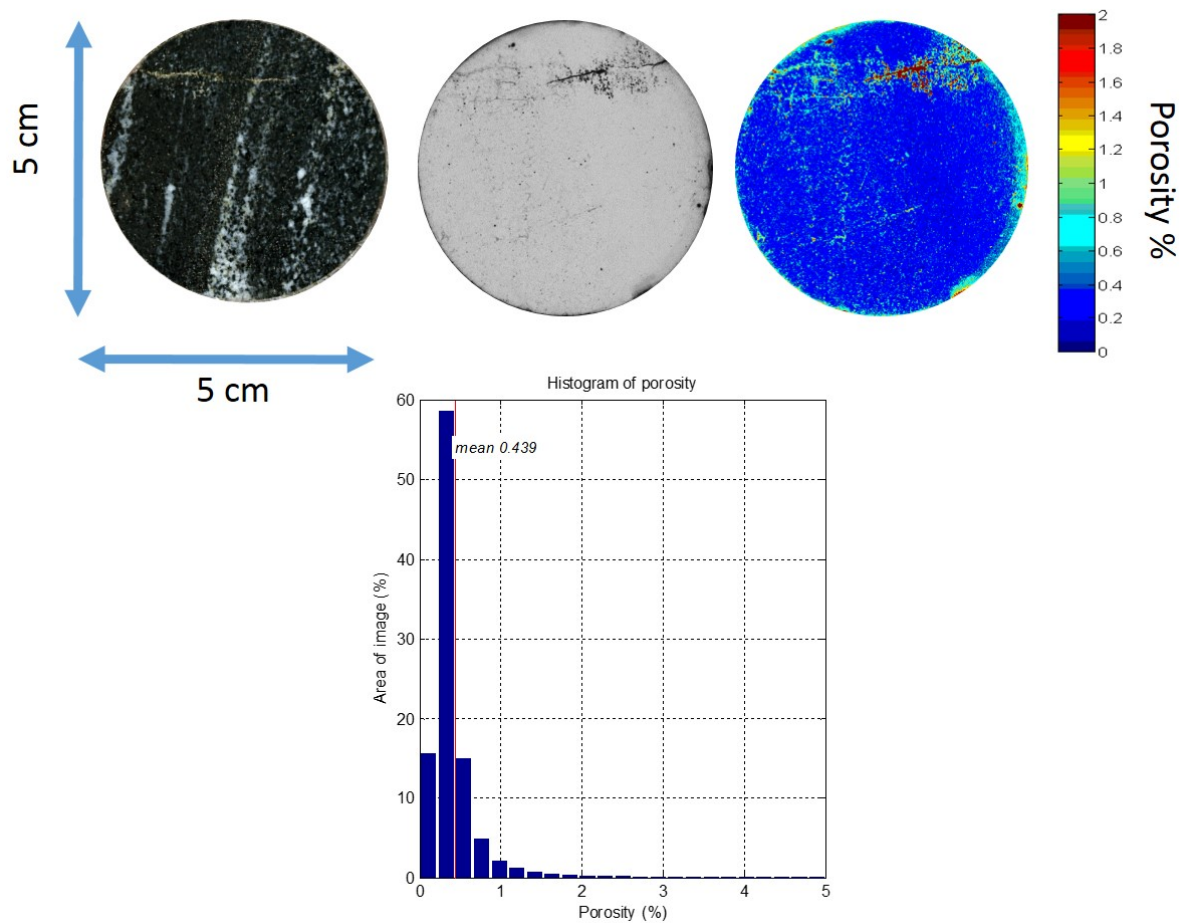


Figure 3. Surface scan (left), autoradiogram (right) and porosity histogram of sample B2_1_B.

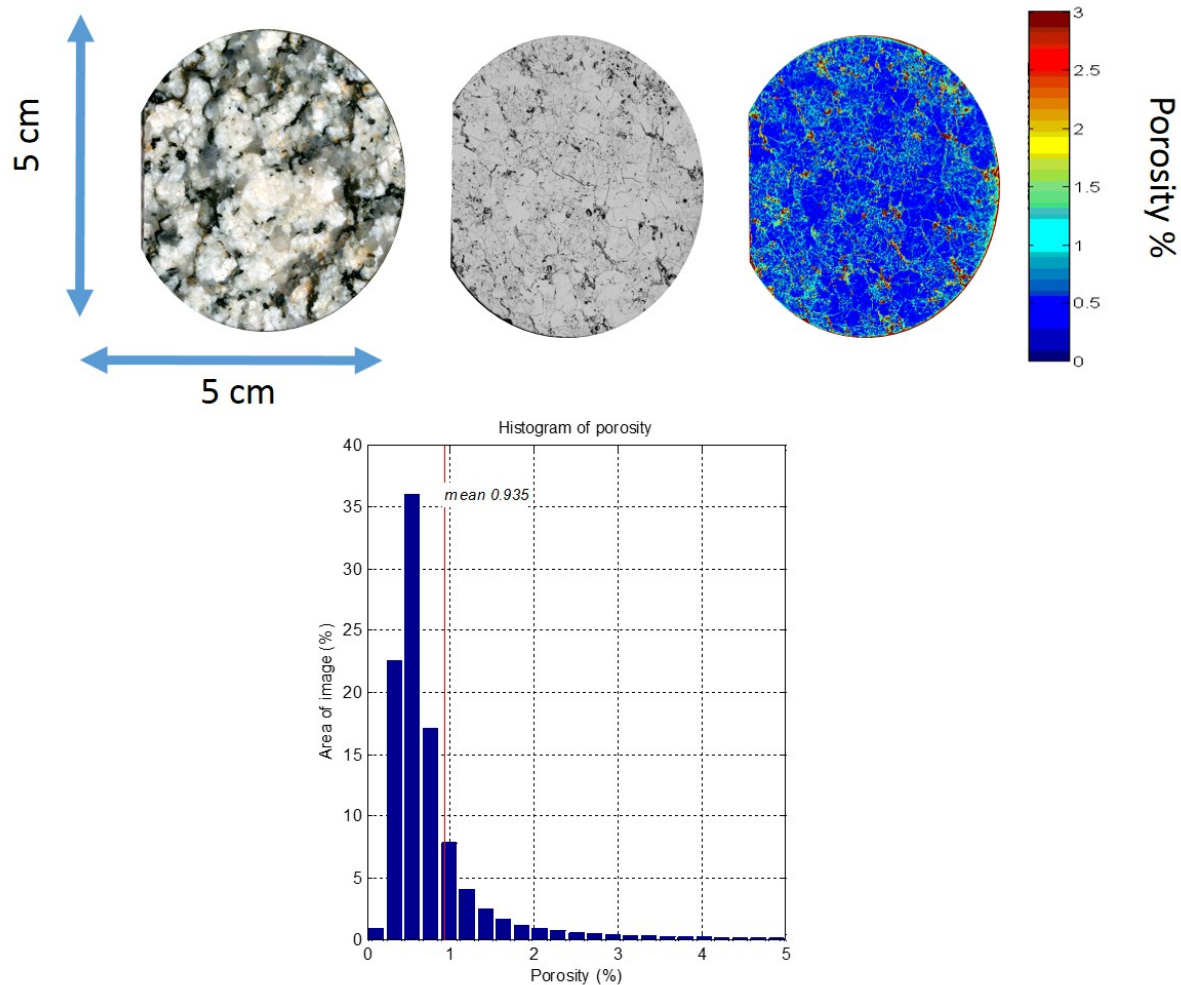


Figure 4. Surface scan (left), autoradiogram (right) and porosity histogram of sample TIV1_90B.

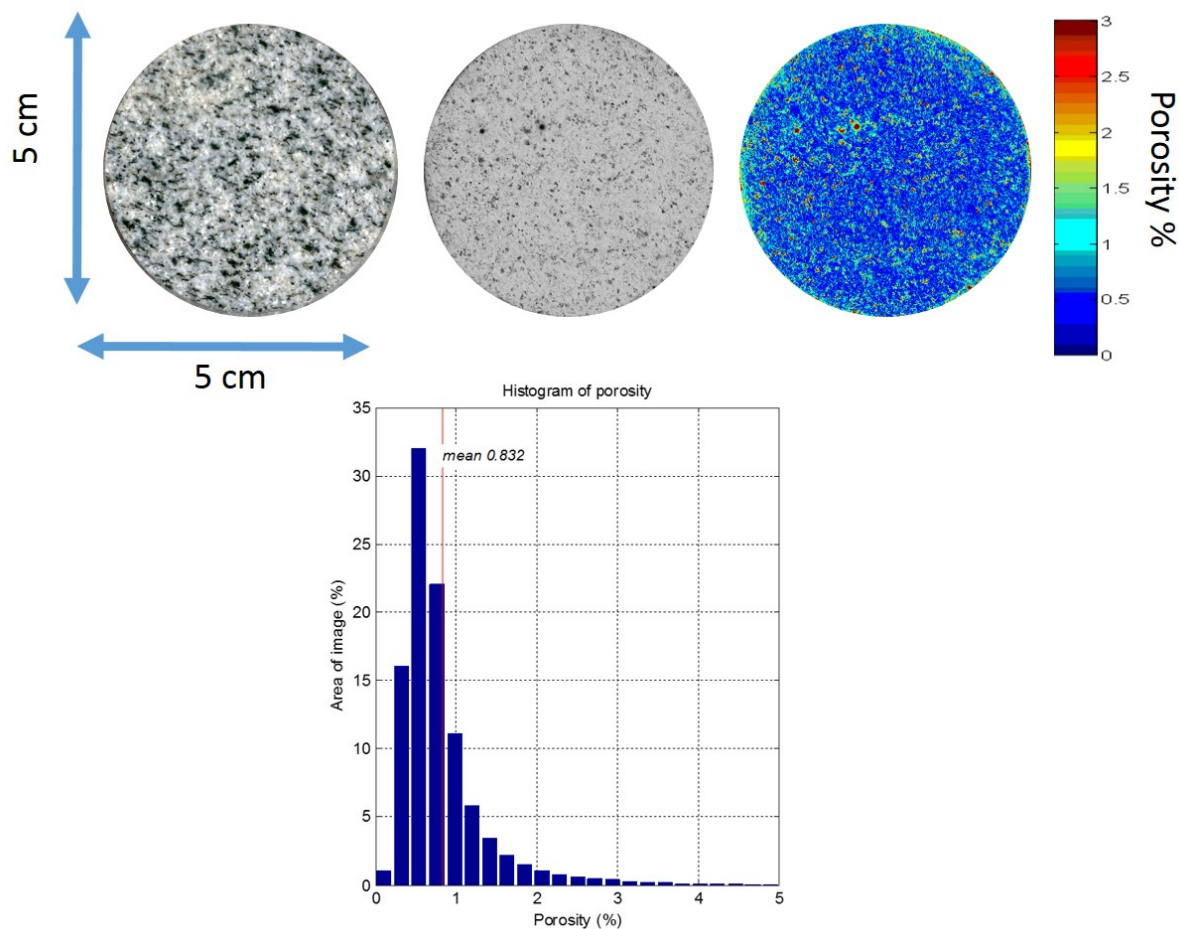


Figure 5. Surface scan (left), autoradiogram (right) and porosity histogram of sample D2_2/3.

Conclusion

The samples were dried, impregnated and polymerised successfully, followed by cutting and polishing. There are plans to do further image analysis from the autoradiography results. These findings would also benefit from electron microscopy-based mineralogical analysis.

 SÚRAO	Radionuclide migration processes in a crystalline rock environment. Final report.	Evidenční označení:
		SÚRAO TZ 333/2018



SÚRAO

SPRÁVA ÚLOŽIŠŤ
RADIOAKTIVNÍCH
ODPADŮ

NAŠE
BEZPEČNÁ
BUDOUCNOST

info@suroao.cz | www.suroao.cz